ASSESSING GREENLAND ICE SHEET MELTWATER LOSSES AT THE PIXEL AND DRAINAGE BASIN SCALE

By

SAMIAH MOUSTAFA

A dissertation submitted to the

Graduate School-New Brunswick

Rutgers, The State University of New Jersey

In partial fulfillment of the requirements

For the degree of

Doctor of Philosophy

Department of Geography

Written under the direction of

Åsa K. Rennermalm

And approved by

____

____

____

____

New Brunswick, New Jersey

May, 2017

ABSTRACT OF THE DISSERTATION

Assessing Greenland ice sheet meltwater losses at the pixel and drainage basin scale

By SAMIAH MOUSTAFA

Dissertation Director:

Dr. Åsa K. Rennermalm

The Greenland Ice Sheet (GrIS) is expected to increase its contributions to sea level rise with atmospheric warming, and it is important to accurately predict future sea level change. Surface meltwater runoff losses, modulated by surface albedo, are two dominant uncertainties in future GrIS sea level rise estimates. The first component of this study characterizes surface albedo in the lower ablation zone, a key variable controlling the surface energy and mass balance of the GrIS, and an important parameter in regional climate models (RCMs). This analysis is expanded in a second study to evaluate satellite albedo retrievals and assess its ability to resolve sub-pixel spatial variability of ablation area albedo. In situ spectral albedo data collected along a transect, Moderate Resolution Imaging Spectroradiometer (MODIS) daily albedo product, and high spatial resolution WorldView-2 (WV-2) data are utilized in these two studies. The results show that the distribution of dominant ice surface types (e.g., snow, bare ice, light-absorbing impurities, and streams) act as an additional mechanism for controlling ablation zone

albedos. This can significantly impact seasonal and inter-annual changes in ablation zone albedo, and subsequent melt. These findings have important implications for current RCMs, which don't fully integrate a seasonally evolving ice surface type's albedo scheme. The second study demonstrates over spatially heterogeneous surfaces, such as in the ablation zone, that a multiple 'point-to-pixel' comparison, utilizing multiple ground albedo observations coinciding with a satellite pixel, is superior to the frequently used single 'point-to-pixel' comparison. This points to the significance of evaluating the spatial representativeness of ground albedo sites (e.g., automatic weather stations) prior to validation of satellite or model-derived albedos.

The second component of this study quantifies meltwater runoff losses, a dominant, yet understudied term of GrIS mass loss, at the drainage-basin scale. To do this, the Modèle Atmosphérique Régionale (MAR) RCM discharge estimates are compared with proglacial river discharge observations at three drainage basins – Thule, Watson, and Nuuk – located north-to-south in west Greenland. I find that MAR poorly resolves daily discharge variability in the Nuuk and Thule basins, but is better able to capture variability at longer time averages. Model-observation agreement is reduced during peak discharge events. The model-observation discharge discrepancies are likely due to an underestimation of cloud cover, from an overestimation of downward shortwave radiation. The discrepancies of model and measurements during peak discharge events is important to understand as they are expected to occur more frequently with continued warming. In a fourth study, annual and daily peak river discharge was unprecedented at all basins in the extreme melt season of 2012. Exceptional flows in all three rivers were observed corresponding with two ice sheet wide surface melt episodes in mid- and late-July 2012.

These results suggest the need to further study runoff processes at the local-, basin- and continental-scale not fully captured by current RCMs. These four studies collectively contribute information that will allow for better understanding of Greenland's complex hydrologic system. Finally, these studies provide the framework to improve physical representation of meltwater runoff and albedo components used in RCMs to project changes in Greenland's mass loss, and subsequent contributions to sea level rise.

Acknowledgements

I want to sincerely thank all of the people that helped make this work possible. I want to especially thank Dr. Åsa Rennermalm, my PhD committee chair, for your unwavering support, guidance, optimism, and encouragement to help me be the best that I can be. Åsa defines what it means to truly be an adviser – your open door policy, your willingness to listen and offer constructive feedback, and your can-do attitude made my experience at Rutgers University unparalleled. You've instilled in me what I hope to emulate as a future adviser, colleague, and friend. I also want to thank the other committee members, Drs. David Robinson, Lora Koenig, and Richard Lathrop for their insight, guidance, and feedback and support as this research progressed and took shape. I also want to thank the faculty and staff of the Rutgers University Geography Department for their support and consistent help. I thank the staff at the Center for Remote Sensing and Spatial Analysis for providing valuable suggestions regarding GIS and remote sensing-related questions. My experiences at NASA Goddard Space Flight Center, under the advisement of Drs. Lora Koenig and Dorothy Hall, were invaluable for shaping this research and establishing new research connections. I especially want to thank my friends, Joanne Bartley, Jenny Kafka Lei, and Sara Duncan, whom have provided continuous support since the beginning of graduate school. Lastly, I would like to thank my family for their unending support. Dad, you believed in me when it felt like no one else did. Mom, your wit and humor always made the ups and downs easier to manage. The support, motivation, love and encouragement of my partner, Louis Huang, cannot be understated. This work here would not have been possible without the support of many through the years, and I thank each and every one of you.

Finally, I would like to acknowledge my co-authors, including: Drs. M.A. Miller, J.R. Mioduszewski, L.S., Koenig, M.G. Hom, C.A. Shuman, M.O. Román, Z. Wang. C.B. Schaaf, L.C. Smith, A. Erb, M. Tedesco, T. Mote, B. Hagerdorn, I. Overeem, R. Sletten, A.B. Mikkelsen, B. Hasholt, D. van As, D.K. Hall, and P. Alexander.

This research was financially supported by the Department of Geography Excellence Fellowship, NASA Earth and Space Science Fellowship grant NNX12AN98H, NASA Cryosphere Program grant NNX11AQ38 (Chapters 2-3) and grant NNX14AH93G (Chapters 4-5), NASA IDS NNX14AD98G (Chapters 4-5), the Rutgers Climate Institute Student Travel Award, and the graduate school of New Brunswick.

Note, that the majority of the work here is done by me. The pronoun “we” is sometimes used, which is more commonly used than “I”. “We” is frequently used in writing scientific papers, and does not signify that the work was done by anyone else.

Table of Contents

List of Tables

List of Illustrations

Chapter 1: Introduction

1.1 Background

Observational records indicate that atmospheric greenhouse gases (GHGs) such as carbon dioxide, nitrous oxide, and methane have increased considerably over the last 200 years (Cubasch et al., 2013). In addition, an increase in global mean annual temperatures have been observed, with average temperatures over the Arctic double the global mean since 1980 (AMAP, 2011). The current time period, suggested as the Anthropocene Epoch (Lewis and Maslin, 2015), is dominated by human activity. This activity has contributed to observed increases in GHGs and therefore temperatures, and a global energy imbalance, with the Earth absorbing more heat content than it is radiating back to space (von Schuckmann et al., 2016). Warming trends are expected to continue in the future, impacting the Arctic and the Greenland Ice Sheet (GrIS). The GrIS is the second largest ice sheet in the world, contributing to changes in sea ice area, mass loss, the surface energy balance (Vaughan et al., 2013), and global sea level rise (Church et al., 2013).

Amplified warming in the Arctic has resulted in measurable changes to several cryospheric components (i.e., snow, sea ice, and ice sheets). Snow cover and sea ice extent, important variables for reflecting away a significant amount of incoming solar radiation, have declined in the Northern Hemisphere (Callaghan et al., 2011; Serreze et al., 2009). Reduction in snow and sea ice cover has implications for the Arctic’s radiative budget, via the ice-albedo feedback. Where, the reduced surface albedo leads to the increase in the surface absorption of the sun’s energy and additional melting when snow and ice retreat (Screen and Simmonds, 2010). Freshwater influx into the ocean from melting snow and ice may also influence ocean circulation (Fichefet et al., 2003) and nutrient availability for phytoplankton (Bhatia et al., 2013). The addition of meltwater from snow and ice to the oceans also contributes to rising sea levels and has societal implications for coastal areas prone to inundation. Changes in each of these components of the Arctic are active indicators of climate change, and have long-term consequences on physical, biological, and social systems (Vaughan et al., 2013). Therefore, it is important that we can accurately quantify current and future changes in the Arctic in the context of a changing climate.

1.2 The Greenland ice sheet

Within the Arctic, the GrIS is the largest body of permanent ice and snow cover, spanning 1.7 million km^2 (Bamber et al., 2001), with the potential to add 7.36 m of sea level rise equivalent (Vaughan et al., 2013), if completely melted. In recent decades, the GrIS has experienced an acceleration of mass loss (Hanna et al., 2013), decreasing from 398 ± 112 Gt yr^{-1} over the 1961-1990 period to 306 ± 120 Gt yr^{-1} over 1991-2015, on average, corresponding to a ~0.47 ± 0.23 mm sea level rise equivalent (from 1991-2015; van den Broeke et al., 2016).

Air temperature over Greenland has increased substantially (by 1.8 °C) since the 1990s (Box et al., 2009), with recent positive trends of 0.55 ± 0.44 °C $decade^{-1}$ over the 2000-2013 period (Hall et al., 2013). Increases in air temperature correspond to recent enhancements in surface melt (Mernild and Liston, 2011), runoff (Mernild and Liston, 2012), and increases in melt area (Mote, 2007; Fettweis et al., 2011; Tedesco, 2007;

Tedesco et al., 2011). The observed increase in surface meltwater runoff accounts for up to two-thirds of the ice sheet's total mass loss (van den Broeke et al., 2009; Enderlin et al., 2014). This recent increase in surface meltwater runoff has driven negative trends in surface mass balance (SMB), with a decrease of -10.2 ± 2.3 Gt yr^2 from 1991-2015 (van den Broeke et al., 2016).

The total mass balance (MB) of the GrIS is expressed as the difference of SMB and solid ice discharge (D), from dynamic losses at the ice-ocean interface. The SMB of the GrIS is defined as the balance between accumulation and ablation terms. Expressed as an equation, SMB = P – RU – SU – ER, where P is total precipitation (snow and rain), RU is meltwater runoff, SU is total sublimation (surface and drifting snow), and ER is the divergence of blowing snow. SMB is a change in mass over time, generally expressed in units of Gt yr^{-1}. Regions where SMB > 0, correspond to the accumulation zone (and, SMB < 0 correspond to the ablation zone). The surface energy balance (SEB) is responsible for determining how much melt energy is available, and expressed as an equation is: $SEB = SW\downarrow(1 - \alpha) + LW_{net} + SH + LH + G_s$, where $SW\downarrow$ is downward shortwave radiation, α is surface albedo, LW_{net} is net longwave radiation, SH and LH are sensible and latent heat fluxes (turbulent terms), and G_s is subsurface heat flux. Net radiation is the summation of SW_{net} and LW_{net}. The SEB is responsible for determining surface meltwater production, and is therefore important for determining RU – the dominant term dictating the recent imbalance of the GrIS. The other important variable, surface albedo (α), modulates downwelling solar radiation, and is therefore important for determining how much energy is available to melt the surface.

Meltwater runoff, RU, is defined as the net surface horizontal divergence of water over an area. Meltwater runoff is a dominant process for GrIS mass loss (Hanna et al., 2013; Enderlin et al., 2014) and is therefore relevant for estimating GrIS contribution's to sea level rise. Meltwater runoff is also an important component of Greenland's hydrologic system. During the summer, meltwater produced at the ice sheet surface runs off via supra-, en-, and sub-glacial pathways (Fig. 1.1). Meltwater that enters en- and sub-glacial networks through moulins, crevasses, supraglacial lakes, and ice fractures can impact ice dynamics (Bartholomew et al., 2012). The influx of meltwater into the glacier bed can temporarily increase ice flow velocities due to bed lubrication and induce transitory seasonal speed-ups dependent upon the efficiency of the sub-glacial drainage system (e.g., Zwally et al., 2002; Sundal et al., 2011; Tedstone et al., 2013; Stevens et al., 2016). Alternatively, meltwater runoff on the ice surface can be transported efficiently in distributed supraglacial streams (Smith et al., 2015), some of which intersects with supraglacial lakes, crevasses and moulins to enter the en- and sub-glacial system, before reaching proglacial rivers downstream of the ice sheet margin. Some of the meltwater that does not immediately runoff is retained by firn or refreezes. The remainder runs off into downstream proglacial rivers (with negligible retention in terrestrial groundwater and pond features). *River discharge*, defined as the surface horizontal water flow in a river, provides a means to directly measure how much meltwater truly escapes the ice sheet from riverine systems. However, few observational studies have been conducted to quantify losses and understand the GrIS hydrologic system (Rennermalm et al., 2012; Smith et al., 2015; Hasholt et al., 2013). This lack of scientific understanding limits our ability to accurately model meltwater runoff, an important climate variable capable of directly affecting inputs to sea level rise.

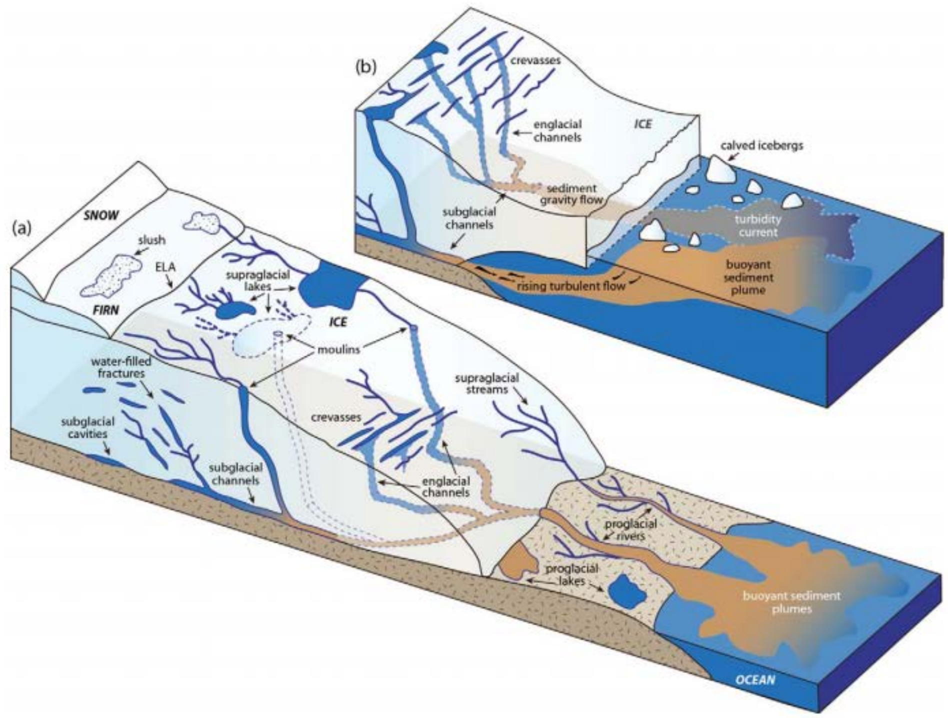

Figure 1.1 Components of Greenland's hydrologic system from the ice sheet interior to terminus for a land-terminating (a) and marine-terminating outlet (b). In (a), above the equilibrium line altitude (ELA) is the accumulation zone where water can percolate through the snow/firn, pool into slush zones, and channelize into supraglacial rivers. Below the ELA is the ablation zone where meltwater pools in supraglacial lakes flows through supraglacial rivers into crevasses and moulins, entering the en- and sub-glacial channels, which ultimately escape into downstream pro-glacial rivers and lakes. Meltwater transport from the ice sheet to oceans accumulates sediment debris. This sediment-rich water reaches the ocean as a buoyant plume. In (b), meltwater escapes the ice sheet via different mechanisms. Sediment-rich sub-glacial discharge is released tens to hundreds of meters below the water surface to rise and form a buoyant plume or turbidity current sub-surface. In this study, the hydrologic system of land-terminating glaciers (a) is investigated only. Source: Chu et al., Progress in Physical Geography, 2013.

Local feedback processes, such as the melt-albedo feedback, covary with increases in surface melt and runoff. This is determined by net solar radiation and surface albedo. *Surface albedo* is defined as the fraction of outgoing solar radiation to incoming solar radiation. Surface albedo modulates the amount of solar radiation absorbed at the ice surface (Stroeve et al., 2013), and therefore, meltwater production. During the summer, the melt-albedo feedback involves increased melting, thereby reducing surface albedo and, by increasing the absorption of solar radiation at the surface, accelerating melt further (Box et al., 2012). Lower surface albedo is driven by enhanced snow grain metamorphic rates (Tedesco et al., 2011), expansion of bare ice area (Alexander et al., 2014) and light-absorbing impurities (Warren and Wiscombe, 1980), dust deposition (Bøggild et al., 2010; Wientjes and Oerlemans, 2010), and the development of hydrologic features (Smith et al., 2015).

The summer of 2012 was marked by extraordinary surface melt extent (Nghiem et al., 2012; Hall et al., 2013), duration (Tedesco et al., 2013) and runoff (Smith et al., 2015). The 2012 extreme melt episode (Fig. 1.2) covered ~97% of the ice sheet surface (Nghiem et al., 2012) coinciding with anomalously warm atmospheric circulation patterns (Fettweis et al., 2013; Hanna et al., 2013). Ice core records indicate a similar melt event had not occurred since 1889 (Keegan et al., 2014). Surface albedo, two standard deviations below the 2003-2012 average (Tedesco et al., 2013), contributed to the extreme surface melt and runoff in 2012 (Stroeve et al., 2013). Amplified hypsometry and depleted firn retention (Mikkelsen et al., 2016) as well as the development of a hydrologically efficient drainage system (Smith et al., 2015) assisted in evacuating the unprecedented surface meltwater runoff, as observed in western Greenland. This ice sheet-wide event was also partly attributed to the enhancement of nonradiative fluxes (Fausto et al., 2016) and cloud formation (Bennartz et al., 2013; Van Tricht et al., 2016). Understanding processes and drivers of extraordinary melt events like 2012 will be increasingly important as they become more frequent in a warming climate (McGrath et al., 2013). These main components of the GrIS are important indicators of climatic change. Developing a robust framework to understand component processes' behavior at local scales up to the entire ice sheet is needed. In this context, it is important to understand how surface meltwater runoff is routed from the ice sheet interior to downstream proglacial rivers and how local mechanisms, namely albedo, control it. This thesis utilizes a multi-scale and multi-methodological approach to gather insight into surface meltwater runoff and albedo processes, in an effort to improve our current and future understanding of Greenland's surface hydrology and its relation to albedo (see Section 1.3).

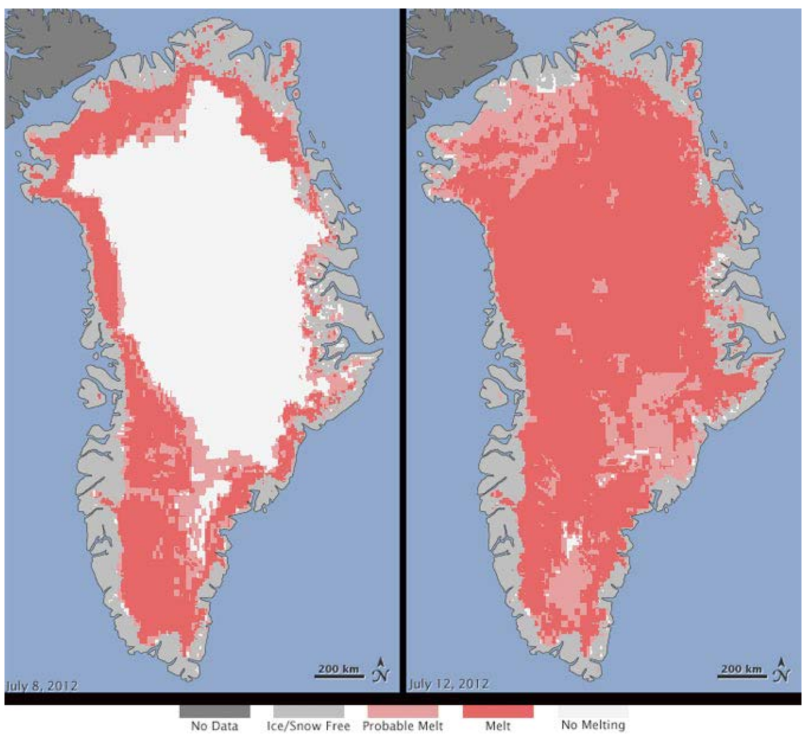

Figure 1.2 Surface melt extent over the GrIS on 8 July (left) and 12 July (right) 2012. Roughly 40% of the ice sheet surface area melted on 8 July. Four days later, nearly 97% of the ice sheet surface was melting. Areas of probable melt (light pink) refer to sites where at least one satellite detected melting. Areas of melt (dark pink) refer to areas where two or three satellites identified melting. Source: Nicolo E. DiGirolamo, SSAI/NASA GSFC, and Jesse Allen, NASA Earth Observatory.

1.3 Science Questions and Dissertation Organization

The aim of this thesis is to quantify meltwater runoff losses from the GrIS and identify the albedo feedbacks and processes between the atmosphere and ice sheet surface that ultimately impact surface melt. Specifically, the work centers around two main science questions. Each question is examined in two chapters each as outlined below. The two main science questions focus on understanding surface albedo and meltwater runoff losses. This thesis investigates each of these components individually and collectively to understand how they intimately link energy balance terms to mass loss.

1.3.1 Science question 1: How does surface albedo vary spatially, and what impact does it have on melting in Greenland's ablation zone?

The first part of the thesis examines surface albedo, a key variable controlling surface energy and mass balance of the GrIS. Over the last decade, a decline in albedo has been observed, assisting in the exceptional 2012 (Tedesco et al., 2013) and recent 2015 (Tedesco et al., 2016) melt years. During the summer months, warmer temperatures melt snow or firn layers to expose underlying bare ice surfaces that reduce surface albedo further. As the melt season progresses, the surface continues to ablate, meltwater ponds and runs off to develop into coherent supraglacial streams, cryoconite holes (water-filled depressions containing mineral dust and microbial communities) populate the surface, and bare ice surfaces melt out further exposing underlying impurities from outcropped layers. In Chapter 2, these features are categorized into distinct surface types with different albedos including: snow, ice, dust and light-absorbing impurities, cryoconite holes, melt ponds, and streams. Ice surface types are more prevalent in the lower elevations of the GrIS (i.e., the ablation area). However, the importance of these surface types on ablation area albedo, and thus, meltwater generation over the melt season, until recently, remained unresolved.

Surface albedo is typically characterized with the MODerate Resolution Imaging Spectroradiometer (MODIS) satellite sensor (Stroeve et al., 2013; Wang et al., 2012, 2014, 2016; Wright et al., 2014) and modeled in regional climate models (RCMs) such as Modèle Atmosphérique Régionale (MAR; Alexander et al., 2014; Tedesco et al., 2016) and Regional Atmospheric Climate MOdel (RACMO2; van Angelen et al., 2012; Noël et al., 2015). Satellite and modeled surface albedo are currently validated using ground observational data from automatic weather stations (AWSs; Knap and Oerlemans, 1996; Steffen and Box, 2001; van As et al., 2013). The current version of RACMO2.3 uses MODIS data to represent spatially varying albedo on the ice surface (Noël et al., 2015), while the latest study on MAR v3.5.2 contains fixed values of albedo and does not vary below albedos less than 0.40 (Fettweis et al., 2016). Although these improvements have made modeled albedos more realistic, RCMs still lack complete representation of processes that drive ice albedo changes, such as spatiotemporal variability in sediment-rich impurities and cryoconite hole coverage. Differences in albedo parameterizations in RCMs can result in large inter-model discrepancies in SMB (Rae et al., 2012; van Angelen et al., 2012), and thus, runoff (up to 42%; Vernon et al., 2013).

To answer the research question, two analyses were conducted. The first analysis, presented in Chapter 2, evaluates the importance of distinct surface types on ablation area albedo and ablation rates using in situ and remotely sensed data. This objective will serve to characterize dominant ice surface types in the lower ablation area, their seasonal evolution, and implications for surface meltwater production and runoff. These efforts will improve our understanding of surface type's contribution to the melt-albedo feedback, and its implications for current and future SMB modeling efforts. My results demonstrate that seasonal changes in GrIS ablation area albedos are driven by changes in the fractional coverage of ice surface types.

The second analysis, presented in Chapter 3, evaluates the spatial heterogeneity of surface albedo in the lower ablation area using satellite imagery and in situ spectral albedo data. This analysis serves to validate the assumption that sub-pixel variability in albedo can be spatially representative up to the pixel footprint. This analysis is important for accurately characterizing and validating ablation area albedos, as satellite albedo retrievals and AWSs are often compared with simulated albedos (Alexander et al., 2014; Tedesco et al., 2016). My results show the importance of multiple surface-based measurements in testing satellite-derived albedo over spatially heterogeneous surfaces and its implications for future ground collection efforts.

1.3.2 Science question 2: What are the meltwater runoff losses from the Greenland ice sheet?

To answer the second science question, this thesis addresses quantifying surface meltwater runoff losses, responsible for up to two-thirds of Greenland's total mass loss (Enderlin et al., 2014). In recent years, runoff has increased (Mernild et al., 2012) exiting at the ice sheet margin via supra-, en-, and sub-glacial drainage networks into downstream fjords, proglacial lakes, and rivers (Fig. 1.1). These positive trends in meltwater runoff are consistent with the recent, extraordinary melt event of July 2012 (Nghiem et al., 2012; Hall et al., 2013), and is expected to dominate future mass loss and sea level rise contributions from the GrIS (Hanna et al., 2013; van den Broeke et al., 2016). Despite the observed increase in meltwater runoff, how much meltwater truly escapes from proglacial rivers to the global ocean is unknown. To accurately determine meltwater runoff contributions to surrounding oceans, an understanding of physical mechanisms governing surface water hydrology is needed. However, direct, long-term observations of discharge from the GrIS are scarce (van As et al., 2012; van As et al., 2017; Hasholt et al., 2013; Mernild and Liston et al., 2012; Mikkelsen et al., 2016; Rennermalm et al., 2012; Smith et al., 2015). In the absence of observations, previous studies have evaluated surface runoff from RCMs (Cullather et al., 2016; van den Broeke et al., 2016; Noël et al., 2016), validated with detailed AWS-forced surface energy balance (SEB) models (e.g., van As et al., 2012; Fausto et al., 2016). Discharge observations are necessary to validate simulated runoff estimates from RCMs (Fettweis et al., 2012; Vernon et al., 2013). Yet, it is unclear how well RCMs estimate runoff from the GrIS. To our knowledge, this is the first study comparing long-term in situ discharge measurements to modeled discharge estimates at the drainage basin scale.

The second objective in this thesis investigates modeled discharge estimates to proglacial river discharge measurements across a latitudinal gradient along west Greenland. In Chapter 4, in situ discharge measurements are compared against simulated discharge from the widely-used MAR model. This analysis helps identify model-observation differences and potential sources of these differences at the drainage basin scale. My results demonstrate the efficacy of the MAR model capturing daily river discharge and its implications for understanding ice sheet hydrology. Finally, in Chapter 5, a smaller-scale study is conducted, focusing on proglacial river discharge variability during the extreme melt season of 2012. This directed analysis will provide insight into the 2012 melt episodes and differences in runoff response across the same drainage basins. These results provide further understanding into peak discharge events and their variability during an exceptional melt season.

1.4 References

Alexander, P. M., Tedesco, M., Fettweis, X., van de Wal, R. S. W., Smeets, C. J. P. P. and van den Broeke, M. R.: Assessing spatio-temporal variability and trends (2000–2013) of modelled and measured Greenland ice sheet albedo, Cryosph. Discuss., 8(4), 3733–3783, doi:10.5194/tcd-8-3733-2014, 2014.

AMAP: Snow, water, ice and permafrost in the Arctic (SWIPA): Climate change and the cryosphere., 2011.

van Angelen, J. H., Lenaerts, J. T. M., Lhermitte, S., Fettweis, X., Kuipers Munneke, P., van den Broeke, M. R., van Meijgaard, E. and Smeets, C. J. P. P.: Sensitivity of Greenland Ice Sheet surface mass balance to surface albedo parameterization: a study with a regional climate model, Cryosph., 6(5), 1175–1186, doi:10.5194/tc-6-1175-2012, 2012.

As, D. Van, Fausto, R. S., Colgan, W. T. and Box, J. E.: Darkening of the Greenland ice sheet due to the melt- albedo feedback observed at PROMICE weather stations, , (m), 69–72, 2013.

van As, D., Hubbard, a. L., Hasholt, B., Mikkelsen, a. B., van den Broeke, M. R. and Fausto, R. S.: Large surface meltwater discharge from the Kangerlussuaq sector of the Greenland ice sheet during the record-warm year 2010 explained by detailed energy balance observations, Cryosph., 6(1), 199–209, doi:10.5194/tc-6-199-2012, 2012.

Bamber, J. L., Layberry, R. L. and Gogineni, S. P.: A new ice thickness and bed data set for the Greenland ice sheet: 1. Measurement, data reduction, and errors, J. Geophys. Res., 106(D24), 33773, doi:10.1029/2001JD900054, 2001.

Bartholomew, I., Nienow, P., Sole, A., Mair, D., Cowton, T. and King, M. A.: Short-term variability in Greenland Ice Sheet motion forced by time-varying meltwater drainage: Implications for the relationship between subglacial drainage system behavior and ice velocity, J. Geophys. Res. Earth Surf., 117(F3), n/a-n/a, doi:10.1029/2011JF002220, 2012.

Bennartz, R., Shupe, M. D., Turner, D. D., Walden, V. P., Steffen, K., Cox, C. J., Kulie, M. S., Miller, N. B. and Pettersen, C.: July 2012 Greenland melt extent enhanced by low-level liquid clouds., Nature, 496(7443), 83–6, doi:10.1038/nature12002, 2013.

Bhatia, M. P., Kujawinski, E. B., Das, S. B., Breier, C. F., Henderson, P. B. and Charette, M. a.: Greenland meltwater as a significant and potentially bioavailable source of iron to the ocean, Nat. Geosci., 6(4), 274–278, doi:10.1038/ngeo1746, 2013.

Bøggild, C. E., Brandt, R. E., Brown, K. J. and Warren, S. G.: The ablation zone in northeast Greenland: ice types, albedos and impurities, J. Glaciol., 56(195), 101–113, doi:10.3189/002214310791190776, 2010.

Box, J. E., Yang, L., Bromwich, D. H. and Bai, L.-S.: Greenland Ice Sheet Surface Air Temperature Variability: 1840–2007*, J. Clim., 22(14), 4029–4049, doi:10.1175/2009JCLI2816.1, 2009.

Box, J. E., Fettweis, X., Stroeve, J. C., Tedesco, M., Hall, D. K. and Steffen, K.: Greenland ice sheet albedo feedback: thermodynamics and atmospheric drivers, Cryosph. Discuss., 6(1), 593–634, doi:10.5194/tcd-6-593-2012, 2012.

van den Broeke, M., Bamber, J., Ettema, J., Rignot, E., Schrama, E., van de Berg, W. J., van Meijgaard, E., Velicogna, I. and Wouters, B.: Partitioning recent Greenland mass loss., Science, 326(5955), 984–6, doi:10.1126/science.1178176, 2009.

van den Broeke, M. R., Enderlin, E. M., Howat, I. M., Kuipers Munneke, P., Noël, B. P. Y., van de Berg, W. J., van Meijgaard, E. and Wouters, B.: On the recent contribution of the Greenland ice sheet to sea level change, Cryosph., 10(5), 1933–1946, doi:10.5194/tc-10-1933-2016, 2016.

Burakowski, E. A., Ollinger, S. V., Lepine, L., Schaaf, C. B., Wang, Z., Dibb, J. E., Hollinger, D. Y., Kim, J., Erb, A. and Martin, M.: Spatial scaling of reflectance and surface albedo over a mixed-use, temperate forest landscape during snow-covered periods, Remote Sens. Environ., 158, 465–477, doi:10.1016/j.rse.2014.11.023, 2015.

Callaghan, T. V., Johansson, M., Brown, R. D., Groisman, P. Y., Labba, N., Radionov, V., Barry, R. G., Bulygina, O. N., Essery, R. L. H., Frolov, D. M., Golubev, V. N., Grenfell, T. C., Petrushina, M. N., Razuvaev, V. N., Robinson, D. a., Romanov, P., Shindell, D., Shmakin, A. B., Sokratov, S. a., Warren, S. and Yang, D.: The Changing Face of Arctic Snow Cover: A Synthesis of Observed and Projected Changes, Ambio, 40(S1), 17–31, doi:10.1007/s13280-011-0212-y, 2011.

Chandler, D. M., Alcock, J. D., Wadham, J. L., Mackie, S. L. and Telling, J.: Seasonal changes of ice surface characteristics and productivity in the ablation zone of the Greenland Ice Sheet, Cryosph., 9(2), 487–504, doi:10.5194/tc-9-487-2015, 2015.

Church, J.A., P.U. Clark, A. Cazenave, J.M. Gregory, S. Jevrejeva, A. Levermann, M.A. Merrifield, G.A. Milne, R.S. Nerem, P.D. Nunn, A.J. Payne, W.T. Pfeffer, D. Stammer and A.S. Unnikrishnan, 2013: Sea Level Change. In: Climate Change 2013: The Physical Science Basis. Contribution of Working Group I to the Fifth Assessment Report of the Intergovernmental Panel on Climate Change [Stocker, T.F., D. Qin, G.-K. Plattner, M. Tignor, S.K. Allen, J. Boschung, A. Nauels, Y. Xia, V. Bex and P.M. Midgley (eds.)]. Cambridge University Press, Cambridge, United Kingdom and New York, NY, USA.

Cubasch, U., Wuebbles, D., Chen, D., Facchini, M. C., Frame, D., Mahowald, N. and Winther, J.-G.: Introduction, in Climate Change 2013 - The Physical Science Basis, edited by Intergovernmental Panel on Climate Change, pp. 119–158, Cambridge University Press, Cambridge., 2013.

Cullather, R. I., Nowicki, S. M. J., Zhao, B. and Koenig, L. S.: A Characterization of Greenland Ice Sheet Surface Melt and Runoff in Contemporary Reanalyses and a Regional Climate Model, Front. Earth Sci., 4(February), 1–20, doi:10.3389/feart.2016.00010, 2016.

Enderlin, E. M., Howat, I. M., Jeong, S., Noh, M.-J., van Angelen, J. H. and van den Broeke, M. R.: An improved mass budget for the Greenland ice sheet, Geophys. Res.

Lett., 41(3), 866–872, doi:10.1002/2013GL059010, 2014.

Dumont, M., Brun, E., Picard, G., Michou, M., Libois, Q., Petit, J., Geyer, M., Morin, S. and Josse, B.: Contribution of light-absorbing impurities in snow to Greenland's darkening since 2009, Nat. Geosci., 7(7), 509–512, doi:10.1038/ngeo2180, 2014.

Fausto, R. S., Van As, D., Box, J. E., Colgan, W., Langen, P. L. and Mottram, R. H.: The implication of nonradiative energy fluxes dominating Greenland ice sheet exceptional ablation area surface melt in 2012, Geophys. Res. Lett., 43(6), 2649–2658, doi:10.1002/2016GL067720, 2016.

Fettweis, X., Tedesco, M., van den Broeke, M. and Ettema, J.: Melting trends over the Greenland ice sheet (1958–2009) from spaceborne microwave data and regional climate models, Cryosph., 5(2), 359–375, doi:10.5194/tc-5-359-2011, 2011.

Fichefet, T., Poncin, C., Goosse, H., Huybrechts, P., Janssens, I. and Le Treut, H.: Implications of changes in freshwater flux from the Greenland ice sheet for the climate of the 21st century, Geophys. Res. Lett., 30(17), n/a-n/a, doi:10.1029/2003GL017826, 2003.

Hall, D. K., Comiso, J. C., DiGirolamo, N. E., Shuman, C. a., Box, J. E. and Koenig, L. S.: Variability in the surface temperature and melt extent of the Greenland ice sheet from MODIS, Geophys. Res. Lett., 40(10), 2114–2120, doi:10.1002/grl.50240, 2013.

Hanna, E., Navarro, F. J., Pattyn, F., Domingues, C. M., Fettweis, X., Ivins, E. R., Nicholls, R. J., Ritz, C., Smith, B., Tulaczyk, S., Whitehouse, P. L. and Zwally, H. J.: Ice-sheet mass balance and climate change, Nature, 498(7452), 51–59, doi:10.1038/nature12238, 2013.

Hasholt, B., Bech Mikkelsen, A., Holtegaard Nielsen, M. and Andreas Dahl Larsen, M.: Observations of Runoff and Sediment and Dissolved Loads from the Greenland Ice Sheet at Kangerlussuaq, West Greenland, 2007 to 2010, Zeitschrift für Geomorphol. Suppl. Issues, 57(2), 3–27, doi:10.1127/0372-8854/2012/S-00121, 2013.

Knap, Wouter H and Oerlemans, J.: The surface albedo of the Greenland ice sheet: satellite- derived and in situ measurements in the Sendre Stromfjord area during the 1991 melt season, J. Glaciol., 42(141), 364–374, 1996.

Keegan, K. M., Albert, M. R., McConnell, J. R. and Baker, I.: Climate change and forest fires synergistically drive widespread melt events of the Greenland Ice Sheet., Proc. Natl. Acad. Sci. U. S. A., 111(22), 7964–7, doi:10.1073/pnas.1405397111, 2014.

Lewis, S. L. and Maslin, M. A.: Defining the Anthropocene, Nature, 519(7542), 171–180, doi:10.1038/nature14258, 2015.

Liang, S., Shuey, C. J., Russ, A. L., Fang, H., Chen, M., Walthall, C. L., Daughtry, C. S. T. and Hunt, R.: Narrowband to broadband conversions of land surface albedo: II. Validation, Remote Sens. Environ., 84, 25–41, 2002.

McGrath, D., Colgan, W., Bayou, N., Muto, A. and Steffen, K.: Recent warming at Summit, Greenland: Global context and implications, Geophys. Res. Lett., 40(10), 2091–2096, doi:10.1002/grl.50456, 2013.

Mote, T. L.: Greenland surface melt trends 1973–2007: Evidence of a large increase in 2007, Geophys. Res. Lett., 34(22), L22507, doi:10.1029/2007GL031976, 2007.

Mernild, S. H., Mote, T. L. and Liston, G. E.: Greenland ice sheet surface melt extent and trends : 1960 – 2010, , 57(204), 621–628, 2011.

Mernild, S. H. and Liston, G. E.: Greenland Freshwater Runoff. Part II: Distribution and Trends, 1960–2010, J. Clim., 25(17), 6015–6035, doi:10.1175/JCLI-D-11-00592.1, 2012.

Mikkelsen, A. B., Hubbard, A., Macferrin, M., Eric Box, J., Doyle, S. H., Fitzpatrick, A., Hasholt, B., Bailey, H. L., Lindb??ck, K. and Pettersson, R.: Extraordinary runoff from the Greenland ice sheet in 2012 amplified by hypsometry and depleted firn retention, Cryosphere, 10(3), 1147–1159, doi:10.5194/tc-10-1147-2016, 2016.

Nghiem, S. V., Hall, D. K., Mote, T. L., Tedesco, M., Albert, M. R., Keegan, K., Shuman, C. A., DiGirolamo, N. E. and Neumann, G.: The extreme melt across the Greenland ice sheet in 2012, Geophys. Res. Lett., 39(20), 1–6, doi:10.1029/2012GL053611, 2012.

Noël, B., Van De Berg, W. J., Van Meijgaard, E., Kuipers Munneke, P., Van De Wal, R. S. W. and Van Den Broeke, M. R.: Evaluation of the updated regional climate model RACMO2.3: Summer snowfall impact on the Greenland Ice Sheet, Cryosphere, 9(5), 1831–1844, doi:10.5194/tc-9-1831-2015, 2015.

Noël, B., Berg, W. J. Van De, Machguth, H., Lhermitte, S., Howat, I. and Fettweis, X.: A daily , 1 km resolution data set of downscaled Greenland ice sheet surface mass balance (1958 – 2015), , 2361–2377, doi:10.5194/tc-10-2361-2016, 2016.

Polashenski, C. M., Dibb, J. E., Flanner, M. G., Chen, J. Y., Courville, Z. R., Lai, A. M., Schauer, J. J., Shafer, M. M. and Bergin, M.: Neither dust nor black carbon causing apparent albedo decline in Greenland's dry snow zone: Implications for MODIS C5 surface reflectance, Geophys. Res. Lett., 42(21), 9319–9327, doi:10.1002/2015GL065912, 2015.

Rae, J. G. L., Aðalgeirsdóttir, G., Edwards, T. L., Fettweis, X., Gregory, J. M., Hewitt, H. T., Lowe, J. a., Lucas-Picher, P., Mottram, R. H., Payne, a. J., Ridley, J. K., Shannon, S. R., van de Berg, W. J., van de Wal, R. S. W. and van den Broeke, M. R.: Greenland ice sheet surface mass balance: evaluating simulations and making projections with regional climate models, Cryosph. Discuss., 6(3), 2059–2113, doi:10.5194/tcd-6-2059-2012, 2012.

Román, M. O., Schaaf, C. B., Woodcock, C. E., Strahler, A. H., Yang, X., Braswell, R. H., Curtis, P. S., Davis, K. J., Dragoni, D. and Goulden, M. L.: The MODIS (Collection V005) BRDF/albedo product: Assessment of spatial representativeness over forested landscapes, Remote Sens. Environ., 113(11), 2476–2498, doi:10.1016/j.rse.2009.07.009, 2009.

von Schuckmann, K., Palmer, M. D., Trenberth, K. E., Cazenave, A., Chambers, D., Champollion, N., Hansen, J., Josey, S. A., Loeb, N., Mathieu, P.-P., Meyssignac, B. and Wild, M.: An imperative to monitor Earth's energy imbalance, Nat. Clim. Chang., 6(2), 138–144, doi:10.1038/nclimate2876, 2016.

Screen, J. a and Simmonds, I.: The central role of diminishing sea ice in recent Arctic temperature amplification, Nature, 464(7293), 1334–1337, doi:10.1038/nature09051, 2010.

Smith, L. C., Chu, V. W., Yang, K., Gleason, C. J., Pitcher, L. H., Rennermalm, A. K., Legleiter, C. J., Behar, A. E., Overstreet, B. T., Moustafa, S. E., Tedesco, M., Forster, R. R., LeWinter, A. L., Finnegan, D. C., Sheng, Y. and Balog, J.: Efficient meltwater drainage through supraglacial streams and rivers on the southwest Greenland ice sheet, Proc. Natl. Acad. Sci., 112(4), 1001–1006, doi:10.1073/pnas.1413024112, 2015.

Steffen, K. and Box, J.: Surface climatology of the Greenland ice sheet: Greenland Climate Network 1995-1999, J. Geophys. Res., 106(D24), 33951–33964, 2001.

Stroeve, J., Box, J. E., Gao, F., Liang, S., Nolin, A. and Schaaf, C.: Accuracy assessment of the MODIS 16-day albedo product for snow: comparisons with Greenland in situ measurements, Remote Sens. Environ., 94(1), 46–60, doi:10.1016/j.rse.2004.09.001, 2005.

Stroeve, J. C., Box, J. E. and Haran, T.: Evaluation of the MODIS (MOD10A1) daily snow albedo product over the Greenland ice sheet, Remote Sens. Environ., 105(2), 155–171, doi:10.1016/j.rse.2006.06.009, 2006.

Stroeve, J., Box, J. E., Wang, Z., Schaaf, C. and Barrett, A.: Re-evaluation of MODIS MCD43 Greenland albedo accuracy and trends, Remote Sens. Environ., 138, 199–214, doi:10.1016/j.rse.2013.07.023, 2013.

Tedesco, M.: Snowmelt detection over the Greenland ice sheet from SSM/I brightness temperature daily variations, Geophys. Res. Lett., 34(2), 1–6, doi:10.1029/2006GL028466, 2007.

Tedesco, M., Fettweis, X., van den Broeke, M. R., van de Wal, R. S. W., Smeets, C. J. P. P., van de Berg, W. J., Serreze, M. C. and Box, J. E.: The role of albedo and accumulation in the 2010 melting record in Greenland, Environ. Res. Lett., 6(1), 14005, doi:10.1088/1748-9326/6/1/014005, 2011.

Tedesco, M., Fettweis, X., Mote, T., Wahr, J., Alexander, P., Box, J. E. and Wouters, B.: Evidence and analysis of 2012 Greenland records from spaceborne observations, a regional climate model and reanalysis data, Cryosph., 7(2), 615–630, doi:10.5194/tc-7-615-2013, 2013.

Tedesco, M., Mote, T., Fettweis, X., Hanna, E., Jeyaratnam, J., Booth, J. F., Datta, R. and Briggs, K.: Arctic cut-off high drives the poleward shift of a new Greenland melting record, Nat. Commun., 7(11723), 6pp, doi:10.1038/ncomms11723, 2016.

Van Tricht, K., Lhermitte, S., Lenaerts, J. T. M., Gorodetskaya, I. V, L'Ecuyer, T. S., Noël, B., van den Broeke, M. R., Turner, D. D. and van Lipzig, N. P. M.: Clouds enhance Greenland ice sheet meltwater runoff, Nat. Commun., 7(May), 10266, doi:10.1038/ncomms10266, 2016.

Vaughan, D.G., J.C. Comiso, I. Allison, J. Carrasco, G. Kaser, R. Kwok, P. Mote, T. Murray, F. Paul, J. Ren, E. Rignot, O. Solomina, K. Steffen and T. Zhang, 2013:

Observations: Cryosphere. In: Climate Change 2013: The Physical Science Basis. Contribution of Working Group I to the Fifth Assessment Report of the Intergovernmental Panel on Climate Change [Stocker, T.F., D. Qin, G.-K. Plattner, M. Tignor, S.K. Allen, J. Boschung, A. Nauels, Y. Xia, V. Bex and P.M. Midgley (eds.)]. Cambridge University Press, Cambridge, United Kingdom and New York, NY, USA.

Vernon, C. L., Bamber, J. L., Box, J. E., van den Broeke, M. R., Fettweis, X., Hanna, E. and Huybrechts, P.: Surface mass balance model intercomparison for the Greenland ice sheet, Cryosph., 7(2), 599–614, doi:10.5194/tc-7-599-2013, 2013.

Wang, Z., Schaaf, C. B., Chopping, M. J., Strahler, A. H., Wang, J., Román, M. O., Rocha, A. V., Woodcock, C. E. and Shuai, Y.: Evaluation of Moderate-resolution Imaging Spectroradiometer (MODIS) snow albedo product (MCD43A) over tundra, Remote Sens. Environ., 117, 264–280, doi:10.1016/j.rse.2011.10.002, 2012.

Wang, Z., Schaaf, C. B., Strahler, A. H., Chopping, M. J., Román, M. O., Shuai, Y., Woodcock, C. E., Hollinger, D. Y. and Fitzjarrald, D. R.: Evaluation of MODIS albedo product (MCD43A) over grassland, agriculture and forest surface types during dormant and snow-covered periods, Remote Sens. Environ., 140, 60–77, doi:10.1016/j.rse.2013.08.025, 2014.

Wang, Z., Erb, A. M., Schaaf, C. B., Sun, Q., Liu, Y., Yang, Y., Shuai, Y., Casey, K. A. and Román, M. O.: Early spring post-fire snow albedo dynamics in high latitude boreal forests using Landsat-8 OLI data, Remote Sens. Environ., 185, 71–83, doi:10.1016/j.rse.2016.02.059, 2016.

Wientjes, I. G. M. and Oerlemans, J.: An explanation for the dark region in the western melt zone of the Greenland ice sheet, Cryosph., 4(3), 261–268, doi:10.5194/tc-4-261-2010, 2010.

Wright, P., Bergin, M., Dibb, J., Lefer, B., Domine, F., Carman, T., Carmagnola, C., Dumont, M., Courville, Z., Schaaf, C. and Wang, Z.: Comparing MODIS daily snow albedo to spectral albedo field measurements in Central Greenland, Remote Sens. Environ., 140, 118–129, doi:10.1016/j.rse.2013.08.044, 2014.

Chapter 2: Multi-modal albedo distributions in the ablation area of the southwestern Greenland Ice Sheet

2.1 Introduction

Surface albedo, defined as the bihemispheric reflectance integrated across the visible and near-infrared wavelengths (Schaepman-Strub et al., 2006), is a key variable controlling Greenland Ice Sheet (GrIS) surface melting. During the melt season, surface albedo modulates absorbed solar radiation at the ice surface and, consequently, the surface energy and mass balance of the ice sheet (Cuffey and Paterson, 2010). Over the last decade, an observed decline in albedo has been linked to less summer snow cover, expansion of bare ice area, and enhanced snow grain metamorphic rates from atmospheric warming, amplified by the melt–albedo feedback (Box et al., 2012; Stroeve et al., 2013; Tedesco et al., 2011). This positive feedback involves increased melting and exposure of bare ice, impurities, and meltwater ponding, reducing surface albedo and, by increasing solar radiation absorption, accelerating melt further (Box et al., 2012; Tedesco et al., 2011).

The GrIS surface has a wide range of surface types with different albedos, including snow, ice, dust and sediment- rich impurities, cryoconite holes, melt ponds, and streams. Yet, the importance of these surface types on ablation area albedos and thus, meltwater production over the melt season is still relatively unresolved (Rennermalm et al., 2013). Current state-of-the-art surface mass balance (SMB) models, such as Modèle Atmosphérique Régionale (MAR) v3.2 and Regional Atmospheric Climate MOdel (RACMO2), consider some variability in surface types by including the presence of meltwater ponding, snow, and bare ice surfaces to characterize seasonal variations in ablation area albedo (Alexander et al., 2014; Van Angelen et al., 2012). Furthermore, RACMO2 considers the presence of black carbon concentrations on snow and is capable of utilizing realistic MODerate Resolution Imaging Spectroradiometer (MODIS) background albedo data (Van Angelen et al., 2012), thereby representing the impact of surface types spatially aggregated to the MODIS resolution. However, few studies have utilized these modeling tools to understand how the distributions of surface types are changing ablation area albedo (e.g., Alexander et al. 2014). This is increasingly important due to enhanced surface melt associated with anomalously warm atmospheric circulation patterns in 2007–2012 (Hall et al., 2013; Nghiem et al., 2012; Tedesco et al., 2013) that may become more frequent in the future. Additionally, some studies suggest that a new control of ice sheet albedo is the deposition and accumulation of light-absorbing impurities advected from snow-free areas and forest fires outside of Greenland (Dumont et al., 2014; Keegan et al., 2014).

The large-scale decline in albedos has been greatest in southwest Greenland (−0.04 to −0.16 per decade trend in June and August for 2000 to 2012, respectively; Stroeve et al., 2013). This is related to stronger warming trends (2–4 °C in some regions; Hanna et al., 2014), early melt onset, a lack of wintertime accumulation (van den Broeke et al., 2008), expansion of bare ice area (Tedesco et al., 2011), high concentration of impurities (cryoconite, dust, and soot), melting of outcropped ice layers enriched with mineral content (Wientjes and Oerlemans, 2010; Wientjes et al., 2011), and enhanced meltwater production and runoff (e.g., Mernild et al., 2012). Seasonal changes in the distribution of different surface types in southwest Greenland's ablation area have considerable influence on the spatiotemporal variability of surface albedos (Chandler et al., 2015; Knap and Oerlemanns, 1996; Konzelmann and Braithwaite, 1995). During the melt season, surface albedo decreases as cryoconite hole coverage increases (Chandler et al., 2015), melt ponds and supraglacial rivers form efficient drainage networks (Lampkin and Van- derBerg, 2013; Kang and Smith, 2013; Smith et al., 2015), crevasses and other types of roughness begin to form, and impurities accumulate from exposure of the underlying ice surface (Wientjes and Oerlemans, 2010). Albedo in western Greenland's ablation area averages around ∼ 0.41 for the duration of the melt season (Wientjes et al., 2011), but can vary from > 0.80 for fresh snow to 0.30–0.60 for bare ice (Cuffey and Patterson, 2010) and ∼ 0.10 for cryoconite surfaces (Bøggild et al., 2010; Chandler et al., 2015; Knap and Oerlemans, 1996). Furthermore, negative albedo trends since 2000 (Box et al., 2012) are linked to an expansion of areas of ablation relative to accumulation facies.

Changes in surface albedo are typically characterized from the MODIS and the Advanced Very High Resolution Radiometer (AVHRR) satellite sensors (e.g., Chandler et al., 2015; Stroeve et al., 2013; Wang et al., 2012; Wright et al., 2014) or modeled with regional climate models (RCMs) such as RACMO2 (Van Meijgaard et al., 2008) and MAR (Fettweis, 2007). Remotely sensed and modeled albedo has been validated with ground measurements from dispersed Greenland Climate Network automatic weather stations (GC-Net AWS; Knap and Oerlemans, 1996; Steffen and Box, 2001). These comparisons reveal that satellite products provide reasonable albedo estimates (Box et al., 2012; Stroeve et al., 2005, 2006, 2013), although discrepancies between different MODIS albedo products have been identified (Alexander et al., 2014). Despite this, RCM surface albedos remain represented in relatively simplistic terms, particularly in regions that frequently experience prolonged bare ice exposure like southwest Greenland (Fettweis et al, 2011; Fitzgerald et al., 2012; Rae et al., 2012; Van Angelen et al., 2012). This is attributed to a lack of surface roughness in the RCMs (Ettema et al., 2010) and relatively simplistic bare ice and impurity albedo schemes (Alexander et al., 2014), resulting in large inter-model differences in runoff (42 % variance; Vernon et al., 2013) despite the existence of spatially distributed ice albedo schemes and inclusion of black carbon contaminants on snow surfaces (Van Angelen et al., 2012). Recent surface albedo observations and snow model simulations of impurity-rich surfaces have been linked to enhanced ice sheet melt (Chandler et al., 2015; Dumont et al., 2014; Keegan et al., 2014), suggesting that incorporating seasonal changes in the albedo distribution of distinct surface types might improve accuracy of modeled meltwater runoff and GrIS sea level rise contributions. These findings point to the importance of a detailed assessment of high spectral, spatial, and temporal resolution albedo data to quantify how different surface types control ablation area albedo and therefore melt.

In this study, we report the results of an assessment of ablation area albedo along the southwestern GrIS for the 2012 and 2013 melt seasons. We use (1) a new high-quality in situ spectral albedo data set collected with an Analytical Spectral Devices Inc. (ASD) spectroradiometer measuring over a wavelength range of 325–1075 nm along a 1.25 km transect during 3 days in June 2013; (2) in situ broadband albedos at two automatic weather stations; and (3) daily MODIS albedo (MOD10A1) product (Hall et al., 2012) between 31 May and 30 August 2012 and 2013 to investigate how ice sheet surface types influence surface albedo and ablation rates; and (4) summer seasonal changes in surface type coverage reported in literature. First, we describe the collection of high-quality in situ spectral albedos, automatic weather station broadband albedos, and ablation stake measurements collected during early 2013 melt season along a fixed transect in the GrIS ablation area. Second, from the MODIS daily albedo data we estimate seasonal changes in the albedo distributions. These distributions were compared with seasonal changes in computed albedo distributions derived by using in situ and literature values of albedos for distinct surface type and fractional area of surface types from a nearby site (1030 m a.s.l.; reported by Chandler et al., 2015). Third, the impact of changing albedo and surface type coverage on surface melt was quantified and compared with transect ablation stake measurements. Finally, we compare these 2013 results with 2012 MOD10A1 data to better understand the overall frequency distribution, spatiotemporal variability, and ablation rates associated with dominant surface types in southwest Greenland's ablation area. This study presents the first high spatial, temporal, and spectral resolution albedo data set collected in the southwestern GrIS ablation area.

2.2 Study site description

The study site is located on the southwestern GrIS approximately 30 km northeast of Kangerlussuaq, Greenland (Fig. 2.1). Albedo measurements were collected along a 1.25 km transect situated between ~ 510 and 590 m a.s.l., well within the ablation area for this region (mean equilibrium line altitude of 1553 m a.s.l.; van de Wal et al., 2012). Two meteorological stations, referred to as Base Met and Top Met stations, were installed near the transect end points by Site E and A (Fig. 2.1), respectively, to derive independent measurements of in situ broadband albedos (300–1100 nm), hereafter α_{base} and α_{top}. In addition, ablation stakes were installed at five sites along the albedo transect and by the Base Met Station to measure ice surface ablation rates. Ice sheet surface types examined included white ice, shallow supraglacial streams, and dirty ice, where dirty ice was qualitatively distinguished from white ice based on visible surface sediments. Visual assessment in the study area revealed that snow had melted before mid-June and no snowfall events occurred between 8 and 26 June 2013. A few small melt ponds (< 1 km^2) were observed in the study area but likely not in sufficient quantity to explain discrepancies between in situ and MODIS albedo-derived estimates.

2.3 Methods

2.3.1 Field spectroscopy measurements

High spatial (~10 m posting), temporal (1–2 days), and spectral (1 nm) resolution spectral albedo measurements, hereafter α_{ASD}, were measured at 325–1075 nm using an ASD Fieldspec HandHeld 2 Spectroradiometer (PANalytical, formerly ASD Inc.). The ASD was mounted on a tripod at 0.4 m distance, fitted with a Remote Cosine Receptor (RCR) foreoptic (with no other foreoptic attached; i.e., bare fiber), and had a 25° field of view corresponding to a spot size of $\sim$0.18 m diameter on the surface.

Spectral albedos were measured along the transect starting at Site E and ending at Site A on 16, 17, 19, 21, 24, and 25 June 2013 between 10:00 and 18:00 local time (12:00–20:00 GMT). After rigorous quality control (see Appendix A and B), only transect observations made on 16, 19, and 25 June were used in analyses. Broadband

α_{ASD} were calculated as a weighted average based on their spectral response curve and the amount of incoming solar radiation over the entire spectral range at each site along the transect. These measurements were compared with MOD10A1 and meteorological station data, as described in Sect. 2.3.3.

2.3.2 Continuous broadband albedo measurements at meteorological stations

Daily average broadband albedos (300–1100 nm), α_{base} and α_{top}, from 8 to 26 June 2013, was computed using Base Met and Top Met stations. Only shortwave flux measured at SZAs < 70° (Stroeve et al., 2005) was used to minimize the cosine response error inherent to the pyranometers (uncertainty increases by ±5 % for SZAs > 70°; Onset Computer Corp., 2010). Expected accuracy of α_{base} and α_{top} is ±10 % based on the intrinsic accuracy and cosine response error of the pyranometers. Although surface roughness effects on measured surface albedos (e.g., Lhermitte et al., 2014) were not quantified here, analyses of α_{top} measurements suggest that they were compromised by these effects, and thus α_{base} alone is used for most analyses. See Appendix C for details on surface installation conditions and tilt uncertainty estimates.

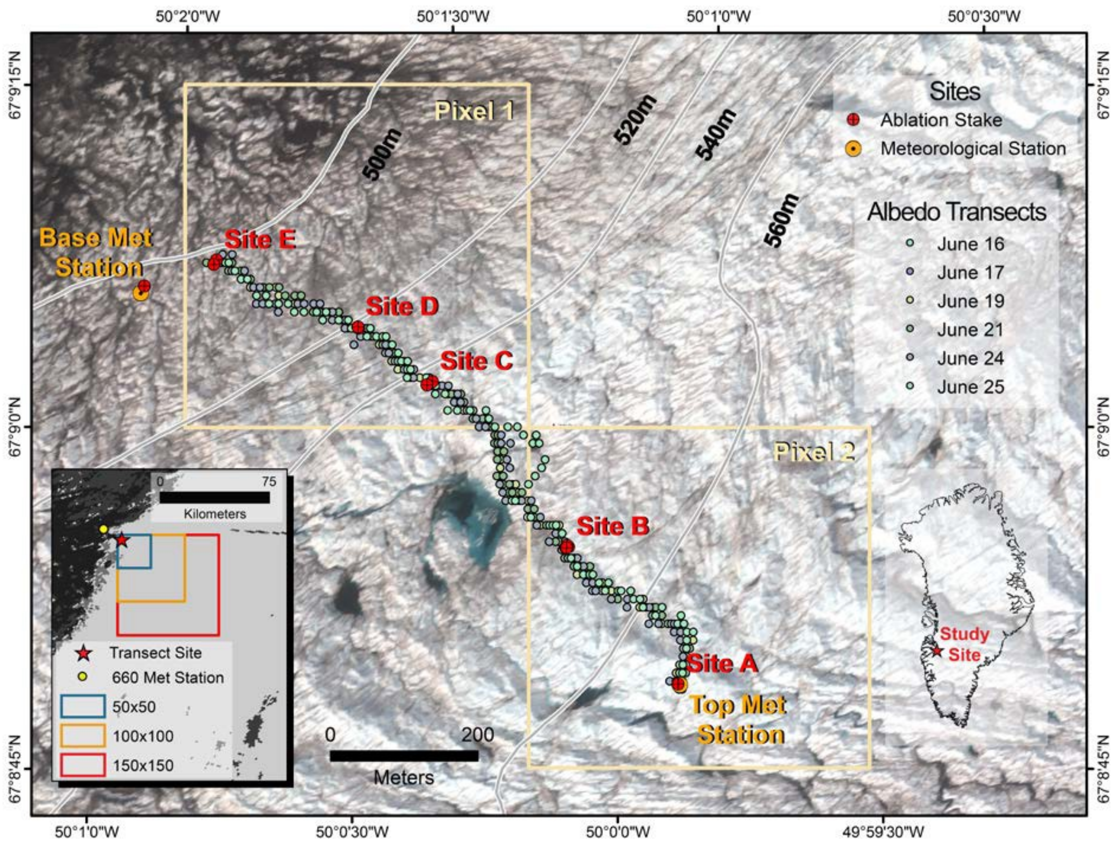

Figure 2.1 23 June 2013 WorldView-2 true color image (bands 5, 3, and 2 RGB) of the study site with elevation contours (m), MODIS pixel extents (yellow boxes), and location of the six albedo transects, ablation stake, and meteorological station sites. Location of three MODIS spatial extent regions overlaid on a 31 May 2013 MOD10A1 image (black box inset).

2.3.3 MODIS albedo data

Daily MODIS broadband albedos (300–3000 nm) were acquired from the MOD10A1 product (Version 005) from NASA's Terra satellite (Hall et al., 2006; Klein and Stroeve, 2002). High-quality flagged MOD10A1 albedo data (periods of high SZA and cloudiness were excluded; Schaaf et al., 2011) from 31 May to 30 August 2012 and 2013 (when SZAs are minimized; e.g., Box et al., 2012) were used in two analyses. First, MOD10A1 albedos for pixels overlapping with our transect site (Fig. 2.1), hereafter $\alpha_{\text{MOD Pixel 1}}$ and $\alpha_{\text{MOD Pixel 2}}$, were compared with observations as described below.

Second, distributions of MOD10A1 albedo were examined at three spatial extents as described in Sect. 2.3.5.

Broadband $\alpha_{MOD\ Pixel\ 1}$ and $\alpha_{MOD\ Pixel\ 2}$ were compared with α_{ASD} and α_{base}. Direct comparison of α_{ASD}, α_{base}, and α_{MOD} absolute values are not possible due to different wavelength ranges, and α_{MOD} is expected to have lower values than the other two data sets. However, relative comparisons of spatial and temporal patterns are reasonable, because the α_{MOD} is dominated by the ASD visible and near-infrared (i.e., 325–1075 nm) wavelengths. In a standard top-of-atmosphere solar irradiance reference spectrum, the 325–1075 nm range comprises 81% of the total irradiance in the 300–3000 nm range. The dominance of reflectance in the ASD visible and near-infrared wavelengths in determining broadband albedos means that α_{MOD} can be used qualitatively to provide spatiotemporal context. High-quality broad-band (325–1075 nm) α_{ASD} data within pixels 1 and 2, hereafter $\alpha_{ASD\ Pixel\ 1}$ and $\alpha_{ASD\ Pixel\ 2}$, were averaged together to indirectly validate $\alpha_{MOD\ Pixel\ 1}$ and $\alpha_{MOD\ Pixel\ 2}$ data and to facilitate comparison between in situ and remotely sensed observations. While absolute values will differ between the data sets, and issues of MODIS pixel (px) separability may exist due to off-nadir footprint effects (Dozier et al., 2008), the difference should not change spatial and temporal patterns.

2.3.4 Ablation and albedo at dominant surface types

Surface melting between 8 and 26 June was estimated using ablation stakes installed at the Base Met Station, hereafter M_{base}, and at five sites across the albedo transect, hereafter $M_{stakeXY}$, where X denotes Sites A–E, and Y denotes surface type –

clean/white ice (W), dirty ice (D), or shallow 5– 10 cm deep streams (S) (Fig. 2.1). Bamboo poles were used as stakes (Hubbard and Glasser, 2005), and ablation rates were recorded every 1–3 days by measuring the distance between the bamboo pole top and ice sheet surface at centimeter-scale resolution.

α_{ASD} spectra were made within 30 m of ablation stakes to identify representative surface type albedos. With the exception of Site D, all sites were relatively homogenous. At Site D, the two surface types could be classified into distinct groupings: clean and dirty ice. Albedos of clean ice at Sites A–C and E, hereafter α_{ASD_AW}, α_{ASD_BW}, α_{ASD_CW}, and α_{ASD_EW}, were estimated by averaging broadband α_{ASD} observations made within 30 m of stakes for each transect date. At Site D, albedos of clean and dirty ice, hereafter α_{ASD_DW} and α_{ASD_DD}, were estimated from the histograms of α_{ASD} observations made within 30 m of stakes for each transect date. At the M_{base} stake, no spectral α_{ASD} observations were made. Instead, α_{ASD_DD} is assumed to be representative of albedos at the Base Met Station, hereafter α_{MET_base}. Stream albedo, hereafter α_{stream}, was determined from occasional α_{ASD} measurements at various shallow surface streams between 13 and 25 June. Cryoconite hole albedo, hereafter α_{cryo}, was parameterized using published values (from Bøggild et al., 2010) of broadband albedos averaged together for damp cryoconite material and cryoconite basin surface types under clear-sky and overcast conditions.

2.3.5 Melt season albedo distributions

Two types of melt season albedo distributions were constructed: (1) computed distributions based on broadband α_{ASD} for distinct surfaces and fractional surface coverage area from Chandler et al. (2015) and (2) observed MODIS derived distributions.

The computed distributions were constructed by assuming that the albedo distribution for each distinct surface is represented by a normal distribution $N(\bar{x}, s)$, $\bar{x} = \overline{\alpha_{ASD}}$ representing surface type and standard deviation (estimated from ASD measurements), s, different for each surface type. Four distributions were constructed: clean ice N(0.56, 0.07), dirty ice N(0.19, 0.05), shallow streams N(0.23, 0.09), and cryoconite holes N(0.10, 0.05). Relative surface coverage of these four dominant surface types was derived at five distinct time periods (1, 19 June, 18, 28 July, and 5 August) over the 2012 melt season from Chandler et al. (2015; see Fig. 2.6a–g) to represent transient ice surface conditions, classified here as “early summer ice”, “dirty ice exposure”, “melt”, “darkening ice”, and “late summer ice”, respectively (Table 2.3). A composite distribution for each distinct time step was calculated as the weighted mean of surface type distributions, where the weights were determined by their relative surface coverage area. Since Chandler et al. (2015) data are from 2012, results were not directly comparable with 2013 MOD10A1 data but should capture melt season evolution.

To compare with the computed distributions, high-quality 2012 and 2013 MOD10A1 data were used to construct observed albedo distributions at three spatial extents (50 × 50, 100 × 100, and 150 × 150 pixel extents; Fig. 2.1). The spatial resolution of the original MOD10A1 data is 463 m at nadir (exact resolution varies with overpass time), corresponding to study areas of 23.2, 46.3, and 69.5 km^2 for the three spatial extents. Using a kernel smoothing density estimator, the average probability density distribution was computed at 0.01 albedo bin widths (range from 0.05 to 1). The seasonal average albedo distribution was calculated at the three spatial extents, and 5-day average albedo distributions and spatial averages were calculated for the 100 × 100 pixel scale for 2012 and 2013 MOD10A1 data.

2.3.6 Identification of snowfall events

To identify possible snowfall events in our study area and MODIS spatial extents, hourly precipitation and air temperature measurements collected by a meteorological station, hereafter 660 Met Station, installed near the ice sheet edge at the proglacial and ice sheet margin interface (Fig. 2.1), were examined. Near-surface air temperature measurements from the shorter Base Met Station time series (available from 8 to 26 June 2013) were also examined to estimate temperature differences between the proglacial and ice surfaces. Tundra near-surface air temperature < 1 °C and precipitation > 0 m were used as criteria to identify dates of likely snowfall events. To validate that solid precipitation fell, NASA's WorldViewer (https://earthdata.nasa.gov/labs/ worldview/) was utilized to browse daily MODIS reflectance imagery (bands 7-2-1 and 3-6-7) to identify textural and brightness changes related to precipitation events.

2.3.7 Computation of relative melt rates

To examine seasonal changes in MODIS albedos, and estimate the importance of distinct surface types, relative surface melt rates were computed using the net shortwave solar radiation equation, observed values of incoming solar radiation from the Base Met

Station on 16, 19, and 25 June, and broadband albedo values for computed and observed distribution methods. The observed incoming solar radiation values were averaged together and kept constant in the relative melt rate calculations to isolate the effects of albedo changes on melt. Net solar radiation (E_R) varies as a function of incoming solar radiation ($E_s^{\downarrow}$) and albedo (α_s), where units of energy are represented as W m^{-2} :

$$E_R = E_s^{\downarrow} (1 - \alpha_s). \quad (1)$$

Melt rate, defined as the heat needed to melt snow/ice when near-surface temperatures are ≥ 0 °C, was computed in units of m s^{-1} (Cuffey and Patterson, 2010):

$$M = E_R(L_f \cdot p_w)^{-1}. \quad (2)$$

where L_f is latent heat of fusion (3.34 × 10^5J kg^{-1}) and p_w is density of water (1000 kg m^{-3}). Since the meteorological station data sets lack surface energy balance terms (i.e., net long-wave radiation, sensible and latent heat fluxes) required to compute the entire energy budget, calculating absolute melt rates was not possible. Instead, the percent difference in estimated melt rates was computed for each distribution relative to the early melt season ablation rates (mean of 4.40 × $10^{-7} m\ s^{-1}$ for “early summer ice” computed distribution; mean of 2.70 × $10^{-7} m\ s^{-1}$ for 31 May–4 June observed MODIS distribution).

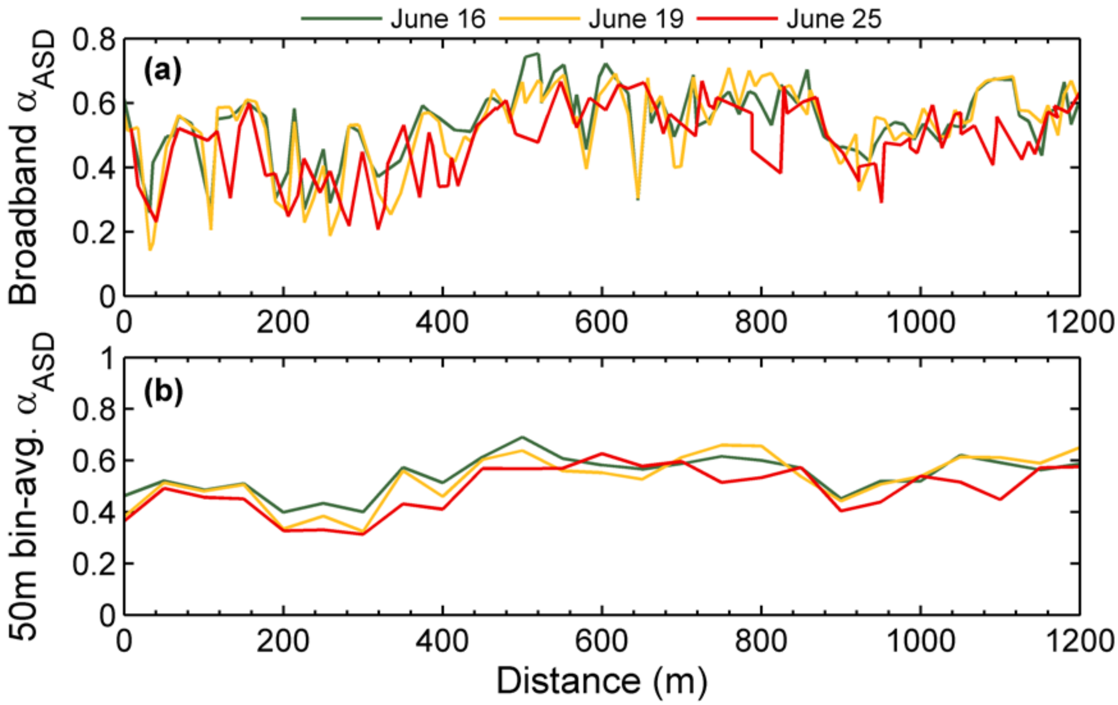

Figure 2.2 High-quality broadband α_{ASD} observations on 16, 19, and 25 June (a) and broadband α_{ASD} averaged in 50 m bins (b) along the length of the transect starting near Site E (0 m) and ending near Site A (1200 m).

2.4 Results

2.4.1 Spatiotemporal patterns in ablation area transect albedo

Spatial variability of broadband α_{ASD} along the transect follows a consistent pattern on all three dates, averaging low values (0.50 ± 0.04) the first ~300 m, followed by increased albedo, reaching a plateau of 0.64 ± 0.07 at ~600 m, and remaining nearly constant with the exception of a dip to 0.44 ± 0.02 at ~900 m (Fig. 2.2a). While discrete α_{ASD} observations often differ from the nearest observation made at another transect time due to slight day-to-day changes in the sample location (Fig. 2.2a), data averaged in 50 m bins covary spatially along the transect gradient (Fig. 2.2b). The spatial variability of broadband α_{ASD} is considerable and varies between a minimum of 0.14 (19 June) and a maximum of 0.75 (16 June; Table 2.1). The high variability in discrete α_{ASD} values over short distances (Fig. 2.2a) is indicative of the heterogeneous surface that characterizes the field site and surrounding ablation area not necessarily captured in α_{base} observations.

Temporal variability in daily average α_{base} follows a nonlinear decline from 8 to 26 June 2013 starting at 0.49 and ending at 0.34 (Fig. 2.3). An increase in α_{base} of 0.11 between 12 and 16 June might be related to tilt errors, which influenced what part of the increasingly heterogeneous surface the instruments were monitoring. Indeed, the net lowering of α_{base} by 0.15 between 8 and 26 June is consistent with $\alpha_{MOD\ Pixel\ 1}$ and $\alpha_{MOD\ Pixel\ 2}$ observations from June to mid-August. $\alpha_{MOD\ Pixel\ 1}$ and $\alpha_{Mod\ Pixel\ 2}$ drop from values slightly above 0.5 in June to 0.24 and 0.37, respectively, around mid-August. Between these dates, sudden increases in albedo could be caused by occasional snowfall events (Fig. 2.3).

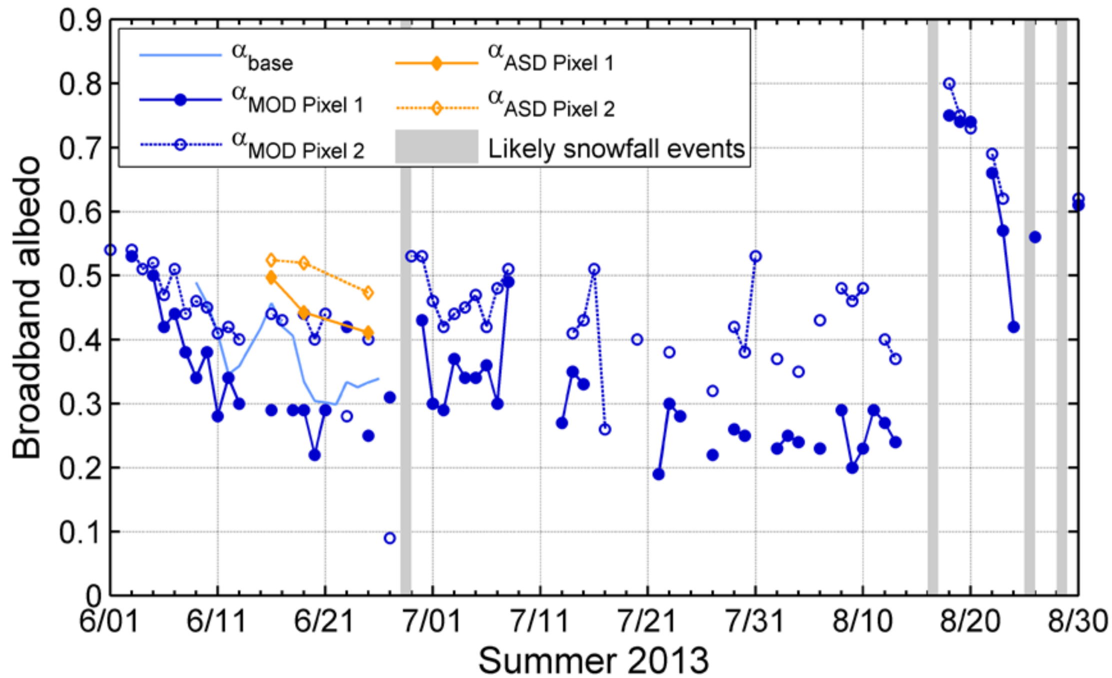

Figure 2.3 High-quality daily average broadband $\alpha_{\mathrm{ASD\ Pixel\ 1}}$ and $\alpha_{\mathrm{ASD\ Pixel\ 2}}$, α_{base} (for SZA < 70°), and $\alpha_{\mathrm{MOD\ Pixel\ 1}}$ and $\alpha_{\mathrm{MOD\ Pixel\ 2}}$ time series for the 2013 melt season. $\alpha_{\mathrm{ASD\ Pixel\ 1}}$ and $\alpha_{\mathrm{ASD\ Pixel\ 2}}$ pixel-averaged values correspond to high-quality ASD transect dates 16, 19 and 25 June.

Potential snowfall events were identified as time periods with 660 Met Station temperatures < 1 °C that coincided with precipitation events. The 1 °C offset is motivated by the environmental lapse rate. This suggests that the higher elevation of the ice sheet would be at freezing, and precipitate as snow. By using this method to identify snowfall events, a brief event likely occurred on 28–29 June (Fig. 2.3) raising MOD10A1 albedos from 0.31 to 0.53 between 27 and 30 June. July MOD10A1 albedos exhibited some temporal variability but were generally lower at the end than the start of the month. It is unclear if they were triggered by snowfall events. While precipitation events occurred several times on the tundra in July, it is unknown whether these events extended to the ice sheet and whether temperatures were sufficiently cold to trigger snow rather than rain.

August MOD10A1 albedos increased from early to late in the month with a snowfall event on 18 August, triggering large increases in albedos to values above 0.75. High-quality daily average broadband $\alpha_{MOD\ Pixel\ 1}$ and $\alpha_{MOD\ Pixel\ 2}$ data do not exhibit the slight increase in α_{base} at the end of June (0.04 from 22 to 26 June), which may be reflected by differences in footprint sizes, a lower α_{ASD} sampling frequency, and α_{base} tilt errors. Instead, $\alpha_{ASD\ Pixel\ 1}$ and $\alpha_{ASD\ Pixel\ 2}$ data exhibit a steady decline over the month of June, while $\alpha_{MOD\ Pixel\ 1}$ and $\alpha_{MOD\ Pixel\ 2}$ data remain relatively constant over the same time period. Absolute magnitudes among the three ground- and satellite-derived albedo products diverge due to sensor, wavelength range, and spatial resolution differences. However, all products have higher albedo values at the beginning as compared with the end of the month of June, prior to the 28–29 June snowfall event.

Table 2.1 Descriptive statistics for high-quality albedo transects. SZA and CC listed for Base Met Station only. “brd” is used to abbreviate broadband.

Transect date	Start time	End time	Min brd αASD	Max brd αASD	Mean brd αASD	Daily average αbase	Daily average αtop	Min SZA (°)	Max SZA (°)	Mean SZA (°)	Min CC	Max CC	Mean CC
16 June	10:32:33	11:53:57	0.260	0.754	0.550	0.404	0.636	45.615	50.454	47.828	0.135	0.176	0.157
19 June	10:39:30	11:35:59	0.141	0.730	0.532	0.316	0.541	46.449	49.925	48.093	0.045	0.084	0.065
25 June	10:20:29	11:11:00	0.210	0.670	0.490	0.333	0.525	47.963	51.525	49.677	0.119	0.138	0.125

Table 2.2 Average broadband α_{ASD} within a 30 m radius of ablation stake sites and classified by surface type. The number within the parenthesis denotes the sample size.

Ablation stake sites	Clean surfaces	Dirty surfaces
Site A	0.641 (4)	-
Site B	0.540 (4)	-
Site C	0.591 (7)	-
Site D	0.530 (4)	0.243 (2)
Site E	0.555 (5)	-

Albedos of dirty and clean ice surfaces are distinctly different for each ablation stake site (Table 2.2). Broadband α_{ASD} spectra made within 30 m of ablation stakes were individually assessed to classify each surface type into two distinct groupings: clean and dirty ice. Only Site D had both dirty and clean ice surfaces. Manual inspection of individual spectra at Site D confirm that samples with α_{ASD} < 0.4 are qualitatively similar to typical spectra for wet or debris-rich ice, as shown in Pope and Reese (2014), and distinctly different from values of α_{ASD} > 0.4.

2.4.2 Melt season albedo distributions

2.4.2.1 2013 computed and observed distributions

Computed albedo frequencies using typical albedo values for four distinct surface types (Table 2.3 and Sect. 2.3.5) and changing area fractions of these surfaces identified at a nearby site by Chandler et al. (2015) reveal a bimodal distribution as the melt season progresses (Fig. 2.4). The relative strength of the first and secondary modes change as the fractional area of darker surfaces expands from “dirty ice exposure” to “melt” distributions and onwards. At the start of the melt season, the abundance of lighter surfaces coincides with a higher probability of high broadband α_{ASD} values. Here, snow and clean ice surfaces dominate and gradually degrade, exposing the impurity-rich surface underneath. As darker surfaces progressively populate the ablation area with the onset of the melt season, computed albedo distributions predict a concomitant higher probability of lower albedos. Thus, there is an apparent dichotomy between darker and lighter surfaces "competing" to control the overall albedo distribution of the ablation area. A transition towards a distribution biased towards lower albedo values is due to darker surfaces shifting the overall distribution and is consistent with high-quality broadband α_{ASD} distributions (Fig. 2.5). Relative melt rates increase sharply (by 25.7%) from "dirty ice exposure" to "melt", coinciding with a strengthening of the second, lower mode in the computed albedo distribution (Table 2.4). Once the secondary mode is established, a smaller increase in melt rates occurred as the mode strengthens from "melt" to "darkening ice" and finally to "late summer ice" (6.7 and 9.1%, respectively).

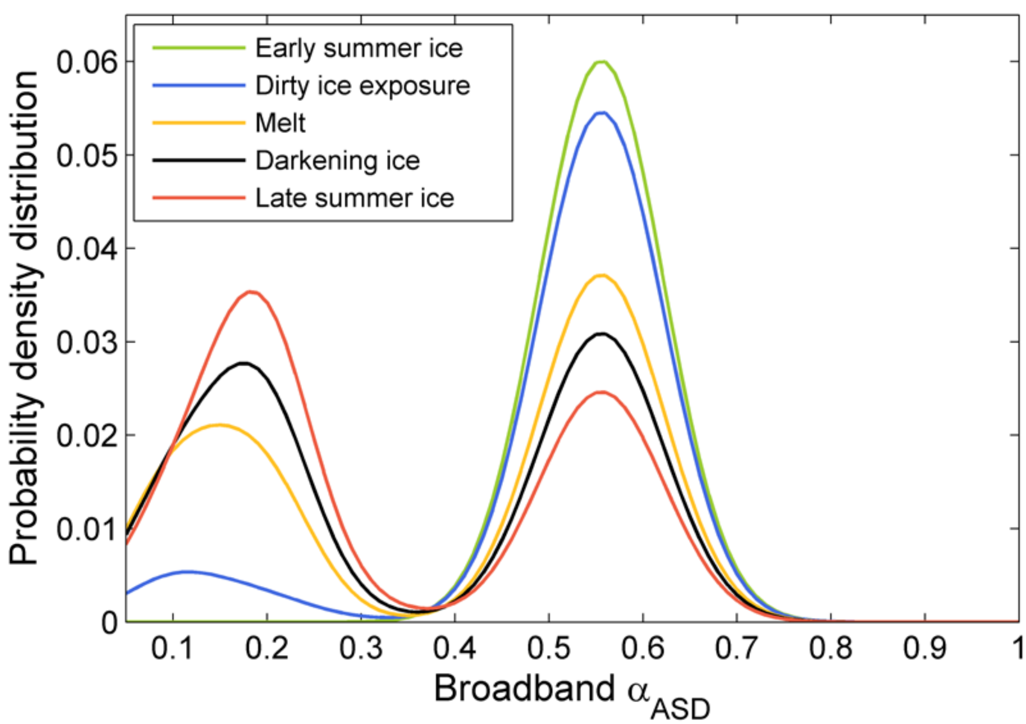

Figure 2.4 Computed albedo distribution for a nearby site of Chandler et al. (2015) simulated

across the melt season based on observed broadband α_{ASD} values for dominant surface types, weighted by their relative surface area coverage. Each surface type is assumed to follow a normal distribution. Computed albedo distributions represent the sum of each surface type's probability distribution function.

Observed 2013 MOD10A1 albedo distributions at three spatial extents (Fig. 2.6) reveal that the bimodal distributions (cf. Fig. 2.4) are manifested at the 100 × 100 MODIS px extent (i.e., 46.3 km^2). While the spatial extent of the MOD10A1 sample influences the seasonal average albedo distribution, two distinct surface types – dark and light surfaces – dominate the seasonal signal (Fig. 2.6). At the smallest spatial extent (50 × 50 px – i.e., 23.2 km^2), lower albedos from darker surfaces of the lower ablation area control the density distribution, while at the largest spatial extent (150 × 150 px – i.e., 69.5 km^2) the probability distribution is primarily influenced by higher albedos from lighter surfaces (e.g., snow) of the upper ablation area. The central tendencies of each mode are ~0.46 and ~0.72, which are much larger than in the computed distributions (~0.18 and ~0.56; cf. Fig. 2.4).

Table 2.3 Seasonal evolution (%) of four surface types at five distinct time steps approximated from Chandler et al. (2015).

Time steps	Classified names	Clean ice	Dirty ice	Streams	Cryoconite holes
1 June	Early summer ice	100	0	0	0
19 June	Dirty ice exposure	90	3	1	6
18 July	Melt	60	20	1	19
28 July	Darkening ice	50	30	3	17
5 August	Late summer ice	40	40	6	14

Table 2.4 Percent difference in melt rate estimates for different albedo probability density functions and averaged incoming solar radiation conditions at Base Met Station from 16, 19, and 25 June relative to "early summer ice" (1 June) distribution.

Time steps	Classified names	Melt rate percent difference (%)
19 June	Dirty ice exposure	8.28
18 July	Melt	34.01
28 July	Darkening ice	40.73
5 August	Late summer ice	49.83

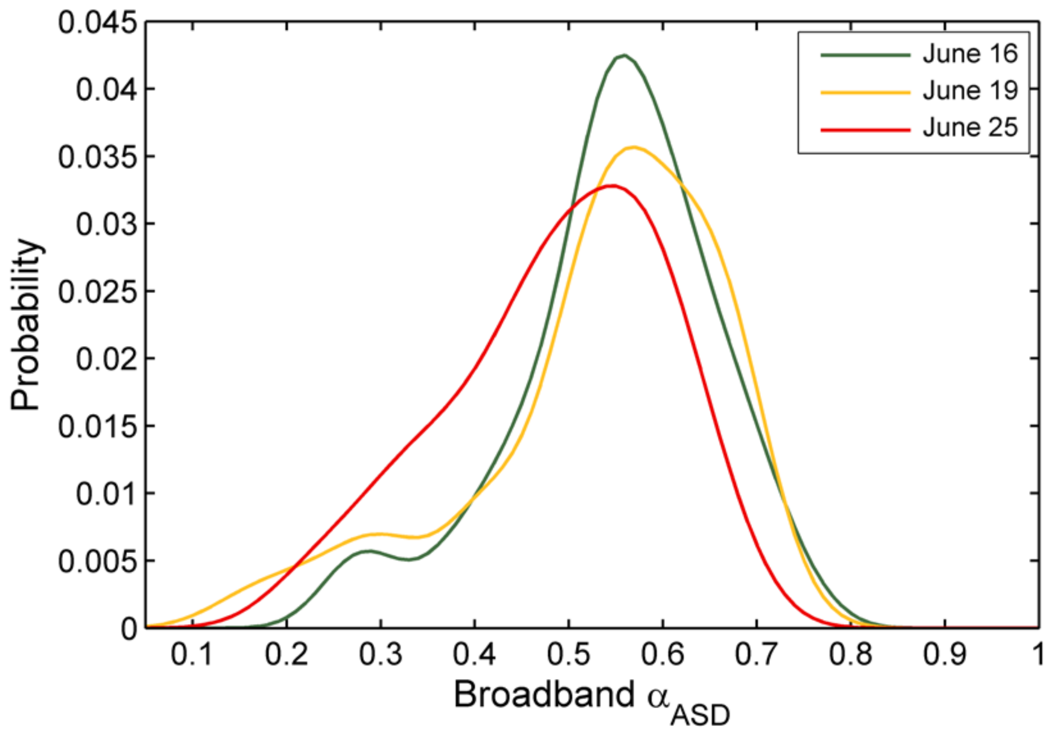

Figure 2.5 Observed distributions of high-quality broadband α_{ASD} transects on 16, 19, and 25 June.

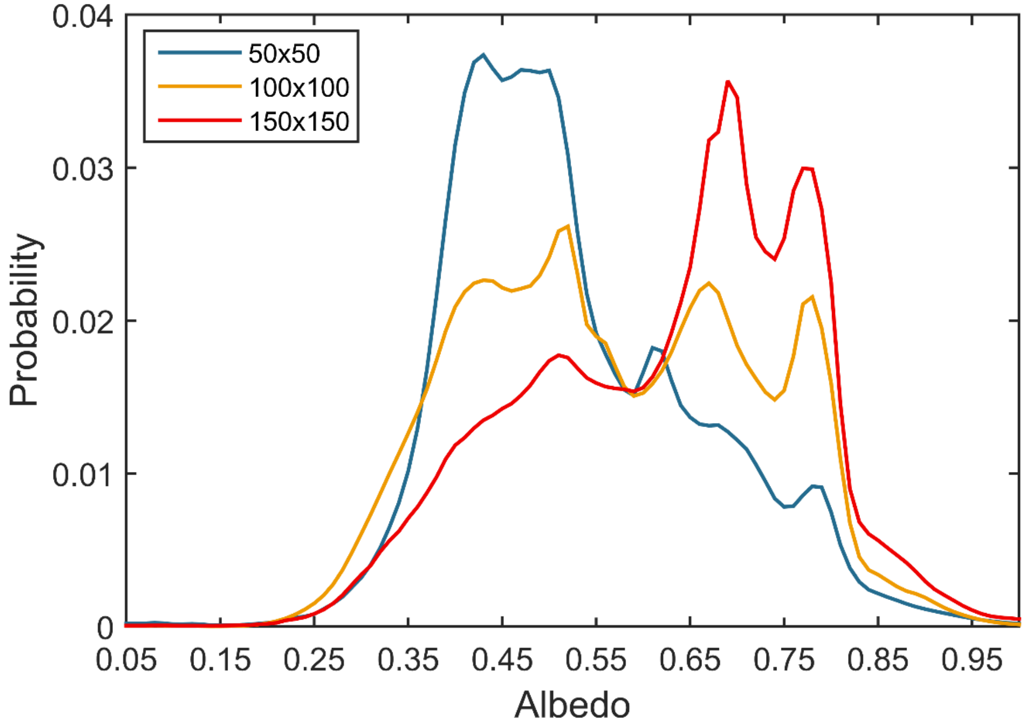

Figure 2.6 MOD10A1 2013 seasonal average albedo probability density distributions at three spatial extents: 50 × 50 MODIS pixels (px), 100 × 100 px, and 150 × 150 px. The bimodal distribution seen at the 100 × 100 px (46.3 km^2) spatial extent is likely the result of almost equal area of snow and ice facies characterizing the two peaks. In contrast, the right and left skew distributions of 50 × 50 px and 150 × 150 px illustrate the dominance of ice and snow surfaces, respectively.

The bimodal distribution identified in the observed 100 × 100 px MODIS albedo distribution in 2013 (Fig. 2.6) is the result of snow and ice surfaces characterizing the two peaks, as each mode centers around typical values of snow and clean ice, respectively. As such, the observed MODIS bimodal distribution is associated with a transition from ice to snow, rather than a change from clean to dirty ice, which caused the two modes in the computed distribution (Fig. 2.4). Indeed, analysis of 2013 meteorological observations reveal that short term snowfall events that fell on top of the underlying ice can result in variations in ablation area albedos (Fig. 2.3). In 2013, the bimodal distribution at the 100

× 100 px spatial extent is likely the result of snow deposition or redistribution of blowing snow (e.g., Gorter et al., 2014; Lenaerts et al., 2014) on top of the ice surface (Fig. 2.6).

MOD10A1 albedo at the 100 × 100 px (i.e., 46.3 km^2) spatial extent transitions from a unimodal distribution with high albedo values at the start of the melt season (31 May–4 June) to a bimodal-like distribution with intermediate albedo values at mid-melt season (20–24 June) and shifts abruptly to a new, unimodal distribution with low albedo values at peak melt season (30 July–3 August; Fig. 2.7). By assuming an unchanged radiation budget, the relative impact of albedo distribution changes on melt rates was quantified. The abrupt shift from a lighter-dominated (high albedo) to darker-dominated (low albedo) surface corresponds to an observed melt rate percent difference increase of 51.5% between the 10–14 July and 20–24 July 5-day average albedo distributions (Fig. 2.8). Before and after this shift, melt rates changed much less from each 5-day average, ranging between ∼10 and 30%, with the exception of the dramatic drop of 103.3% when the melt season ends in late August.

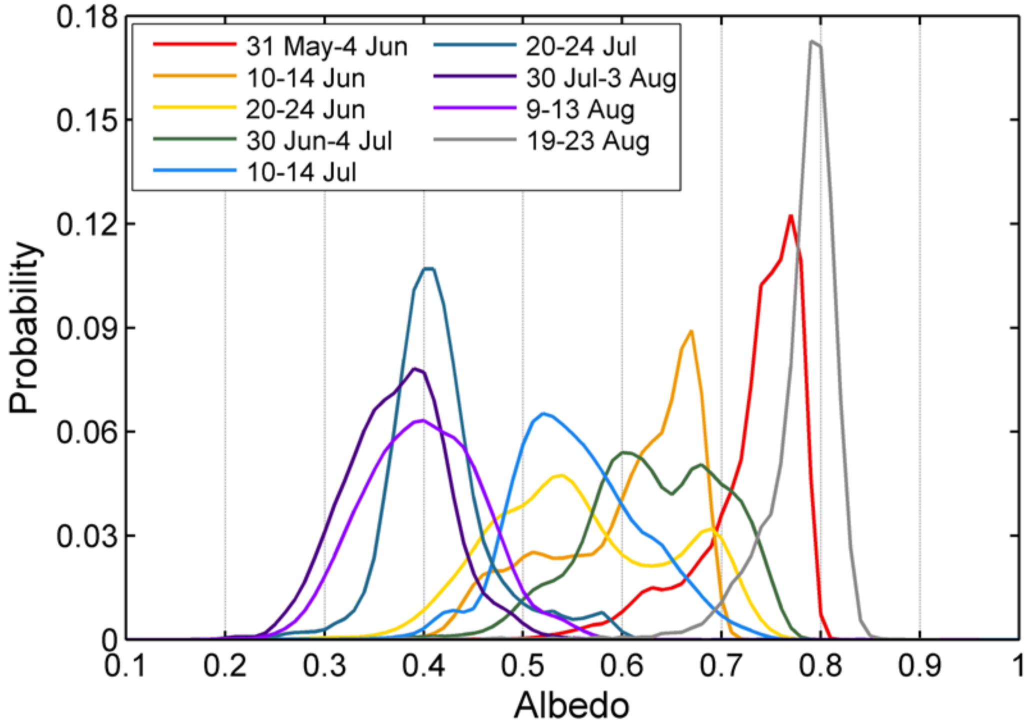

Figure 2.7 100 × 100 px 5-day averages over the 2013 melt season. Every other 5-day average line is plotted.

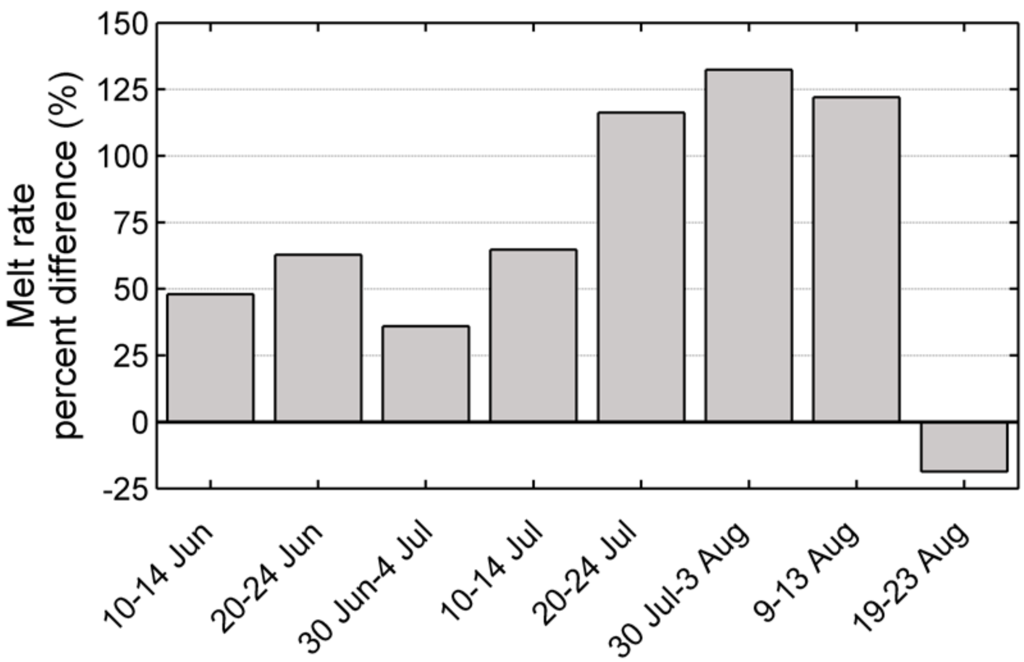

Figure 2.8 Percent difference in melt rate estimates for 100 × 100 px 5-day average albedo distributions for the 2013 melt season relative to 31 May–4 June 5-day average albedo distribution. Melt rates are calculated with identical radiation budget conditions to isolate the effect of albedo distribution changes.

The bimodality seen in the 30 June–4 July 5-day average distribution (Fig. 2.7) coincides with a brief period of higher MODIS albedo values (~0.6–0.7), indicative of snow. Identification of a snowfall event on 28–29 June 2013 (Fig. 2.3) confirms the source of the bimodal distribution observed in the 30 June–4 July 5-day average (Fig. 2.7), corresponding to a brief "jump" in the probability density distribution to higher albedos.

2.4.2.2 Differences between 2012 and 2013 observed albedo distributions

While the 2013 MODIS albedo bimodal distributions shown in Figs. 2.6 and 2.7 are a result of snow and ice albedos, analysis of MODIS 2012 data reveals a more complex, multimodal albedo distribution (Fig. 2.9). These distributions cannot be explained by the presence or absence of snow and ice alone. The 2012 MODIS observations are characterized by generally lower albedos, with six out of nine 5-day average albedo distributions ranging mostly between 0.2 and 0.5 compared to three out of nine 5-day average albedo distributions in 2013 (cf. Fig. 2.7 and 2.10). These low albedos are confirmed by the average seasonal MODIS 2012 albedo distributions, where a higher probability of albedos is centered on ~0.35, compared to two peaks at ~0.45 and ~0.7, in 2013 at the 100 × 100 px spatial extent (cf. Figs. 2.6 and 2.9). The higher probability of these very low albedos observed in 2012 are likely due to dust, sediment, and impurity-rich ice in the so-called 'dark-band' region (Wientjes and Oerlemans, 2010). The identification of this dark zone feature is presented in Sect. 2.4.2.3.

2.4.2.3 2012 vs. 2013 spatial albedo maps

The presence of the dark-band region is confirmed by the diagonal band of very low albedos (< ~0.35) in the 2012 MODIS seasonal average at the 100 × 100 px extent (Fig. 2.11). However, the presence of the dark-band region is not visible in 2013 when albedo gradually increases from west to east (Fig. 2.12). The lack of the dark zone feature in 2013 is likely due to snow covering the dark band for most of the season. Overall, 2012 exhibits substantially lower ablation area albedos (Fig. 2.10), while 2013 reveals higher ablation area albedos in the MODIS spatial averages (Fig. 2.7). The large inter- and intra-annual variability in MODIS ablation area albedos may be indicative of the large spatial variability in surface types that characterize the lower elevations of the ablation area. Alternatively, a larger distribution in cryoconite hole coverage may have also contributed to low albedos (~0.25) observed in the 2012 MODIS seasonal averages (Fig. 2.9).

2.4.3 Relative melt rates

Observed ablation rates, derived from stake readings, are typically higher for dark surfaces (dirty ice and streams) than light surfaces (clean ice; Fig. 2.13). Clean ice surfaces have higher broadband α_{ASD} values (mean of 0.57), corresponding to lower average ablation rates (5.38 × 10–7 $m\ s^{-1}$). In contrast, dirty ice and stream surfaces have lower mean broadband α_{ASD} values (0.24), corresponding to higher average ablation rates (6.75 × $10^{-7} m\ s^{-1}$). The observed mean difference between light and dark surface ablation rates is $1.37 \times 10^{-7} m\, s^{-1}$. Melt rate calculations (Eqs. 1 and 2) resulted in a lower average ablation rate for clean ice surfaces ($4.24 \times 10^{-7} m\, s^{-1}$) and a higher average ablation rate for dark ice surfaces ($7.56 \times 10^{-7} m\, s^{-1}$), corresponding to a mean difference of $3.33 \times 10^{-7} m\, s^{-1}$. Differences between observed and calculated melt rates could be due to ablation stake measurement errors and simplification of calculations (e.g., no consideration of long-wave radiation or turbulent heat fluxes). Regardless, in both cases relative melt rates between light and dark surfaces are considerably different and thus, useful for investigating seasonal melt rate changes as described below.

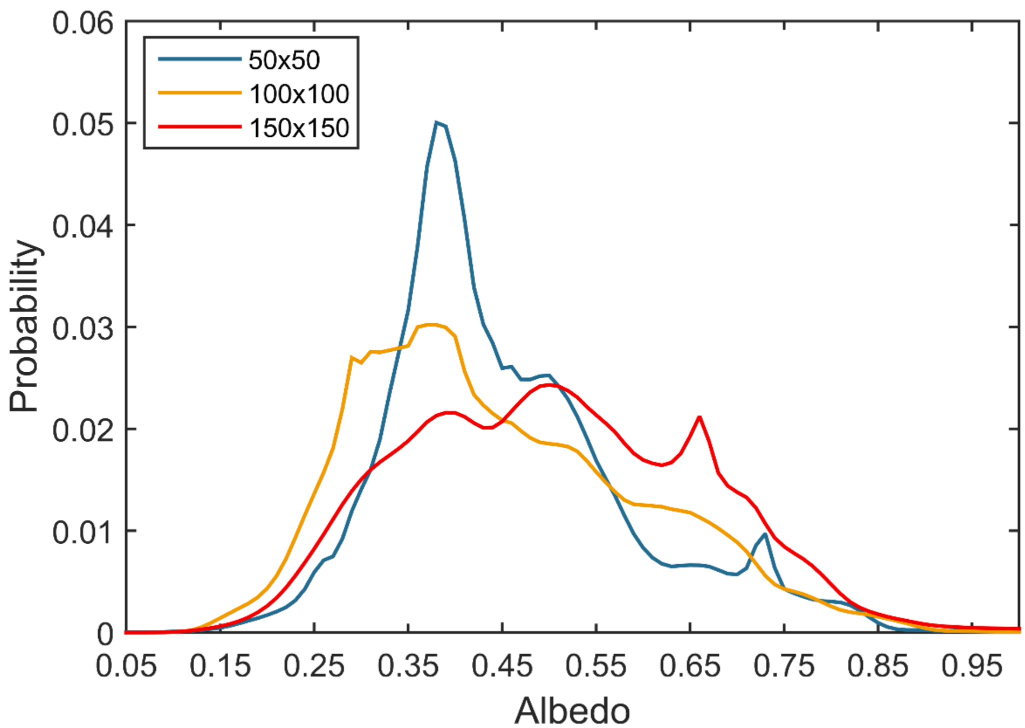

Figure 2.9 MODIS 2012 seasonal average albedo probability density distributions at three spatial extents. The MODIS 2012 seasonal average albedo probabilities for the 100 × 100 px and 150 × 150 px reveal a high probability of low albedo values (0.2–0.3). This is likely influenced by the expansion of the “dark-band” region in these spatial extents.

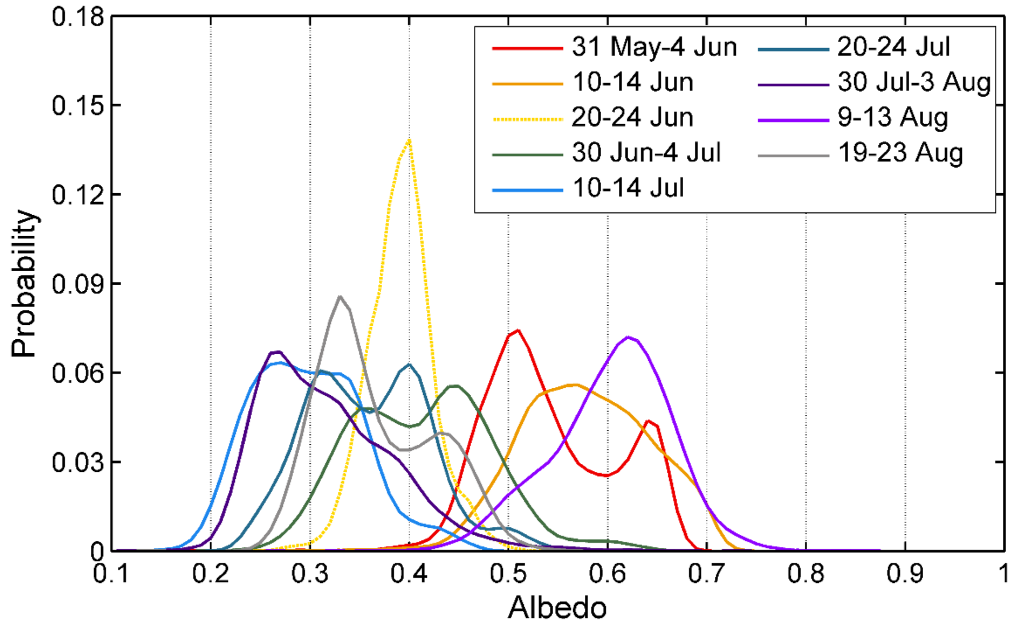

Figure 2.10 MODIS 100 100 px spatial extent 5-day average albedo distributions for the 2012 melt season. Note that the 20–24 June 5-day average (yellow stippled line) is most likely erroneous due to an outlier in the MODIS data on 21–22 June 2012.

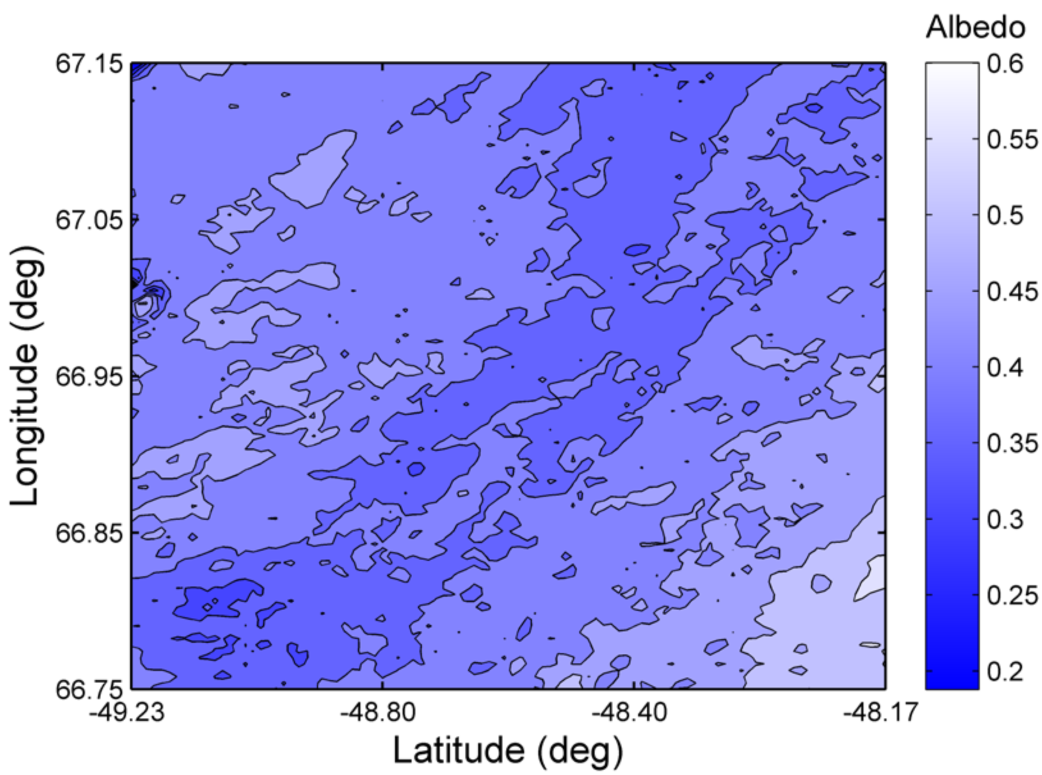

Figure 2.11 MODIS 2012 seasonal average for the 100 × 100 spatial extent. A region of dark ice, known as the “dark band”, extends through our study area (< ~0.35, shown in bright blue colors).

The spread in observed clean ice broadband albedo values results in greater variability in observed ablation rate estimates (Fig. 2.13). In contrast, minimal broadband albedo variability is observed for dirty ice surfaces. Few dirty ice albedo measurements were sampled as compared to clean ice surfaces. Differences in observed ablation rates for streams are due to a lack of albedo measurements taken over these surfaces. While ablation rates were measured at several ablation stake stream sites, only occasional α_{ASD} measurements were collected over these surfaces. Considerable spread in ablation rates for stream observations could be explained by varying stream depth (Legleiter et al., 2014). The depth of these streams determines the attenuation and scattering of radiant energy, thereby influencing the observed albedo measurements. Sensible heat flux from the stream water, not accounted for in radiative estimates, may also be a mechanism for increased melting.

2.5 Discussion

2.5.1 The importance of surface types in observed and computed ablation area albedos

GrIS ablation area albedos are strongly influenced by the presence or absence of impurity-rich debris on its surface. Clean ice and dust-covered, dirty ice have distinctly different albedos, resulting in a left-skewed albedo distribution in the middle and end of June (Fig. 2.5). This pattern is supported by computed and remotely sensed albedo distributions, revealing that a multi-modal distribution develops seasonally. A modest melt or snowfall event can trigger a sudden switch from a high to low albedo mode or vice versa, drastically changing ablation rates. These findings suggest that shifts in dominant surface type from snow to bare ice and clean ice to impurity-rich surfaces are important drivers in abruptly increasing seasonal ice sheet melt rates.

The first quality-controlled in situ ablation area albedo data set collected along a 1.25 km transect during 3 days in June 2013 is presented. Albedo data collected during in situ transect dates resemble an early summer ice surface classified in Chandler et al. (2015) and Knap and Oerlemans (1996; Fig. 2.4). Here, remaining snow cover and superimposed ice gradually melts, revealing underlying impurities and cryoconite holes. Visual assessment and continuous monitoring in the field revealed that the ice surface along the transect was snow-free from 8 to 26 June 2013. This period corresponds to a nonlinear decrease in albedos (Fig. 2.3). Accumulation of exposed below-surface impurities (Wientjes and Oerlemans, 2010), the gradual erosion of snow patches in local depressions on the ice surface (van den Broeke et al., 2011), as well as the activation and development of the hydrologic system and cryoconite hole coverage (Chandler et al., 2015) may mitigate the rate of change in ablation area albedos. Turbulent sensible heat fluxes from adjacent proglacial areas provide an additional explanation for the nonlinear decline in ground albedo measurements, serving to limit the melt–albedo feedback's influence (van den Broeke et al., 2011).

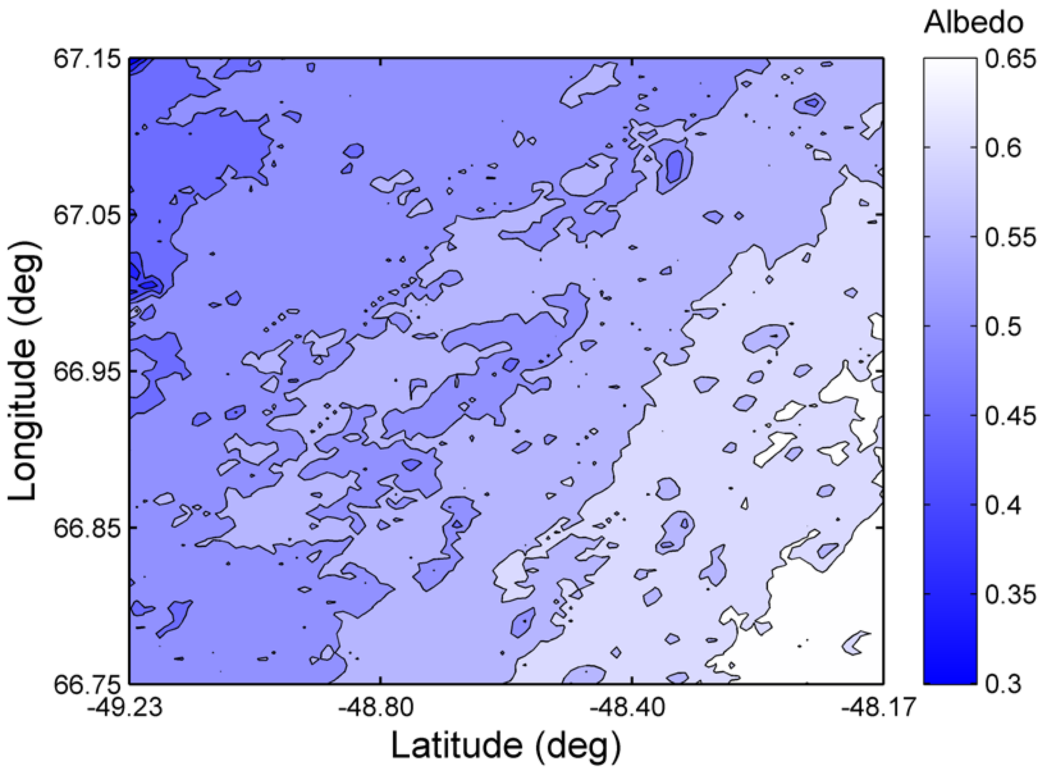

Figure 2.12 MODIS 2013 seasonal average for the 100 × 100 px spatial extent. Overall higher MODIS albedo values are observed in 2013 without a "dark-band" region surface expression.

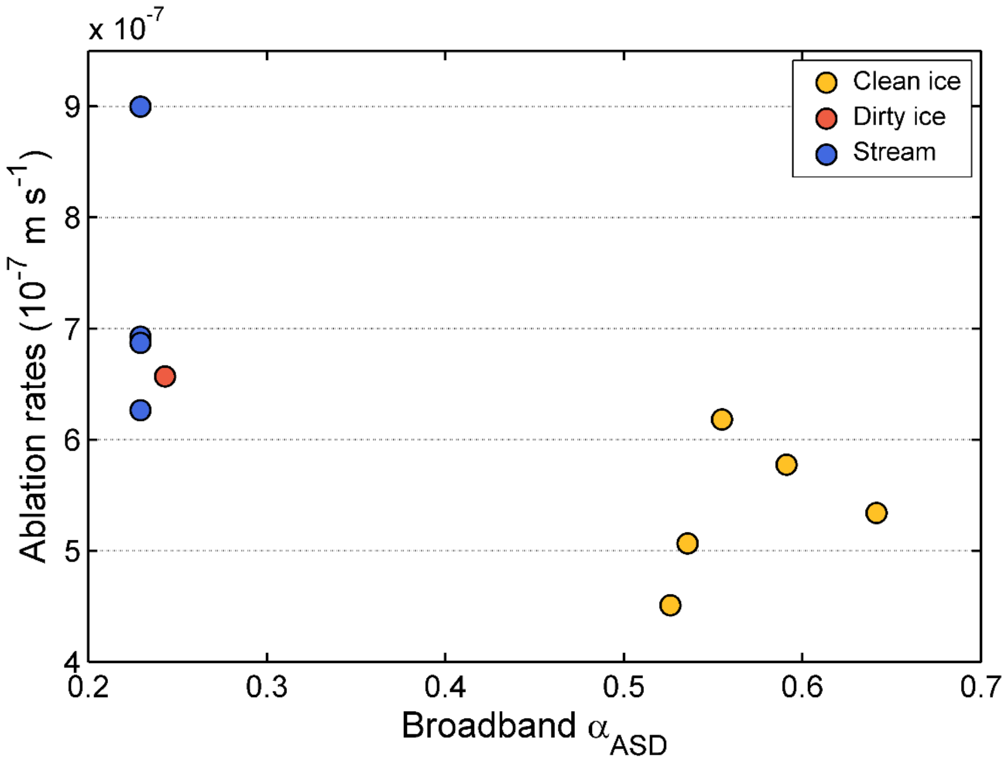

Figure 2.13 Observed ablation rates and broadband α_{ASD} for different ice surface types.

Under the assumptions that distinct surface types albedos follow a normal distribution, a bimodal probability distribution preferentially develops as ablation area albedo decreases rapidly over the melt season due to development of an efficient meltwater drainage system, increase in cryoconite hole coverage, and accumulation of debris-rich sediments (Fig. 2.4). An increase in debris-rich and stream surfaces over the melting season (Fig. 2.4) is likely responsible for the enhanced frequency of low albedo values identified in the observed α_{ASD} distribution from 16 to 25 June (Fig. 2.5). However, the observed changes at transect sites appear to be more gradual than for the MODIS data (Figs. 2.7 and 2.10). This may be due to a lack of snow cover influencing the local albedo distribution and a lower temporal sampling frequency. The lack of a pronounced secondary mode with lower albedo values in the observed left-skewed distributions (Fig.

2.5) compared to the modeled bimodal distribution (Fig. 2.4) may be related to different melt season conditions (2012 vs. 2013) and a corresponding range of surface types captured along the transect which undersamples dark surfaces (e.g., dirty ice and stream surfaces; Table 2.2). Chandler et al. (2015) surface types cover a wider range of surface types and, thus, albedos.

Compared to reality, the computed distribution (Fig. 2.4) probably overemphasizes each mode and does not account for darkening due to ice crystal growth over the melting season. The observed albedo distributions reveal abrupt and variable shifts in the seasonal albedo distribution (Figs. 2.7 and 2.10). At certain spatial extents, these albedo distributions transition from a high- to low-dominated mode (Fig. 2.6), enabling enhanced melt rates (Table 2.4 and Fig. 2.8). Alexander et al. (2014) also observed bimodal albedo distributions for Greenland's ablation area by analyzing MAR and MODIS products between 2000 and 2013. Alexander et al. (2014) attribute the dominant modes to the presence of snow and ice (and firn). This is in agreement with the analysis of the 2013 conditions but disagrees with 2012 conditions. This discrepancy could be due to the larger study area that includes areas unaffected by dust from deposition and outcropped ice layers and a 13-year averaging period suppressing outlier years like 2012 used in Alexander et al. (2014).

The 2013 bimodal albedo distributions (Fig. 2.7) shifts from higher to lower albedo modes in the melt season (Fig. 2.4) indicating that a switch in dominant surface type (i.e., from light to dark) during the melt season, and not solely grain size metamorphism, is largely responsible for lowering albedo in snow-free ablation areas. Furthermore, results from the MODIS data (Figs. 2.7 and 2.10) suggest that a transition from a light- to dark-dominated surface is abrupt rather than gradual, likely associated with the addition and removal of snow. The transition is more gradual in the left-skewed observed (Fig. 2.5) and computed albedo distributions (Fig. 2.4), likely reflecting changes in impurity content and different data set time sampling. Consistent with Chandler et al. (2015), the initial drop in MODIS ablation area albedos is likely due to both the transition from dry to wet and patchy snow surfaces. Successive lowering of albedos after snow melt is predominantly due to an increase ice crystal size (Box et al., 2012) and possibly also by expansion of darker surface area coverage (e.g., cryoconite holes, accumulation of impurities, and stream organization) and melting of dust-enriched ice layers. These distributions correspond to percent differences (e.g., 51.5% between the 10–14 July and 20–24 July 5-day averages) in melt rate estimates that are substantial over the melt season (Table 2.4 and Fig. 2.8) and highlight the importance of considering the albedo of ablation area surface types. The higher melt rates associated with darker surfaces (Fig. 2.13) may lead to lighter surfaces becoming topographically prominent. In theory, this should enhance sensible heat transfer to the lighter surfaces, increasing their ablation. Future studies should consider quantifying the effects of surface roughness on ablation area albedos (e.g., Warren et al., 1998; Zhuravleva and Kokhanovsky, 2011).

Recent studies have proposed scenarios of future atmospheric warming, in which excess deposition of light-absorbing impurities (Dumont et al., 2014) and black carbon from increased forest fire frequency or incomplete fuel combustion (Keegan et al., 2014) will promote accumulation of impurities, contributing to amplified surface melting. If these findings are confirmed, these effects will likely be exacerbated in southwest Greenland’s ablation area, where continued negative albedo trends (Stroeve et al., 2013) and increasingly warmer average summer temperatures (Keegan et al., 2014), in conjunction with bare ice, light-absorbing impurities, and cryoconite holes, are expected to dominate.

2.5.2 Insights from 2012 and 2013 melt seasons' albedo distributions

The spatial distribution of snow cover and background bare ice albedos is important for understanding temporal changes in 2012 and 2013 MODIS albedo distributions (Figs. 2.11 and 2.12). Compared to 2013, snow melt in 2012 was more pronounced and reached higher elevations (Tedesco et al., 2014), allowing the dark-band feature to be exposed, resulting in a lower seasonal albedo mode (Fig. 2.9).

The large albedo distribution changes from one MODIS 5-day average to another in 2012 (Fig. 2.10) is likely due to variability in meltwater ponding on the ice surface and perhaps deposition of wind-blown dust from tundra regions but not necessarily increases in melted-out debris from internal ice layers at such short timescales. However, exposure of dust and sediment-rich ice surfaces probably caused the high probability of considerably low 2012 MODIS albedo values relative to 2013. This is expected since it was identified as an extreme melt year with early onset snow melt (e.g., Nghiem et al., 2012; Tedesco et al., 2013; Figs. 2.9 and 2.10), while 2013 was a normal melt year in the 1979–2013 context (Tedesco et al., 2014). Given the coarse resolution of the MODIS pixel, it is likely that it averages out finer-scale details of distinct surface types (e.g., dirty ice and cryoconite hole surfaces) along the ice sheet edge. It is hypothesized that higher spatial resolution satellite imagery may be able to capture such regions closer to the ice sheet margin. We postulate that the area of these regions may grow in size over the melting season as demonstrated on local scales by Chandler et al. (2015) in situ observations.

The bimodal distribution observed in the 2013 MODIS data (Fig. 2.4) appears to be governed by the relative extent of clean ice and snow surfaces. This aligns with findings from current SMB models, as the majority of variability in the overall Greenland ablation area albedos is driven by the deposition, change, and removal of snow (Alexander et al., 2014; Van Angelen et al., 2012). However, 2012 MODIS albedo distributions cannot be explained by transitions from snow to ice and vice versa. Instead, the 2012 MODIS albedo distributions likely reflect abrupt shifts in ablation area albedos from the exposure of impurities on the ice surface in the so-called "dark-band" region as well as ice crystal growth and expansion of dirty ice areas, even with the presence of a few snowfall events. As such, dust and impurities on Greenland's ice sheet surface can influence surface albedos in the ablation area. The current state of SMB models are capable of simulating albedo as a function of meltwater ponding (Alexander et al., 2014) and impurities from atmospheric dust deposition on snow (Van Angelen et al., 2012). The models might be improved by incorporating the melting out of dust and sediments in outcropped ice layers, found in the dark-band region.

2.6 Conclusion

A first high-quality in situ spectral albedo data set collected along a fixed transect is presented for southwest Greenland's ablation area. Previous studies have attributed an increase in melt season duration, less snowfall accumulation, enhanced snow grain metamorphism rates and melt–albedo feedback as primary mechanisms for lowering ablation area albedos. Here, we demonstrate an additional control on albedos in the ablation area, namely the distribution of distinct surface types such as snow, clean ice, impurity-rich ice, melt ponds, and streams and examine their modulation on surface ablation. The spatial extent of each of these surface types result in a multi-modal albedo distributions in the ablation area. Analysis of MODIS data suggests that a multi-modal distribution and, consequentially, a shift from light- to dark-dominated surfaces and sensitivity to melting of outcropped ice layers characterize seasonal changes in Greenland's ablation area and therefore melt rates.

Continued atmospheric warming coinciding with a darkening ice surface will increase the ice sheet surface meltwater production and runoff. Here, we show the importance of the distribution of dirty ice surfaces, which are likely the result of accumulation of impurities melted out from internal ice layers (at longer timescales, e.g., summer 2012) rather than contemporary deposition of atmospherically transported dust (except perhaps at short timescales). Future research should investigate the importance of surface accumulation of impurities and if its surface area can change to significantly influence GrIS albedo and surface ablation. Analysis of spatiotemporal variability in albedos using higher spatial resolution imagery is needed to adequately characterize surface types, particularly for dust and sediment-rich surfaces, to improve our understanding of the contribution of ablation area albedos to GrIS mass loss.

Appendix A: Field spectroscopy measurements

At the start of each transect, the ASD was calibrated to current hemispherical atmospheric conditions by orienting the RCR skyward along a nadir-viewing angle. Subsequent measurements were taken with the ASD rotated 180° to view the ice surface. Under changing sky conditions, the instrument was recalibrated. Each transect consisted of ∼100 sample locations roughly 10 m apart. Despite changing ice conditions rapidly deteriorating temporary location markers, GPS locations reveal that sample sites in consecutive transects were gathered in close proximity (Fig. 2.1). While samples were not taken from exactly the same sites, preventing a point-by-point comparison, transect sample distributions and smoothed spatial patterns can be analyzed for change over time. Sample sites along each transect were selected based on distance. If a spectrum site intersected with a stream, melt pond, or cryoconite hole, the nearest ice surface was sampled instead. To capture spectral albedos of different ice surface types, separate measurements of streams, dirty ice, and white ice were collected. At each sample location, five consecutive spectra consisting of 10 dark currents per scan and 10 white reference measurements were recorded and averaged.

Apparent outliers were identified using the Spectral Analysis and Management System software to identify outliers. Outliers were defined as physically unrealistic spectral albedo values (> 1.0) and raw spectra that were markedly different to the other spectra across the entire spectral range (visible and near-infrared wavelengths) taken for the same sample. For 16 June, 20 spectra were deemed outliers (total spectra collected = 555); for 19 June, 17 spectra were deemed outliers (total spectra collected = 560); and for

25 June, 12 spectra were deemed outliers (total spectra collected = 480). The outliers for these transect dates comprise less than 4% of all spectra collected and thus, likely had an insignificant impact on the final albedo calculations. On 17 June, spectra with unrealistic > 1.0 values were collected, as will be shown in Appendix B. All data from this day were considered low quality and removed from the data set.

Appendix B: Quality control of α_{ASD} data

To ensure a high-quality α_{ASD} data set, an impact assessment of variable cloud conditions (i.e., irregular lighting due to transient clouds) and high SZAs during late afternoon albedo transect collections was made. Key et al. (2001) reported a 4–6% increase in albedos, on average, under cloudy conditions. Albedo readings have also been reported as unreliable at SZAs beyond 70° due to an increase in diffuse radiation reaching the ice surface (Schaaf et al., 2011; Stroeve et al., 2005, 2013; Wang et al., 2012).

As a proxy for cloud cover, relative cloud cover (CC) was calculated every second as the ratio of modeled clear-sky and observed incoming solar radiation similar to Box (1997). Clear-sky incoming shortwave fluxes at the surface were calculated with a solar radiance model (Iqbal, 1988). Model inputs of water vapor content, surface pressure, aerosol optical depth at 380 and 500 nm, and area optical thickness were estimated from the Kangerlussuaq AEROsol Robotic NETwork (AERONET) station (Holben et al., 2001). SZA was also modeled with the solar radiance model using latitude, longitude, time of day, and day of year at the Base Met Station. α_{ASD} collected under high CC variability and SZAs approaching extreme angles were subsequently removed. Filtering α_{ASD} data under these criteria ensured the production of a high-quality data set necessary for subsequent analysis.

Cloud cover and radiative conditions varied among transects (Fig. B1). The majority of α_{ASD} measurements were made at small SZAs (∼10:30–12:00 LT), except on 21 and 24 June, when observations were made in late afternoon (15:30–16:30 and 16:40–17:50 LT, respectively). Incoming solar radiation fluxes exhibited considerable range of diurnal variability (average 662 ± 83 W m^{-2}). Outgoing solar radiation displayed a similar range of variability at lower magnitudes (average 239 ± 18 W m^{-2}) during transect dates. Derived CC reveals a daily range in cloud fractions roughly consistent with incoming solar radiation observations which on average remained low (∼0.13), indicating that the majority of the transect measurements were collected during nearly cloud-free conditions. During transect times, half-hourly α_{base} changed linearly with SZA yet remained fairly stable (Fig. B2a). Above 80° SZA, half-hourly α_{base} variability increased, confirming that 70° SZA was a suitable threshold for daily average albedo calculations. Installation tilt and heterogeneous and changing surface conditions likely contributed locally to “unstable” α_{base} observations at higher SZAs. A hysteresis observed in αtop observations (data not shown) is attributed primarily to a low installation height (0.5 m) but may also be partly due to changing surface conditions. These effects can compromise the accurate representation of illumination and viewing geometries, resulting in reduced albedo estimates at high SZAs (Kuhn, 1974; Wang et al., 2012; Dumont et al., 2012). As such, Top Met Station measurements, and α_{base} at SZAs greater than 70°, were excluded for most analyses. Despite its limitations, α_{top} data were used for α_{ASD} comparison described below.

A high range of CC variability, instead of consistently high CC, was found to be responsible for saturating α_{ASD} readings on 17, 21, and 24 June (Fig. B2b). Continuous recalibration of the ASD instrument on 17 and 24 June was inadequate to overcome variable lighting conditions, resulting in saturated α_{ASD} readings (> 1). During 21 June, α_{ASD} data did not saturate despite variable sky conditions (0.01–0.52 CC range). Variable cloud conditions on 17, 21, and 24 of June effectively increased the amount of downwelling long-wave radiation relative to shortwave radiation available at the surface, of which the net effect results in a larger portion of solar radiation available to be reflected by the ice surface (Grenfell and Perovich, 2004; Román et al., 2010; Wang et al., 2012). This can translate to an increase in spectral albedo estimates by ~0.06 over active melting ice surfaces (Grenfell and Perovich, 2004).

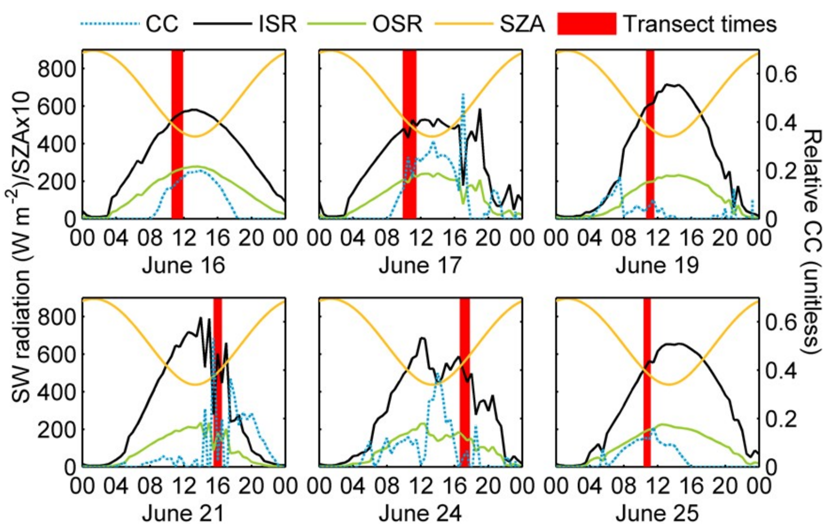

Figure B1. Radiative conditions during transect dates at the Base Met Station, including incoming solar radiation (ISR, black line), outgoing solar radiation (OSR, green line; left y-axis), modeled relative cloud cover (CC, blue stippled line; right y axis), and solar zenith angles (SZA, yellow line right axis). Red shaded regions show α_{ASD} data collection times.

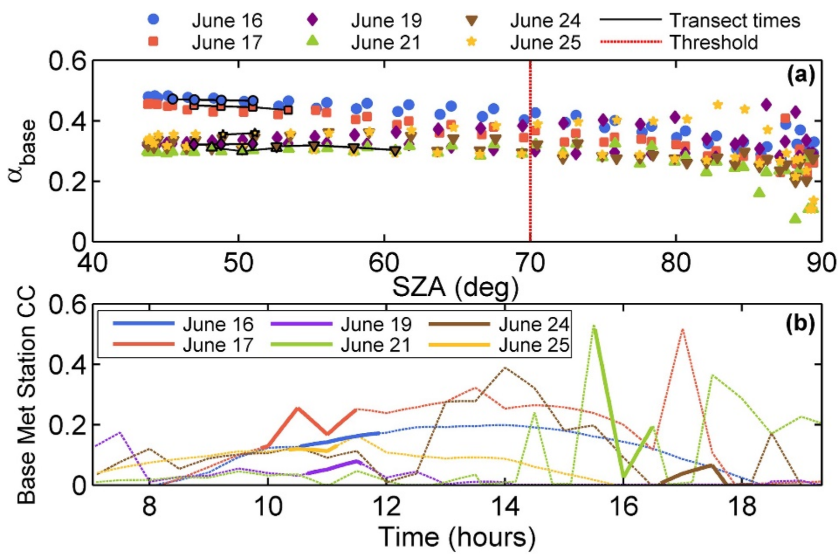

Figure B2. (a) Half-hourly broadband α_{base} measurements as a function of SZA. Symbols and colors correspond to transect dates. Transect times correspond to the black line. A SZA threshold at 70° is represented by the red stipple line. **(b)** Relative CC determined at α_{base} as a function of time during transect dates. Symbols and colors correspond to transect dates. Transect times correspond to bold lines.

By removing the majority of shortcomings and uncertainties identified in transect radiative and surface conditions, a high-quality albedo data set was produced. Optimal SZA, CC, and radiative conditions were observed for 16, 19, and 25 June. α_{ASD} data collected on 17, 21, and 24 June were identified as low quality based on their dependence on SZA, CC variability, and issues with albedo saturation and were subsequently removed from further analysis (Fig. B2). The first and last high-quality α_{ASD} measurements closest to the AWSs were compared and reveal that they agree reasonably well with α_{base} and α_{top} data (Fig. B3). As much as 62 % of α_{ASD} variance is explained by α_{base} and α_{top} ($\alpha_{ASD} = 0.27\alpha_{MET} + 0.46$, where α_{MET} is α_{base} and α_{top} combined). The discrepancy is likely due to differences in exact sample locations and instrumentation. Table 2.1 provides summary statistics related to high-quality α_{ASD} and transect conditions.

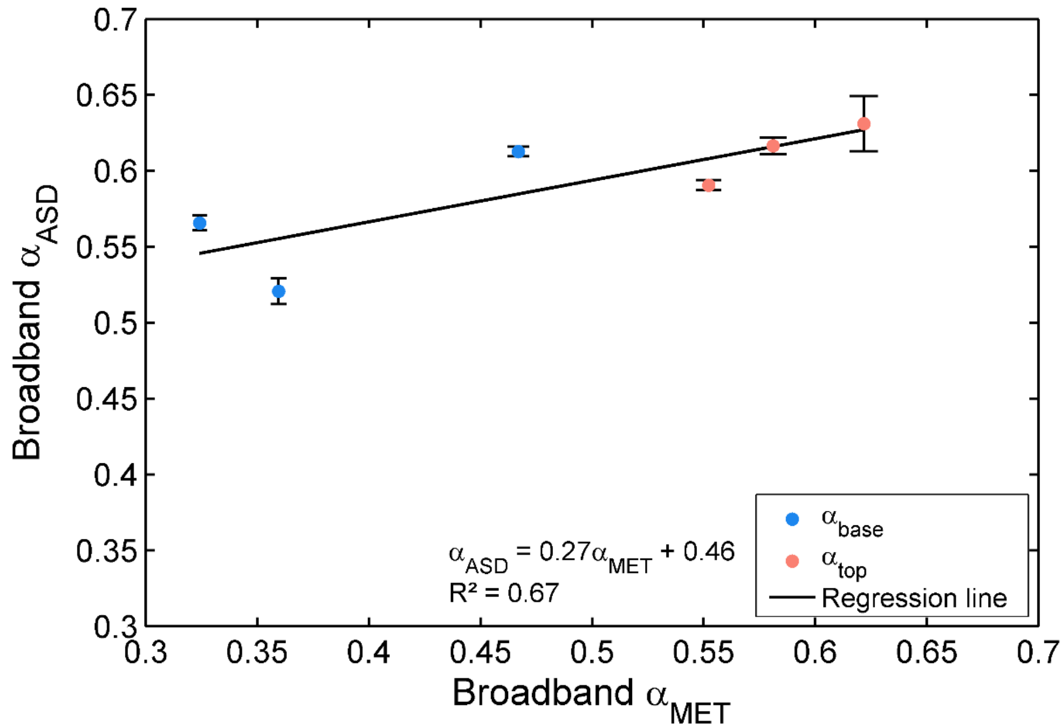

Figure B3. Broadband α_{base} (blue dots) and α_{top} (pink dots) vs. α_{ASD} and α_{MET} (i.e., both α_{base} andα_{top}) measurements fitted to a linear regression equation (R^2 = 0.67). The value of α_{ASD} error is based on the standard deviation of individual α_{ASD} measurements.

Appendix C: Installation of meteorological stations

The Top Met Station was installed upon a homogeneous clean ice surface, and the Base Met Station was installed above a heterogeneous surface of mixed clean and dirty ice. Both stations measured solar radiation fluxes every 0.5 h at 300–1100 nm, using S-LIB-M003 silicon pyranometers and a U30 data logger (Table C1; ± 5% or 10 W m^{-2} precision; Onset Computer Corp., 2010) from 8 to 26 June. Sensors were attached to a pole drilled into the ice at 1.5 m above the surface and were kept relatively constant at this height but occasionally tilted off level. After a period of heavy melting, the Top Met Station was re-drilled and installed at 0.5 m height and remained at this height as melting seized. A very large hysteresis in α_{top} as a function of SZA suggests that the low installation height resulted in α_{top} errors due to a disproportionally large influence of surface roughness on its measurements. Despite not having observed tilt information for the AWSs, we use a theoretical tilt (see Fig. 3b) in Van den Broeke et al. (2004) to provide a reasonable uncertainty range. Assuming a tilt of 1° on 18 January at Kohnen station, Antarctica (75° S, 0°) is associated with ~15 W m^{-2} offset in net shortwave at noon local time. This is associated with an absolute error of 5% with a tilt of 1°. Here, we assume double the uncertainty (± 10%).

Table C1. Meteorological station sites and associated variables.

Site	Latitude	Longitude	Elevation (m)	Start date	End date
Base Met Station	67.151629	50.027993	511.3	8 June	26 June
Top Met Station	67.146857	50.001186	586.0	14 June	26 June

2.7 References

Alexander, P. M., Tedesco, M., Fettweis, X., van de Wal, R. S. W., Smeets, C. J. P.cP., and van den Broeke, M. R.: Assessing spatiotemporal variability and trends in modelled and measured Greenland Ice Sheet albedo (2000–2013), The Cryosphere, 8, 2293– 2312, doi:10.5194/tc-8-2293-2014, 2014.

Bøggild, C. E., Brandt, R. E., Brown, K. J., and Warren, S. G.: The ablation zone in northeast Greenland: ice types, albedos and impurities, J. Glaciol., 56, 101–113, doi:10.3189/002214310791190776, 2010.

Box, J. E., Fettweis, X., Stroeve, J. C., Tedesco, M., Hall, D. K., and Steffen, K.: Greenland ice sheet albedo feedback: thermodynamics and atmospheric drivers, The Cryosphere, 6, 821–839, doi:10.5194/tc-6-821-2012, 2012.

Chandler, D. M., Alcock, J. D., Wadham, J. L., Mackie, S. L., and Telling, J.: Seasonal changes of ice surface characteristics and productivity in the ablation zone of the Greenland Ice Sheet, The Cryosphere, 9, 487-504, doi:10.5194/tc-9-487-2015, 2015.

Cuffey, K. and Paterson, W. S. B.: The Physics of Glaciers, 4th Edn., Elsevier Inc., Burlington and Oxford, 2010.

Dozier, J., Painter, T. H., Rittger, K. and Frew, J. E.: Timespace continuity of daily maps of fractional snow cover and albedo from MODIS, Adv. Water Resour., 31, 1515–1526, doi:10.1016/j.advwatres.2008.08.011, 2008.

Dumont, M., Gardelle, J., Sirguey, P., Guillot, A., Six, D., Rabatel, A., and Arnaud, Y.: Linking glacier annual mass balance and glacier albedo retrieved from MODIS data, The Cryosphere, 6, 1527–1539, doi:10.5194/tc-6-1527-2012, 2012.

Dumont, M., Brun, E., Picard, G., Michou, M., Libois, Q., Petit, J., Geyer, M., Morin, S., and Josse, B.: Contribution of lightabsorbing impurities in snow to Greenland's darkening since 2009, Nat. Geosci., 7, 509–512, doi:10.1038/ngeo2180, 2014.

Ettema, J., van den Broeke, M. R., van Meijgaard, E., van de Berg, W. J., Box, J. E., and Steffen, K.: Climate of the Greenland ice sheet using a high-resolution climate model – Part 1: Evaluation, The Cryosphere, 4, 511–527, doi:10.5194/tc-4-511-2010, 2010.

Fettweis, X.: Reconstruction of the 1979–2006 Greenland ice sheet surface mass balance using the regional climate model MAR, The Cryosphere, 1, 21–40, doi:10.5194/tc-1-21-2007, 2007.

Fettweis, X., Tedesco, M., van den Broeke, M., and Ettema, J.: Melting trends over the Greenland ice sheet (1958–2009) from spaceborne microwave data and regional climate models, The Cryosphere, 5, 359–375, doi:10.5194/tc-5-359-2011, 2011.

Fitzgerald, P. W., Bamber, J. L., Ridley, J. K., and Rougier, J. C.: Exploration of parametric uncertainty in a surface mass balance model applied to the Greenland ice sheet, J. Geophys. Res., 117, F01021, doi:10.1029/2011JF002067, 2012.

Gorter, W., van Angelen, J. H., Lenaerts, J. T. M. and van den Broeke, M. R.: Present and future near-surface wind climate of Greenland from high resolution regional climate modelling, Clim. Dyn., 42, 1595–1611, doi:10.1007/s00382-013-1861-2, 2014.

Grenfell, T. C. and Perovich, D. K.: Seasonal and spatial evolution of albedo in a snow-ice-land-ocean environment, J. Geophys. Res., 109, C01001, doi:10.1029/2003JC001866, 2004.

Hall, D. K., Riggs, G. A., and Salomonson, V. V.: MODIS Snow and Sea Ice Products 2006: Earth Science Satellite Remote Sensing – Volume I: Science and Instruments, edited by: Qu, J. J., Gao, W., Kafatos, M., Murphy, R. E., and Salomonson, V. V., Springer, New York, 154–181, 2006.

Hall, D. K., Comiso, J. C., DiGirolamo, N. E., Shuman, C. A., Box, J. E., and Koenig, L. S.: Variability in the surface temperature and melt extent of the Greenland ice sheet from MODIS, Geophys. Res. Lett., 40, 2114–2120, doi:10.1002/grl.50240, 2013.

Hanna, E., Fettweis, X., Mernild, S. H., Cappelen, J., Ribergaard, M. H., Shuman, C. A., Steffen, K., Wood, L., and Mote, T. L.: Atmospheric and oceanic climate forcing of the exceptional Greenland ice sheet surface melt in summer 2012, Int. J. Climatol., 34, 1022–1037, doi:10.1002/joc.3743, 2014.

Holben, N., Tanr, D., Smirnov, A., Eck, T. F., Slutsker, I., Newcomb, W. W., Schafer, J. S., Chatenet, B., Lavenu, F., Kaufman, J., Castle, J. Vande, Setzer, A., Markham, B., Clark, D., Halthore, R., Karneli, A., Neill, N. T. O., Pietras, C., Pinker, T., Voss, K., and Zibordi, G.: An emerging ground-based aerosol climatology?: aerosol optical depth from AERONET, J. Geophys. Res., 106, 12067–12097, 2001.

Hubbard, B. and Glasser, N. F.: Field techniques in glaciology and glacial geomorphology, John Wiley & Sons, 2005.

Iqbal, M.: Spectral and total sun radiance under cloudless skies, in: Physical Climatology for Solar and Wind Energy, edited by: Guzzi, R. and Justus, C. G., World Scientific, Singapore, 196– 242, 1988.

Keegan, K. M., Albert, M. R., McConnell, J. R., and Baker, I.: Climate change and forest fires synergistically drive widespread melt events of the Greenland Ice Sheet., P. Natl. Acad. Sci. USA., 111, 7964–7967, doi:10.1073/pnas.1405397111, 2014.

Klein, A. G. and Stroeve, J.: Development and validation of a snow albedo algorithm for the MODIS instrument, Annals of Glaciol., 34, 45–52, 2002.

Knap, W. H. and Oerlemans, J.: The surface albedo of the Greenland ice sheet: satellite derived and in situ measurements in the Sendre Stromfjord area during the

1991 melt season, J. Glaciol., 42, 364–374, 1996.

Konzelmann, T. and Braithwaite, R. J.: Variations of ablation, albedo and energy balance at the margin of the Greenland ice sheet, Kronprins Christian Land, eastern north Greenland, J. Glaciol., 41, 174–182, 1995.

Kuhn, M.: Anisotropic reflection from sastrugi fields, Antarc. J. US, 9, 123–125, 1974.

Lampkin, D. J. and VanderBerg, J.: Supraglacial melt channel networks in the Jakobshavn Isbrae region during the 2007 melt season, Hydrol. Process., doi:10.1002/hyp.10085, 2013.

Legleiter, C. J., Tedesco, M., Smith, L. C., Behar, A. E., and Overstreet, B. T.: Mapping the bathymetry of supraglacial lakes and streams on the Greenland ice sheet using field measurements and high-resolution satellite images, The Cryosphere, 8, 215–228, doi:10.5194/tc-8-215-2014, 2014.

Lenaerts, J. T. M., Smeets, C. J. P. P., Nishimura, K., Eijkelboom, M., Boot, W., van den Broeke, M. R., and van de Berg, W. J.: Drifting snow measurements on the Greenland Ice Sheet and their application for model evaluation, The Cryosphere, 8, 801– 814, doi:10.5194/tc-8-801-2014, 2014.

Lhermitte, S., Abermann, J., and Kinnard, C.: Albedo over rough snow and ice surfaces, The Cryosphere, 8, 1069–1086, doi:10.5194/tc-8-1069-2014, 2014.

Van Meijgaard, E., van Ulft, L. H., Van de Berg, W. J., Bosveld, F. C., Van den Hurk, B., Lenderink, G., and Siebesma, A. P.: The KNMI regional atmospheric climate model RACMO version 2.1, Tech. Rep. 302, Royal Netherlands Meteorological Institute, De Bilt, 2008.

Mernild, S. H. and Liston, G. E.: Greenland freshwater runoff. Part II: Distribution and trends, 1960–2010, J. Climate, 25, 6015– 6035, doi:10.1175/JCLI-D-11-00592.1, 2012.

Nghiem, S. V., Hall, D. K., Mote, T. L., Tedesco, M., Albert, M. R., Keegan, K., Shuman, C. A., DiGirolamo, N. E., and Neumann, G.: The extreme melt across the Greenland Ice Sheet in 2012, Geophys. Res. Lett., 39, 1–6, doi:10.1029/2012GL053611, 2012.

Onset Computer Corp.: Silicon Pyranometer Smart Sensor (Part # S-LIB-M003), available at: http://wpc.306e. edgecastcdn.net/80306E/onsetcomp_com/files/manual_pdfs/ 6708-D-MAN-S-LIB.pdf (last access: 14 August 2013), 2010.

Rae, J. G. L., Aðalgeirsdóttir, G., Edwards, T. L., Fettweis, X., Gregory, J. M., Hewitt, H. T., Lowe, J. A., Lucas-Picher, P., Mottram, R. H., Payne, A. J., Ridley, J. K., Shannon, S. R., van de Berg, W. J., van de Wal, R. S. W., and van den Broeke, M. R.: Greenland ice sheet surface mass balance: evaluating simulations and making projections with regional climate models, The Cryosphere, 6, 1275–1294, doi:10.5194/tc-6-1275-2012, 2012.

Rennermalm, A. K., Moustafa, S. E., Mioduszewski, J., Chu, V. W., Forster, R. R., Hagedorn, B., Harper, J. T., Mote, T. L., Robinson, D. A., Shuman, C. A., Smith, L. C. and Tedesco, M.: Understanding Greenland ice sheet hydrology using an integrated multi-scale approach, Environ. Res. Lett., 8(1), 015017, doi:10.1088/1748-9326/8/1/015017, 2013.

Román, M. O., Schaaf, C. B., Lewis, P., Gao, F., Anderson, G. P., Privette, J. L., Strahler, A. H., Woodcock, C. E., and Barnsley, M.: Assessing the coupling between surface albedo derived from MODIS and the fraction of diffuse skylight over spatiallycharacterized landscapes, Remote Sens. Environ., 114, 738–760, doi:10.1016/j.rse.2009.11.014, 2010.

Schaaf, C. B., Liu, J., Gao, F., and Strahler, A. H.: Aqua and Terra MODIS albedo and reflectance anisotropy products, in: Remote Sensing and Global Environmental Change, 549–561, Springer, New York, 2011.

Schaepman-Strub, G., Schaepman, M. E., Painter, T. H., Dangel, S., and Martonchik, J. V.: Reflectance quantities in optical remote sensing – definitions and case studies, Remote Sens. Environ., 103, 27–42, doi:10.1016/j.rse.2006.03.002, 2006.

Smith, L. C., Chu, V. W., Yang, K., Gleason, C. J., Pitcher, L. H., Rennermalm, A. K., Legleiter, C. J., Behar, A. E., Overstreet, B. T., Moustafa, S. E., Tedesco, M., Forster, R. R., LeWinter, A. L., Finnegan, D. C., Sheng, Y., and Balog, J.: Supraglacial rivers on the Greenland Ice Sheet, P. Natl. Acad. Sci. USA, doi:10.1073/pnas.1413024112, 2015.

Stroeve, J., Box, J. E., Gao, F., Liang, S., Nolin, A., and Schaaf, C.: Accuracy assessment of the MODIS 16-day albedo product for snow: comparisons with Greenland in situ measurements, Remote Sens. Environ., 94, 46–60, doi:10.1016/j.rse.2004.09.001, 2005.

Stroeve, J. C., Box, J. E., and Haran, T.: Evaluation of the MODIS (MOD10A1) daily snow albedo product over the Greenland Ice Sheet, Remote Sens. Environ., 105, 155–171, doi:10.1016/j.rse.2006.06.009, 2006.

Stroeve, J., Box, J. E., Wang, Z., Schaaf, C., and Barrett, A.: Re-evaluation of MODIS MCD43 Greenland albedo accuracy and trends, Remote Sens. Environ., 138, 199–214, doi:10.1016/j.rse.2013.07.023, 2013.

Tedesco, M., Fettweis, X., van den Broeke, M. R., van de Wal, R. S. W., Smeets, C. J. P. P., van de Berg, W. J., Serreze, M. C., and Box, J. E.: The role of albedo and accumulation in the 2010 melting record in Greenland, Environ. Res. Lett., 6, 014005, doi:10.1088/1748-9326/6/1/014005, 2011.

Tedesco, M., Fettweis, X., Mote, T., Wahr, J., Alexander, P., Box, J. E., and Wouters, B.: Evidence and analysis of 2012 Greenland records from spaceborne observations, a regional climate model and reanalysis data, The Cryosphere, 7, 615–630, doi:10.5194/tc-7-615-2013, 2013.

Tedesco, M., Box, J. E., Cappelen, J., Fettweis, X., Jensen, T., Mote, T. L., Rennermalm, A. K., Smith, L. C., van de Wal, R. S. W., and Wahr, J.: The Arctic: Greenland Ice Sheet in “State of the Climate 2013.” Bull. Am. Meteorol. Soc., 95, S136–S137, 2014.

Van Angelen, J. H., Lenaerts, J. T. M., Lhermitte, S., Fettweis, X., Kuipers Munneke, P., van den Broeke, M. R., van Meijgaard, E. and Smeets, C. J. P. P.: Sensitivity of Greenland Ice Sheet surface mass balance to surface albedo parameterization: a study with a regional climate model, The Cryosphere, 6, 1175–1186, doi:10.5194/tc-6-1175-2012, 2012.

van den Broeke, M., van As, D., Reijmer, C., and van de Wal, R.: Assessing and improving the quality of unattended radiation observations in Antarctica, J. Atmos. Ocean. Tech., 21, 1417–1431, doi:10.1175/1520-0426(2004)0212.0.CO;2, 2004.

van den Broeke, M., Smeets, P., Ettema, J., van der Veen, C., van de Wal, R., and Oerlemans, J.: Partitioning of melt energy and meltwater fluxes in the ablation zone of the west Greenland ice sheet, The Cryosphere, 2, 179–189, doi:10.5194/tc-2- 179-2008, 2008.

van den Broeke, M. R., Smeets, C. J. P. P., and van de Wal, R. S. W.: The seasonal cycle and interannual variability of surface energy balance and melt in the ablation zone of the west Greenland ice sheet, The Cryosphere, 5, 377–390, doi:10.5194/tc-5-377-2011, 2011.

Van de Wal, R. S. W., Boot, W., Smeets, C. J. P. P., Snellen, H., van den Broeke, M. R., and Oerlemans, J.: Twenty-one years of mass balance observations along the K-transect, West Greenland, Earth Syst. Sci. Data, 4, 31–35, doi:10.5194/essd-4-31-2012, 2012.

Wang, Z., Schaaf, C. B., Chopping, M. J., Strahler, A. H., Wang, J., Román, M. O., Rocha, A. V., Woodcock, C. E., and Shuai, Y.: Evaluation of Moderate-resolution Imaging Spectroradiometer (MODIS) snow albedo product (MCD43A) over tundra, Remote Sens. Environ., 117, 264–280, doi:10.1016/j.rse.2011.10.002, 2012.

Warren, S. G., Brandt, R. E., and O'Rawe Hinton, P.: Effect of surface roughness on bidirectional reflectance of Antarctic snow, J. Geophys. Res., 103, 25789, doi:10.1029/98JE01898, 1998.

Wientjes, I. G. M. and Oerlemans, J.: An explanation for the dark region in the western melt zone of the Greenland ice sheet, The Cryosphere, 4, 261–268, doi:10.5194/tc-4-261-2010, 2010.

Wientjes, I. G. M., Van de Wal, R. S. W., Reichart, G. J., Sluijs, A., and Oerlemans, J.: Dust from the dark region in the western ablation zone of the Greenland ice sheet, The Cryosphere, 5, 589– 601, doi:10.5194/tc-5-589-2011, 2011.

Wright, P., Bergin, M., Dibb, J., Lefer, B., Domine, F., Carman, T., Carmagnola, C., Dumont, M., Courville, Z., Schaaf, C., and Wang, Z.: Comparing MODIS daily snow albedo to spectral albedo field measurements in Central Greenland, Remote Sens. Environ., 140, 118–129, doi:10.1016/j.rse.2013.08.044, 2014.

Yang, K. and Smith, L. C.: Supraglacial streams on the Greenland Ice Sheet delineated from combined spectral–shape information in high-resolution satellite imagery, IEEE Geosci. Remote Sens. Lett., 10, 801–805, doi:10.1109/LGRS.2012.2224316, 2013.

Zhuravleva, T. B. and Kokhanovsky, A. A.: Influence of surface roughness on the reflective properties of snow, J. Quant. Spectrosc. Radiat. Transf., 112, 1353–1368, doi:10.1016/j.jqsrt.2011.01.004, 2011.

Chapter 3: Evaluation of satellite remote sensing albedo retrievals over the ablation area of the southwestern Greenland ice sheet

3.1 Introduction

The Greenland Ice Sheet (GrIS), is rapidly losing mass at a rate that has quadrupled between 1992-2011 (Shepherd et al., 2012). Increased meltwater production and runoff (e.g., Mernild and Liston, 2012) accounts for half or more of total mass loss (van den Broeke et al., 2009; Enderlin et al., 2014; Khan et al., 2014), which has occurred in concert with increasing near-surface air temperatures (Hall et al., 2013) and an observed decline in surface albedo (e.g., Box et al., 2012; Stroeve et al., 2013). Monitoring changes in albedo is crucial given its importance in modulating the surface energy balance, and consequentially, melt and mass balance of the ice sheet.

Albedo is defined as the fraction of radiant exitance energy to downwelling solar irradiance integrated across the visible, near-infrared, and shortwave-infrared wavelengths (Schaepman-Strub et al., 2006). Albedo is particularly important for the surface energy balance in ice and snow covered areas of the Arctic, including Greenland (van den Broeke et al., 2011; Vernon et al., 2013). On the GrIS, the high albedo of snow (> 0.80) reflects much more solar radiation than darker melting or bare ice surfaces (0.30-0.60; e.g., Moustafa et al., 2015). Over a typical ice sheet melting season, snow melts over vast areas uncovering the ice surface below, effectively reducing albedo. The darker surface leads to increased solar radiation absorption, which further enhances snowmelt. Additionally, ice crystal growth over the melting season reduces albedo. This positive feedback loop is called the ice-albedo feedback and is one of the drivers for the marked GrIS albedo trend for 2000-2011 (-0.056 ± 0.007 June-August; Box et al., 2012).

Greenland albedos have declined the most in the southwestern ice sheet's ablation area (Alexander et al., 2014; Stroeve et al., 2013). This is related to an expansion of bare ice area (Tedesco et al., 2011), high concentration of impurities and melting of outcropped tilted sediment-rich ice layers (Wientjes et al., 2011), and enhanced meltwater production and runoff (Mernild et al., 2012). Furthermore, recent studies have identified the considerable influence of seasonal evolution of ice sheet surface types (e.g., snow cover, bare ice, impurity-rich ice) have on the high spatiotemporal variability in ablation area albedos (Alexander et al., 2014; Chandler et al., 2015; Moustafa et al., 2015). As the melt season progresses, the spatial and temporal variability can be very high (Alexander et al. 2014; Moustafa et al. 2015; Tedesco et al. 2016) due to processes discussed below.

GrIS albedo have mainly been characterized with the Moderate Resolution Imaging Spectroradiometer (MODIS) and the Advanced Very High Resolution Radiometer (AVHRR) satellite sensors (e.g., Box et al., 2012; Chandler et al., 2015; Stroeve et al., 2005, 2006, 2013; Wang et al., 2012; Wright et al., 2014). These remotely sensed albedo measurements have been validated with data from up to 17 ground measurements sites (Stroeve et al., 2013) from the dispersed Greenland Climate Network Automatc Weather Stations (GC-Net AWS; Knap and Oerlemans, 1996; Steffen and Box, 2001) using a so-called 'point-to-pixel' method, hereafter, single point-to-pixel method. In this method, the AWS GC-Net time series at individual points are compared to the satellite-derived albedo retrieval from the overlapping pixel. Comparisons reveal that satellite albedo products provide reasonable albedo estimates (Box et al., 2012;

Stroeve et al., 2005, 2006, 2013), and compare well with these in situ albedo GC-Net AWS measurements (e.g., root-mean-square-error (RMSE) of 0.067 for the Version 005 MCD43A albedo data product; Stroeve et al., 2013). However, it is recognized that unless the surface is homogeneous or an adequate number of dispersed ground point measurements are collected within a pixel during satellite overpasses, then a 'point-to-pixel' comparison may be insufficient (Liang et al., 2002; Román et al., 2009). These discrepancies are exacerbated by rough surfaces (Lhermitte et al., 2014; Rippin et al., 2015; Ryan et al., 2016), large scan angles (Painter et al., 2009; Campagnolo et al., 2016), and larger (> 75˚) solar zenith angles (SZAs; Stroeve et al., 2005, 2006; Wang et al., 2012). The ablation area in southwest Greenland is exactly the kind of spatially heterogeneous surface where a sparse network of single point AWS stations may be inadequate for validation of remotely sensed albedo products.

A more suitable validation method for heterogeneous ablation areas could involve data collection at multiple points (hereafter, multiple 'point-to-pixel' method) similar to Wright et al. (2014)'s study where the Version 006 MCD43A albedo data product was re-evaluated against in situ albedo measurements collected at several sites along a transect in the accumulation zone at Summit, Greenland. Whereas Wright et al. (2014) applied their method to a spatially homogenous area, it could easily be adapted for heterogeneous surfaces. Regardless if single or multiple points are used for validation of remotely sensed albedo, these studies point out the fallacy in assuming that point in situ observations are spatially representative of coarser satellite products (i.e., point observations are assumed to be representative at pixel scales; Román et al., 2009), and the need to capture more point observations within a MODIS gridded area (Wright et al., 2014). Therefore, given the varying spatial resolution of in situ and satellite products, scaling errors may occur if albedos differ at different sampling domains, observational locations (Lhermitte et al., 2014), and over rapid changes in surface conditions (e.g., seasonal changes in ablation area ice surface types).

A methodology that quantifies the spatial representativeness of a ground albedometer site for validating the MODIS daily albedo product was developed by Román et al., (2009). In this method, spatial representativeness is referred to as the degree to which in situ albedo measurements are able to resolve the spatial variability of the surrounding ablation area surface extending up to the satellite footprint. This validation technique provides an improved understanding of remotely sensed albedo product uncertainty, and the efficacy of single 'point-to-pixel' comparisons, as well as the satellite and in situ data's capacity to capture spatial and temporal features that characterize the ablation area. Because the in situ retrievals may have shortcomings in representing heterogeneous ground conditions, we argue that it is more appropriate to consider this spatial representative method as a methodology for comparison rather than a validation in its own right. This spatial representative method has been useful for inter-comparisons of surface and satellite albedo in snow-free (e.g., Román et al., 2009, 2010) and seasonally snow-covered tundra (e.g., Wang et al., 2012, 2014) environments, but has not yet been applied to glaciers and ice sheets.

Here we adapt Román et al.'s (2009) and Wang et al.'s (2012, 2014) method to perform a robust spatial inter-comparison of in situ spectral albedo measurements with satellite retrievals of narrow and broad band albedo from the GrIS. In contrast to Román et al. (2009) and Wang et al. (2012, 2014), who used single point in situ observations, our study uses several points along a transect (i.e., a multiple point-to-pixel comparison) similar to Wright et al. (2014). Our transect data was collected with an Analytical Spectral Devices Inc. (ASD) spectroradiometer over southwest Greenland's ablation area, near the town of Kangerlussuaq, during the 2013 melt season, and has undergone a thorough quality assessment (Moustafa et al,. 2015) and freely available (Appendix 3A; Moustafa et al., 2016). The geographical extent of the ground albedo data set allows for careful evaluation of two MODIS pixels, using data from the recently developed MODIS (Version 006) MCD43A daily albedo retrievals. Due to the fixed time period of in situ albedo data collected, temporal variability of albedo is not explicitly assessed in this study. As far as we know, the high density of ground measurements allows for the first-ever spatial characterization of the lower GrIS ablation area's heterogeneous surface as well as an assessment of the utility of each MODIS narrow band. Furthermore, we investigate within-MODIS pixel spatial variability at an intermediate scale between in-situ and MODIS observations by using a high-resolution WorldView-2 (WV-2) image. While MODIS MCD43A albedo is reported at a 500 m gridded resolution, the data product utilizes multiple MODIS surface reflectance values collected at varying view zenith angles. View geometry, variable pixel footprint size, and surface topography have been identified as contributing significant variability to the MODIS snow and albedo data products, but these are not analyzed in this study. Instead, our study only utilizes published MODIS data (assuming fixed pixel sizes at this latitude) that are readily available. A discussion of view zenith angles, adjacency effects, and surface roughness's importance on satellite albedo retrievals is provided in Section 5. Lastly, a comparison between the errors of single and multiple point-to-pixel methods is conducted.

3.2 Data

3.2.1 In situ spectroscopy data

Spectral albedo, hereafter α_{ASD}, were measured using an ASD Fieldspec HandHeld 2 spectroradiometer at 325-1075 nm with a spectral resolution of 1 nm along a transect. The α_{ASD} measurements were collected every ~10 m. The ASD instrument was mounted to a tripod at 0.4 m height, fitted with a Remote Cosine Receptor (RCR) foreoptic, and had a 25º field of view (FOV) corresponding to a circular footprint of ~0.18 m diameter on the surface.

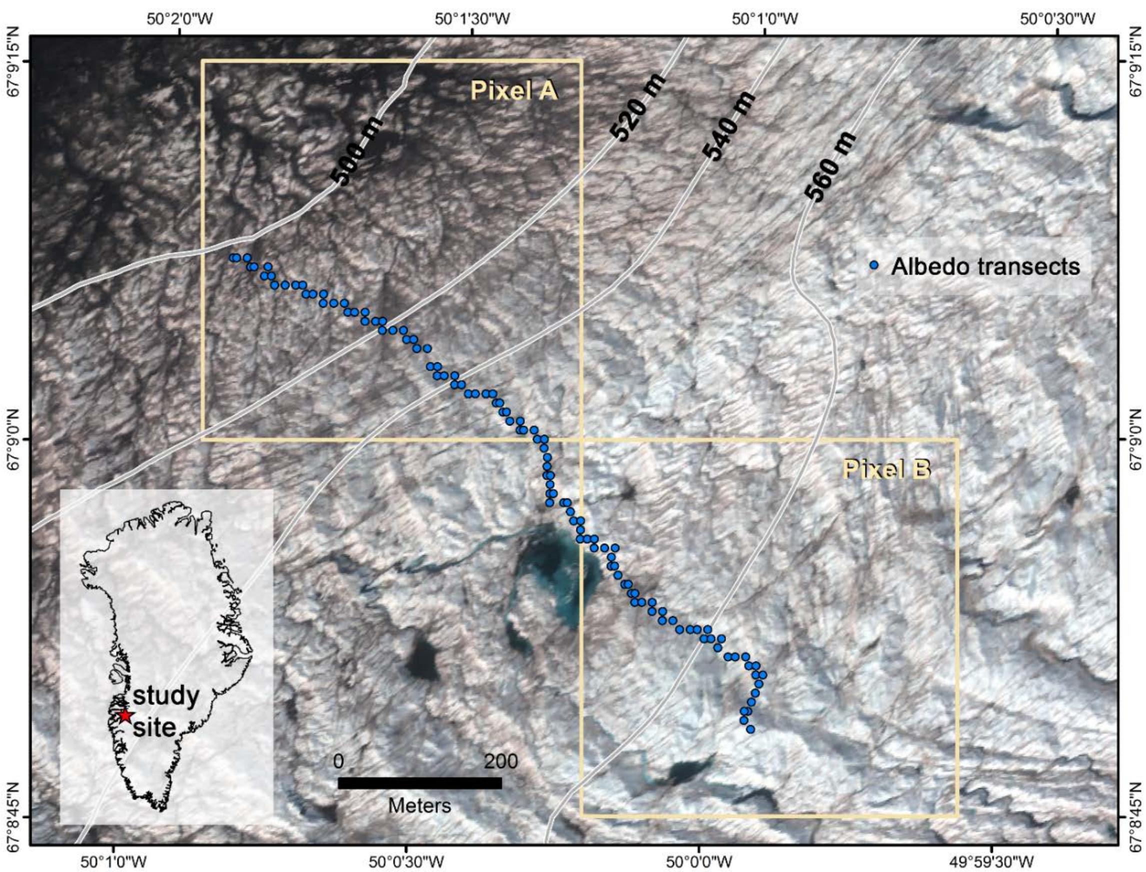

Figure 3.1 Map of the study area in southwest Greenland's ablation area. MODIS nominal pixel extents (yellow boxes), and location of the point ASD in situ measurements in the two transects (blue points).

Here, we used α_{ASD} measured on 16 and 19 June 2013 between 10:00 and 12:00 local time (12:00 – 14:00 UTC) along a 1.25 km transect positioned between ~510 and 590 m a.s.l., in southwest Greenland (Fig. 3.1, data available at Moustafa et al., 2016; see Appendix 3A). This is well within the ablation area for this region (mean equilibrium line altitude of 1553 m a.s.l.; van de Wal et al., 2012). The ASD was calibrated at the start of each transect to current hemispherical atmospheric conditions by orienting the RCR skyward, along a nadir-viewing angle. Subsequent measurements were taken with the ASD rotated 180° to view the ice surface. Under changing sky conditions, the instrument was recalibrated. Each transect consisted of ~100 sample locations. These locations were biased toward the brighter surface types as the darker surfaces were logistically challenging to access (e.g. impassable meltwater features and shaded crevasses). Rigorous quality control was performed on the data and is detailed in Moustafa et al. (2015).

The α_{ASD} ground observations fall within two MODIS pixels, named Pixel A and Pixel B, and were compared to MODIS narrow bands and the broad band visible (0.3-0.7µm) products, as described below. To compare α_{ASD} with MODIS wavebands, spectral albedo measurements within the pixel were interpolated, normalized, and numerically integrated to match the relative spectral response of the MODIS bandwidths. The limited spectral range of our ASD instrument prevented evaluation of the MODIS broad band shortwave (0.3-5.0µm) product.

3.2.2 MODIS (MCD43A) Version 006 daily albedo product

Within the MODIS MCD43 v006 collection, we evaluate derived blue-sky albedo from the MCD43A3 albedo product. Blue-sky albedo is calculated as a function of diffuse (white-sky albedo; WSA) and direct (black-sky albedo; BSA; Román et al., 2010). The effects of multi-scattering and anisotropic diffuse illumination of bright snow surfaces are considered for the calculation of MODIS blue-sky albedo at these high latitude locations (Román et al., 2010; Wang et al., 2012). The BRDF characterizes scattering of radiation at the Earth's surface as a function of solar illumination and view geometry for MODIS narrow and broad bands. The MCD43A1 product provides the model weighting parameters to simulate the surface's reflective character at a nominal 500 m gridded resolution (Campagnolo et al., 2016).

The MCD43A3 albedo product delivers both WSA and BSA at local solar noon for seven MODIS narrow bands (bands 1-7) and three broad bands (0.3-0.7µm, 0.7-5.0µm, and 0.3-5.0µm). The WSA and BSA are reconstructed daily based on a centered moving window of 16 days of Aqua and Terra surface reflectance input data, with heavier weights assigned to observations closer to the day of interest, to characterize the best BRDF possible. Compared to previous MCD43 versions, the v006 product includes more clear-sky scenes, and corrects for MODIS sensor degradation identified on both the Terra and Aqua satellites (e.g., Wang et al., 2012). This should make the v006 product better able, than previous versions, at capturing daily albedo (as demonstrated in Wright et al., 2014).

Surface blue-sky albedo, hereafter α_{MODIS}, for Pixels A and B, $\alpha_{MOD\ Pixel\ A}$ and $\alpha_{MOD\ Pixel\ B}$, respectively, is calculated similar to Román et al. (2010) using the MCD43A3 product (only 'high quality' were used in this study; QA flag = 0), and performing atmospheric correction with AOD data (Lewis and Barnsley et al., 1994; Román et al., 2010) from a nearby AEROsol robotic NETwork (AERONET; Holben et al., 2001; http://aeronet.gsfc.nasa.gov/) station located in Kangerlussuaq (67.017, -50.690; ~50 m a.s.l., 30 km away from the transect). AOD observations collected at 550 nm were extrapolated as a function of surface elevation to the ground transect validation sites using the MODTRAN5 radiative transfer model (Berk et al., 2006) so that MODIS AOD corrections could be determined at each in situ observational point (thus providing a "MODIS" pixel value for each in situ location). However, because of the very small elevation differences within the transects, the AOD variations have a very small impact on MODIS albedo (~0.03-0.05). Therefore, for simplicity, we select the AOD-corrected MODIS albedo calculated at the in situ point obtained at the median transect time as a single, pixel-wide MODIS blue-sky albedo for each pixel. A temporal scale mismatch exist between ground α_{ASD} and α_{MODIS} retrievals due to differences in sampling times.

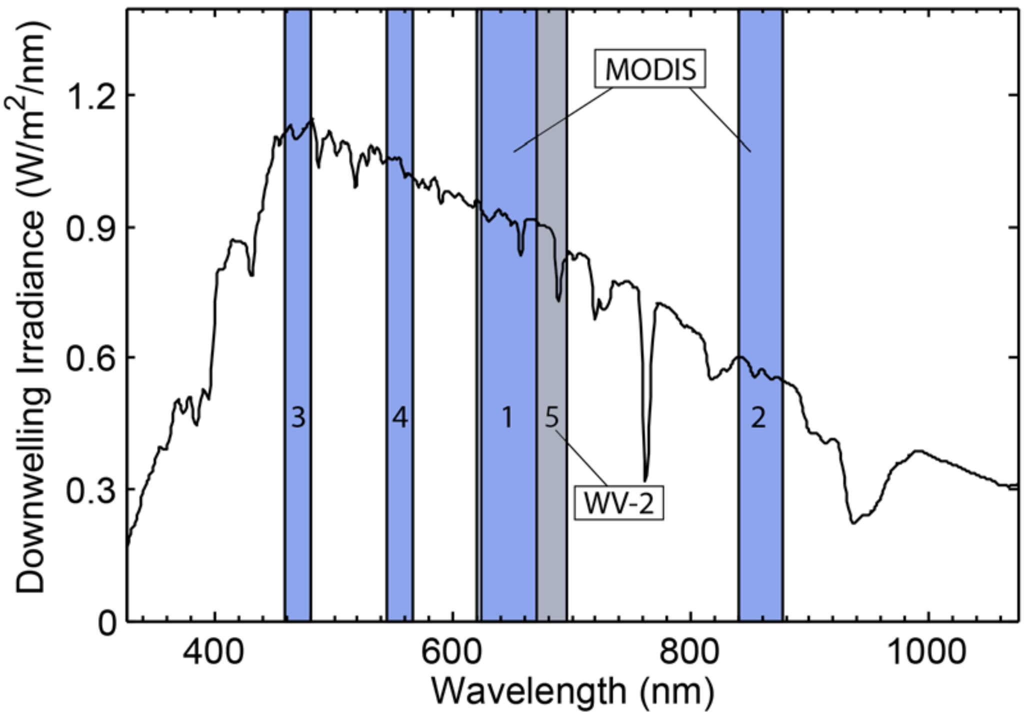

Figure 3.2 Averaged downwelling irradiance measured with the ASD for two transect dates (black line) and wavelength ranges (blue bars) for MODIS visible and near-infrared wavebands (bands 1-4; 459-479 nm; 545-565 nm; 620-670 nm; 841-876 nm), and the WV-2 red waveband (band 5) in the grey bar.

Albedo for a total of five MODIS bands were calculated: four narrow bands (bands 1-4) and one visible broad band channel (0.3-0.7µm; Fig. 2.2). Visible (0.3-0.7µm) broad band albedo estimate was calculated by using the empirical narrow-to-broadband function provided in Stroeve et al. (2005):

$$\alpha_{VIS_{Stroeve}} = 0.3591\alpha_{b1} + 0.510\alpha_{b3} + 0.1322\alpha_{b4} - 0.009 \quad (1)$$

Where α_{b1}, α_{b3}, and α_{b4} is albedo for bands 1, 3, and 4, respectively.

3.3.3 Red band surface reflectance derived from WorldView-2 data

WV-2 multispectral data (2 m spatial resolution) from 23 June 2013 (the available image closest in time to the June 16th and 19th in situ data collection) was obtained from the Polar Geospatial Center (PGC; http://www.pgc.umn.edu/). This data was converted from raw digital numbers (DN) to top-of-the-atmosphere (TOA) radiance via radiometric calibration by using the image gains and offsets provided in the WV-2 metadata:

$$L_\lambda = Gain \cdot Pixel\ value + Offset \qquad (2)$$

Where L_λ is TOA radiance with units of W/(m^2 sr μm).

Using the L_λ as input, WV-2 surface reflectance, hereafter ρ_{WV2}, was computed using the Fast Line-of-sight Atmospheric Analysis of Hypercubes (FLAASH) atmospheric correction model (Matthew et al., 2000), assuming a Lambertian surface. The FLAASH model was implemented using a sub-Arctic summer atmospheric profile with a rural aerosol model (blended small and large particle sizes) and water vapor (2.08 g/cm^2). Only the red band (630-690 nm) ρ_{WV2} data was used since it corresponds closely to the MODIS red band (Band 1; 620-670 nm; Fig. 3.2). Visible broad band albedo was not calculated because narrowband-to-broadband coefficients for WV-2 data are non-existent and non-trivial to determine.

3.3 Methods

3.3.1 Ground, WV-2, and MODIS comparison routine

The pixel scale albedo was determined with MODIS as described above, and compared with the mean α_{ASD} and mean ρ_{WV2} values for Pixel A and B, respectively, and for the June 16 and 19th transect dates separately. To examine the potential error of using a single ground control point (i.e., single point-to-pixel method) to evaluate α_{MODIS}, MATLAB's ksdensity function (kernel smoothing function) was used to estimate the probability density distribution of the difference of α_{MODIS} and individual α_{ASD} values from each observational point.

3.3.2 Spatial representativeness

MODIS sub-pixel variability was characterized with semiovariograms, a widely applied geostatistical technique (Carroll and Cressie, 1996; Davis, 1986; Isaaks and Srivastava, 1989; Matheron, 1963), which has been used in MODIS validation to assess the spatial representativeness of ground and tower-based albedo measurements (e.g., Burakowski et al., 2015; Román et al., 2009, 2010; Wang et al., 2012, 2014, 2016). Variogram analysis is a way to quantify spatial autocorrelation, or the degree to which similar albedo values cluster together in space on the ice surface, from three spatial attributes. Variogram models can be used to extract geostatistical attributes (e.g., sill, range, nugget effect) that aid in revealing patterns of spatial variability and scaling effects related to remotely sensed data (Woodcock et al., 1988a, 1988b; Dent and Grimm, 1999).

Given that the footprint of the ASD instrument (~0.18 m in diameter) is considerably smaller than the 500 m nominally gridded MODIS pixel, high resolution ρ_{WV2} data was used as an intermediate between the ground and satellite albedo retrievals. Due to computational limitations, the spatial representativeness analysis was conducted using ρ_{WV2} data at a 480 m x 480 m spatial domain. Regardless, the analysis domain is very close to the MODIS nominal resolution and will therefore provide insights into scaling of albedo.

Using methodology presented in Román et al. (2009), semivariograms were calculated from the ρ_{WV2} data that intersect with the MODIS Pixel A and B footprints (Fig. 2.1). The variogram estimator, $\gamma_E(h)$, was used to determine half the mean-squared-difference between albedo values that are within a set distance (e.g., nominal resolution of 2 m for WV-2):

$$\gamma_E(h) = 0.5 \cdot \frac{\sum_{i=1}^{N(h)} (z_{xi} - z_{xi+h})^2}{N(h)} \tag{3}$$

Where z_{xi} is surface reflectance at pixel location x; z_{xi+h} is surface reflectance of another pixel within a lag distance h; and $N(h)$ is the number of paired data at distance h. Then, the geospatial attributes – range (a), sill (c), and nugget effect (c_0) – were identified by fitting a spherical variogram model (Matheron, 1963) to the variogram estimator $\gamma_E(h)$:

$$\gamma_{sph}(h) = \begin{cases} c_0 + c \cdot \left(1.5 \cdot \frac{h}{a} - 0.5 \left(\frac{h}{a}\right)^3\right), & 0 \le h \le a \\ c_0 + c, & h > a \end{cases} \tag{4}$$

The range (a) is defined as the distance at which samples of a biophysical variable (albedo) and the ground location (ASD point measurements) no longer correlate. For a satellite footprint that is larger than the ground footprint, a spatially representative site will have a range less than or equal to the satellite footprint. The sill (c) is the maximum semivariance value at which the range stabilizes into an asymptote and describes the maximum overall variation. The nugget effect (c_0) is the value when the variogram does not reach zero variance at $h = 0$ and depends on the variance related to small scale variability and/or measurement errors (Noreus et al., 1997). The nugget effect is demonstrative of purely random variability.

The semiovariogram parameters are interpreted as outlined in Wang et al. (2014), where small sill values indicate more homogenous surfaces where ground observations have higher likelihood of being spatially representative, and range values express the minimum ground observation footprint needed to capture the spatial variability.

3.4 Results

3.4.1 Analysis of surface albedo for MODIS gridded pixel footprints

By averaging multiple ASD observations and comparing it with a MODIS pixel-wide value, we effectively conduct a multiple 'point-to-pixel' comparison, where $\alpha_{\mathrm{MOD\ Pixel\ A}}$, across all five MODIS bands (i.e., Bands 1-4 and one visible broad band), are 6-7% lower (range (min/max) 0.37 to 0.53) than $\alpha_{\mathrm{ASD\ Pixel\ A}}$ (range ± standard error (SE) 0.44 ± 0.01 to 0.59 ± 0.02; Table 3.1) on June 16th. $\alpha_{\mathrm{MOD\ Pixel\ A}}$ on June 19th is also lower (4-6%) (range of 0.35 to 0.51) than $\alpha_{\mathrm{ASD\ Pixel\ A}}$ (range of 0.39 ± 0.01 to 0.57 ± 0.03; Table 3.1). Part of this difference is due to a known undersampling of darker surfaces (e.g., cryoconite holes, small melt ponds and streams) in Pixel A. In contrast, $\alpha_{\mathrm{MOD\ Pixel\ B}}$ across all five MODIS bands varies band-by-band and is generally higher (range of 0.44 to 0.70) than in $\alpha_{\mathrm{ASD\ Pixel\ A}}$ (range of 0.48 ± 0.01 to 0.63 ± 0.01; Table 3.2) on June 16th. Only one of the $\alpha_{\mathrm{MOD\ Pixel\ B}}$ bands (Band 2) on June 16th is lower (4%) than the $\alpha_{\mathrm{ASD\ Pixel\ B}}$, while the others bands can be up to 7% larger (Table 3.2). $\alpha_{\mathrm{MOD\ Pixel\ B}}$ on June 16th across all five MODIS bands is equivalent to the $\alpha_{\mathrm{MOD\ Pixel\ B}}$ on June 19th (range of 0.44 to 0.70; Table

3.2). $\alpha_{MOD\ Pixel\ B}$ are 1% higher than in $\alpha_{ASD\ Pixel\ B}$ on both transect dates (range of 0.48 ± 0.06 to 0.63 ± 0.09 on June 16th; 0.43 ± 0.01 to 0.69 ± 0.02 on June 19th; Table 3.2). Most of the $\alpha_{MOD\ Pixel\ B}$ bands on both transect dates are equal or larger than $\alpha_{ASD\ Pixel\ B}$ except for Band 2 on June 16th (0.44 in α_{MOD} versus 0.48 ± 0.06 in α_{ASD}) and Band 3 on June 19th (0.67 in α_{MOD} versus 0.69 ± 0.13 in α_{ASD}; Table 3.2). These differences are related to the higher albedos from lighter surfaces (e.g., clean ice and snow) of the upper ablation area characterizing Pixel B. Scatter plots of α_{MOD} and α_{ASD} confirm that MODIS retrievals were consistently lower as compared to in situ albedo values in Pixel A (Fig. 3.3a-b). There is high correlation (r^2 = 0.99) between α_{MOD} and α_{ASD}, and the slopes of the best linear fit are close to one in Pixel A (1.09 and 0.88 for June 16th and 19th, respectively; Fig. 3.3a-b). Strong correlation between in situ albedo and MODIS retrievals is also observed in Pixel B (r^2 = 0.99; Fig. 3.3c-d), however, there is less agreement of the best fit line along the 1:1 line (1.65 versus 0.95 for June 16th and 19th, respectively; Fig. 3.3c-d). This disagreement is linked to a difference in signage related to one band (Band 2) out of five bands on June 16th in Pixel B (Fig. 3.3c). Despite this, the majority of bands reveal that $\alpha_{MOD\ Pixel\ B}$ is higher than α_{ASD} or nearly the same (as the SEs overlap) on June 16th (Fig. 3.3c). Unlike June 16th, Pixel B on June 19th exhibits the best agreement between satellite retrievals and in situ albedo (slope is nearly equal to 1) and the 1:1 line is within the standard error range (Fig. 3.3d). Dissimilar α_{MODIS} and α_{ASD} values for the near-infrared (Band 2) albedo values (Tables 3.1 and 2; Fig. 3.3) is likely due to the high absorption tendencies of snow and ice found in the near-infrared wavelengths of the electromagnetic spectrum.

Table 3.1 Average ASD albedos, standard error (SE) and pixel-wide MODIS blue sky albedos based on mean elevation for MCD43A v006 blue-sky visible, near-infrared, and visible broad band albedos (bands 1-4 and VIS_Stroeve) for Pixel A.

MODIS band	Pixel A			
	$\alpha_{\text{MOD Pixel A June 16}}$	$\alpha_{\text{MOD Pixel A June 19}}$	$\alpha_{\text{ASD Pixel A June 16}} \pm$ SE	$\alpha_{\text{ASD Pixel A June 19}} \pm$ SE
Band 1	0.48	0.46	0.55 ± 0.02	0.53 ± 0.02
Band 2	0.37	0.35	0.44 ± 0.01	0.39 ± 0.01
Band 3	0.53	0.50	0.59 ± 0.02	0.56 ± 0.03
Band 4	0.53	0.51	0.58 ± 0.02	0.57 ± 0.03
VIS_Stroeve	0.51	0.48	0.57 ± 0.02	0.54 ± 0.02

Table 3.2 Average ASD albedos, standard error (SE) and pixel-wide MODIS blue sky albedos based on mean elevation for MCD43A v006 blue-sky visible, near-infrared, and visible broad band albedos (bands 1-4 and VIS_Stroeve) for Pixel B.

MODIS band	Pixel B			
	$\alpha_{\text{MOD Pixel B June 16}}$	$\alpha_{\text{MOD Pixel B June 19}}$	$\alpha_{\text{ASD Pixel B June 16}} \pm$ SE	$\alpha_{\text{ASD Pixel B June 19}} \pm$ SE
Band 1	0.63	0.63	0.59 ± 0.01	0.62 ± 0.01
Band 2	0.44	0.44	0.48 ± 0.01	0.43 ± 0.01
Band 3	0.67	0.67	0.63 ± 0.01	0.69 ± 0.02
Band 4	0.70	0.70	0.63 ± 0.01	0.69 ± 0.02
VIS_Stroeve	0.66	0.66	0.61 ± 0.01	0.66 ± 0.02

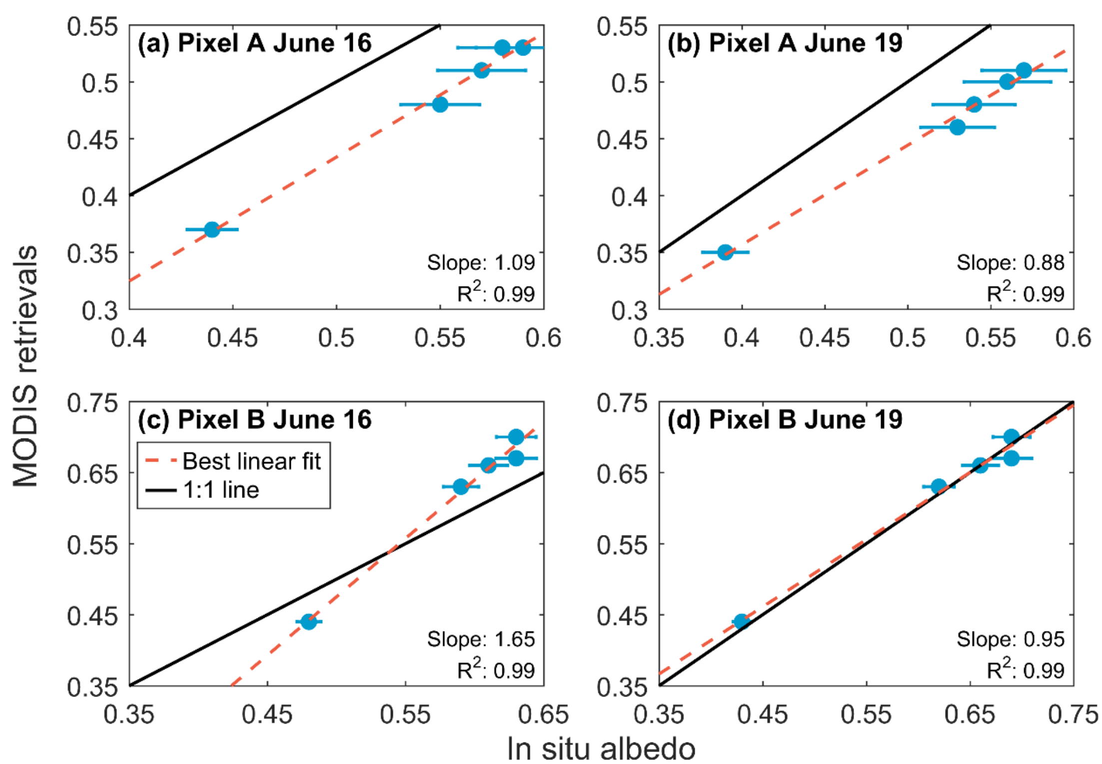

Figure 3.3 α_{ASD} versus α_{MODIS} scatterplots for Pixel A and B on June 16th and 19th transect dates for Bands 1-4 and VIS_Stroeve, and corresponding standard errors of the mean.

To assess the potential error associated with the single 'point-to-pixel' method, we quantified the frequency distribution of differences between α_{ASD} and α_{MODIS} for each MODIS waveband and transect date. Regardless of day (June 16 or 19), pixel (A or B), or band, distributions were wide ranging from ~±0.4, which is a considerable error given that albedo vary from 0 to 1 (Figs. 3.4 and 3.5). Had only one validation point been selected that at random coincided with the 10th or 90th percentiles of the ASD-MODIS error distribution, α_{ASD} would have been -0.32 or +0.43 (averaged for all bands) smaller/larger than α_{MODIS} in Pixel A and -0.30 or +0.24 (averaged for all bands) smaller/larger than α_{MODIS} in Pixel B on June 16th (Fig. 3.4). As expected from Tables 3.1 and 3.2, error distributions for June 16th reveal that α_{ASD} central tendencies are brighter than α_{MOD} across all bands for Pixel A, while α_{ASD} central tendencies are darker than α_{MOD} across all bands for Pixel B with the exception of Band 2 in the near-infrared (Fig. 3.1). Similarly to June 16th, if only one validation point had been selected on June 19th, that randomly coincided with the 10th and 90th percentiles of the ASD-MODIS error distribution, α_{ASD} would have been -0.46 or +0.43 smaller/larger than α_{MODIS} in Pixel A and -0.30 or +0.40 smaller/larger than α_{MODIS} in Pixel B (Fig. 3.5). On June 19th, the error distribution reveals that α_{ASD} central tendencies are brighter than α_{MODIS} across all bands for Pixel A, while α_{ASD} central tendencies are nearly equivalent to α_{MOD} across all bands for Pixel B except for Band 3 (Fig. 3.5).

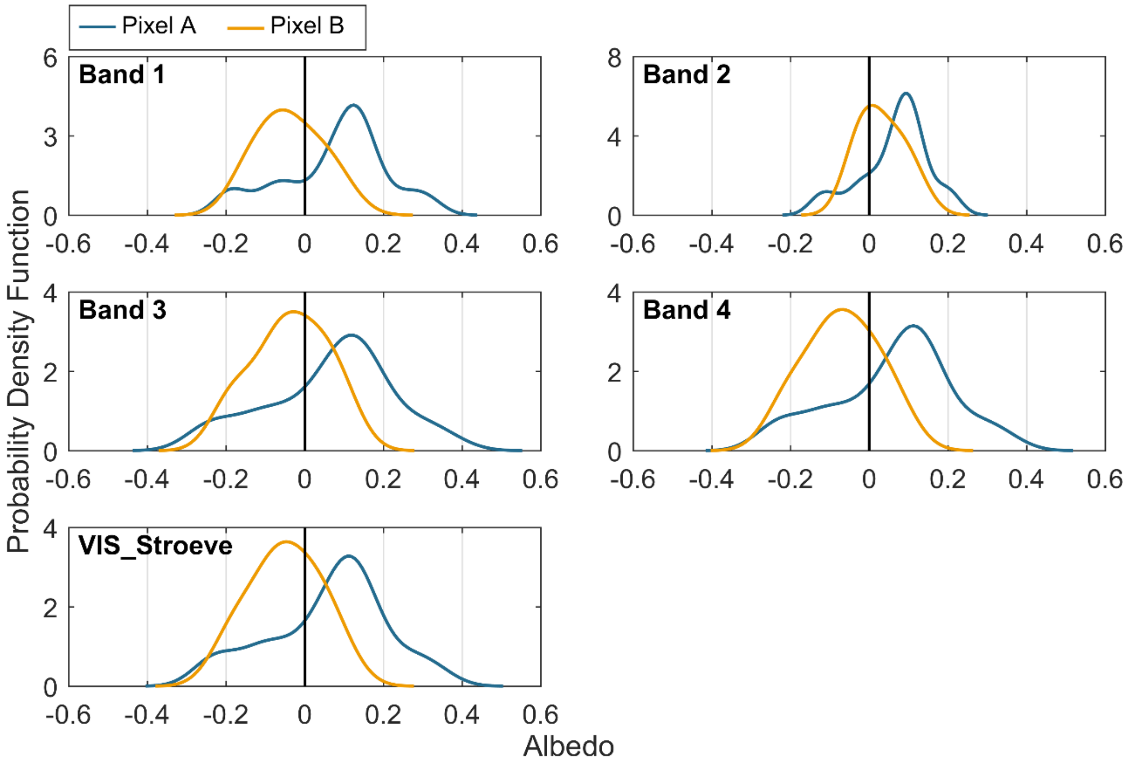

Figure 3.4 Normalized frequency distributions of α_{ASD} minus α_{MODIS} error distributions for Pixel A (blue colored lines) and Pixel B (orange colored lines) for June 16.

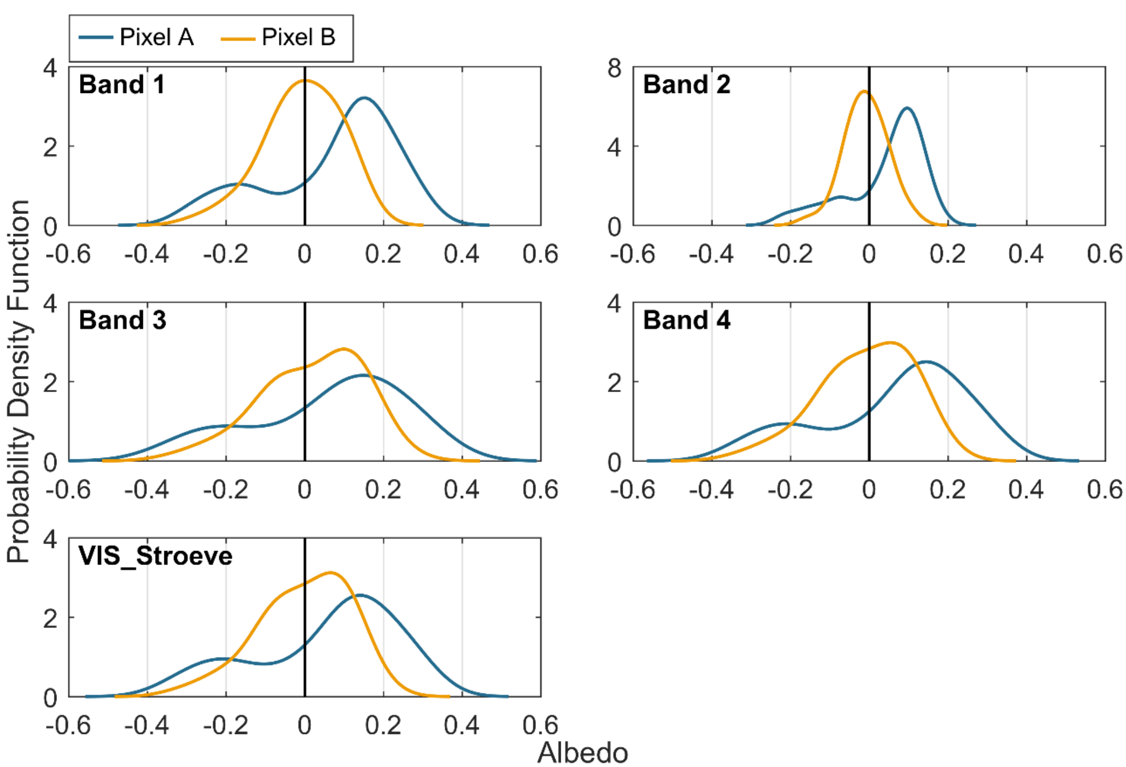

Figure 3.5 Normalized frequency distributions of α_{ASD} minus α_{MODIS} error distributions for Pixel A (blue colored lines) and Pixel B (orange colored lines) for June 19.

3.4.2 Analysis of sub-pixel variability

A multiple 'point-to-pixel' comparison between α_{MODIS} and ρ_{WV2}, and α_{ASD} retrievals is conducted for the red narrow band only (since it corresponds closely to only the MODIS red band). The frequency distribution in Pixel A shows that α_{ASD} overestimates ρ_{WV2} red band reflectance (0.53), and the ρ_{WV2} red band central tendency reflectance aligns (0.46) with the α_{MODIS} (0.46) (Fig. 2.6; Table 3.1). The α_{MODIS} value and the central tendencies of the ρ_{WV2}, and α_{ASD} values converge in Pixel B (0.63, 0.63, and 0.62, respectively; Fig. 2.6; Table 3.1). Despite the error between ρ_{WV2} and α_{ASD} in Pixel A (Fig. 3.6), we assume that the spatial analysis of WV-2 red-band data may be representative of all WV-2 narrow bands. In the future, development of coefficients for narrow-to-broadband and BRDF-to-albedo conversion can improve the accuracy of fine-scale WV-2 satellite retrievals of albedo in the ablation area.

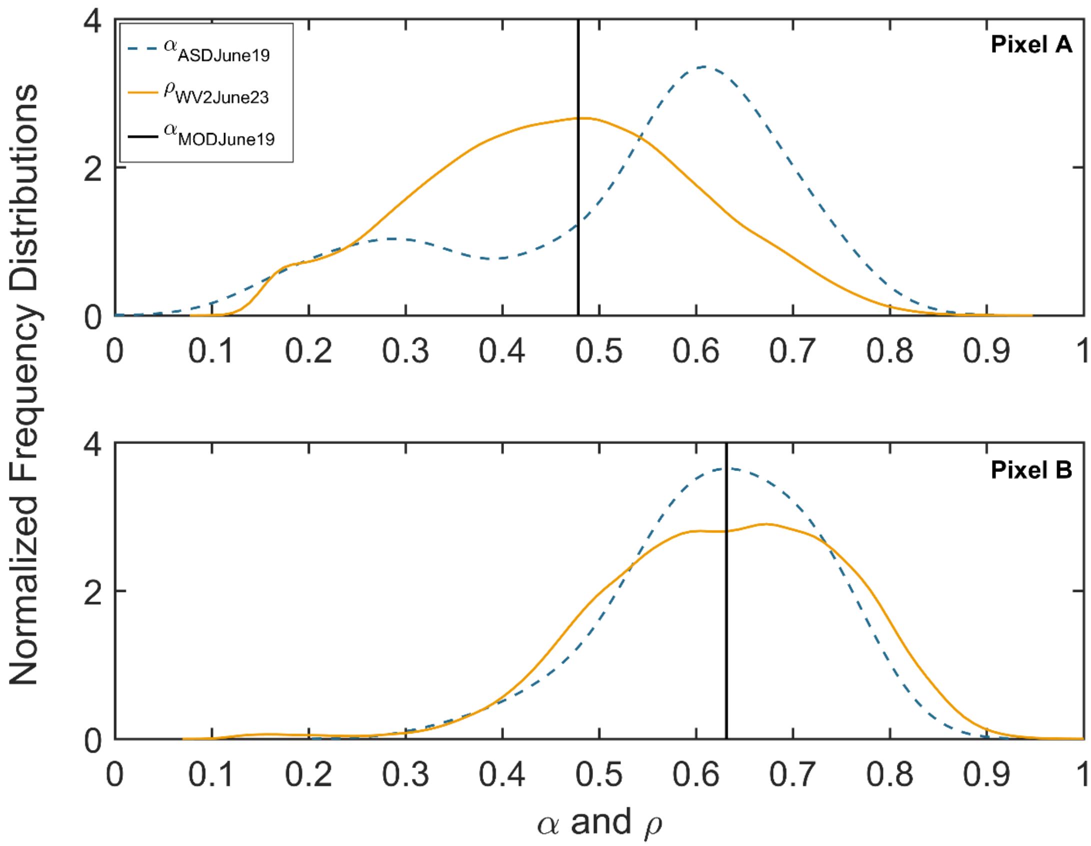

Figure 3.6 Normalized frequency distributions of individual α_{ASD} and α_{MODIS} for June 19th (blue and black lines, respectively) and average pixel-wide ρ_{WV2} for June 23rd (orange line) for Pixel A (top) and Pixel B (bottom).

The $\rho_{WV2\ Pixel\ B}$ semivariogram is relatively homogeneous shown by the stabilizing variance with distance between observations and low range value (29 m; Fig. 3.7b; Table 3.3). This suggests that spatial correlation vanishes when observations are more than 29 m apart. The WV-2 composite image for Pixel B confirms a more uniform surface (Fig. 3.7a), corroborated by the low sill value ($7.5*10^{-3}$ cf. $18.4*10^{-3}$ for Pixel A), and lower maximum overall variance compared to Pixel A (Table 3.3). The presence of a small melt pond and supraglacial river occupying the southeast quadrant is one small source of heterogeneity in the spatial structure of Pixel B (Fig. 3.7a).

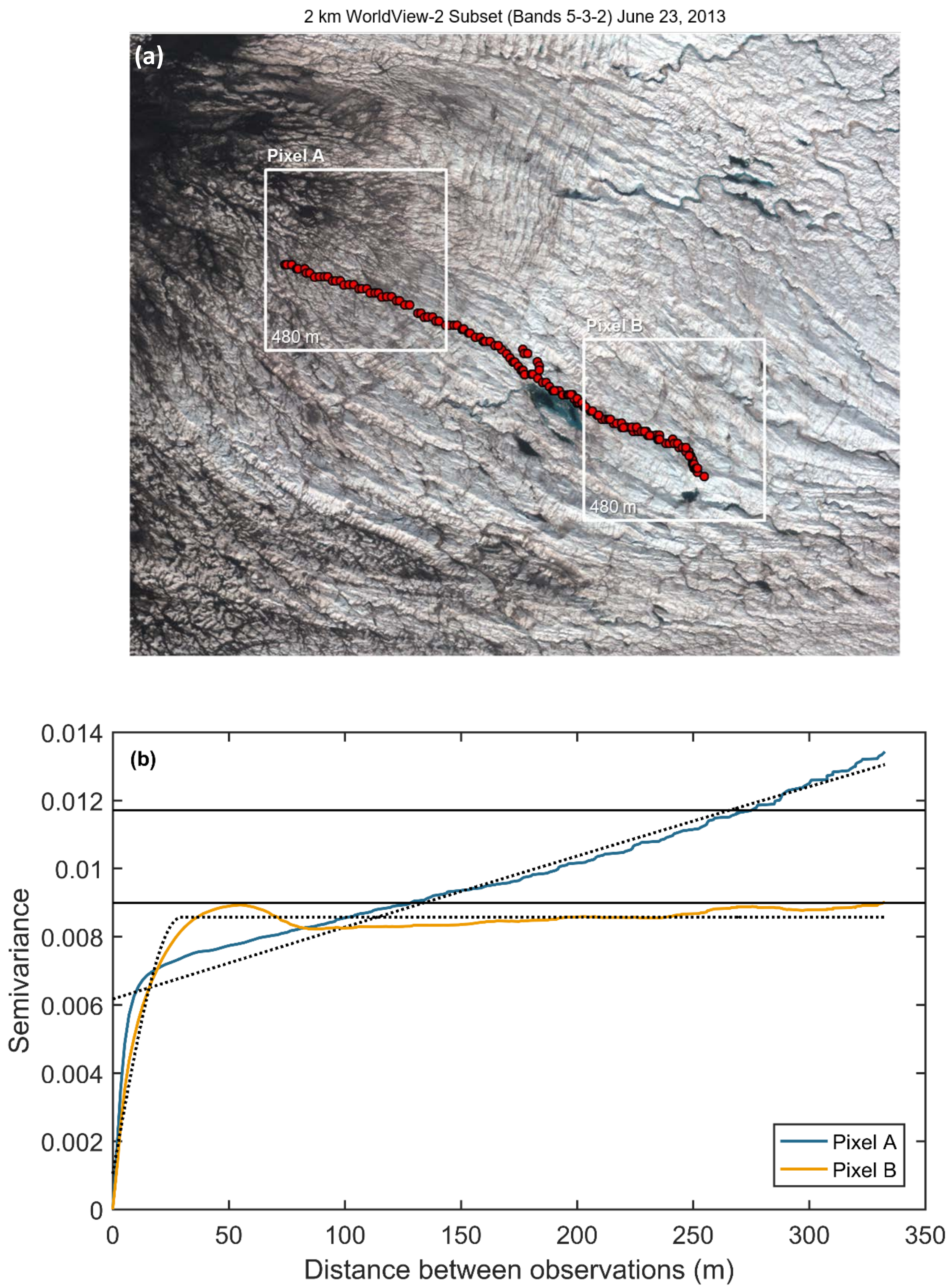

Figure 3.7 (a) Red band surface reflectance composite of WorldView-2 (WV-2) and corresponding semivariogram functions, variogram estimator (colored lines), spherical model (dotted curves), and sample variance (black lines) using the 480 m region for Pixel A (blue line)

and Pixel B (orange line), centered over the ablation area of southwest Greenland on 23 June 2013 (b).

Table 3.3 Characteristics of WV-2 semivariograms and their estimated spatial attributes from the spherical model for MODIS Pixels A and B at the 480 m spatial scale.

Spatial scale	Pixels							
	Pixel A				Pixel B			
	Sill (c)	Nugget effect (c_o)	Range (a) in meters	variance	Sill (c)	Nugget effect (c_o)	Range (a) in meters	variance
480 m	$18.4*10^{-3}$	$6.2*10^{-3}$	No estimate	$11.7*10^{-3}$	$7.5*10^{-3}$	$10.4*10^{-4}$	29	$9.0*10^{-3}$

3.5 Discussion

A clear result of this study is that the southwest GrIS's ablation area is characterized by pronounced MODIS sub-pixel variability. Highly heterogeneous albedo values within two MODIS pixel footprints were observed with two independent methods – in situ data collected with a hand held ASD spectroradiometer, and sub-meter scale resolution WV-2 satellite data. This finding implies that the traditional method of assessing MODIS albedo accuracy over the GrIS by using single point albedo observations (often observed at AWSs) can lead to erroneous validation results if spatial representativeness is not taken into consideration (e.g., Lhermitte et al., 2014). We quantify that this error can be as large (small) as 0.43 (-0.32) for Pixel A and as large (small) as 0.30 (-0.30) for Pixel B, by examining the 10th and 90th percentile average error difference between in situ α_{ASD} and satellite α_{MODIS} probability density distributions (Figs. 3.4 and 3.5). The large spatial variability in albedos identified in this study is not surprising and has been reported elsewhere (e.g., Alexander et al., 2014; Tedesco et al., 2016), but it is rarely considered in validation studies. Several studies have evaluated the

MODIS albedo products by single ‘point-to-pixel’ comparison (e.g., Box et al., 2012; Stroeve et al., 2005, 2006, 2013), which implicitly assumes that the GC-Net ground measurement sites were representative of the satellite footprint. However, this is only appropriate in areas of relatively small spatial variability, such as in the accumulation zone. For instance, at Summit, Greenland, or in areas above the equilibrium line, spatial inhomogeneity is small, and thus, the MODIS validation is robust (e.g., Wright et al., 2014). A benefit of single-point AWS data relative to multiple point field campaign studies such as Wright et al. 2014 and this study, are that they provide continuous time series of albedo. Additional AWS networks are available in the ablation area (e.g., Program for Monitoring of the Greenland Ice Sheet (PROMICE) and the K-Transect; van den Broeke et al., 2011; van As et al., 2011, 2012), but their spatial representativeness should be examined before used in validation studies. While this study doesn’t provide an analysis of the temporal continuity of albedo during the melt season, AWSs offer an additional benefit of providing a continuous time series unlike an in situ dataset collected over a fixed time period, and should also be incorporated in forthcoming studies.

Our data collection improves the single point comparison by having 103 and 129 sample locations within each MODIS pixel footprint, Pixels A and B, respectively. The multiple point-to-pixel estimates reveal that MODIS satellite albedo is 4-7% lower in Pixel A and between -4% and +7% in Pixel B as compared to in situ ASD observations. From this, we can conclude that even in the challenging environment of the high latitudes, MODIS is close to the stated accuracies of the daily albedo product (0.05; Román et al., 2010), despite our in situ data collection undersampling darker surfaces. The undersampling of dark surfaces and differences in actual (off-nadir, multi-angle views, and geolocation accuracy differences considered) vs. artificial (gridded) MODIS pixel sizes can explain why α_{MODIS} is lower than α_{ASD} in Pixel A (as well as the darker surfaces present in this pixel). These trends of lower MODIS albedos in Pixel A is expected because it captures darker, more heterogeneous ice surfaces, while higher MODIS albedos in Pixel B is related to the pixel capturing brighter ice and snow surfaces. This is further verified by the α_{ASD} frequency distribution overestimating red band albedo in Pixel A, while ρ_{WV2} and α_{MOD} frequency distributions central tendencies align (Fig. 3.6). Additionally, $\alpha_{MOD\ Pixel\ A}$ may be biased low due to the challenges of reconstructing satellite-derived albedos under strong adjacency conditions where the nearby tundra surface with distinctly lower albedos may also be captured as part of the MODIS effective footprint (e.g., Campagnolo et al., 2016). In contrast, Pixel B varies from band-to-band, with different signage on Band 2 for June 16th and Band 3 for June 19th (Table 3.2). However, the rest of the bands reflect equal or higher α_{MODIS} values than α_{ASD}, confirmed by scatter plots (Fig. 3.3). The very small difference between α_{MODIS} and α_{ASD} in Pixel B are statistically insignificant (because they are within the range of the standard error; Table 3.2), and is likely due to the lesser spatial heterogeneity characterizing the surface falling within the pixel. This is reinforced by the alignment of the α_{MOD}, α_{ASD}, and ρ_{WV2} central tendencies (mean of 0.63) for all wavebands in Pixel B (Fig. 3.6; Table 3.1).

This finding is further supported by the spatial representative analysis with the WV-2 semivariograms, which reveals marked spatial heterogeneity in Pixel A, and reduced variability within Pixel B. In Pixel A, the semivariogram's variance does not stabilize at any distance within the 480 m range (due to the limited range of the WV-2 values), indicating that the spatial attribute values of the fitted variogram model are likely not completely reliable (Table 3.3). This suggests that the variogram model may not be robust enough to confidently interpret results for Pixel A, and a range value cannot be estimated. The model's inability to spatially autocorrelate (semivariance asymptotes) may also be related to the limited statistical area (480 m), the MODIS pixel's proximity to the ice-free tundra region, where factors such as viewing zenith angle and geolocation uncertainties (e.g., Xin et al., 2012) may come into play as well as the considerable influence of dust deposition from the terminal moraine and nearby braided river plains.

In contrast, Pixel B fits better to the spherical model (Fig. 3.7b). In geostatistics, data with such a good fit to a spherical model may be considered an 'ideally-shaped' semivariogram. The range of influence remains low (29 m) in Pixel B (Table 3.3), beyond such distance, the ρ_{WV2} samples become independent of one another. Given that this range does not change up to the actual MODIS pixel size, spacing ground observations with a footprint of at least 30 m or more would be able to capture the spatial variability within Pixel B. Such footprints are entirely within reach for AWSs, given that Kipp and Zonen pyranometers installed at 4 m height have a 50.5 m footprint (FOV = 81°; Wang et al. 2012), and when considering the cosine response (weighting function) of the sensor (e.g., Lhermitte et al., 2014). While each in situ observation collected in this study only has a footprint of 0.18 m, the use of multiple data points increases the effective footprint. The low spatial attribute values observed in Pixel B suggests that the ice surface is more homogeneous allowing for ground observations to more adequately characterize the albedos within the pixel. Therefore, the Pixel B results from Fig. 3.7b and Table 3.3 suggest that multiple 'point-to-pixel' comparisons between ground and satellite measurements is likely acceptable due to the more homogeneous surface within the pixel.

Additionally, the semivariogram data (Fig. 3.7b) reveals the importance of the MODIS source area. The results from Pixel A and B are diametrically distinct. These differences are accentuated by the spatial variability characterizing each pixel. This is best demonstrated when we compare the geostatistical attribute values for Pixel A and B. The sill value in Pixel A is nearly 2.5 times the magnitude of Pixel B (Table 3.3), meaning that the overall variability is substantially higher in Pixel A. This exemplifies the dissimilarity in the landscape spatial structure between two neighboring pixels. In Pixel A, a reliable range estimate was not computed, but should be greater than 500 m (MODIS gridded pixel size) as compared to Pixel B's 29 m range. The statistical area captures and averages out different ice surface types, albedos, and high spatial variability characterizing the study area. As such, the footprint of MODIS may not matter as much in the interior of the ice sheet, but is important to consider in the ablation area (southwest and west Greenland), where a large number of melt ponds and lakes are present (e.g., Selmes et al., 2011; Leeson et al., 2012). Indeed, this conclusion agrees with observations over a homogenous, spatially representative surface, where changing the size of the statistical area may not be necessary (e.g., Cescatti et al., 2012). These findings highlight the importance of considering landscape heterogeneity in the point-to-pixel comparison and applying geostatistical methods for quantifying spatial variability in fine resolution satellite imagery.

The band-by-band comparison illustrates the significance of assessing satellite albedo retrievals at the narrow band scale. The range of MODIS and ASD narrow band albedo values can vary quite a bit between different transect dates and across all bands (Tables 3.1 and 3.2). With the exception of the near-infrared band (Band 2), only slight differences in α_{ASD} and α_{MOD} estimates exist band-by-band in Pixel B. The albedo differences don't appear to be band dependent for both pixels, which suggest that the broad band error estimate (VIS_Stroeve) is representative of albedo values in each narrow band. Small differences in ρ_{WV2} and α_{MODIS} red band reflectance and albedo values may be due to differences in our assumption that WV-2 data represents lambertian reflectance, while the MODIS daily albedo product accounts for the BRDF effect. The spectral range mismatch between ρ_{WV2} and α_{MODIS} red bands might offset this albedo difference.

Several studies have identified view geometry as a significant error source (Xin et al., 2012) in MODIS snow mapping algorithms in forested areas (e.g., Liu et al., 2008; Painter et al., 2009). Despite assuming a fixed MODIS pixel footprint in this study, wider footprints prior to resampling is expected due to variations in viewing zenith angle (Campagnolo et al., 2016) and the MODIS point spread function (Wolfe et al., 2002). In essence, the effective spatial resolution of the pixels is larger than the nominal grid and this has been found to affect the detectable snow fraction area (e.g., Liu et al., 2008) and sub-pixel snow reflectances derived from MODIS (e.g., Dozier et al., 2008). Surface roughness may also contribute to MODIS shadowing effects, but has not been assessed over the GrIS. In addition, the utilization of large view geometries can result in overlap of adjacent grid cells (Wolfe et al., 1998; Campagnolo et al., 2016). This has implications for our α_{ASD} ground observations, as some of these point measurements in Pixel A may 'spill over' into Pixel B, and vice versa, depending upon the effective pixel footprint size.

This study demonstrates the shortcomings of using a single point method for validating MODIS albedo in the heterogeneous ablation area, and the value of semiovariograms to identify the critical footprint of those observations. Although in situ data sampling at multiple sites along a transect is a better representation of MODIS pixel albedo than sampling at a single point, it still falls short. Random or regular, evenly distributed sampling locations may provide more spatial representative sampling. However, such in situ sampling schemes are impossible to implement due to sometimes impassible terrain (crevasses, deep melt pond and streams). Furthermore, the number of in situ albedo sampling points that have been used in MODIS comparison and validations studies are extremely small relative to the very high number of MODIS pixels covering the entire GrIS (nearly 74 million pixels). Despite this, our small-scale study provides a benchmark for future studies that may analyze the spatial representativeness of multiple AWSs in the ablation area. Therefore, we recommend sampling of ‘near ground’ data by using low flying airborne or unmanned autonomous vehicles to overcome the limitations of the single ‘point-to-pixel’ validation method and limited spatial extent. This is possible, given the increasing availability of airborne imagery (e.g., Operation IceBridge Digital Mapping System; Dominguez, 2014), and adaptation of unmanned aerial vehicles (e.g., Ryan et al., 2015). Instead of ground references points, ground references areas could then be used for validation. However, maintaining and expanding the current network of AWSs with ground point observations are also critical, as they provide a continuous time series of albedo. These ground reference areas and points should also be analyzed with variogram analysis, as implemented in this study, to provide a more sophisticated comparison that identify the footprints needed by in situ observations to be spatially representative. If WV-2 imagery is not available, medium-resolution (30 m) Landsat 8 Operational Land Imager (OLI) data, with its improved radiometric resolution, can provide derived surface reflectance information over snow and ice surfaces, without saturating (e.g., Wang et al., 2016) and can cover a larger spatial extent (unlike WV-2). Previous spatial representativeness studies have demonstrated the efficacy of utilizing Landsat imagery for semivariogram analysis over terrestrial surfaces (e.g., Burakowski et al., 2015; Román et al., 2009, 2010; Wang et al., 2012, 2014). Access to the new, higher spatial resolution (20 m) Sentinel-2 data, will offer an additional means of assessing the landscape heterogeneity of albedo in the ablation zone.

3.6 Conclusions

This study compares the MODIS v006 MCD43A daily albedo product with high-quality in situ ASD albedo data, and WV-2 data spanning two MODIS satellite pixels, Pixels A and B, for southwest Greenland's ablation area. Using a multiple point-to-pixel comparison, we found that $\alpha_{\text{MOD Pixel A}}$ and $\alpha_{\text{MOD Pixel B}}$ ranged from 4-7% lower, and between -4% and +7%, respectively, of in situ α_{ASD} observations, and is nearly within the stated accuracy of the MODIS daily albedo product. $\alpha_{\text{MOD Pixel A}}$ is lower than in situ α_{ASD} measurements probably due to undersampling of dark surface in the in situ data, and high surface heterogeneity within the pixel. While, $\alpha_{\text{MOD Pixel B}}$ was characterized by reduced error because the pixel contained a brighter, more spatially homogeneous surface. The variogram analysis of high spatial resolution WV-2 imagery confirms the importance of knowing the actual effective MODIS footprint size and view geometry for validation efforts between satellite retrievals and in situ measurements. Despite our in situ data being sampled in a way that they were biased towards low albedo surfaces, we still are able demonstrate that multiple point-to-pixel comparison can improve upon single point-to-pixel validation technique. Assuming a single point-to-pixel comparison, we quantify that in extreme cases (10^{th} and 90^{th} percentiles of the in situ α_{ASD} and satellite α_{MODIS} difference probability density distributions), the error is, on average for all bands, -0.32 or 0.43 for Pixel A and -0.30 or 0.30 for Pixel B. Given the high potential for biased sampling of in situ albedo in the ablation area, we suggest that future studies adopt ‘near ground’ sampling with low-flying vehicles (airborne or unmanned), utilize distributed albedo networks (including GC-Net and PROMICE stations), and high spatial resolution satellite imagery.

Appendix 3A: Field spectroscopy data set

The 2013 spectral and broadband albedo dataset is permanently archived, published, and freely available in the PANGAEA data repository found here (Moustafa et al., 2016): https://doi.pangaea.de/10.1594/PANGAEA.867917

3.7 References

van As, D., Fausto, R. S., Ahlstrøm, A. P., Andersen, S. B., Andersen, M. L., Citterio, M., Edelvang, K., Gravesen, P., Machguth, H., Nick, F. M., Nielsen, S. and Weidick, A.: Programme for Monitoring of the Greenland Ice Sheet (PROMICE): first temperature and ablation records, Geol. Surv. Denmark Greenl. Bull., 23, 73–76, 2011.

van As, D., Hubbard, A. L., Hasholt, B., Mikkelsen, A. B., Van den Broeke, M. R. and Fausto, R. S.: Large surface meltwater discharge from the Kangerlussuaq sector of the Greenland ice sheet during the record-warm year 2010 explained by detailed energy balance observations, Cryosph., 6, 199–209, doi:10.5194/tc-6-199-2012, 2012.

Alexander, P. M., Tedesco, M., Fettweis, X., van de Wal, R. S. W., Smeets, C. J. P. P. and van den Broeke, M. R.: Assessing spatio-temporal variability and trends (2000–2013) of modelled and measured Greenland ice sheet albedo, The Cryosphere Discuss., 8(4), 3733–3783, doi:10.5194/tcd-8-3733-2014, 2014.

Berk, A., Anderson, G. P., Acharya, P. K., Bernstein, L. S., Muratov, L., Lee, J., & Lockwood, R. B. MODTRAN5: 2006 update. In Defense and Security Symposium (pp. 62331F-62331F). International Society for Optics and Photonics, 2006.

Box, J. E., Fettweis, X., Stroeve, J. C., Tedesco, M., Hall, D. K., and Steffen, K.: Greenland ice sheet albedo feedback: thermodynamics and atmospheric drivers, The Cryosphere, 6, 821-839, doi:10.5194/tc-6-821-2012, 2012.

van den Broeke, M., Bamber, J., Ettema, J., Rignot, E., Schrama, E., van de Berg, W. J., van Meijgaard, E., Velicogna, I. and Wouters, B.: Partitioning recent Greenland mass loss., Science, 326(5955), 984–6, doi:10.1126/science.1178176, 2009.

van den Broeke, M. R., Smeets, C. J. P. P. and Van de Wal, R. S. W.: The seasonal cycle and interannual variability of surface energy balance and melt in the ablation zone of the west Greenland ice sheet, Cryosph., 5(2), 377–390, doi:10.5194/tc-5-377-2011, 2011.

Burakowski, E.A., Ollinger, S. V., Lepine, L., Schaaf, C.B., Wang, Z., Dibb, J.E., Hollinger, D.Y., Kim, J., Erb, A., Martin, M., 2015. Spatial scaling of reflectance and surface albedo over a mixed-use, temperate forest landscape during snow-covered periods. Remote Sens. Environ. 158, 465–477. doi:10.1016/j.rse.2014.11.023.

Carroll, S. S., & Cressie, N. A comparison of geostatistical methodologies used to estimate snow water equivalent. Water Resources Bulletin, 32, 267−278, 1996.

Campagnolo, M. L., Sun, Q., Liu, Y., Schaaf, C., Wang, Z., & Román, M. O. Estimating the effective spatial resolution of the operational BRDF, albedo, and nadir reflectance products from MODIS and VIIRS. Remote Sens. Environ., 175, 52-64, 2016.

Cescatti, A., Marcolla, B., Santhana Vannan, S. K., Pan, J. Y., Román, M. O., Yang, X., Ciais, P., Cook, R. B., Law, B. E., Matteucci, G., Migliavacca, M., Moors, E., Richardson, A. D., Seufert, G. and Schaaf, C. B.: Intercomparison of MODIS albedo retrievals and in situ measurements across the global FLUXNET network, Remote Sens. Environ., 121, 323–334, doi:10.1016/j.rse.2012.02.019, 2012.

Chandler, D. M., Alcock, J. D., Wadham, J. L., MacKie, S. L. and Telling, J.: Seasonal changes of ice surface characteristics and productivity in the ablation zone of the Greenland Ice Sheet, Cryosphere, 9(2), 487–504, doi:10.5194/tc-9-487-2015, 2015.

Davis, J. C. Statistics and data analysis in geology. New York: Wiley, 1986.

Dent, C. L., & Grimm, N. B. Spatial heterogeneity of stream water nutrient concentrations over successional time. Ecology, 80(7), 2283-2298, 1999.

Dominguez, R.: IceBridge DMS L1B Geolocated and Orthorectified Images, Boulder, Colorado USA: NASA National Snow and Ice Data Center Distributed Active Archive Center, available at: http://dx.doi.org/10.5067/OZ6VNOPMPRJ0, 2010 (updated 2014).

Dozier, J., Painter, T.H., Rittger, K., Frew, J.E., 2008. Time–space continuity of daily maps of fractional snow cover and albedo from MODIS. Adv. Water Resour. 31, 1515–1526. doi:10.1016/j.advwatres.2008.08.011.

Enderlin, E. M., Howat, I. M., Jeong, S., Noh, M.-J., van Angelen, J. H. and van den Broeke, M. R.: An improved mass budget for the Greenland ice sheet, Geophys. Res. Lett., 41(3), 866–872, doi:10.1002/2013GL059010, 2014.

Hall, D. K., Comiso, J. C., DiGirolamo, N. E., Shuman, C. A., Box, J. E. and Koenig, L. S.: Variability in the surface temperature and melt extent of the Greenland ice sheet from MODIS, Geophys. Res. Lett., 40(10), 2114–2120, doi:10.1002/grl.50240, 2013.

Holben, N., Tanr, D., Smirnov, A., Eck, T. F., Slutsker, I., Newcomb, W. W., Schafer, J. S., Chatenet, B., Lavenu, F., Kaufman, J., Castle, J. Vande, Setzer, A., Markham, B., Clark, D., Halthore, R., Karneli, A., Neill, N. T. O., Pietras, C., Pinker, T., Voss, K. and Zibordi, G.: An emerging ground-based aerosol climatology : Aerosol optical depth from AERONET, J. Geophys. Res., 106(Dll), 12,067–12,097, 2001.

Isaaks, E. H., & Srivastava, R. M. An introduction to applied geostatistics.NewYork: Oxford University Press, 1989.

Khan, S. a, Kjaer, K. H., Bevis, M., Bamber, J. L., Wahr, J., Kjeldsen, K. K., Bjork, A. a, Korsgaard, N. J., Stearns, L. a, van den Broeke, M. R., Liu, L., Larsen, N. K. and Muresan, I. S.: Sustained mass loss of the northeast Greenland ice sheet triggered by regional warming, Nat. Clim. Chang., 4(4), 292–299, doi:10.1038/nclimate2161, 2014.

Knap, W. H. and Oerlemans, J.: The surface albedo of the Greenland ice sheet: satellite¬ derived and in situ measurements in the Sendre Stromfjord area during the 1991 melt season, J. Glaciol., 42(141), 364–374, 1996.

Leeson, A. A., Shepherd, A., Palmer, S., Sundal, A. and Fettweis, X.: Simulating the growth of supraglacial lakes at the western margin of the Greenland ice sheet, Cryosphere, 6(5), 1077–1086, doi:10.5194/tc-6-1077-2012, 2012.

Lhermitte, S., Abermann, J. and Kinnard, C.: Albedo over rough snow and ice surfaces, Cryosph., 8(3), 1069–1086, doi:10.5194/tc-8-1069-2014, 2014.

Liang, S., Fang, H. and Chen, M.: Atmospheric correction of Landsat ETM+ land surface imagery – Part I: Methods, IEEE Trans. Geosci. Remote Sens., 39(11), 2490–2498, doi:10.1109/36.964986, 2001.

Liang, S., Shuey, C. J., Russ, A. L., Fang, H., Chen, M., Walthall, C. L., Daughtry, C. S. T. and Hunt, R.: Narrowband to broadband conversions of land surface albedo: II. Validation, Remote Sens. Environ., 84, 25–41, 2002.

Liu, J., Melloh, R. A., Woodcock, C. E., Davis, R. E., Painter, T. H., & McKenzie, C. (2008). Modeling the view angle dependence of gap fractions in forest canopies: implications for mapping fractional snow cover using optical remote sensing. Journal of Hydrometeorology, 9, 1005–1019.

Lewis, P., & Barnsley, M. J. Influence of the sky radiance distribution on various formulations of the earth surface albedo. 6th International Symposium on Physical Measurements and Signatures in Remote Sensing, ISPRS (pp. 707−715). Val d'Isere, France: CNES, 1994.

Matheron, G. Principles of geostatistics. Economic Geology, 58, 1246–1266. http://dx.doi.org/10.2113/gsecongeo.58.8.1246, 1963.

Matthew, M. W., S. M. Adler-Golden, A. Berk, S. C. Richtsmeier, R. Y. Levine, L. S. Bernstein, P. K. Acharya, G. P. Anderson, G. W. Felde, M. P. Hoke, A. Ratkowski, H.-H. Burke, R. D. Kaiser, and D. P. Miller. Status of Atmospheric Correction Using a MODTRAN4-based Algorithm. SPIE Proceedings, Algorithms for Multispectral, Hyperspectral, and Ultraspectral Imagery VI. Vol. 4049, pp. 199-207, 2000.

Mernild, S. H. and Liston, G. E.: Greenland Freshwater Runoff. Part II: Distribution and Trends, 1960–2010, J. Clim., 25(17), 6015–6035, doi:10.1175/JCLI-D-11-00592.1, 2012.

Moustafa, S. E., Rennermalm, A. K., Smith, L. C., Miller, M. A., Mioduszewski, J. R., Koenig, L. S., Hom, M. G. and Shuman, C. A.: Multi-modal albedo distributions in the ablation area of the southwestern Greenland Ice Sheet, Cryosph., 9(3), 905–

923, doi:10.5194/tc-9-905-2015, 2015.

Moustafa, S. E.; Rennermalm, A. K.; Mioduszewsk, J. R.; Smith, L. C.: Spectral and broadband albedo transects in the lower ablation zone, Southwest Greenland, June 2013. Dataset #867917 (DOI registration in progress), 2016.

Noreus, J. P., Nyborg, M. R., & Hayling, K. L. The gravity anomaly field in the Gulf of Bothnia spatially characterized from satellite altimetry and in situ measurements. Journal of Applied Geophysics, 37, 67–84. http://dx.doi.org/10.1016/S0926-9851(97) 00007-4, 1997.

Painter, T.H., Rittger, K., McKenzie, C., Slaughter, P., Davis, R.E., Dozier, J., 2009. Retrieval of subpixel snow covered area, grain size, and albedo from MODIS. Remote Sens. Environ. 113, 868–879. doi:10.1016/j.rse.2009.01.001

Rippin, D.M., Pomfret, A., King, N., 2015. High resolution mapping of supra-glacial drainage pathways reveals link between micro-channel drainage density, surface roughness and surface reflectance. Earth Surf. Process. Landforms 40, 1279–1290. doi:10.1002/esp.3719.

Román, M. O., Schaaf, C. B., Woodcock, C. E., Strahler, A. H., Yang, X., Braswell, R. H., Curtis, P. S., Davis, K. J., Dragoni, D. and Goulden, M. L.: The MODIS (Collection V005) BRDF/albedo product: Assessment of spatial representativeness over forested landscapes, Remote Sens. Environ., 113(11), 2476–2498, doi:10.1016/j.rse.2009.07.009, 2009.

Román, M. O., Schaaf, C. B., Lewis, P., Gao, F., Anderson, G. P., Privette, J. L., Strahler, A. H., Woodcock, C. E. and Barnsley, M.: Assessing the coupling between surface albedo derived from MODIS and the fraction of diffuse skylight over spatially-characterized landscapes, Remote Sens. Environ., 114(4), 738–760, doi:10.1016/j.rse.2009.11.014, 2010.

Ryan, J. C., Hubbard, A. L., Box, J. E., Todd, J., Christoffersen, P., Carr, J. R., Holt, T. O. and Snooke, N.: UAV photogrammetry and structure from motion to assess calving dynamics at Store Glacier, a large outlet draining the Greenland ice sheet, Cryosph., 9(1), 1–11, doi:10.5194/tc-9-1-2015, 2015.

Ryan, J. C., Hubbard, A., Stibal, M., Box, J. E., and team, T. D. S. P.: Attribution of Greenland's ablating ice surfaces on ice sheet albedo using unmanned aerial systems, The Cryosphere Discuss., doi:10.5194/tc-2016-204, in review, 2016.

Schaaf, C. B., Liu, J., Gao, F., and Strahler, A. H.: Aqua and Terra MODIS albedo and reflectance anisotropy products, in: Remote Sensing and Global Environmental Change, 549– 561, Springer, New York, 2011.

Schaaf, C., Strahler, A., Feng Gao, Lucht, W., Yufang Jin, Xiaowen Li, Xiaoyang Zhang, Tsvetsinskaya, E., Muller, J.-P., Lewis, P., Barnsley, M., Roberts, G., Doll, C., Shunlin Liang, Roy, D. and Privette, J.: Global albedo, BRDF and nadir BRDF-adjusted reflectance products from MODIS, in IEEE International Geoscience and Remote Sensing Symposium, vol. 2, pp. 1188–1190, IEEE., 2002.

Schaepman-Strub, G., Schaepman, M. E., Painter, T. H., Dangel, S. and Martonchik, J. V.: Reflectance quantities in optical remote sensing—definitions and case studies, Remote Sens. Environ., 103(1), 27–42, doi:10.1016/j.rse.2006.03.002, 2006.

Selmes, N., Murray, T. and James, T. D.: Fast draining lakes on the Greenland Ice Sheet, Geophys. Res. Lett., 38(15), n/a–n/a, doi:10.1029/2011GL047872, 2011.

Steffen, K. and Box, J.: Surface climatology of the Greenland ice sheet: Greenland Climate Network 1995-1999, J. Geophys. Res., 106(D24), 33951–33964, 2001.

Stroeve, J., Box, J. E., Gao, F., Liang, S., Nolin, A. and Schaaf, C.: Accuracy assessment of the MODIS 16-day albedo product for snow: comparisons with Greenland in situ measurements, Remote Sens. Environ., 94(1), 46–60, doi:10.1016/j.rse.2004.09.001, 2005.

Stroeve, J. C., Box, J. E. and Haran, T.: Evaluation of the MODIS (MOD10A1) daily snow albedo product over the Greenland ice sheet, Remote Sens. Environ., 105(2), 155–171, doi:10.1016/j.rse.2006.06.009, 2006.

Stroeve, J., Box, J. E., Wang, Z., Schaaf, C. and Barrett, A.: Re-evaluation of MODIS MCD43 Greenland albedo accuracy and trends, Remote Sens. Environ., 138, 199–214, doi:10.1016/j.rse.2013.07.023, 2013.

Tedesco, M., Fettweis, X., van den Broeke, M. R., van de Wal, R. S. W., Smeets, C. J. P. P., van de Berg, W. J., Serreze, M. C. and Box, J. E.: The role of albedo and accumulation in the 2010 melting record in Greenland, Environ. Res. Lett., 6(1), 014005, doi:10.1088/1748-9326/6/1/014005, 2011.

Tedesco, M., Doherty, S., Fettweis, X., Alexander, P., Jeyaratnam, J., and Stroeve, J.: The darkening of the Greenland ice sheet: trends, drivers, and projections (1981–2100), The Cryosphere, 10, 477-496, doi:10.5194/tc-10-477-2016, 2016.

Vernon, C.L., Bamber, J.L., Box, J.E., van den Broeke, M.R., Fettweis, X., Hanna, E., Huybrechts, P., 2013. Surface mass balance model intercomparison for the Greenland ice sheet. Cryosph. 7, 599–614. doi:10.5194/tc-7-599-2013

Van de Wal, R. S. W., Boot, W., Smeets, C. J. P. P., Snellen, H., van den Broeke, M. R. and Oerlemans, J.: Twenty-one years of mass balance observations along the K-transect, West Greenland, Earth Syst. Sci. Data, 4(1), 31–35, doi:10.5194/essd-4-31-

2012, 2012.

Wientjes, I. G. M., Van de Wal, R. S. W., Reichart, G. J., Sluijs, A. and Oerlemans, J.: Dust from the dark region in the western ablation zone of the Greenland ice sheet, The Cryosphere, 5, 589–601, doi:10.5194/tc-5-589-2011, 2011.

Wang, Z., Schaaf, C. B., Chopping, M. J., Strahler, A. H., Wang, J., Román, M. O., Rocha, A. V., Woodcock, C. E. and Shuai, Y.: Evaluation of Moderate-resolution Imaging Spectroradiometer (MODIS) snow albedo product (MCD43A) over tundra, Remote Sens. Environ., 117, 264–280, doi:10.1016/j.rse.2011.10.002, 2012.

Wang, Z., Schaaf, C. B., Strahler, A. H., Chopping, M. J., Román, M. O., Shuai, Y., Woodcock, C. E., Hollinger, D. Y. and Fitzjarrald, D. R.: Evaluation of MODIS albedo product (MCD43A) over grassland, agriculture and forest surface types during dormant and snow-covered periods, Remote Sens. Environ., 140, 60–77, doi:10.1016/j.rse.2013.08.025, 2014.

Wang, Z., Erb, A.M., Schaaf, C.B., Sun, Q., Liu, Y., Yang, Y., Shuai, Y., Casey, K.A., Román, M.O., 2016. Early spring post-fire snow albedo dynamics in high latitude boreal forests using Landsat-8 OLI data. Remote Sens. Environ. 185, 71–83. doi:10.1016/j.rse.2016.02.059

Wolfe, R. E., Roy, D. P., & Vermote, E. (1998). MODIS land data storage, gridding, and compositing methodology: Level 2 grid. IEEE Transactions on Geoscience and Remote Sensing, 36,1324–1338.

Wolfe, R.E., Nishihama, M., Fleig, A.J., Kuyper, J. a., Roy, D.P., Storey, J.C., Patt, F.S., 2002. Achieving sub-pixel geolocation accuracy in support of MODIS land science. Remote Sens. Environ. 83, 31–49. doi:10.1016/S0034-4257(02)00085-8

Woodcock, C. E., Strahler, A. H., & Jupp, D. L. B. The use of variograms in remote sensing: I. Scene models and simulated images. Remote Sensing of Environment, 25, 323–348, 1988a.

Woodcock, C. E., Strahler, A. H., & Jupp, D. L. B. The use of variograms in remote sensing: II. Real digital images. Remote Sensing of Environment, 25,349–379, 1988b.

Wright, P., Bergin, M., Dibb, J., Lefer, B., Domine, F., Carman, T., Carmagnola, C., Dumont, M., Courville, Z., Schaaf, C. and Wang, Z.: Comparing MODIS daily snow albedo to spectral albedo field measurements in Central Greenland, Remote Sens. Environ., 140, 118–129, doi:10.1016/j.rse.2013.08.044, 2014.

Xin, Q., Woodcock, C.E., Liu, J., Tan, B., Melloh, R.A., Davis, R.E., 2012. View angle effects on MODIS snow mapping in forests. Remote Sens. Environ. 118, 50–59. doi:10.1016/j.rse.2011.10.029

Chapter 4: How to improve modeling of drainage basin runoff losses in Greenland

4.1 Introduction

The Greenland ice sheet (GrIS) is the largest freshwater reservoir in the Northern Hemisphere, capable of adding ~7 m of sea level rise, if melted completely (Bamber et al., 2013). Mass loss has accelerated over the last two decades (Tedesco et al., 2011, 2013; Nghiem et al., 2012), increasing sea level rise rates from 0.09 mm yr^{-1} in 1992-2001 to 0.59 mm yr^{-1} in 2002-2011 (Vaughan et al., 2013). Surface melt and subsequent runoff is an increasingly important driver of this accelerating mass loss (Shepherd et al., 2012). Increased surface meltwater runoff is attributed to increases in near-surface air temperature (Hall et al., 2013), melt area extent (Fettweis et al., 2011; Tedesco, 2007; Tedesco et al., 2011), and a darkening of the ice surface (e.g., Box et al., 2012; Moustafa et al., 2015; Tedesco et al., 2016). Runoff increases have also driven negative trends in surface mass balance (SMB), by 10.2 ± 2.3 Gt yr^{-2} from 1991-2015 (van den Broeke et al., 2016). These trends are consistent with the recent, unprecedented melt event of July 2012 that resulted in surface melt of nearly 97% of the GrIS (Hall et al., 2013; Nghiem et al., 2012). Runoff is now the dominant process for mass loss, accounting for at least half or more of Greenland's total mass loss (Enderlin et al., 2014). Despite runoff's increasing importance, there is a lack of model and measurement comparisons. Differences in model representation of physical processes and varying spatial resolution can result in large inter-model discrepancies in SMB (Hanna et al., 2013), and estimated runoff, up to 42% (Vernon et al., 2013). Therefore, there is a need to assess model estimates of runoff.

One of the most widely used models to understand Greenland mass balance is the Modèle Atmosphérique Régionale (MAR) regional climate model (RCM). Most recently, MAR has been used to validate melt extent and runoff derived from reanalysis data (Cullather et al., 2016) and the drainage efficiency of supraglacial rivers from in situ measurements in southwest Greenland (Smith et al., 2015). The MAR model has been validated in numerous studies (e.g., Tedesco et al., 2011, 2013, 2016; Fettweis et al., 2005, 2013, 2016; Vernon et al., 2013; Rae et al., 2012; van Angelen et al., 2012; Alexander et al., 2014, 2016), but modeled runoff has not been evaluated on a drainage basin-scale. The benefit of a basin scale inter-comparison is that integrated model runoff over a basin area can be compared with proglacial river discharge measurements. This will give insights into model performance over an area (i.e., drainage basin) instead of point comparisons (e.g., with automatic weather stations (AWSs) or ablation stakes). However, this approach is still prone to uncertainties in drainage basin delineation (e.g., Lindbäck et al., 2015) and river discharge derivation techniques (i.e., the process of converting river stage into discharge using a rating curve; e.g., Hasholt et al., 2013; Rennermalm et al., 2012; Overeem et al., 2015).

To assess model estimates of runoff on a basin scale, direct measurements of river discharge are needed. Proglacial river discharge can be compared to modeled runoff by integrating modeled outflow over a drainage basin area. However, long-term observations of discharge from Greenland are scarce (e.g., van As et al., 2012; Mernild et al., 2010; Rennermalm et al., 2012; Rennermalm et al., 2013; Smith et al., 2015; Mikkelsen et al., 2016). This is primarily due to logistical reasons and Greenland total runoff is instead approximated from satellite-derived surface elevation changes (Pritchard et al., 2009) or supplemented by SMB models (e.g., Ettema et al., 2009; Fettweis et al., 2012, 2016; Vernon et al., 2013; van den Broeke et al., 2016). In the absence of systematic, dispersed discharge measurements, SMB models rely on surface energy balance (SEB) calculations driven by local ice sheet surface climatology to simulate runoff estimates. Comparisons with detailed, AWS-forced SMB models have been conducted (e.g., van As et al., 2012, 2017), but few RCMs have been compared with in situ discharge observations (e.g., van As et al., 2014). Despite advances in SMB modeling of the GrIS (e.g., Vernon et al., 2013), physical processes impacting SMB such as meltwater production, retention and release (Rennermalm et al., 2013b), thermal erosion processes in supraglacial lakes (Selmes et al., 2011), perennial firn aquifer systems (Forster et al., 2013; Koenig et al., 2014), ice lenses formation (de la Peña et al., 2015), firn refreezing, compaction, and percolation (Van Angelen et al., 2013; Charalampidis et al,. 2015), need to be improved. Without improvement of these transport, storage, and removal processes, current SMB models may over- or under-estimate Greenland’s runoff contributions to global sea level rise.

In this thesis, we investigate MAR model runoff estimates by comparing them with in situ proglacial river discharge measurements. Our primary objective is to compare MAR discharge estimates with observational discharge measurements for three drainage basins – North River (Thule), Watson, and Naujat Kuat (Nuuk) – moving from north-to-south along West Greenland. MAR is integrated for several catchment realizations to evaluate the importance of uncertainty in drainage basin delineations on model discharge estimates. The performance of MAR discharge estimates is assessed, model-observation differences are evaluated against AWS data, and sources of uncertainty from drainage basin delineations, gauging data, and the MAR model are examined.

4.2 Data and Methods

4.2.1 The MAR regional climate model

The MAR v3.5.2 version (hereafter, MAR) is used here to derive surface runoff, surface energy balance components, and meteorological terms over the three study sites (Gallée and Schayes, 1994; Gallée, 1997; Lefebre et al., 2003; Fettweis et al., 2005, 2013, 2016). This version uses a 20 km horizontal spatial resolution (Fettweis et al., 2016). MAR is a coupled atmospheric model (Gallée and Schayes 1994) with a land surface scheme, specifically the Soil Ice Snow Vegetation Atmosphere Transfer scheme (SISVAT; De Ridder and Gallée, 1998). Furthermore, MAR incorporates a multilayer snow model called CROCUS (Brun et al., 1992) to simulate snow and ice albedo, snow grain properties, as well as energy and mass fluxes within the snowpack layers. The CROCUS model setup is detailed in Fettweis et al. (2011) and Fettweis (2007). Lateral and boundary forcing conditions are supplied from the European Centre for Medium-Range Weather Forecasts (ECMWF) Interim Reanalysis (ERA-Interim; see http://www.ecmwf.int/en/research/climate-reanalysis/era-interim; Dee et al., 2011). See Fettweis (2007) and Fettweis et al. (2013) for additional details on the MAR model. In this study, we use the 2004-2014 time period for comparison with available years of in situ discharge data.

4.2.2 The MAR runoff scheme

Runoff, a negative term in SMB, is typically defined as the summation of rainfall (RF) and meltwater production (M) minus refreeze (R) and meltwater/rainwater retention (RE) in units of mm water equivalent per day (or year). The CROCUS snow model within MAR approximates meltwater refreezing across a vertical grid of varying thickness layers as a function of temperature, density, and liquid water content (Reijmer et al., 2012). A portion of liquid meltwater is retained in the snowpack when the maximum liquid water content is reached (Lefebre et al., 2003). The irreducible water saturation, also known as the snow layer maximum water content, is a critical parameter in determining meltwater percolation and retention within the model (e.g., Vionnet et al., 2012). Details of the retention and refreezing parameterization are provided in Brun et al. (1992) and Reijmer et al. (2012). The fraction of meltwater produced at the surface is determined by the spatial and temporal distribution of surface albedo and surface temperature within MAR's atmospheric model. The rate of runoff is prescribed by Lefebre et al. (2003) as a function of three constants (c_1, c_2, c_3) and surface slope, S (see eqn. 1). Within MAR v3.5.2, c_1 = 0.3, c_2 = 25, and c_3 = 140 days and S = 0.02, based on observations at Swiss Camp, and serve as the model's runoff delay function. While no physical meltwater routing routine exists in MAR, this runoff delay function serves as an approximation for the transit time between meltwater production and outflow at the ice sheet margin. This runoff scheme is prescribed for snow and ice sheet runoff only following Zuo and Oerlemans (1996). Land runoff from ice-free areas in MAR is primarily a function of the difference between precipitation and the water vapor gradient regulating evapotranspiration rates (Ridder and Schayes, 1997).

4.2.3 In situ discharge data

Proglacial river discharge was measured at three drainage basins – Thule, Watson, and Nuuk, located north-to-south in west Greenland (Fig. 4.1). Discharge at each of these sites were collected differently and an optimal drainage basin area was selected from several possible basin realizations detailed below.

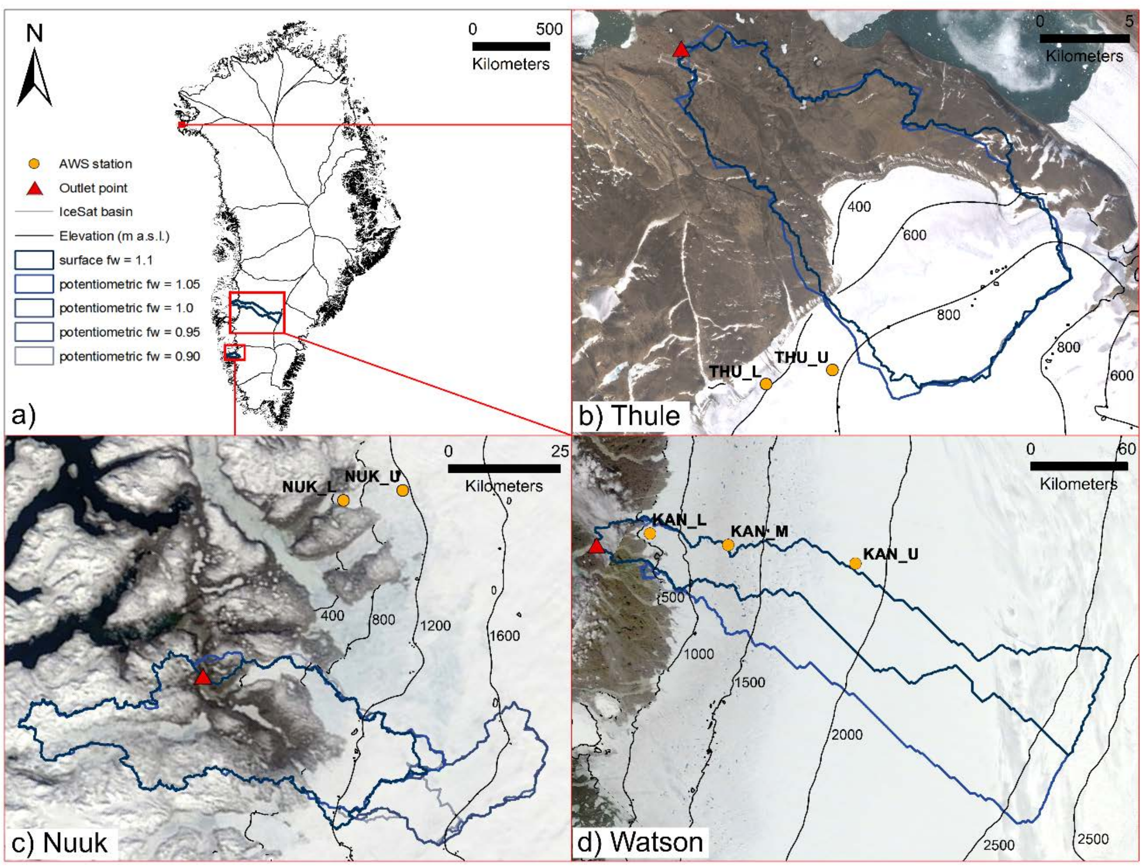

Figure 4.1 Panel (a) shows the location of the study area (red) and catchment delineations (blue) overlaid with IceSat-derived drainage basins (Zwally et al., 2012). Panels (b), (c), and (d) show five watershed delineation scenarios created from different combinations of surface (GIMP 30 m

digital elevation model; Howat et al., 2014) and bedrock topography (150 m digital elevation model; Morlighem et al., 2014) and flotation factors (fw), overlain with the location of PROMICE automatic weather stations, and gauging station, for Thule, Nuuk, and Watson, respectively. The background is a 6 July 2010 MODIS 250 m true color image.

4.2.3.1 Thule

The North River, located in the northern part of the Pituffik Peninsula in Northwest Greenland (Fig. 4.1b), is referred to as the Thule basin in this study. The total basin area computed in this study is 219 km^2 (using a flotation factor (Fw) = 1.1 provides the best catchment fit; see Section 4.2.4 below for details), of which 118 km^2 is ice area from the Støre Landgletcher glacier (54% of the drainage basin), and reaches a maximum elevation of 950 m a.s.l. (no equilibrium line area (ELA) is established here). This region lacks an extensive sub-glacial hydrologic system, and is likely frozen to the bedrock year-round (Butkovich, 1959).

Proglacial discharge measurements and river stage were collected from a bridge 20 km west of the ice sheet edge, along the North River near the Thule Air Base (Fig. 4.1b) from 2004 to 2006 and 2011 to 2012. River stage was measured every 5 to 15 minutes using a Campbell ultrasonic (2004-2006) and radar (2011-2012) instrument attached 8 m above the stream bed. River stage measurements were collected throughout the melt season to capture a range of stages to construct a rating curve (Dingman, 2015). Two different methods were used to collect discharge, depending upon stage levels: 1) at low and medium river stage, observations were made with the velocity-area method (TC, 2007); and 2) at high river stage (>1.2 m), observations were conducted using the float method to measure surface velocity, and assuming a uniform velocity profile. About twelve discharge measurements were collected each year and combined to produce a rating curve. Using an error propagation method similar to Rennermalm et al. (2012), the combined estimated discharge error is 27%.

4.2.3.2 Watson

This study estimates the Watson River drains an ice sheet area of 20,109 km^2 (Fw=0.90; total catchment area of 20,739 km^2) of the land-terminating Kangerlussuaq sector of the western GrIS (Fig. 4.1d). Several other studies have estimated the Watson River basin area to be 12,000-12,500 km^2 (van As et al., 2017; Mikkelsen et al., 2016). The catchment is 97% glaciated and ranges from 300 m a.s.l. to the ice divide at 2560 m a.s.l., with an ELA of 1553 m a.s.l. (van de Wal et al., 2012, 2015).

Since 2006, stage height has been recorded nearby the Watson River Bridge in Kangerlussuaq, about 22 km from the ice sheet edge (Hasholt et al., 2013). The dataset has been revised several times as new and more precise discharge observations have been employed (van As et al., 2017). Here, we present discharge observations from van As et al. (2017) from the time period 2009-2013. Using pressure transducers, river level was measured and recorded as hourly averages. Discharge measurements were collected across a range of stage heights to produce a rating curve. Three methods were used to construct a stage-discharge relationship, and are detailed in van As et al. (2017). An uncertainty value of 15% is assigned to all Watson river discharge measurements.

4.2.3.3 Nuuk

The Naujat Kuat River, hereafter referred to as the Nuuk basin, is located 11 km from the ice sheet margin, in west Greenland. The river drains into the Ameragdla fjord, a tributary of the Lyseefjord, located south of Greenland's capital, Nuuk. The total catchment area computed here is 1676 km^2 (Fw=1.1), with an ice area of 492 km^2 (29% glaciated; Fig. 4.1c) and maximum elevation of 1558 m. The drainage basin is well below the regional ELA and has been estimated to have an ice area of ~356 km^2 (Overeem et al., 2015). Here, we present discharge observations from Overeem et al. (2015).

Discharge measurements were continuously collected from the Naujat Kuat River in 2011 to 2014. Stage height was measured with a Campbell sonic ranger and sampled hourly. Velocity measurements were collected with the float method and water surface slope from site visits in June 2010, July 2011, and August 2012. River cross-sectional area was computed using a 3D bedrock constriction model from four photographs taken on 6 April 2012 during very low flow. Photographs were processed in a structure-from-motion package (Bundler and Patch-based Multi-view Stereo Software) to produce a dense point cloud. Using identifiable ground reference points (e.g., boulder), the model was scaled, to produce a final 2D cross-sectional area. A stage-discharge relationship was determined using both in situ and modeled estimates. Model estimates were included to augment sparse in situ stage-discharge measurements and to overcome turbulent river flow conditions. Modeled stage-discharge estimates were calculated using a fluid-mechanics model (Kean and Smith, 2005; Kean and Smith, 2010). Channel geometry, channel roughness, and water surface slope from the model were used to estimate cross-sectional velocity and discharge from stage height observations. A set of sensitivity experiments were conducted for each cross section, and the model was iterated over a range of channel roughness and slope values. The sensitivity experiment that best fit the observed stage-discharge relationship was used. With a limited observational record and uncertainties in model parameterization, the sensitivity experiments estimate discharge uncertainty at 56%. More details are provided in Overeem et al. (2015).

4.2.4 Watershed delineations, identification of optima flotation factor, and uncertainty quantification

Five watershed delineation scenarios were derived for each upstream gauge site to quantify how uncertainties in catchment area propagate to MAR runoff estimates. Each catchment was delineated from surface and bedrock topography digital elevation models (DEMs). The potentiometric method, where surface and bedrock topography are used to calculate hydraulic potential (Cuffey and Paterson, 2010), was used for delineating each watershed. The hydropotentiometric equation is:

$$-\nabla\phi_h = -p_i g\left[f_w \nabla S + \left[\frac{p_w}{p_i} - f_w\right]\nabla B\right] \quad (1)$$

Where $-\nabla\phi_h$ is the flow gradient, p_i is ice and p_w is water density (provide constants here), ∇S is surface and ∇B is bedrock topography, and f_w is flotation fraction. DEMs of surface (Greenland Ice Mapping Project (GIMP) 30 m; Howat et al., 2014) and bedrock (150 m; Morlighem et al., 2014) topography were used for ∇S and ∇B, respectively. The floatation fraction, f_w, the ratio of subglacial water pressure to ice overburden pressure, varied for each delineation routine, to account for varying influences of the surface and bed on water flow. Five f_w values were used to generate a range of bed-to-surface dominated watershed area delineations for each catchment: $f_w =$

$1.1, 1.05, 1.0, 0.95,$ and 0.90 (where, $f_w = 1.1$ considers surface topography only). The delineation routine was adapted from Rennermalm, *in prep.* (2017) and modeled in ArcGIS using a D8 approach to calculate contributing area (Tarboton, 1997) in the hydrology toolset. This delineation method incorporates f_w, which determines the ratio of water pressure to overburden pressure (instead of assuming that ice overburden pressure is equal to water pressure; Cuffey and Paterson, 2010). The delineated watershed areas were used to quantify a range of uncertainty on MAR runoff estimates. Unlike Nuuk and Thule, the Watson watershed was delineated differently, accounting for hydropotentiometric flow below 1 km elevation, and surface topography only above 1 km elevation. For details regarding the watershed delineation scheme, see Rennermalm, et al., *in prep*, (2017). The flotation factor producing the best-fit basin area to observed discharge data was identified and used in subsequent analyses. The watershed delineation analysis, resulting areas, and subsequent MAR runoff estimates are provided in Figures 4.1 and 4.2.

4.2.5 Identification of optimal temporal averaging

Since the MAR model contains a routing delay function that has not been tested, we postulate that the best model-observed discharge fit may not occur at the daily average time scale. To evaluate this hypothesis, an evaluation of modeled-observed discharge is conducted at multiple temporal averages, including a daily, 5-, 10-, and 20-day means (jumping not moving averages). Scatter plots of these multiple temporal scale averages were produced and identification of an optimal time average for comparison was determined.

4.2.6 Model evaluation with PROMICE data

Near-surface conditions modeled by MAR were compared with daily June, July, and August (JJA) measurements from the Programme for Monitoring of the Greenland Ice Sheet (PROMICE; Ahlstrom et al., 2008) Automatic Weather Stations (AWS) nearest to each basin. The MAR values corresponding to each AWS was derived from each overlapping MAR grid cell. The MAR model simulates several parameters for two surface conditions, land or ice, for the entire simulation domain regardless of the surface type. This includes runoff and surface temperature variables. To calculate MAR drainage basin runoff, we use the GIMP project land surface classification (Howat et al., 2014) to identify the contribution from land and ice, respectively. In reality, MAR grid cell containing the AWS stations closest to the ice margin may cover both land and ice. However, when comparing MAR with station data, we select the data from the simulation that assumes an ice sheet surface only to match surface type at the AWS station locations. A list of the seven weather stations used in this study are provided in Table 4.1. From each station, downwelling shortwave radiation (SWD), downwelling longwave radiation (LWD), near-surface air temperature (ST), and albedo (AL) variables were used. Linear regression analysis, and Pearson correlation coefficient was used to evaluate fit and corresponding statistical significance.

Table 4.1 Seven PROMICE stations used to validate MAR primary drivers of melt.

AWS	Latitude (°N)	Longitude (°E)	Elevation (m)	Study Period
THU_L	76.40	68.27	570	2011-2012
THU_U	76.42	68.15	770	2011-2012
KAN_L	67.10	49.95	680	2009-2013
KAN_M	67.07	48.83	1270	2009-2013
KAN_U	67.00	47.02	1840	2009-2013
NUK_L	64.48	49.53	540	2011-2014
NUK_U	64.51	49.27	1130	2011-2014

4.2.7 Modeled surface melt evaluation with a positive degree day model

Near-surface air temperature is frequently used to estimate surface melt (e.g., Ohmura, 2001; Hock, 2005). This can be used in lieu of explicitly solving for all surface energy balance (SEB) terms. The positive degree day (PDD) model is an efficient, commonly used method to estimate surface melt from near-surface air temperatures. The PDD method integrates the cumulative sum of near-surface air temperatures (2 m) above the 0 °C melting point, for a given time period, and multiplied by the degree-day factor for ice constant, to solve for surface melt (Cuffey and Paterson, 2010):

$$M = f_i \sum (T_{2m} - T_0)\, \Delta t \qquad (2)$$

Where, f_i is an empirically-derived coefficient relating $\sum(T_{2m} - T_0)$, the summation of air temperatures collected at a 2 m height (in °C) when T_{2m} is greater than a given threshold, T_0, used to estimate assimilated heat energy available for melting, M, over a given time interval, Δt. Here, f_i is 0.008 m day^{-1} °C^{-1}, based on observations over ice in Greenland (e.g., Braithwaite and Zhang, 2000); Δt is daily for the JJA time interval; T_0 is set to the melting point of snow/ice, 0 °C; to solve for M in meters. The PDD-derived melt estimates were computed at each PROMICE station based on the ST variable and at their corresponding MAR grid cells using modeled near-surface air temperature. To conservatively estimate periods of melt, only temperatures above T_0 for three consecutive days were used to approximate melt.

4.2.8 Richards-Baker Flashiness Index

To characterize daily observed peak discharge events, and by extension, the hydrologic efficiency of meltwater transport from the ice sheet to the gauging station, we evaluate the 'flashiness' of each basin. The flashiness of a river reflects the regularity and rapidity of short-lived changes in river discharge. This can be quantified using the Richards-Baker (R-B) Flashiness Index formula (Baker et al., 2004):

$$R - B\ Index = \frac{\sum_{i=1}^{n} |q_i - q_{i-1}|}{\sum_{i=1}^{n} q_i} \tag{3}$$

Where, q is average daily flow in day i to day $i-1$, representing the length of the streamflow time series over the melt season (JJA), divided by the sum of daily discharge over the melt season. The $R - B\ Index$ represents a dimensionless value with high values representing more 'flashy' flow. We expect to see a higher flashiness value in a basin with less melt area such as the Thule basin.

4.3 Results

4.3.1 Comparison of observational discharge and MAR runoff estimates

Model-observation discrepancies vary for each catchment and catchment delineation realization (Fig. 4.2). The Thule catchment realizations demonstrate the best coherency in modeled discharge, hereafter Q_M, estimates, with differences in average JJA Q_M estimates within three percent (~2.80%) for all flotation factors, relative to Fw=1.1 (Fig. 4.2a-e). Thule MAR modeled runoff is insensitive to changes in the floatation factor used, with average JJA Q_M overestimating average JJA observed river discharge, hereafter Q_O, 23.27% for Fw=1.05, 35.30% for Fw=1.0, and ~37% for Fw=1.1, 1.0, 0.95, and 0.90. Evidence from prior research suggests that Thule's glaciated area is cold-based, implying that surface topography dictates flow in this region (as suggested in Section 4.2.3.1). The consistency of Thule's catchment delineations (Fig. 4.1b), despite varying surface and potentiometric combinations, gives us confidence that Thule's surface (Fw=1.1) drainage basin delineation is representative and well-suited for further analyses. Assuming that only surface topography dictates water flow in the catchment (i.e., Fw=1.1), Q_M overestimates Thule daily seasonal (JJA) Q_O by as much as 46.11% (hereafter, computed as the mean MAR minus observed discharge difference) in 2011, corresponding to a 19.37 $m^3\ s^{-1}$ discharge difference, on average (Table 4.2 and Fig. 4.2a). The exception to this overestimation is during peak discharge events (Fig. 4.2a-e). For instance, Thule daily Q_O peak at 66.53 ± 17.96 $m^3\ s^{-1}$ (± one standard deviation) on 18 July 2004 and at 76.24 ± 20.58 $m^3\ s^{-1}$ on 20 August 2004 (Fig. 4.2a). While, Thule Q_M

peaks at 28.68 ± 4.30 $m^3 s^{-1}$ and 26.35 ± 3.95 $m^3 s^{-1}$ on the corresponding dates, results in an underestimation of 132% and 189%, respectively. The underestimation of Thule daily observed peak discharge by Q_M is accentuated in the extreme melt year of 2012 (Fig. 4.2e).

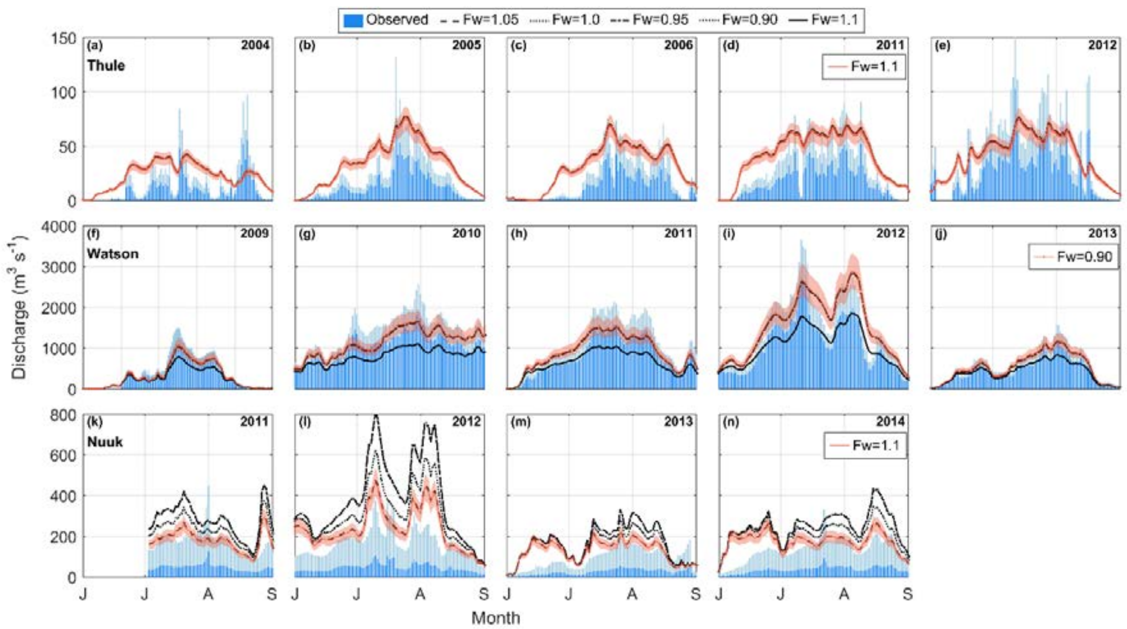

Figure 4.2 Daily average discharge from the MAR model (Q_M) for five different catchment realizations from surface and potentiometric delineation methods (black lines) and observed proglacial river discharge (Q_O; stacked dark blue lines) for Thule (2004-2006 and 2011-2012; a-e), Watson (2009-2013; f-j), and Nuuk (2011-2014; k-n) basins. Stacked light blue lines are ± 27%, ± 15%, and ± 56% error bars in Q_O calculations for Thule, Watson, and Nuuk, respectively. The bold red line represents the best fit drainage basin scenario (Fw value) of Q_M and light orange shading is ± 15% uncertainty.

The Watson catchment demonstrates better agreement (cf. Thule and Nuuk basins in Fig. 4.2) between daily model-observed discharges. All basin realizations result in similar daily Q_M estimates except for the Fw=1.1 drainage basin delineation. The average JJA Q_M overestimates average JJA Q_O by 1.40%, 1.61%, 0.75% and 4.35% for Fw = 1.05, 1.0, 0.95, and 0.90, respectively, and underestimates Q_O by -37.06% for Fw=1.1

(Fig. 4.2f-j). The Fw=0.90 catchment delineation for the Watson basin is designated the optimal delineation of observed daily discharge, as recommended by a recent study with similar basin area (van As et al., 2017; Fig. 4.2f-j). Daily Q_M largely captures inter- and intra-annual variability in Watson daily Q_O, and are nearly within observational uncertainty bounds. This good agreement between daily modeled-observed discharge is exemplified in 2013, where the Watson basin average difference is minimized, with model-observation discharge values within 2.23% of each other (mean difference of 35.94 m^3 s^{-1}; and Fig. 4.2j). During the extreme melt season of 2012, average daily Q_O peaked at 3188.76 ± 478.31 m^3 s^{-1} on 11 July 2012 corresponding to a Q_M of 2683.57 ± 402.54 m^3 s^{-1} (Fig. 4.2i). This represents a modeled underestimation of peak discharge of ~19%. Integrating Watson mean daily Q_O over the melt season (JJA) results in a total discharge of 4.51 ± 0.03, 7.43 ± 0.04, and 4.16 ± 0.03 km^3 for lower melt years (2009, 2011, and 2013, respectively) and a total discharge of 9.87 ± 0.03 and 10.30 ± 0.06 km^3 for higher melt years (2010 and 2012, respectively; Table 4.4). These total discharge volumes are lower than the corresponding total MAR discharge volumes in 2012 and 2013 (8.55 ± 0.04 and 4.44 ± 0.03 km^3, respectively) and higher than total MAR discharge volumes from 2009-2011 (3.13 ± 0.02, 6.39 ± 0.02, and 5.09 ± 0.02 km^3, respectively; Table 4.4).

Table 4.2 Mean discharge difference (m^3 s^{-1}) and mean percent difference (%) between MAR and observed daily discharge JJA data for Fw=1.1 (THU and NUK) and Fw=0.90 (WAT). Eqn: (Mean MAR- Mean OBS)/ Mean MAR * 100.

THU	2004	2005	2006	2011	2012

Discharge Difference (m^3 s^{-1})	11.11	15.10	13.72	19.37	5.12
Percent Difference (%)	43.01	38.15	44.29	46.11	20.17
WAT	**2009**	**2010**	**2011**	**2012**	**2013**
Discharge Difference (m^3 s^{-1})	-44.97	-67.77	-13.39	297.30	35.94
Percent Difference (%)	-7.70	-5.41	3.56	21.57	2.23
NUK	**2011**	**2012**	**2013**	**2014**	-
Discharge Difference (m^3 s^{-1})	70.15	127.98	68.97	90.54	-
Percent Difference (%)	37.44	51.56	47.80	50.72	-

Greater variability in modeled catchment delineations is observed for the Nuuk basin (Fig. 4.2k-n). Regardless of flotation factor used and large uncertainties in observed river discharge (± 56%), MAR is overestimating daily Q_O for all years (2011-2014) in the Nuuk basin. The Nuuk drainage basin realizations result in average JJA Q_M overestimating average JJA Q_O by 50.69%, 51.44%, 67.25%, 67.02%, and 61.02% for Fw=1.1, 1.05, 1.0, 0.95, and 0.90, respectively. Accounting for surface topography only (Fw=1.1) produces the closest approximation of Nuuk Q_O, and is used for comparison of subsequent results. The Nuuk basin exhibits the largest overestimation in daily Q_M, by as much as 51.56% (127.98 $m^3 s^{-1}$) in 2012 (Table 4.2 and Fig. 4.2l). Nuuk's annual total Q_O volumes range from 0.46 ± 0.00 km^3 in 2013 (low melt year) to 0.87 ± 0.00 km^3 in 2012 (high melt year), corresponding to Q_M total discharge volumes of 1.01 ± 0.00 km^3 and 1.89 ± 0.00 km^3, respectively (Table 4.5). These model-observation annual totals differ by a factor of over two. A small observational data gap in Nuuk 2011 data (data starts on 3 July instead of 1 June; Fig. 4.2k) may partly explain for model-observation differences in total volume calculations. Large differences in Nuuk daily Q_M occur between drainage basin delineations, as described earlier. For instance, on 10 July 2012, the peak Q_O is 240.40 ± 134.65 $m^3 s^{-1}$, corresponding to a peak Q_M of 465.78 ± 69.87 $m^3 s^{-1}$, for the Fw=1.1 catchment. This was followed closely by a peak Q_M of 476.25 ± 71.44 $m^3 s^{-1}$, 621.63 ± 93.24 $m^3 s^{-1}$, 801.07 ± 120.16 $m^3 s^{-1}$, and 809.65 ± 121.45 $m^3 s^{-1}$ at Fw=1.05, Fw=1.0, Fw=0.95, and Fw=0.90, respectively (Fig. 4.2l). This corresponds to Nuuk Q_M estimates overestimating Q_O by as much as ~70% during peak discharge events. These differences are partly linked to difficulties in delineating the Nuuk basin, difficulties in measuring proglacial river discharge at this gauging site, and the model's inability to capture large daily, intra- and inter-annual variability.

Given that the MAR model has a routing delay that remains untested, we theorize that Q_M may better fit Q_O after temporal averaging. To test this, an evaluation of seasonal model-observation discharge as scatter plots averaged at multiple temporal scales is conducted (5-, 10-, and 20-day means; Fig. 4.3). The model-observed discharge data is integrated over the same time periods and for the optimal drainage basin delineations identified above (i.e., Fw=1.1 for Thule and Nuuk; Fw=0.90 for Watson). A general improvement in model-observation agreement is realized at 5-, 10-, and 20-day averages for all basins (cf. Figs. 4.2 and 4.3). This is particularly so for the Thule and Watson basins, while the greatest overestimation and disagreement is observed for the Nuuk basin, regardless of the temporal sampling average used (Fig. 4.3i-l). At the daily timescale, the Q_M is larger than Q_O for the Thule basin (by 13.09 m^3 s^{-1}, hereafter, on average seasonally), with a moderate correlation (r^2 = 0.55) and slope of the best fit line (0.63; Fig. 4.3a). The Watson daily model-observed discharge comparison is excellent with a high correlation (r^2 = 0.86), a slope close to one (0.96), and a strong correlation coefficient (r=0.93; Fig. 4.3e). While the daily Watson Q_M slightly overestimates Q_O (by 42.33 m^3 s^{-1}; Fig. 4.3e), this may be explained by a few MAR daily runoff outliers, likely corresponding to peak discharge events (e.g., July 2010 and 2012). The comparison of Nuuk daily model-observed discharge reveals the greatest overestimation of Q_O (by 92.49

m^3 s^{-1}), with a low correlation (r^2 = 0.41) and large Root Mean Square Difference (RMSD = 109.72 m^3 s^{-1}; Fig. 4.3i).

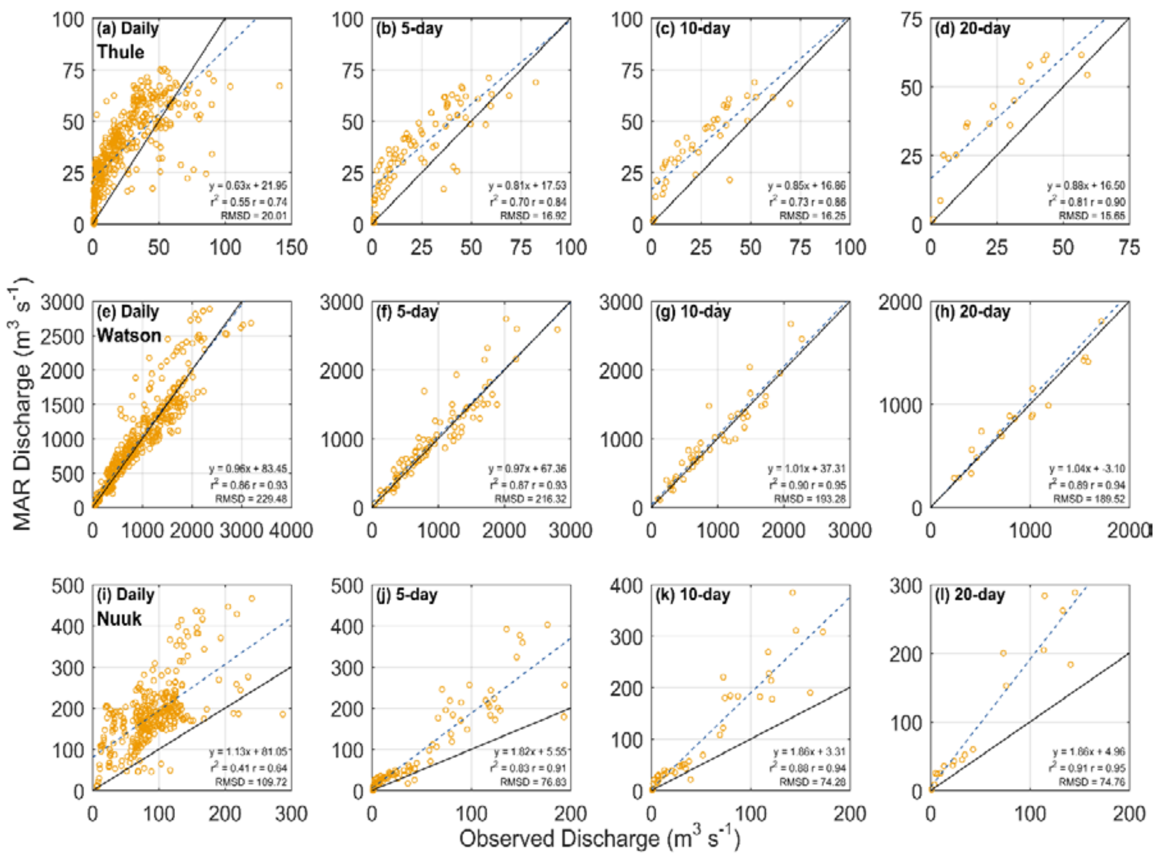

Figure 4.3 Scatter plot of MAR v3.5.2 daily (a, e, i), 5-day (b, f, j), 10-day (c, g, k), and 20-day (d, h, l) average JJA runoff (m^3 s^{-1}) versus observed average discharge (m^3 s^{-1}) for Thule (a-d; years 2004-2006 and 2011-2012) basin for the Fw=1.1 scenario, Watson (e-h; years 2009-2013) for the Fw=0.90 scenario, and Nuuk (i-l; years 2011-2014) basin for the Fw=1.1 scenario. The black solid line is the 1:1 line and the blue stippled line is the linear regression line. The linear equation, correlation of linear fit (r), coefficient of determination (r^2), and root mean squared difference (RMSD) of linear fit statistics are provided in each subplot.

At the 5-day averaged timescale, Q_M overestimates discharge less, and provides better agreement between model-observed discharge than on a daily basis (cf. Fig. 4.3b, f, j and Fig. 4.3a, e, and i). More specifically, when Q_M is compared with Q_O at the pentadal timescale, the correlation (r^2 = 0.70, 0.87, and 0.83) and the bias (RMSD = 16.92, 216.32, and 76.83 $m^3 s^{-1}$; Fig. 4.3b, f, and j) improves for Thule, Watson, and Nuuk basins, respectively. The most noticeable improvement in model-observation agreement is observed at the 5-day average of the Nuuk basin, where Q_M overestimation of Q_O is reduced (by 47.99 $m^3 s^{-1}$) and a stronger linear correlation coefficient (r = 0.91) is observed (Fig. 4.3j). At the larger temporal scales (10- and 20-day), further reduction in model-observation discrepancies is observed for all basins (Fig. 4.3c-d, g-h, and k-l). At the 10- and 20-day timescale, the correlation between model-observed discharge is higher ($r^2 > 0.73$, $r^2 > 0.89$, and $r^2 > 0.88$ for Thule, Watson and Nuuk, respectively), and smaller reductions in Q_M bias is observed (cf. RMSD in Fig. 4.3c-d, g-h, and k-l). Increasing the temporal averaging appears to improve the coherency between model-observation discharge, but comes with further data reduction. As the temporal sampling increases, the sample size decreases from n=409, 445, and 330 (daily) to n=17, 20, and18 (20-day) for Thule, Watson, and Nuuk, respectively.

4.3.2 Comparison of near-surface conditions

The comparison of observed and modeled discharge reveals reasonable fit for the Watson basin, but large model overestimation in Nuuk and Thule basins (Fig. 4.2). To examine if these overestimations could be traced back to factors governing ice sheet melt and subsequent runoff, we assess primary drivers of melt (defined here as SWD, LWD, ST, and AL), simulated by MAR and observed at nearby PROMICE AWSs. Scatter plots of model-observation near-surface conditions reveal biases exist for each variable, at different elevations (AWS_L is lower elevation, AWS_M is middle elevation, and AWS_U is upper elevation), and for each PROMICE station (Figs. 4.1-4.6). At the lower elevations of the Thule basin, MAR overpredicts SWD (by 24.16 W m^{-2}, hereafter represented as the average difference; Fig. 4.1a), underpredicts LWD (by 32.55 W m^{-2}; Fig. 4.1c), underestimates ST (0.35 °C; Fig. 4.1e), and overestimates AL (0.15; Fig. 4.1g) as compared to PROMICE observations at the THU_L station from 2011-2012 (no data available from 2004-2006). The THU_L correlation is lowest for LWD (r^2 = 0.45) and AL (r^2 = 0.51) with correspondingly high biases (RMSD = 37.40 W m^{-2} and 0.17, respectively). Similar trends are observed at the higher elevation THU_U station near the Thule catchment, with the exception of ST (Fig. 4.1b, d, and f). Where, MAR overestimates (underestimates) SWD (LWD) radiations by 29.70 W m^{-2} (-27.59 W m^{-2}), on average (Fig. 4.1b and d). Biases remain high for radiative fluxes, with RMSD = 59.03 W m^{-2} (33.88 W m^{-2}) for SWD (LWD) at THU_U (Fig. 4.1b and d). Unlike at

THU_L, MAR overpredicts ST at THU_U (0.43 °C; Fig. 4.4f). No AL data is available at THU_U during 2011-2012.

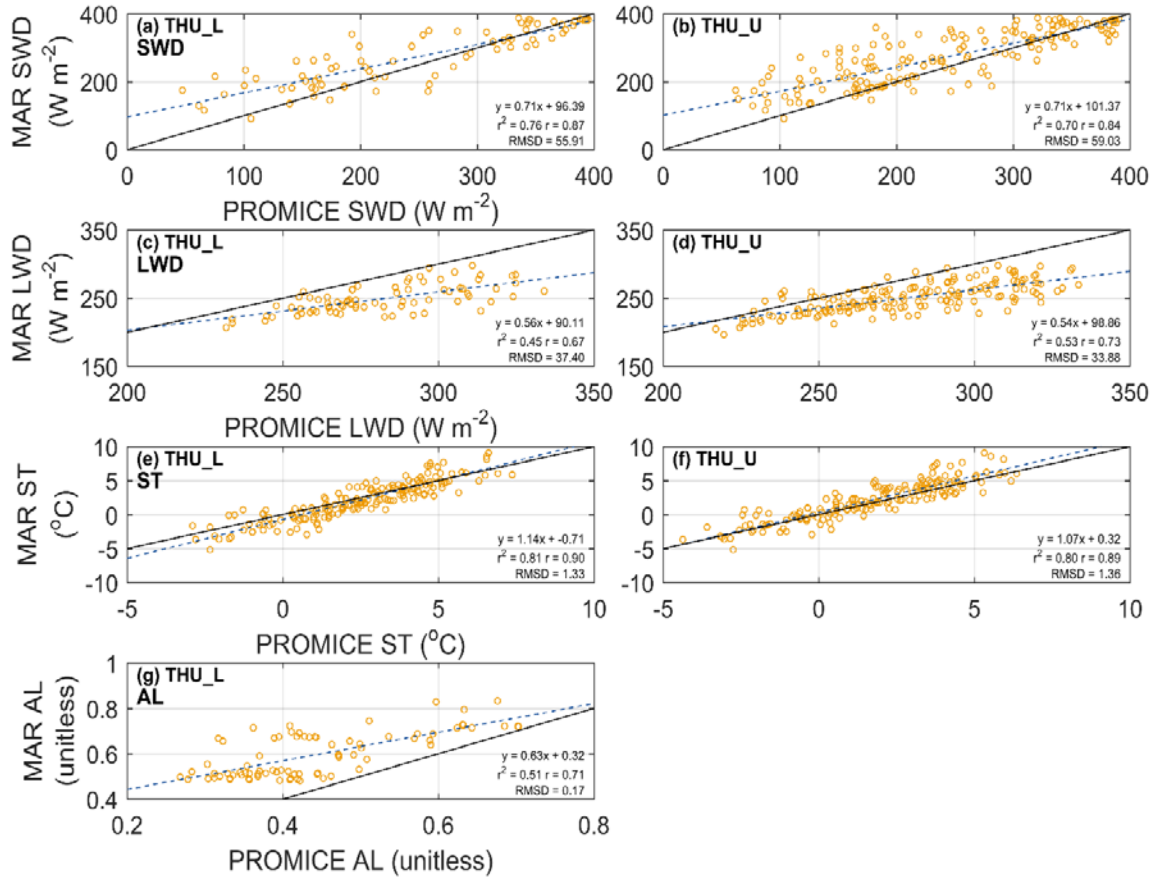

Figure 4.4 Scatter plots of daily PROMICE automatic weather stations versus MAR shortwave downward radiation (SWD; W m^{-2}; a-b), longwave downward radiation (LWD; W m^{-2}; c-d), and near-surface temperature (ST; °C; e-f) for THU_L and THU_U over 2011-2012. Surface albedo (AL; unitless; g) is only available for THU_L in 2011. The black solid line is the 1:1 line and the blue stippled line is the linear regression line. The linear equation, correlation of linear fit (r), coefficient of determination (r^2), and root mean squared difference (RMSD) of linear fit statistics are provided in each subplot.

MAR follows a similar pattern seen at the PROMICE stations near the Thule basin, but with some noticeable differences at the KAN_M station (Fig. 4.5). At KAN_L, the lowest PROMICE station within the Watson catchment, MAR SWD (LWD) is higher (lower) than river discharge by 25.67 W m^{-2} (-28.32 W m^{-2}; Fig. 4.5a and d), on average, consistent with the discrepancies observed at the Thule PROMICE stations (cf. Figs. 4.4a and c, 4.5a and d). There is moderate correlation r^2 = 0.56 (r^2= 0.48) and relatively high (low) RMSD of 62.12 W m^{-2} (34.39 W m^{-2}) for SWD (LWD). While MAR underpredicts (overpredicts) ST (AL) by 1.05 °C (0.06), on average, at the KAN_L station (Fig. 4.5g and j), the spread in ST (AL) data is minimized (as compared to variability in SWD and LWD data; cf. Fig. 4.5a and d). As we move upwards in elevation (from KAN_L to KAN_M), the KAN_M station reveals a slight increase in the correlation (by 12.05%) and decrease in RMSD (by -16.09%) for SWD (cf. Fig. 4.5a and b). Despite this, MAR still overestimates SWD at KAN_M, yet less so (decrease by 52.27% from KAN_L to KAN_M). At KAN_M, minor improvement in LWD model-observed agreement is observed, with MAR continuing to be lower (by -19.65 W m^{-2}) than observed downward longwave fluxes (Fig. 4.5e). When MAR is compared to observed near-surface air temperatures at KAN_M, there is excellent correlation (r^2 = 0.79), but unlike at lower elevations (at KAN_L), MAR overestimates ST (by 0.24 °C; Fig. 4.5h) and similar to what is observed at THU_U (Fig. 4.4f). At KAN_M, there is greater spread in model-observation surface albedos (max/min range of 0.32 and 0.46 for MAR and observations, respectively), resulting in a larger overestimation (by 0.12) of KAN_M albedo observations (cf. lower elevation albedos at KAN_L; cf. Fig. 4.5j and k). At the higher elevation KAN_U station, model-observation discrepancies diminish (Fig. 4.5c, f, i, and l). At KAN_U, MAR overestimation (underestimation) SWD (LWD) is reduced by 3.11 W m^{-2} (-18.56 W m^{-2}), on average, as compared to lower elevation stations (cf. Fig. 4.5c and f, Fig. 4.5a-b and d-e). These results are corroborated by excellent (fair) correlation for SWD (LWD), with an $r^2 = 0.71$ ($r^2 = 0.50$) and lower RMSD of 39.58 W m^{-2} (slight increase in RMSD of 31.23 W m^{-2} from KAN_M to KAN_U). Similar to KAN_L (but, different from KAN_M), MAR ST is cold-biased, yet less so (by -0.23 °C), with the slope of the best fit line (0.87) close to one (Fig. 4.5i). Despite poor agreement ($r^2 = 0.26$) in AL at KAN_U (Fig. 4.5l), the model-observation discrepancies are insignificant (-0.01), due to MAR's ability to capture higher albedos at higher elevations of the Watson basin. Lower variability in albedos at higher elevations are expected (as the surface becomes more homogeneous), which is supported by the reduced spread in model-observation albedos (AL range of 0.20 and 0.22 for MAR and observations, respectively).

The percent change (over or underestimation) in daily seasonal primary drivers of melt are provided in Table 4.6.

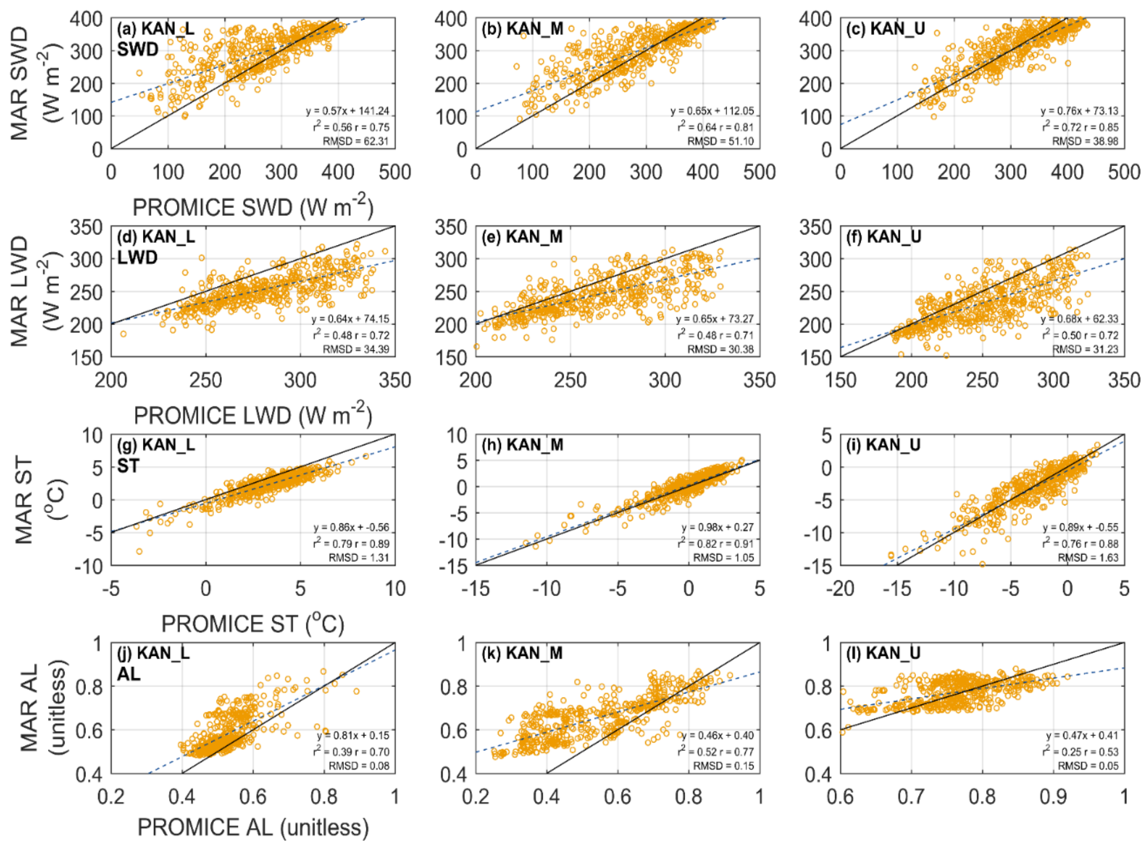

Figure 4.5. Same as Figure 4 but for KAN_L, KAN_M, and KAN_U from 2009-2013.

Similar to the PROMICE stations at Thule and Watson, the Nuuk stations reveal comparable trends (Fig. 4.6), with noticeable differences in ST at lower elevations (NUK_L; Fig. 4.6e). As observed at THU and KAN stations, MAR overestimates (underestimates) SWD (LWD) consistently at lower and higher elevations (NUK_L and NUK_U; Fig. 4.6a-b and c-d). However, there is poorer agreement in SWD (LWD) at the higher elevation, NUK_U station, with an $r^2 = 0.22$ ($r^2 = 0.36$; Fig. 4.6b and d) than at the lower NUK_L station (Fig. 4.6a and c). And, the MAR overprediction of SWD and LWD is greater at NUK_U, with an increase in SWD (LWD) by 63.84% (6.71%), on average. Contrasting MAR’s underprediction of ST at lower elevations of THU and KAN sites, MAR ST is considerably larger than observed surface temperatures at the lower elevation NUK_L station (by the average difference of 3.67 °C; Fig. 4.6e). While at the NUK_U station, MAR overestimates ST slightly (by 0.15 °C; Fig. 4.6f), similar to ST trends at THU_U (but not KAN_U; cf. Figs. 4.4f, 4.5i, and 4.6f). The considerable range of albedo values observed at NUK_L (range of 0.77 and 0.37 for observed and MAR, respectively) and poor correlation (r^2 = 0.36), results in a large overestimation of AL by MAR (0.12; Fig. 4.6g). Finally, similar to NUK_L, low correlation (r^2 = 0.38), a weak linear fit (slope of 0.39), and large, yet a reduced spread in surface albedos (0.57 and 0.36 for observed and MAR, respectively), results in MAR overprediction of surface albedo at NUK_U (by 0.07; Fig. 4.6h).

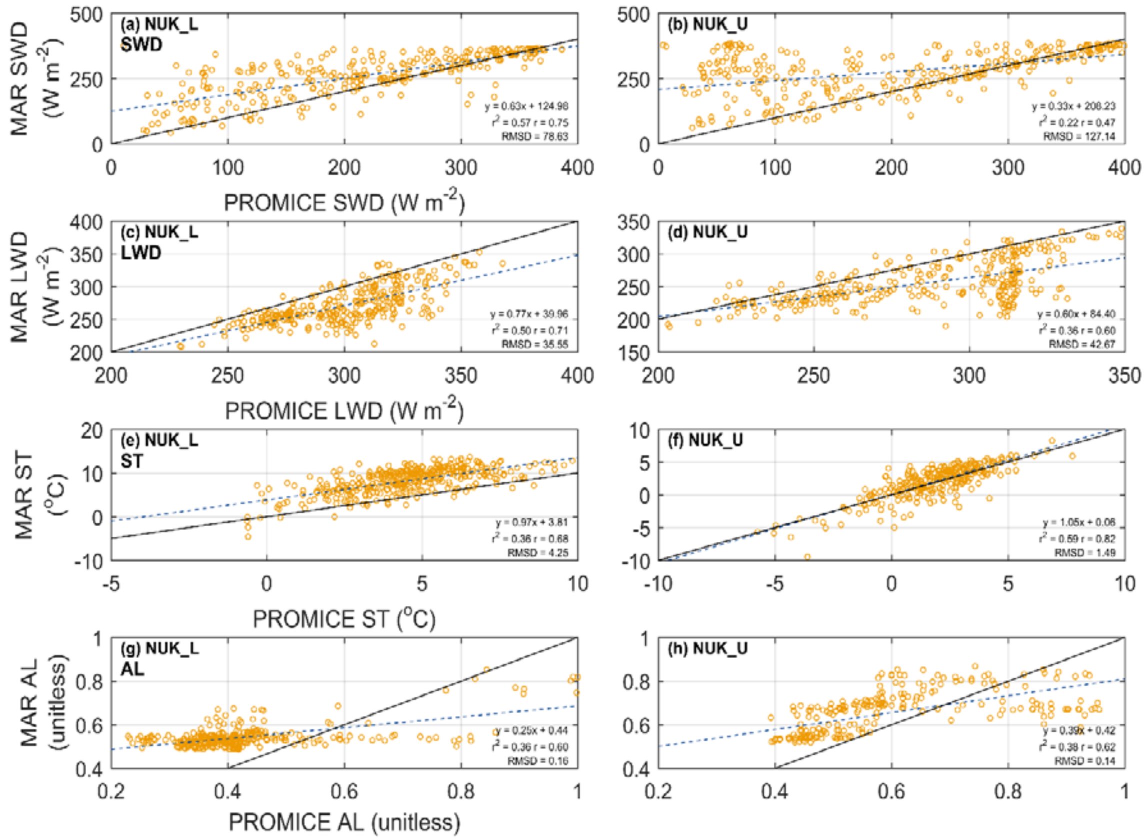

Figure 4.6. Same as Figure 4, but for NUK_L and NUK_U from 2011-2014.

4.3.3 Assessment of meltwater production estimates

Total melt differences (MAR – PROMICE) derived from a PDD model reveal a possible source of discrepancies in model-observation estimates of surface melt, and by extension, runoff (Fig. 4.7). Near the Thule catchment, MAR underestimates (overestimates) meltwater generation at THU_L (THU_U) by 0.14 m and 0.14 m (0.29 and 0.25 m) in 2011 and 2012, respectively (Fig. 4.7a). A similar trend in melt rate difference is observed at the lower elevation KAN_L station (Fig. 4.7b), where MAR largely underpredicts cumulative melt by 4.76 m from 2009-2013. Dissimilar to the KAN_L station results, MAR overestimates melt at the KAN_M and KAN_U stations by 0.20 m and 0.06 m, on average, across all years (Fig. 4.7b). Unlike the lower elevation trends of THU_L and KAN_L, MAR melt rates are markedly higher than observations at NUK_L (range from 1.74 m to 3.01 m) from 2011-2014 (Fig. 4.7c). Finally, MAR overestimates melt rates at NUK_U by 0.48 m, 0.12 m, and 0.91 m in 2011, 2012, and 2014, respectively. These results are consistent with trends observed at THU_U and KAN_U, the exception being in 2013, where MAR underestimates total melt at NUK_U by 0.44 m.

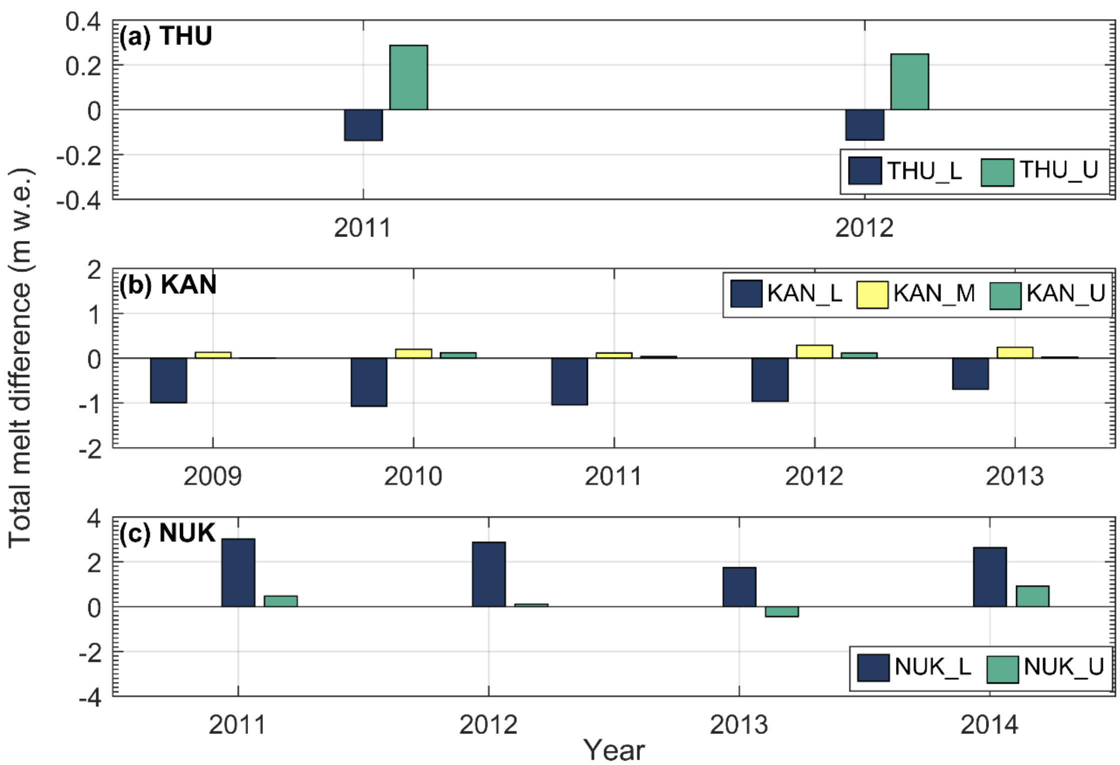

Figure 4.7 Total melt difference (MAR-OBS; m w.e.) derived from the MAR PDD variable and PROMICE surface temperature JJA observations from (a) Thule (THU_L and THU_U), (b),

Watson (KAN_L, KAN_M, and KAN_U), and (c) Nuuk (NUK_L and NUK_U). A positive value is an overestimation and a negative value is an underestimation of PROMICE melt.

Table 4.3 Thule total modeled runoff volumes (km^3) for the best fit catchment realization, observed proglacial river discharge (km^3) ± one standard deviation, and percent change in daily JJA discharge (bolded percentages represent an overestimation by MAR) for 2004-2006 and 2011-2012. Eqn: MAR-OBS/Mean OBS * 100

Year	Discharge	Runoff (Fw=1.1)	Percent Error	R-B Index
2004	0.10 ± 0.00	0.18 ± 0.00	**69.90**	0.45
2005	0.15 ± 0.00	0.27 ± 0.00	**82.01**	0.24
2006	0.13 ± 0.00	0.24 ± 0.00	**84.68**	0.28
2011	0.19 ± 0.00	0.32 ± 0.00	**66.63**	0.24
2012	0.28 ± 0.00	0.32 ± 0.00	**12.58**	0.32

Table 4.4 Watson total modeled runoff volumes (km^3) for the best fit catchment realization, observed proglacial river discharge (km^3) ± one standard deviation, and percent change in daily JJA discharge (bolded percentages represent an overestimation by MAR) for 2009-2013. Eqn: MAR-OBS/Mean OBS * 100

Year	Discharge	Runoff (Fw=0.90)	Percent Error	R-B Index
2009	4.51 ± 0.03	3.13 ± 0.02	-7.92	0.07
2010	9.87 ± 0.03	6.39 ± 0.02	-5.46	0.06
2011	7.43 ± 0.04	5.09 ± 0.02	-1.36	0.07
2012	10.30 ± 0.06	8.55 ± 0.04	**22.94**	0.09
2013	4.16 ± 0.03	4.44 ± 0.03	**6.80**	0.09

Table 4.5 Nuuk total modeled runoff volumes (km^3) for the best fit catchment realization, observed proglacial river discharge (km^3) ± one standard deviation, and percent change in daily JJA discharge (bolded percentages represent an overestimation by MAR) for 2011-2014. Eqn: MAR-OBS/Mean OBS * 100

Year	Discharge	Runoff (Fw=1.1)	Percent Error	R-B Index
2011	0.57 ± 0.00	0.93 ± 0.00	**63.71**	0.09
2012	0.87 ± 0.00	1.89 ± 0.00	**117.31**	0.11
2013	0.46 ± 0.00	1.01 ± 0.00	**119.08**	0.09
2014	0.68 ± 0.00	1.40 ± 0.00	**105.94**	0.08

Table 4.6 Percent change in daily JJA SWD, LWD, ST, and AL (bolded percentages represent an overestimation by MAR) for THU, KAN, and NUK PROMICE stations. Eqn: MAR-OBS/Mean OBS * 100

Station	SWD	LWD	ST	AL
THU_L	**9.70**	-11.57	-14.10	**34.87**
THU_U	**12.16**	-9.93	**25.31**	**-**
KAN_L	**9.86**	-10.04	-30.19	**10.05**
KAN_M	**4.47**	-7.43	**1.04**	**17.47**
KAN_U	-0.77	-7.38	**7.54**	**0.86**
NUK_L	**19.79**	-9.67	**78.21**	**26.95**
NUK_U	**34.50**	-10.77	**8.41**	**11.41**

4.4 Discussion

Other studies have compared Greenland river discharge observations at single rivers with ice sheet estimates. But, this study is the first to compare model discharge (Q_M) estimates with proglacial river discharge (Q_O) at three drainage basins in Greenland. In the 2004-2014 study period, model-observation comparisons were augmented with an investigation of how drainage delineation methodology and forcing variables may explain differences between models and measurements. Choice of drainage delineation methodology, specifically the relative importance of surface and basal topography determined by the floatation factor (Fw), showed to be a major influence on modeled discharge. Water flow dictated by surface topography only (Fw=1.1) provides the best fit for model-observation discharge at the Thule and Nuuk basins (Fig. 4.2). However, incorporating sub-glacial topography, and therefore a representative flotation factor (here, Fw=0.90) is important for delineating the Watson River basin, as other studies have identified moulins and crevasses as important surface features for transporting meltwater to the glacier bed in southwest Greenland (e.g., Smith et al., 2015; Yang et al., 2016). Daily Q_M estimates are within the range of Q_O in the Watson basin, yet predominantly overestimate daily Q_O from the Thule and Nuuk basins (Figs. 4.2 and 4.3). While absolute values are not represented well in the model for the Nuuk and Thule basins, daily Q_M is able to capture the general variability in daily discharge across all sites particularly when averaged over five days or longer (Fig. 4.3). The model-observation daily discharge differs markedly during peak discharge events such as the exceptional melt season of 2012 in the Thule and Watson basins (Fig. 4.2e and i). During high melt episodes, Q_M is dampened, and may be partly attributed to the MAR runoff delay function. Better agreement between model and observed discharge is seen as the average timescale period increases (Fig. 4.3). A ten-day average provides the best fit in model-observed discharge (r^2 between 0.73 and 0.90), but a five-day average is almost as good (r^2 between 0.7 and 0.83). Large discrepancies in variables governing surface melt are observed, and the model is commonly larger than observations for incoming solar radiation, surface albedo, and surface temperature, with some notable exceptions and consistently lower for downward infrared fluxes (Figs. 4.4-4.6; Table 4.6). These positive and negative biases translate into varying melt rates at lower-to-higher elevations, as prescribed by the PDD-derived total melt difference calculations (Fig. 4.7).

Due to a runoff delay function that appears to dampen daily ice sheet runoff too much, MAR resolves daily discharge poorly in Thule and Nuuk basins (Fig. 4.2), but capturing variability improves at longer time aggregations of 5-, 10-, and 20-day averages (Fig. 4.3). Scatter plots of different temporal averaging confirm this discharge variability, where r^2 values are equal to or greater than 0.7 for 5-, 10-, and 20-day averages at all three basins (Fig. 4.3b-d, f-h, and j-l). At the daily timescale, Q_M is poor at capturing absolute discharge values (Fig. 4.2; Tables 4.3-4.5). Daily discharge at the Nuuk basin reveals the largest model-observation discrepancies, with overall positive biases in Q_M estimates (Table 4.5). The percent errors in Nuuk basin Q_M can be as large as ~120% overestimation of Q_O in 2013 (Table 4.5). These findings are consistent with discrepancies between RACMO2 and river discharge for the Nuuk basin in Overeem et al. (2015). Despite smaller daily discharge magnitudes, MAR consistently overestimates daily Q_O for all years, with percent errors as high as ~85% in 2006 (Table 4.3). The best agreement in daily discharge occurs at the Watson Basin, where Q_O is underestimated slightly in 2009-2011 and overestimates in 2012-2013 (Table 4.4). The largest positive bias in Watson daily discharge is observed during the extreme melt event of 2012 (Fig. 4.2i), with the percent error ~23% (Table 4.4). These results contradict the consistent overestimation (by 38%, on average) of Watson river total seasonal discharge volumes predicted by RACMO2 shown in Overeem et al. (2015). This discrepancy may be explained by differences in model runoff representations, where RACMO2 does not incorporate a lag time between meltwater generation and runoff, and due to the fact that a previous version of the Watson discharge data set is used with considerably lower values (van As et al., 2012). Cullather et al. (2016) found that MAR runoff at the macro-basin scale (cf. Basins 6 and 8 in Figure 4.9) was larger in the latter half of the melt season for 2000-2012 compared to other RCMs. This hysteresis may be partly attributed to the MAR runoff delay function, which is important for larger area basins such as the Watson River, but not necessarily for smaller basins similar to Thule and Nuuk with shorter water transport times from the ice sheet to the proglacial river. The runoff delay function is important, nonetheless, as it provides more realistic runoff values, as demonstrated with the river discharge collected at the Watson River fitted with a transit delay function (van As et al., 2017). Van As et al. (2017) also found intra-seasonal variations in the routing delay, requiring shorter delay adjustments particularly after high melt episodes (e.g., July 2012). These seasonal variations in routing delays is likely due to the rapid formation of a hydrologically-efficient en-glacial and sub-glacial transport system after peak meltwater periods (Bartholomew et al., 2011; Palmer et al., 2011). As extreme melt events are expected to become more frequent in a warming climate (McGrath et al., 2013), improving the skill of the MAR runoff delay function is crucial for accurately estimating future peak runoff events. Furthermore, integration of more recent surface hydrology observations (Smith et al., 2015; Gleason et al., 2016) should be incorporated into the MAR runoff delay function, to modernize parameters currently applied (Lefebre et al., 2003) to simulate a realistic time lag for meltwater runoff transport from inception to outflow at the ice sheet margin.

Daily Q_M estimates are dampened, and therefore, do not capture peak daily Q_O events well (Fig. 4.2). This is best exemplified during the record-setting melt episode from 10-14 July 2012 impacting 97% of the ice sheet surface area (Nghiem et al., 2012). On 11 July 2012, Watson Q_O peaked at 3188.76 ± 478.31 m^3 s^{-1}. Similar Watson peak river discharge (~3100 m^3 s^{-1}) was recorded from other studies (van As et al., 2017; Mikkelsen et al., 2016). Yet, MAR underestimated this peak discharge event by ~19% (Fig. 4.2i). Similar underestimation of runoff on 12 July 2012 was found for the Thule basin, but by an extraordinary -110% (cf. Q_O of 141.12 ± 38.08 m^3 s^{-1} and Q_M of 67.05 ± 10.06 m^3 s^{-1}; Fig. 4.2e). Underestimation of modeled peak discharge events, like the mid-July 2012 melt event, has been acknowledged as problematic (Fausto et al., 2016). Fausto et al. (2016) found that the HIRHAM RCM underestimated melt rates up to 56% during exceptional melt episodes in July 2012, through an underestimation of turbulent energy fluxes. This highlights the importance of accurately quantifying turbulent flux terms in RCMs.

The Nuuk basin is an exception to the modeled peak discharge underestimation observed at the Thule and Watson basins. A reversed pattern of overestimation of modeled discharge at Nuuk was observed in 2012 (Fig. 4.2l), irrespective of extreme melt episodes (Fig. 4.2k-n). While Fausto et al. (2016) identified an underestimation in modeled (HIRHAM) melt at the NUK_U PROMICE station by 31% (no data available at NUK_L), our Nuuk PDD-derived meltwater production estimates indicate an overestimation at both NUK_L and NUK_U, corresponding to an overestimation in Q_M by ~48% on 10 July 2012 (cf. Q_O of 240.40 ± 134.65 m^3 s^{-1} and Q_M of 465.78 ± 69.87 m^3 s^{-1}). This suggests that the overestimation observed for the Nuuk basin during excessive melt and non-melt episodes cannot be explained by differences in nonradiative fluxes, but likely from uncertainties in drainage basin delineation (cf. Fig. 4.2k-n modeled runoff estimates for each flotation factor), uncertainties in river discharge collection, and radiative terms (see below). Evidence for uncertainties in the drainage basin delineation at Nuuk is indicated by the increasingly large basin area with flotation factor (Fig. 4.1c), and could be explained by errors in the surface or bedrock topography datasets (Howat et al., 2014; Morlighem et al., 2014). Alternative drainage basin delineation methods, such as the probability-based catchment method described in Carroll et al. (2016), should be investigated further and adopted to increase the range of likely drainage basin delineations further. However, better constraining of the local topography and better understanding of the basin's specific hydrologic transport pathways (e.g., van As et al., 2012; Fitzpatrick et al., 2014; Smith et al., 2015; Yang et al., 2016), and potential for water piracy may also be needed (Lindbäck et al., 2015). This method may be superior to drainage basins calculated based on bed and surface slope in regions with hydrologically-complex watersheds containing rapidly evolving supraglacial rivers, lakes, and fractures such as in west and southwest Greenland (e.g., van As et al., 2012; Fitzpatrick et al., 2014; Smith et al., 2015; Yang et al., 2016), such as the Watson River (van As et al., 2017; Lindbäck et al., 2015).

Radiative terms, particularly SWD, offer an additional explanation for model-observation discrepancies in discharge. The largest positive bias in discharge is observed at Nuuk and can be partly attributed to the model overestimation of SWD (up to ~35% at NUK_U; Table 4.6). This overestimation of SWD at Nuuk is likely due to an underestimation of cloud cover, and has been identified in the MAR (Fettweis et al., 2016) and RACMO2.3 (Van Tricht et al., 2016) models. Van Tricht et al. (2016) found that clouds have an impact of limiting meltwater refreezing and identify that the average cloud radiative effect is high over the Nuuk basin and near the ice sheet margin of the Watson basin, and slightly lower over the Thule basin (cf. Figure 4.2b in Van Tricht et al. (2016)). Van Tricht's et al. (2016) findings, despite its coarse resolution, are the first continental assessment of cloud radiative effects based on satellite observations.

This cloud radiative effect diminishes as we move inland and to higher elevations of western GrIS (van Tricht et al., 2016). This may explain why the Watson drainage basin exhibits the best agreement in model-observation discharge (Fig. 4.2f-j), and is linked to a smaller average error among the three basins (Table 4.6). Despite the large cloud radiative effect at the margin, the Watson basin extends far inland to a region with lower cloud radiative effect (Van Tricht et al., 2016), and which is known as one of the sunniest and driest areas in Greenland (van As et al., 2012). Despite the reasonable fit in Watson discharge, the KAN station data suggests cooler surface temperatures at lower elevations (KAN_L; Table 4.6), which would correspond to lower melt rates, as observed in our PDD melt totals (Fig. 4.7). This contradiction is puzzling as it doesn't fit the model-observation discharge results. Differences in model-observation discharge may be partly linked to uncertainties associated with river discharge measurements. Discharge observations at the Watson River are difficult, and has been revised several times (Hasholt et al., 2013; van As et al., 2017). Sub-glacial water piracy provides an additional means for explaining differences in model-observation discharge. Catchment piracy has been observed at the Watson River (Lindbäck et al, 2015), with the sub-glacial boundary temporarily widening to overlap almost 30% of a neighboring catchment during the melt season. However, the net area change due to water piracy occurred at high elevations and subsequent runoff increase of the Watson basin was small, and likely doesn't explain for large differences in model-observation discharge, even in a large basin area (van As et al., 2017). An alternative explanation to the model-observation discharge differences at Watson could be due to meltwater retention, as identified by several studies (e.g., Rennermalm et al. 2013; Smith et al., 2015; Overeem et al., 2015; Mikkelesen et al., 2016). However, during the exceptional melt year of 2012, meltwater retention was probably less than in other years due to the presence of perched superimposed ice layers (Machguth et al., 2016; Mikkelsen et al., 2016) that forced surface meltwater to run off in efficient, supraglacial channels. With more extreme melt episodes, a reduction in firn storage capacity, and the formation of thicker ice lens, future extreme melt events may result in more extraordinary, abrupt pulses of runoff to downstream proglacial rivers, and ultimately, to GrIS contributions to sea level rise.

Based on the model-observation results, the Thule basin is considered the best site for examining model-observation differences. This is supported by the nearly constant catchment delineations despite varying flotation factors (Fig. 4.1b). While all basin comparisons may suffer from model errors with simulated runoff and forcing variables, errors with in situ discharge observation, and drainage basin size, only the Thule basin minimizes the errors due to drainage basin size. The small variations in Thule basin size suggest that water piracy from adjacent catchments is not likely. Furthermore, the high flashiness of the Thule basin indicates that meltwater evacuates rapidly (Table 4.3), due to the small basin size, and is therefore ideal for assessing RCMs without a runoff delay function (e.g., RACMO and HIRHAM). These findings highlight the need for future river discharge analyses to find and compare model discharge with 'Thule-like' basins.

No systematic explanation for model-observation discrepancies can be identified at the three drainage basins (Figs. 4.4-4.6). However, some consistencies in modeled drivers of melt are observed. Across all PROMICE stations, we see a consistent overestimation in downwelling shortwave radiation, with the slight exception of the higher elevation KAN_U station, and consistent underestimation in downward longwave radiation (Table 4.6). Furthermore, MAR overestimates surface albedo at all elevations and sites (Table 4.6). These findings, with the exception of KAN_U SWD, are consistent with the findings of MAR v3.5.2 comparisons in Fettweis et al. (2016) and RACMO2.3 comparisons in Van Tricht et al. (2016). Yet, the MAR cold-bias of -0.65 °C observed in summer months in Fettweis et al. (2016) is at odds with our surface temperature findings

(Table 4.6). Instead, we observe a positive bias in MAR surface temperatures at middle and higher elevation stations (THU_U, KAN_M, KAN_U), and exceptional positive biases at both NUK stations. The different results may be partly attributed to the aggregation of all PROMICE stations in Fettweis et al. (2016), while our study provides an individual assessment of each station. The considerably large overestimation of surface temperature at NUK_L (~78%) is likely due to the station's low elevation (540 m), its location within the overlapping MAR grid cell (averaging surface temperatures of both land and ice), and its distance from the Nuuk basin (linear distance of ~42 km), contributing to a warm bias. A similar study comparing runoff from several basins in the Nuuk region with MAR v3.2 and RACMO2 RCMs, found no offset in downward shortwave radiation, an underestimation in downward longwave radiation, and an overestimation in surface albedo (van As et al., 2014). However, this study differs in that the drainage basins assessed are located north of our Nuuk basin (with different hydrometeorological conditions), discharge measurements were collected from Tasersuaq Lake, and used aggregated weather station data on- and off-ice from PROMICE and other operators including Danish Meteorological Institute, Asiaq (Greenland Survey), and Greenland airports (van As et al., 2014). Contrasting to our observed positive anomalies in surface temperatures and therefore PDD-derived melt at NUK_L (+1.7-3.0 m from 2011-2014), van As et al. (2014) models observed an underestimation in surface melt at NUK_L of 5-7 m yr^{-1}, equating to an underestimation of net ablation by ~30-50%. Despite these differences, van As et al. (2014) found good agreement in RACMO2 and MAR v3.2 model-observation runoff estimates and temporal variability at the basin scale, with the exception of high melt years (2010-2012; see Figure 4). While the MAR model contains a runoff delay, RACMO has yet to incorporate a runoff delay function. The Nuuk basin is a medium-sized basin (relative to Thule and Watson basins) and a moderate flashiness index (relative to Thule (highest R-B index) and Watson (lowest R-B index); Tables 4.3-4.5), indicative of a moderate time lag required. This time lag appears accurate as several hydrologic features have been identified in the Nuuk basin, including a dammed proglacial lake and several melt ponds (Overeem et al., 2015). Van As et al. (2014) found that basins North of our Nuuk basin, required a one-week delay for RACMO2 runoff. This one-week delay may be a good starting point for adopting and developing a more realistic time lag for our Nuuk basin, and may be a source for improving the correspondence between model-observation discharges (Fig. 4.2k-n).

A consistent modeled overestimation of bare ice albedo is observed at all sites (Table 4.6). This positive bias in albedo due to the absence of an impurity-albedo parameterization scheme in MAR v3.5.2, restricting albedo values to occur below 0.40 (Tedesco et al., 2016), despite values below 0.4 observed at the PROMICE stations (Figs. 4.4g, 4.5j-l, and 4.6g-h). Several studies recommend the improvement of the bare ice albedo scheme in MAR and other regional climate models, as it is one of the most important physical variables influencing SMB estimates (van Angelen et al., 2012; Tedesco et al., 2016; Fettweis et al., 2016). This study supports these recommendations and encourages future work to incorporate a spatiotemporally evolving bare ice albedo scheme, particularly in spatial heterogeneous regions of the ice sheet (e.g., lower ablation areas coinciding with lower PROMICE stations and the ‘dark band’ region of West Greenland; e.g., Moustafa et al., 2015), which takes into account an impurity scheme (e.g., cryoconite holes, dark ice, and melt ponds) and changes in biological activity (Chandler et al., 2015) into future MAR versions.

Based on the findings of this study, a more realistic MAR runoff delay function is needed to capture daily discharge variability at the basin-scale. This is particularly important for capturing peak discharge events, which are expected to become more frequent in the future. Improvements in radiative and albedo schemes as well as accurate cloud representations should be priorities in future versions of MAR and other RCMs. Similar drainage basins to the Thule basin should be identified and used for future comparison of model-observation discharge at the basin-scale. This study assessed the ability of MAR to simulate basin discharge, which is a widely used model to estimate current and future GrIS SMB. However, the framework used here should not just be applied to MAR, but should be used to examine other RCMs to improve the overall ability to constrain Greenland's contribution to global sea levels rise.

4.5 Conclusions

In this study, an inter-comparison between model-observation discharge at three basins located north-to-south in west Greenland is conducted. MAR poorly resolves daily discharge variability in the Nuuk and Thule basins (r^2 range of 0.41 to 0.55), but is better able to capture variability on 5-, 10-, and 20-day averages based on high ($r^2 > 0.70$) correlation coefficients. The variability in the Watson basin is well represented by MAR at all-time aggregations, but the fit increases somewhat with longer time averages. The agreement between model-observation discharge is reduced during peak discharge events, such as the exceptional melt season of 2012, for the Thule and Watson basins.

The peak discharge events are underestimated by as much as 110% and 19% at the Thule and Watson basins, on 11 and 12 July 2012, respectively. For the optimal drainage basin delineation, MAR overestimated discharge at the Thule and Nuuk basins, while the Watson basin obtained a good fit. The average error for all available observational years is 63.2%, 3%, and 101.5% of the mean JJA observed river discharge for Thule, Watson, and Nuuk, respectively.

No systematic explanation for discrepancies between model-observation discharge across the three sites is discernable. Comparison of model-observation discharge discrepancies are likely caused by an underestimation of cloud cover, brighter surface albedos than are actually realized on the ice sheet surface, and a frequent warm-bias in near-surface air temperatures. Despite these competing forces on melt and subsequent runoff, it appears that overestimation of downward shortwave fluxes dominated, contributing to the overestimation of discharge observed at the Thule and Nuuk basins.

Based on our findings, we determine that the Thule basin is the best site to examine model-observation differences because it has the smallest uncertainty in drainage basin extent, and additional ‘Thule-like’ catchments should be identified to further investigate modeled runoff at the basin-scale. The framework developed to assess MAR’s ability to assess SMB forcings and runoff across three basins should be applied to evaluate other RCMs. Given the strong, increasing trends in runoff dominating SMB, it is crucial to improve the radiative processes, surface albedo schemes and delay function in MAR given its importance for determining current and future estimates of runoff contributions to GrIS SMB.

4.6 References

Alexander, P. M., Tedesco, M., Fettweis, X., van de Wal, R. S. W., Smeets, C. J. P. P. and van den Broeke, M. R.: Assessing spatio-temporal variability and trends (2000–2013) of modelled and measured Greenland ice sheet albedo, Cryosph. Discuss., 8(4), 3733–3783, doi:10.5194/tcd-8-3733-2014, 2014.

Alexander, P. M., Tedesco, M., Schlegel, N.-J., Luthcke, S. B., Fettweis, X. and Larour, E.: Greenland Ice Sheet seasonal and spatial mass variability from model simulations and GRACE (2003–2012), Cryosph., 10(3), 1259–1277, doi:10.5194/tc-10-1259-2016, 2016.

van Angelen, J. H., Lenaerts, J. T. M., Lhermitte, S., Fettweis, X., Kuipers Munneke, P., van den Broeke, M. R., van Meijgaard, E. and Smeets, C. J. P. P.: Sensitivity of Greenland Ice Sheet surface mass balance to surface albedo parameterization: a study with a regional climate model, Cryosph., 6(5), 1175–1186, doi:10.5194/tc-6-1175-2012, 2012.

van Angelen, J. H., M. Lenaerts, J. T., van den Broeke, M. R., Fettweis, X. and van Meijgaard, E.: Rapid loss of firn pore space accelerates 21st century Greenland mass loss, Geophys. Res. Lett., 40(10), 2109–2113, doi:10.1002/grl.50490, 2013.

van As, D., Hubbard, a. L., Hasholt, B., Mikkelsen, a. B., van den Broeke, M. R. and Fausto, R. S.: Large surface meltwater discharge from the Kangerlussuaq sector of the Greenland ice sheet during the record-warm year 2010 explained by detailed energy balance observations, Cryosph., 6(1), 199–209, doi:10.5194/tc-6-199-2012, 2012.

Van As, D., Andersen, M. L., Petersen, D., Fettweis, X., Van Angelen, J. H., Lenaerts, J. T. M., Van Den Broeke, M. R., Lea, J. M., Bøggild, C. E., Ahlstrøm, A. P. and Steffen, K.: Increasing meltwater discharge from the Nuuk region of the Greenland ice sheet and implications for mass balance (1960-2012), J. Glaciol., 60(220), 314–322, doi:10.3189/2014JoG13J065, 2014.

van As, D., Bech Mikkelsen, A., Holtegaard Nielsen, M., Box, J., Claesson Liljedahl, L., Lindbäck, K., Pitcher, L. and Hasholt, B.: Hypsometric amplification and routing moderation of Greenland ice sheet meltwater release, Cryosph. Discuss., (January), 1–30, doi:10.5194/tc-2016-285, 2017.

Bamber, J. L., Griggs, J. A., Hurkmans, R. T. W. L., Dowdeswell, J. A., Gogineni, S. P., Howat, I., Mouginot, J., Paden, J., Palmer, S., Rignot, E. and Steinhage, D.: A new bed elevation dataset for Greenland, Cryosph., 7(2), 499–510, doi:10.5194/tc-7-499-2013, 2013.

Bartholomew, I., Nienow, P., Sole, A., Mair, D., Cowton, T., Palmer, S. and Wadham, J.: Supraglacial forcing of subglacial drainage in the ablation zone of the Greenland ice sheet, Geophys. Res. Lett., 38(8), n/a-n/a, doi:10.1029/2011GL047063, 2011.

van den Broeke, M. R., Enderlin, E. M., Howat, I. M., Kuipers Munneke, P., Noël, B. P. Y., van de Berg, W. J., van Meijgaard, E. and Wouters, B.: On the recent contribution of the Greenland ice sheet to sea level change, Cryosph., 10(5), 1933–1946, doi:10.5194/tc-

10-1933-2016, 2016.

Brun, E., David, P., Sudul, M. and Brunot, G.: A nutnerical tnodel to simulate snow-cover stratigraphy for operational avalanche forecasting, J. Glaciol., 38(128), 13–22, 1992.

Box, J. E., Fettweis, X., Stroeve, J. C., Tedesco, M., Hall, D. K. and Steffen, K.: Greenland ice sheet albedo feedback: thermodynamics and atmospheric drivers, Cryosph. Discuss., 6(1), 593–634, doi:10.5194/tcd-6-593-2012, 2012.

Brun, E., David, P., Sudul, M. and Brunot, G.: A nutnerical tnodel to simulate snow-cover stratigraphy for operational avalanche forecasting, J. Glaciol., 38(128), 13–22, 1992.

Butkovich, T. R.: Thermal Expansion of Ice, Journal of Applied Physics, 30(3), 350-353, 1959.

Chandler, D. M., Alcock, J. D., Wadham, J. L., Mackie, S. L. and Telling, J.: Seasonal changes of ice surface characteristics and productivity in the ablation zone of the Greenland Ice Sheet, Cryosph., 9(2), 487–504, doi:10.5194/tc-9-487-2015, 2015.

Charalampidis, C., Van As, D., Box, J. E., Van Den Broeke, M. R., Colgan, W. T., Doyle, S. H., Hubbard, A. L., MacFerrin, M., Machguth, H. and P. Smeets, C. J. P.: Changing surface-atmosphere energy exchange and refreezing capacity of the lower accumulation area, West Greenland, Cryosphere, 9(6), 2163–2181, doi:10.5194/tc-9-2163-2015, 2015.

Chen, J. L., Wilson, C. R. and Tapley, B. D.: Interannual variability of Greenland ice losses from satellite gravimetry, J. Geophys. Res., 116(B7), B07406, doi:10.1029/2010JB007789, 2011.

Cuffey, K. and Paterson,W. S. B.: The Physics of Glaciers, 4th Edn., Elsevier Inc., Burlington and Oxford, 2010.

Cullather, R. I., Nowicki, S. M. J., Zhao, B. and Koenig, L. S.: A Characterization of Greenland Ice Sheet Surface Melt and Runoff in Contemporary Reanalyses and a Regional Climate Model, Front. Earth Sci., 4(February), 1–20, doi:10.3389/feart.2016.00010, 2016.

Dee, D. P., Uppala, S. M., Simmons, A. J., Berrisford, P., Poli, P., Kobayashi, S., Andrae, U., Balmaseda, M. A., Balsamo, G., Bauer, P., Bechtold, P., Beljaars, A. C. M., van de Berg, L., Bidlot, J., Bormann, N., Delsol, C., Dragani, R., Fuentes, M., Geer, A. J., Haimberger, L., Healy, S. B., Hersbach, H., H??lm, E. V., Isaksen, L., K??llberg, P., K??hler, M., Matricardi, M., Mcnally, A. P., Monge-Sanz, B. M., Morcrette, J. J., Park, B. K., Peubey, C., de Rosnay, P., Tavolato, C., Th??paut, J. N. and Vitart, F.: The ERA-Interim reanalysis: Configuration and performance of the data assimilation system, Q. J. R. Meteorol. Soc., 137(656), 553–597, doi:10.1002/qj.828, 2011.

De Ridder, K. and Gallée, H.: Land surface-induced regional climate change in Southern Israel, J. Appl. Meteorol., 37, 1470–1485, doi:10.1175/1520 0450(1998)037<1470:LSIRCC>2.0.CO;2, 1998.

Dingman, S. L.: Physical hydrology, Waveland press, 2015.

Enderlin, E. M., Howat, I. M., Jeong, S., Noh, M.-J., van Angelen, J. H. and van den Broeke, M. R.: An improved mass budget for the Greenland ice sheet, Geophys. Res. Lett., 41(3), 866–872, doi:10.1002/2013GL059010, 2014.

Ettema, J., van den Broeke, M. R., van Meijgaard, E., van de Berg, W. J., Bamber, J. L., Box, J. E. and Bales, R. C.: Higher surface mass balance of the Greenland ice sheet revealed by high-resolution climate modeling, Geophys. Res. Lett., 36(12), L12501, doi:10.1029/2009GL038110, 2009.

Fausto, R. S., van As, D., Box, J. E., Colgan, W., Langen, P. L. and Mottram, R. H.: The implication of nonradiative energy fluxes dominating Greenland ice sheet exceptional ablation area surface melt in 2012, Geophys. Res. Lett., (April), doi:10.1002/2016GL067720, 2016.

Fettweis, X., Gallée, H., Lefebre, F. and van Ypersele, J. P.: Greenland surface mass balance simulated by a regional climate model and comparison with satellite-derived data in 1990-1991, Clim. Dyn., 24(6), 623–640, doi:10.1007/s00382-005-0010-y, 2005.

Fettweis, X.: Reconstruction of the 1979–2006 Greenland ice sheet surface mass balance using the regional climate model MAR, Cryosph., 1, 21–40, doi:10.5194/tcd-1-123-2007, 2007.

Fettweis, X., Mabille, G., Erpicum, M., Nicolay, S. and den Broeke, M. Van: The 1958–2009 Greenland ice sheet surface melt and the mid-tropospheric atmospheric circulation, Clim. Dyn., 36(1–2), 139–159, doi:10.1007/s00382-010-0772-8, 2011.

Fettweis, X., Franco, B., Tedesco, M., van Angelen, J. H., Lenaerts, J. T. M., van den Broeke, M. R. and Gallée, H.: Estimating the Greenland ice sheet surface mass balance contribution to future sea level rise using the regional atmospheric climate model MAR, Cryosph., 7(2), 469–489, doi:10.5194/tc-7-469-2013, 2013.

Fettweis, X., Box, J. E., Agosta, C., Amory, C., Kittel, C. and Gallée, H.: Reconstructions of the 1900–2015 Greenland ice sheet surface mass balance using the regional climate MAR model, Cryosph. Discuss., (November), 1–32, doi:10.5194/tc-2016-268, 2016.

Forster, R. R., Box, J. E., van den Broeke, M. R., Miège, C., Burgess, E. W., van Angelen, J. H., Lenaerts, J. T. M., Koenig, L. S., Paden, J., Lewis, C., Gogineni, S. P., Leuschen, C. and McConnell, J. R.: Extensive liquid meltwater storage in firn within the Greenland ice sheet, Nat. Geosci., 7(12), 1–4, doi:10.1038/ngeo2043, 2013.

Gleason, C. J., Smith, L. C., Chu, V. W., Legleiter, C. J., Pitcher, L. H., Overstreet, B. T., Rennermalm, A. K., Forster, R. R. and Yang, K.: Characterizing supraglacial meltwater channel hydraulics on the Greenland Ice Sheet from in situ observations, Earth Surf. Process. Landforms, 41(14), 2111–2122, doi:10.1002/esp.3977, 2016.

Hall, D. K., Comiso, J. C., DiGirolamo, N. E., Shuman, C. a., Box, J. E. and Koenig, L. S.: Variability in the surface temperature and melt extent of the Greenland ice sheet from MODIS, Geophys. Res. Lett., 40(10), 2114–2120, doi:10.1002/grl.50240, 2013.

Hanna, E., Navarro, F. J., Pattyn, F., Domingues, C. M., Fettweis, X., Ivins, E. R., Nicholls, R. J., Ritz, C., Smith, B., Tulaczyk, S., Whitehouse, P. L. and Zwally, H. J.: Ice-sheet mass balance and climate change, Nature, 498(7452), 51–59, doi:10.1038/nature12238, 2013.

Hasholt, B., Bech Mikkelsen, A., Holtegaard Nielsen, M. and Andreas Dahl Larsen, M.: Observations of Runoff and Sediment and Dissolved Loads from the Greenland Ice Sheet at Kangerlussuaq, West Greenland, 2007 to 2010, Zeitschrift für Geomorphol. Suppl. Issues, 57(2), 3–27, doi:10.1127/0372-8854/2012/S-00121, 2013.

Hock, R.: Glacier melt: a review of processes and their modelling, Prog. Phys. Geogr., 29(3), 362–391, doi:10.1191/0309133305pp453ra, 2005.

Koenig, L. S., Miège, C., Forster, R. R. and Brucker, L.: Initial in situ measurements of perennial meltwater storage in the Greenland firn aquifer, Geophys. Res. Lett., 41, 1–5, doi:10.1002/2013GL058083, 2014.

Lefebre, F., Gallée, H., vanYpersele, J. and Greuell, W.: Modeling of snow and ice melt at ETH Camp (West Greenland): A study of surface albedo, J. Geophys. Res., 108, 4231, doi:10.1029/2001JD001160, 2003.

Lindbäck, K., Pettersson, R., Hubbard, A. L., Doyle, S. H., van As, D., Mikkelsen, A. B. and Fitzpatrick, A. A.: Subglacial water drainage, storage, and piracy beneath the Greenland ice sheet, Geophys. Res. Lett., 42(18), 7606–7614, doi:10.1002/2015GL065393, 2015.

Machguth, H., MacFerrin, M., van As, D., Box, J. E., Charalampidis, C., Colgan, W., Fausto, R. S., Meijer, H. A. J., Mosley-Thompson, E. and van de Wal, R. S. W.: Greenland meltwater storage in firn limited by near-surface ice formation, Nat. Clim. Chang., advance on(January), 1–6, doi:10.1038/nclimate2899, 2016.

McGrath, D., Colgan, W., Bayou, N., Muto, A. and Steffen, K.: Recent warming at Summit, Greenland: Global context and implications, Geophys. Res. Lett., 40(10), 2091–2096, doi:10.1002/grl.50456, 2013.

Mernild, S. H., Liston, G. E., Hiemstra, C. a. and Christensen, J. H.: Greenland Ice Sheet Surface Mass-Balance Modeling in a 131-Yr Perspective, 1950–2080, J. Hydrometeorol., 11(1), 3–25, doi:10.1175/2009JHM1140.1, 2010.

Mikkelsen, A. B., Hubbard, A., Macferrin, M., Eric Box, J., Doyle, S. H., Fitzpatrick, A., Hasholt, B., Bailey, H. L., Lindbäck, K. and Pettersson, R.: Extraordinary runoff from the Greenland ice sheet in 2012 amplified by hypsometry and depleted firn retention, Cryosphere, 10(3), 1147–1159, doi:10.5194/tc-10-1147-2016, 2016.

Morlighem, M., Rignot, E., Mouginot, J., Seroussi, H. and Larour, E.: Deeply incised submarine glacial valleys beneath the Greenland ice sheet, Nat. Geosci., 7(6), 418–422, doi:10.1038/ngeo2167, 2014.

Moustafa, S. E., Rennermalm, A. K., Smith, L. C., Miller, M. A., Mioduszewski, J. R., Koenig, L. S., Hom, M. G. and Shuman, C. A.: Multi-modal albedo distributions in the ablation area of the southwestern Greenland Ice Sheet, Cryosphere, 9(3), 905–923, doi:10.5194/tc-9-905-2015, 2015.

Nghiem, S. V., Hall, D. K., Mote, T. L., Tedesco, M., Albert, M. R., Keegan, K., Shuman, C. A., DiGirolamo, N. E. and Neumann, G.: The extreme melt across the Greenland ice sheet in 2012, Geophys. Res. Lett., 39(20), 1–6, doi:10.1029/2012GL053611, 2012.

Ohmura, A.: Physical Basis for the Temperature-Based Melt-Index Method, J. Appl. Meteorol., 40(4), 753–761, doi:10.1175/1520-0450(2001)040<0753:PBFTTB>2.0.CO;2, 2001.

Overeem, I., Hudson, B., Welty, E., Mikkelsen, A., Bamber, J., Petersen, D., Lewinter, A. and Hasholt, B.: River inundation suggests ice-sheet runoff retention, J. Glaciol., 61(228), 776–788, doi:10.3189/2015JoG15J012, 2015.

de la Peña, S., Howat, I. M., Nienow, P. W., van den Broeke, M. R., Mosley-Thompson, E., Price, S. F., Mair, D., Noël, B. and Sole, a. J.: Changes in the firn structure of the western Greenland Ice Sheet caused by recent warming, Cryosph., 9(3), 1203–1211, doi:10.5194/tc-9-1203-2015, 2015.

Pritchard, H. D., Arthern, R. J., Vaughan, D. G. and Edwards, L. a: Extensive dynamic thinning on the margins of the Greenland and Antarctic ice sheets., Nature, 461(7266), 971–5, doi:10.1038/nature08471, 2009.

Rae, J. G. L., Aðalgeirsdóttir, G., Edwards, T. L., Fettweis, X., Gregory, J. M., Hewitt, H. T., Lowe, J. a., Lucas-Picher, P., Mottram, R. H., Payne, a. J., Ridley, J. K., Shannon, S. R., van de Berg, W. J., van de Wal, R. S. W. and van den Broeke, M. R.: Greenland ice sheet surface mass balance: evaluating simulations and making projections with regional climate models, Cryosph. Discuss., 6(3), 2059–2113, doi:10.5194/tcd-6-2059-2012, 2012.

Reijmer, C. H., van den Broeke, M. R., Fettweis, X., Ettema, J. and Stap, L. B.: Refreezing on the Greenland ice sheet: a comparison of parameterizations, Cryosph., 6(4), 743–762, doi:10.5194/tc-6-743-2012, 2012.

Rennermalm, A. K., Smith, L. C., Chu, V. W., Forster, R. R., Box, J. E. and Hagedorn, B.: Proglacial river stage, discharge, and temperature datasets from the Akuliarusiarsuup Kuua River northern tributary, Southwest Greenland, 2008–2011, Earth Syst. Sci. Data, 4(1), 1–12, doi:10.5194/essd-4-1-2012, 2012.

Rennermalm, A. K., Smith, L. C., Chu, V. W., Box, J. E., Forster, R. R., Van den Broeke, M. R., Van As, D. and Moustafa, S. E.: Evidence of meltwater retention within the Greenland ice sheet, Cryosph., 7(5), 1433–1445, doi:10.5194/tc-7-1433-2013, 2013.

Rennermalm, A. K., et al., Drainage basin delineation, in preparation, 2017.

Ridder, K. De and Schayes, G.: The IAGL Land Surface Model, J. Appl. Meteorol., 36(2), 167–182, doi:10.1175/1520-0450(1997)036<0167:TILSM>2.0.CO;2, 1997.

Selmes, N., Murray, T. and James, T. D.: Fast draining lakes on the Greenland Ice Sheet, Geophys. Res. Lett., 38(15), n/a-n/a, doi:10.1029/2011GL047872, 2011.

Shepherd, A., Ivins, E. R., A, G., Barletta, V. R., Bentley, M. J., Bettadpur, S., Briggs, K. H., Bromwich, D. H., Forsberg, R., Galin, N., Horwath, M., Jacobs, S., Joughin, I., King, M. a, Lenaerts, J. T. M., Li, J., Ligtenberg, S. R. M., Luckman, A., Luthcke, S. B., McMillan, M., Meister, R., Milne, G., Mouginot, J., Muir, A., Nicolas, J. P., Paden, J., Payne, A. J., Pritchard, H., Rignot, E., Rott, H., Sørensen, L. S., Scambos, T. a, Scheuchl, B., Schrama, E. J. O., Smith, B., Sundal, A. V, van Angelen, J. H., van de Berg, W. J., van den Broeke, M. R., Vaughan, D. G., Velicogna, I., Wahr, J., Whitehouse, P. L., Wingham, D. J., Yi, D., Young, D. and Zwally, H. J.: A reconciled estimate of ice-sheet mass balance., Science (80-.)., 338(6111), 1183–9, doi:10.1126/science.1228102, 2012.

Smith, L. C., Chu, V. W., Yang, K., Gleason, C. J., Pitcher, L. H., Rennermalm, A. K., Legleiter, C. J., Behar, A. E., Overstreet, B. T., Moustafa, S. E., Tedesco, M., Forster, R. R., LeWinter, A. L., Finnegan, D. C., Sheng, Y. and Balog, J.: Efficient meltwater drainage through supraglacial streams and rivers on the southwest Greenland ice sheet, Proc. Natl. Acad. Sci., 112(4), 1001–1006, doi:10.1073/pnas.1413024112, 2015.

TC, 2007, Hydrometry, Subcommittee SC 1, Velocity area methods. ISO 748:2007(en) Hydrometry—Measurement of liquid flow in open channels using current-meters or floats.

Tedesco, M.: Snowmelt detection over the Greenland ice sheet from SSM/I brightness temperature daily variations, Geophys. Res. Lett., 34(2), 1–6, doi:10.1029/2006GL028466, 2007.

Tedesco, M., Fettweis, X., van den Broeke, M. R., van de Wal, R. S. W., Smeets, C. J. P. P., van de Berg, W. J., Serreze, M. C. and Box, J. E.: The role of albedo and accumulation in the 2010 melting record in Greenland, Environ. Res. Lett., 6(1), 14005, doi:10.1088/1748-9326/6/1/014005, 2011.

Tedesco, M., Fettweis, X., Mote, T., Wahr, J., Alexander, P., Box, J. E. and Wouters, B.: Evidence and analysis of 2012 Greenland records from spaceborne observations, a regional climate model and reanalysis data, Cryosph., 7(2), 615–630, doi:10.5194/tc-7-615-2013, 2013.

Tedesco, M., Mote, T., Fettweis, X., Hanna, E., Jeyaratnam, J., Booth, J. F., Datta, R. and Briggs, K.: Arctic cut-off high drives the poleward shift of a new Greenland melting record, Nat. Commun., 7(11723), 6pp, doi:10.1038/ncomms11723, 2016.

Van Tricht, K., Lhermitte, S., Lenaerts, J. T. M., Gorodetskaya, I. V, L'Ecuyer, T. S., Noël, B., van den Broeke, M. R., Turner, D. D. and van Lipzig, N. P. M.: Clouds enhance Greenland ice sheet meltwater runoff, Nat. Commun., 7(May), 10266, doi:10.1038/ncomms10266, 2016.

Screen, J. a and Simmonds, I.: The central role of diminishing sea ice in recent Arctic temperature amplification, Nature, 464(7293), 1334–1337, doi:10.1038/nature09051, 2010.

Smith, L. C., Chu, V. W., Yang, K., Gleason, C. J., Pitcher, L. H., Rennermalm, A. K., Legleiter, C. J., Behar, A. E., Overstreet, B. T., Moustafa, S. E., Tedesco, M., Forster, R. R., LeWinter, A. L., Finnegan, D. C., Sheng, Y. and Balog, J.: Efficient meltwater drainage through supraglacial streams and rivers on the southwest Greenland ice sheet, Proc. Natl. Acad. Sci., 112(4), 1001–1006, doi:10.1073/pnas.1413024112, 2015.

Steffen, K. and Box, J.: Surface climatology of the Greenland ice sheet: Greenland Climate Network 1995-1999, J. Geophys. Res., 106(D24), 33951–33964, 2001.

Stroeve, J., Box, J. E., Gao, F., Liang, S., Nolin, A. and Schaaf, C.: Accuracy assessment of the MODIS 16-day albedo product for snow: comparisons with Greenland in situ measurements, Remote Sens. Environ., 94(1), 46–60, doi:10.1016/j.rse.2004.09.001, 2005.

Stroeve, J. C., Box, J. E. and Haran, T.: Evaluation of the MODIS (MOD10A1) daily snow albedo product over the Greenland ice sheet, Remote Sens. Environ., 105(2), 155–171, doi:10.1016/j.rse.2006.06.009, 2006.

Stroeve, J., Box, J. E., Wang, Z., Schaaf, C. and Barrett, A.: Re-evaluation of MODIS MCD43 Greenland albedo accuracy and trends, Remote Sens. Environ., 138, 199–214, doi:10.1016/j.rse.2013.07.023, 2013.

Tedesco, M.: Snowmelt detection over the Greenland ice sheet from SSM/I brightness temperature daily variations, Geophys. Res. Lett., 34(2), 1–6, doi:10.1029/2006GL028466, 2007.

Tedesco, M., Fettweis, X., van den Broeke, M. R., van de Wal, R. S. W., Smeets, C. J. P. P., van de Berg, W. J., Serreze, M. C. and Box, J. E.: The role of albedo and accumulation in the 2010 melting record in Greenland, Environ. Res. Lett., 6(1), 14005, doi:10.1088/1748-9326/6/1/014005, 2011.

Tedesco, M., Fettweis, X., Mote, T., Wahr, J., Alexander, P., Box, J. E. and Wouters, B.: Evidence and analysis of 2012 Greenland records from spaceborne observations, a regional climate model and reanalysis data, Cryosph., 7(2), 615–630, doi:10.5194/tc-7-615-2013, 2013.

Tedesco, M., Mote, T., Fettweis, X., Hanna, E., Jeyaratnam, J., Booth, J. F., Datta, R. and Briggs, K.: Arctic cut-off high drives the poleward shift of a new Greenland melting record, Nat. Commun., 7(11723), 6pp, doi:10.1038/ncomms11723, 2016.

Van Tricht, K., Lhermitte, S., Lenaerts, J. T. M., Gorodetskaya, I. V, L'Ecuyer, T. S., Noël, B., van den Broeke, M. R., Turner, D. D. and van Lipzig, N. P. M.: Clouds enhance Greenland ice sheet meltwater runoff, Nat. Commun., 7(May), 10266, doi:10.1038/ncomms10266, 2016.

Vaughan, D.G., J.C. Comiso, I. Allison, J. Carrasco, G. Kaser, R. Kwok, P. Mote, T. Murray, F. Paul, J. Ren, E. Rignot, O. Solomina, K. Steffen and T. Zhang, 2013: Observations: Cryosphere. In: Climate Change 2013: The Physical Science Basis. Contribution of Working Group I to the Fifth Assessment Report of the Intergovernmental Panel on Climate Change [Stocker, T.F., D. Qin, G.-K. Plattner, M. Tignor, S.K. Allen, J. Boschung, A. Nauels, Y. Xia, V. Bex and P.M. Midgley (eds.)]. Cambridge University Press, Cambridge, United Kingdom and New York, NY, USA.

Vernon, C. L., Bamber, J. L., Box, J. E., van den Broeke, M. R., Fettweis, X., Hanna, E.

and Huybrechts, P.: Surface mass balance model intercomparison for the Greenland ice sheet, Cryosph., 7(2), 599–614, doi:10.5194/tc-7-599-2013, 2013.

Vionnet, V., Brun, E., Morin, S., Boone, A., Faroux, S., Le Moigne, P., Martin, E. and Willemet, J. M.: The detailed snowpack scheme Crocus and its implementation in SURFEX v7.2, Geosci. Model Dev., 5(3), 773–791, doi:10.5194/gmd-5-773-2012, 2012.

van de Wal, R. S. W., Boot, W., Smeets, C. J. P. P., Snellen, H., van den Broeke, M. R. and Oerlemans, J.: Twenty-one years of mass balance observations along the K-transect, West Greenland, Earth Syst. Sci. Data, 4(1), 31–35, doi:10.5194/essd-4-31-2012, 2012.

Zuo, Z. and Oerlemans, J.: Modelling albedo and specific balance of the Greenland ice sheet: Calculations for the Søndre Strømfjord transect, J. Glaciol., 42(141), 305–316, doi:10.3198/1996JoG42-141-305-317, 1996.

Chapter 5: Record discharge from three Greenland ice sheet drainage basins in 2012

5.1. Introduction

The extreme melt year of 2012 on the Greenland ice sheet (GrIS) has been documented by numerous modeling, climatology, remote sensing, and observational studies (Nghiem et al., 2012; Hall et al., 2013; Bennartz et al., 2013; Tedesco et al., 2013b; Smith et al., 2015; Fausto et al., 2016; Mikkelsen et al., 2016; McGrath et al., 2013). Summer 2012 was marked by two extreme melt episodes that covered ~98.6% (~79.2%) of the ice sheet surface on 12 (29) July 2012 (Nghiem et al., 2012), extending to the upper elevations of the ice divide (McGrath et al., 2013). A blocking high pressure system, corresponding to a strong, negative summer North Atlantic Oscillation (NAO) anomaly (-2.4 standard deviations below the NAO average for JJA in 1981-2010) contributed to the exceptional melt observed (Hanna et al., 2014; Overland et al., 2012; Box et al., 2013). This caused warm southerly air flow to advect over west Greenland that promoted spatiotemporally-extensive melting (Box et al., 2013), record-setting temperatures to be observed (Hall et al., 2013), and surface albedo two standard deviations below the 2003-2012 average (Tedesco et al., 2013b), contributing to unprecedented mass loss, and subsequent sea level rise equivalent of 1.2 mm (van den Broeke et al., 2016). The same blocking high pressure pattern has been observed in prior high melt years, including summers 2007 and 2010 (Box et al., 2013). Low-level liquid clouds (Bennartz et al., 2013) and turbulent heat fluxes (Fausto et al., 2016) contributed to the exceptional melt in 2012.

Several studies have evaluated proglacial discharge in 2012 in the Watson (Overeem et al., 2015; Mikkelsen et al., 2016; van As et al., 2017) and Isortoq Rivers (Smith et al., 2015) in southwest Greenland. Additional studies of proglacial discharge in 2012 were conducted in south Greenland in the Naujat Kuat River (Overeem et al., 2015) and Tasersuaq Lake (van As et al., 2014). Mikkelsen et al. (2016) and van As et al. (2017) found that runoff from the Watson River in 2012 was amplified by catchment hypsometry and impenetrable superimposed ice layers in the percolation zone. The 2012 extreme melt conditions revealed the importance of supraglacial river features for efficiently channelizing meltwater drainage as observed from time-lapse camera and high resolution satellite imagery (Smith et al., 2015) and the potential for considerable storage mechanisms (Overeem et al., 2015) and meltwater generation in the Nuuk region (>50 km^3 in 2012; van As et al., 2014). Evaluating the extreme melt year of 2012 is important, as extreme events are expected to become more frequent with anticipated anthropogenic atmospheric warming (McGarth et al., 2013). No previous study have examined how the extreme melt year of 2012 manifested itself across multiple river drainage basins

In this study, we investigate the extreme melt season of 2012 by quantifying river discharge at three sites, located north-to-south, in west Greenland. An inter-comparison of river discharge from three drainage basins – Thule, Watson, and Nuuk is conducted. Peak discharge events are identified and the timing of these events is compared. The covariance of primary drivers of melt with peak discharge events is examined. Finally, the spatial distribution of large atmospheric circulation patterns is co-located with variations in drainage basin discharge.

5.1.1. Overview of the water transport pathway from the ice sheet surface to proglacial rivers

The GrIS is experiencing an increasing negative trend in surface mass balance (SMB) driven by increases in runoff (Enderlin et al., 2014). Meltwater runoff has increased its rate from 1.3 ± 1.1 Gt yr^{-2} in 1961-1990 to 8.4 ± 2.3 Gt yr^{-2} in 1991-2015 (van den Broeke et al., 2016). The increase in meltwater runoff impacts not only Greenland's SMB and therefore sea level rise, but also affects supraglacial, englacial, and subglacial processes. Persistent melting affects local surface processes such as the albedo-melt feedback, reducing surface albedo, leading to an increase in the absorption of incoming solar radiation, which further enhances melting (Box et al., 2012). In the lower accumulation zone, the percolation zone retains and refreezes a portion of the meltwater that is generated, increasing its density in firn layers (e.g., Harper et al., 2012). The percolation zone has been identified as a buffering mechanism, capable of offsetting future sea level rise (Pfeffer et al., 1991; Harper et al. 2012). However, a recent study by de la Peña et al. (2015) found a steep increase in firn-ice content, which decreases the capacity of the percolation zone to retain meltwater. This is confounded by the occurrence of more supraglacial lake features at higher elevations (Banwell et al., 2012; Leeson et al., 2015).

Below the equilibrium line, in the summer months, meltwater runs off into supraglacial rivers (Smith et al., 2015) or is temporarily stored in lower elevation supraglacial lakes. Some supraglacial lakes overflow or drain rapidly into the sub-glacial environment (e.g., Doyle et al., 2013; Tedesco et al., 2013a; Palmer et al., 2015). Alternatively, meltwater intersects with moulins, crevasses and ice fractures. Meltwater that runs off into en- and sub-glacial systems can influence ice sheet dynamics (e.g., Zwally et al., 2002; Sundal et al., 2011; Tedstone et al., 2013; Stevens et al., 2016). Some of this meltwater evacuates from the ice sheet margin, contributing to downstream proglacial river discharge. Proglacial river discharge includes contributions from both melt- and rain-water that is not retained in the supra-, en-, sub-glacial systems and lost to evaporation or groundwater systems.

5.2 Data and Methods

5.2.1 In situ discharge data

Proglacial river discharge was measured at three basins, Thule, Watson, and Nuuk, from north-to-south (*see Fig. 4.1*). Discharge at each of these sites were collected using different methods as described below. In this study, river discharge is presented in this study as a daily average in units of m^3 s^{-1}.

5.2.2 Thule

The North River, located in the northern part of the Pituffik Peninsula in Northwest Greenland (*Fig. 4.1b*), is referred to as the Thule basin in this study. Proglacial discharge measurements and river stage were collected from a bridge 20 km west of the ice sheet edge, along the North River near the Thule Air Base (*Fig. 4.1b*) in 2012. River stage was measured every 5 to 15 minutes using a Campbell radar instrument attached 8 m above the stream bed. River stage measurements were collected throughout the melt season to capture a range of stages to construct a rating curve (e.g. Dingman, 2015). Two different methods were used to collect discharge, depending upon stage levels: 1) at low and medium river stage, observations were made with the velocity-area method (TC, 2007); and 2) at high river stage (>1.2 m), observations were conducted using the float method to measure surface velocity, and assuming a uniform velocity profile. About twelve discharge measurements were collected and combined to produce a rating curve. Using an error propagation method similar to Rennermalm et al. (2012), the combined estimated discharge error is 27%.

5.2.3 Watson

The Watson River drains the land-terminating Kangerlussuaq sector of the western GrIS (*Fig. 4.1d*). Stage height were recorded nearby the Watson River Bridge in Kangerlussuaq, about 22 km from the ice sheet edge (Hasholt et al., 2013). The dataset has been revised several times as new and more precise discharge observations have been employed (van As et al., 2017). Using pressure transducers, river level was measured and recorded as hourly averages. Discharge measurements were collected across a range of stage heights to produce a rating curve. Three methods were used to construct a stage-discharge relationship, and are detailed in van As et al., (2017). An uncertainty value of 15% is assigned to all Watson river discharge measurements.

5.2.4 Nuuk

The Naujat Kuat River, hereafter referred to as the Nuuk basin, is located 11 km from the ice sheet margin, in south Greenland, draining a mix of tundra (63-75%; Overeem et al., 2015) and upstream ice area (*Fig. 4.1c*). The river drains into the Ameragdla fjord, a tributary of the Lyseefjord, located south of Greenland's capital, Nuuk. Here, discharge observations are from Overeem et al. (2015).

Discharge measurements were continuously collected from the Naujat Kuat River in 2012, with a hiatus from 1 to 12 June. Stage height was measured with a Campbell sonic ranger and sampled hourly. Velocity measurements were collected with the float method and water surface slope from a site visit in August 2012. River cross-sectional area was computed using a 3D bedrock constriction model from four photographs taken on 6 April 2012 during very low flow. Photographs were processed in a structure-from-motion package (Bundler and Patch-based Multi-view Stereo Software) to produce a dense point cloud. Using identifiable ground reference points (e.g., boulder), the model was scaled, to produce a final 2D cross-sectional area. A stage-discharge relationship was determined using both in situ and modeled estimates. Model estimates were included to augment sparse in situ stage-discharge measurements and to overcome turbulent river flow conditions. Modeled stage-discharge estimates were calculated using a fluid-mechanics model (Kean and Smith, 2005; Kean and Smith, 2010). Channel geometry, channel roughness, and water surface slope from the model were used to estimate cross-sectional velocity and discharge from stage height observations. A set of sensitivity experiments were conducted for each cross section, and the model was iterated over a range of channel roughness and slope values. The sensitivity experiment that best fit the observed stage-discharge relationship was used. With a limited observational record and uncertainties in model parameterization, the sensitivity experiments estimate discharge uncertainty at 56%. More details are provided in Overeem et al. (2015).

5.2.5 Inter-comparison of river discharge

An inter-comparison of river discharge is conducted to examine outflow at each basin during summer melt season (JJA) 2012. Through time series analysis, peak discharge events are identified; magnitudes and timing at each respective basin are compared. To compare seasonal (JJA) flow relative to previous melt years (here, available discharge years included: Thule from 2004-2006 and 2011-2012; Watson from 2007-2013; and Nuuk from 2012-2014), total seasonal discharge volumes are computed and normalized relative to the 2012 melt season (Q_{2012}).

To compare daily variability over the melting season, all three basins were transformed to a common scale by normalized daily discharge time series using the z-score method:

$$z = \frac{(X - \mu)}{\sigma} \quad (1)$$

Where, X is the value of the daily observed discharge, μ is the average of daily discharge over the melt season, and σ is standard deviation. z, also known as the standard score, indicates how many standard deviations daily observed discharge is from the mean.

5.2.6 Meteorological measurements from PROMICE stations

Near-surface conditions collected from nearby Programme for Monitoring of the Greenland Ice Sheet (PROMICE; Ahlstrom et al., 2008) Automatic Weather Stations (AWSs) were compared with river discharge. Variations in primary drivers of melt were evaluated against proglacial river discharge to determine if they co-occurred during peak discharge events. Two AWSs were identified in or near each basin (*see Fig. 4.1*). Six of the seven AWSs used in Chapter 4 were used in this study (*see Table 4.1*). To avoid cluttering, only meteorological variables from lower (AWS_L) and upper (AWS_U) elevation stations are presented (i.e., AWS_M at the middle elevation is excluded here), where AWS_U corresponds to each station three-letter naming convention (i.e., THU, KAN, and NUK correspond to Thule, Watson, and Nuuk basins, respectively). Each AWS recorded near-surface air temperature (ST; at 2 m), shortwave downward radiation (SWD), longwave downward radiation (LWD), and surface albedo (AL). Surface albedo at the Thule basin was not measured in 2012 and is not presented in subsequent analyses. To examine if surface processes covary with river discharge variability and peak discharge events, time series plots of daily meteorological variables are plotted against daily river discharge at each basin.

5.2.7 Geopotential heights

500 mb geopotential height fields, hereafter GPH, were obtained from the 20th century reanalysis (20CR) daily composites (version V2c; hereafter, 20CR) to determine the summer 2012 atmospheric circulation patterns and their correlation with surface meteorological and river discharge variability. The GPH variable is selected because it represents the integration of both large-scale atmospheric patterns and the heat content of an air mass that falls within the 700 – 500 hPa range often used to characterize Greenland ice sheet's atmospheric conditions (e.g., Mioduszewski et al., 2016). The GPH is the height of a pressure surface above average sea level, where warmer air masses correspond to higher heights and vice versa. Furthermore, the GPH anomalies provide the deviation of GPHs from mean values, with positive GPH anomalies corresponding to temperatures above the average, and vice versa for negative anomalies. Lastly, GPH contours and their distance between one another can be used to make inferences regarding wind speed and direction (with faster winds corresponding to tightly spaced contours and vice versa).

The 20CR is NOAA-CIRES's comprehensive global atmospheric circulation data set that spans the 1850-2014 period (Compo et al., 2011). The 20CR data set is produced by integrating surface pressures, monthly sea surface temperature, and sea ice distributions as boundary conditions within an Ensemble Kalman Filter data assimilation framework (Whitaker and Hamill, 2002; Compo et al., 2011). It has a 2° spatial resolution and 28 vertical hybrid sigma-pressure levels (Juang, 2005) to produce a global analysis every 6-hours of the 20th century. Uncertainty is quantified from a 56 member ensemble. The V2c is the same as the version 2 model, with an updated sea ice boundary condition from the Centennial in situ Observation-Based Estimates sea surface temperature data set (COBE; Hirahara et al., 2014), additional observations of surface pressure from the International Surface Pressure Databank (ISPD version 3.2.9; Cram et al., 2015), and new pentad Simple Ocean Data Assimilation with sparse input (SODAsi.2) sea surface temperature fields (Giese et al., 2016). The 20CR data set validation reveals good agreement within three-days of operational numerical weather prediction (NWP) forecasts in the Northern Hemisphere (Compo et al., 2011) and over Greenland (e.g., Hanna et al., 2011). A recent study found good agreement between the 20CRV2c reanalysis data set and ERA-Interim data that is used to force the MAR (v3.5.2) regional climate model (RCM).

For this study, daily anomalies of 500 mb GPHs corresponding to the first extreme melt event period in mid-July 2012 (10 to 12 July 2012) are examined. In addition, five-day anomalies across the main portion of the 2012 melt season (1 July to 9 August) are examined to characterize the seasonal progression of atmospheric circulation patterns and attribute their role in the second melt episode (28 July to 4 August 2012). The 500 GPH fields are evaluated within the 58° – 85° N and 280° – 350° W domain. The reanalysis plots were created using the National Oceanic and Atmospheric Administration (NOAA)/Earth System Research Laboratory (ESRL) Physical Sciences Division, Boulder, Colorado website at: http://www.esrl.noaa.gov/psd/.

5.3 Results

5.3.1 Inter-comparison of river discharge in 2012

Annual total discharge volumes vary by melt season and drainage basin, but the 2012 melt season is unprecedented across all basins (Fig. 5.1). The cumulative observed discharge volume is 3.2, 48.1, and 10.1 km^3 for the 2012 melt season at the Thule, Watson, and Nuuk basins, respectively. The Thule basin demonstrates the largest departure from previous melt season cumulative discharge values (difference of 0.30 between 2011 and 2012 in the values normalized relative to 2012 discharge totals, Q_{2012}) and from the Watson and Nuuk basins (Fig. 5.1). Thule's 2011 melt season trails the 2012 melt season for second highest discharge volume (0.70 of Q_{2012}). Thule's 2004-2006 melt seasons are considerably lower (range between ~0.37 and 0.52 of the 2012 seasonal discharge) than 2011-2012. In contrast, the Watson basin experienced nearly a similar total discharge volume in 2010 to the 2012 melt season (0.96 vs. 1 relative to Q_{2012}; Fig. 5.1).

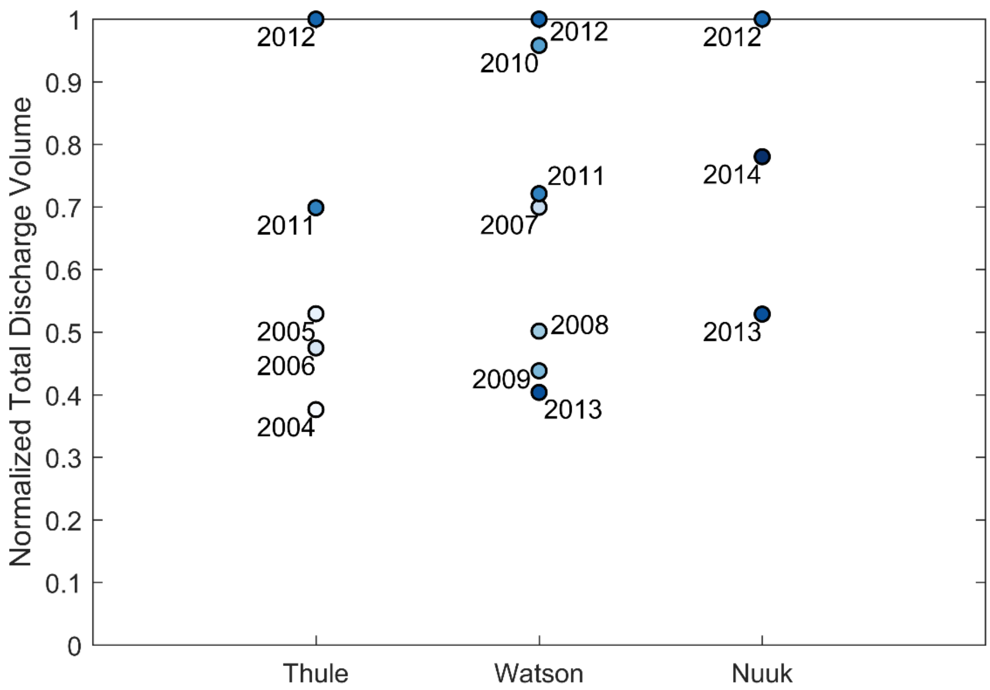

Figure 5.1 Total discharge volume for each basin for available years of discharge data normalized relative to total discharge volumes in 2012 (i.e. each year's seasonal (JJA) discharge was divided with the total JJA discharge in Q_{2012}). Discharge data is available at Thule in 2004-2006 and 2011-2012, Watson in 2007-2013, and Nuuk in 2012-2014.

Interestingly, following the 2012 melt season, the 2013 melt season reveals the lowest cumulative discharge volume (0.40 of Q_{2012}) of the entire Watson basin record (2007-2013). The 2007 (0.70 of Q_{2012}) and 2011 (0.72 of Q_{2012}) melt seasons succeed the Watson basin's 2010 and 2012 highest melt seasons. Different from the Thule and Watson basins, the Nuuk basin reveals nearly equal staggering between annual total discharge volumes between 2012 and 2014 (difference of 0.22 in normalized values relative to Q_{2012}) as well as 2013 and 2014 (difference of 0.25 in normalized values relative to Q_{2012}; Fig. 5.1). Similar to Watson's 2013 melt season (0.40 of Q_{2012}), Nuuk's

2013 melt season discharge is lowest (0.53 of Q_{2012}), but the total magnitude is larger for the Nuuk basin relative to Q_{2012} (cf. Watson basin 2013; Fig. 5.1).

5.3.2 Peak discharge events

The 2012 melt season is unprecedented at all three basins (as shown in Section 5.3.1), prompting an investigation into the identification and timing of daily peak discharge events. As mentioned previously, two melt episodes, on 12 and 29 July 2012, are identified with ice sheet wide or nearly ice sheet wide melt (Nghiem et al., 2012). A consistent one-day time step characterizes the progression of the first melt episode from south-to-north (Fig. 5.2). The Nuuk basin peaks first on 10 July 2012, followed by Watson on 11 July 2012 and then the Thule basin on 12 July 2012. Somewhat surprisingly, the Thule basin experienced the largest departure, 3.50 standard deviations above the average (cf. +2.89 and +2.56 standard deviations for Nuuk and Watson, respectively) during the first peak discharge event (on 12 July 2012, for the Thule basin). Dissimilar to Thule and Watson basins, Nuuk experienced secondary and tertiary peaks shortly after the 10 July 2012 peak discharge event on 16 and 19 July 2012 (Fig. 5.2).

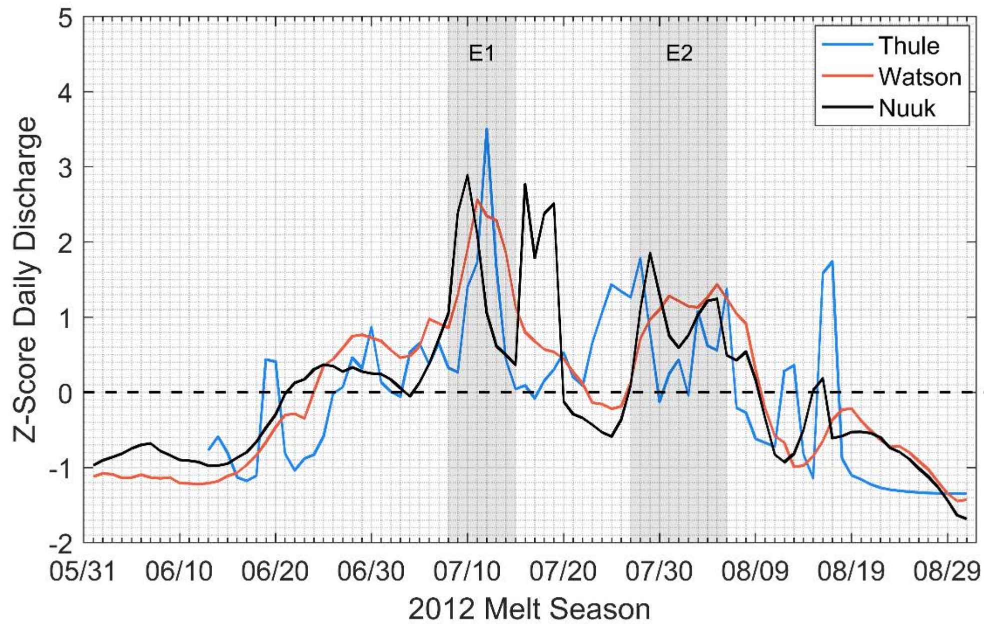

Figure 5.2 Normalized (z-scores) seasonal (JJA) daily discharge for Thule (blue line), Watson (red line), and Nuuk (black line). E1 refers to the first melt episode from 8-15 July 2012 (gray shaded area). E2 refers to the second melt episode from 27 July to August 6 2012 (gray shaded area). A late season discharge pulse on 17 August is only observed in the Thule basin.

These secondary and tertiary peaks are similar in magnitude to the first peak discharge event, +2.77 and +2.51 standard deviations above the seasonal mean. On 15 July 2012, one day prior to the secondary peak in the Nuuk basin, the standard deviation reduced substantially (0.36), representing a reduction of -2.41 standard deviations. This indicates that the Nuuk basin experienced the largest daily discharge variability during the first melt episode and in the 2012 melt season.

The second ice sheet-wide melt episode concentrated in late July reveals less coherency in the peak timing across all basins (Fig. 5.2). In other words, a latitudinal gradient of peak daily discharge timing is not observed. The second peak discharge event is characterized by lower deviations from the mean, consistent with the reduced melt extent observed on the ice sheet (~80%; Nghiem et al., 2012). During the second melt episode, the northernmost basin, Thule, exhibits the first peak discharge event, +1.78 standard deviations above normal, on 28 July 2012 (Fig. 5.2). The Nuuk basin followed Thule, peaking at +1.85 standard deviations above the mean, on 29 July 2012. A delay in the second melt episode and downstream discharge response is observed for the Watson basin (Fig. 5.2). The Watson basin peaks past the late July mark, on 5 August 2012 instead, at +1.44 standard deviations above the average. This secondary peak daily discharge event at the Watson basin is superseded by a similar, slightly lower magnitude peak discharge event on 31 July 2012 (+1.28 standard deviations). Despite being lower in magnitude, the second peak discharge period at the Watson basin is longer in duration and exhibits less daily discharge variability (sustained from ~29 July to 8 August 2012). Finally, a late season pulse of meltwater reaches the Thule gauging station on 17 August 2012, spiking the daily discharge +1.74 standard deviations above the average (Fig. 5.2). To put it into perspective, this late season pulse in the Thule basin exceeded the Watson basin second peak discharge event (by +0.30 in z-score values), and is roughly comparable to the second peak discharge event departures with itself (cf. +1.78 to +1.74 for 28 July and 17 August at Thule, respectively) and the Nuuk basin (cf. +1.85 to +1.74 for 29 July and 17 August at Nuuk and Thule, respectively).

5.3.3 Correspondence of near-surface conditions with peak discharge events

Time series of SWD/LWD, ST and AL at lower and upper elevations reveal temporal and elevation differences in meteorological, and by extension, hydrologic variables (Figs. 5.3-5.5). Thule basin shortwave and longwave downwelling radiation is only available from the upper elevation station in 2012 (Fig. 5.3a). Large inter-annual variability in SWD/LWD is observed (Fig. 5.3a). During the first peak discharge event on 12 July 2012, lower SWD (151 W m^{-2}) and high, sustained LWD (333.50 W m^{-2}) is observed in the Thule AWS (Fig. 5.3a). The second peak melt event on 28 July 2012 exhibited the same, low SWD (151 W m^{-2}) and similar, high LWD (319.50 W m^{-2}). Thule basin near-surface air temperatures were above freezing at the beginning of the melt season (~4.6 °C) on 2 June 2012 at both lower and upper elevations (Fig. 5.3b). However, these above-freezing temperatures didn't persist until after 24 June 2012. These warm conditions continued up until 8 August 2012, with intermittent freezing and non-freezing temperatures occurring after 8 August 2012 (Fig. 5.3b). During the two peak discharge events (12 and 28 July 2012), air temperatures near Thule basin are well above the freezing point – 3.64 °C and 1.68 °C, respectively. These meteorological conditions contributed to two daily discharge peaks of 141.10 m^3 s^{-1} and 91.38 m^3 s^{-1} on 12 and 28 July 2012, respectively (Fig. 5.3c). Thule's late season pulse observed on 17 August 2012 in Fig. 5.2 corresponds to similar conditions described in the previous two peak discharge events – lowered SWD, higher LWD, and above-freezing temperatures, resulting in a peak discharge of 90.12 m^3 s^{-1} (Fig. 5.3c).

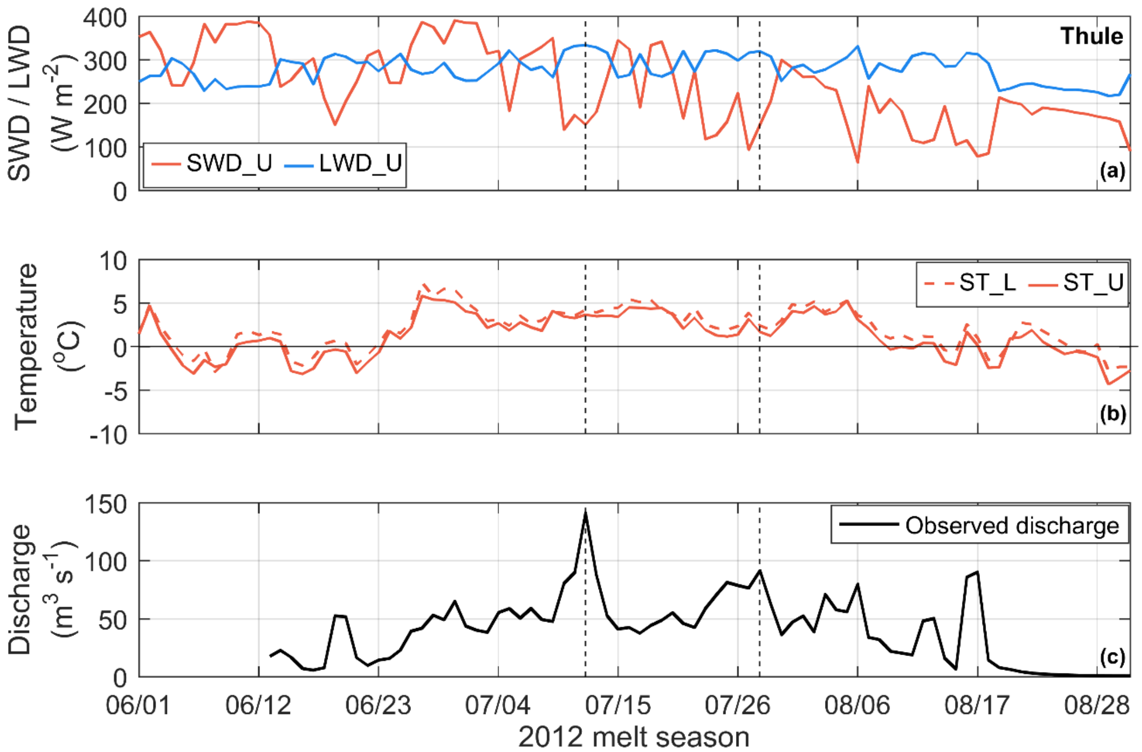

Figure 5.3 Meteorological records and river discharge measurements for the Thule basin during 2012, including (a) incoming shortwave and longwave radiation (SWD and LWD) at THU_U (red and blue solid lines). No SWD/LWD data is available at THU_L in 2012. Panel (b) shows daily average near-surface air temperatures (ST) at THU_L (red stippled line) and THU_U (red solid line). Panel (c) contains proglacial discharge (black solid line). The dashed vertical black lines indicate the occurrence of the two peak discharge events occurring on 12 and 28 July 2012.

The Watson basin is characterized by distinct differences in the temporal and elevation distribution of melt energy available in the 2012 melt season (Fig. 5.4). Throughout the melt season, SWD (LWD) fluxes are lower at the KAN_L (KAN_U) stations as compared to SWD (LWD) fluxes at the KAN_U (KAN_L) stations (Fig. 5.4a), corresponding to elevation differences. During the 11 July 2012 peak discharge event for the Watson basin, SWD_L (SWD_U) is 314.70 W m^{-2} (278.90 W m^{-2}) and LWD_L (LWD_U) is 290.90 W m^{-2} (301.3 W m^{-2}; Fig. 5.4a). The convergence of SWD and LWD fluxes during the first peak discharge event is not observed during the second peak melt event. The 5 August 2012 peak discharge event reveals similar LWD fluxes (324.70 W m^{-2} and 299.60 W m^{-2} for lower and upper elevations, respectively), and lowered SWD fluxes (170.80 W m^{-2} and 204.30 W m^{-2} for lower and upper elevations, respectively) as compared to the first peak discharge event (Fig. 5.4a). Near-surface air temperatures from KAN_U, located above the equilibrium line in this region, indicate oscillating temperatures hovering around the 0 °C line starting in mid-June 2012 (Fig. 5.4b). Anomalously warm temperatures at KAN_U is observed between 8 and 13 July 2012 contributing to upper elevation surface melt corresponding to the period of high pressure and clear sky conditions (Fig. 5.4a-b; Nghiem et al., 2012). A similar trend in upper elevation station air temperatures is observed during the second peak discharge event (2.06 °C on 5 August 2012 at KAN_U; Fig. 5.4b). Above-freezing temperatures sustained nearly the entire melt season at the lower elevation KAN_L station (Fig. 5.4b). The extensive surface melt experienced at the Watson basin is amplified by lower surface albedos at lower and upper elevation stations (Fig. 5.4c). Surface albedo is 0.45 (0.64) and 0.45 (0.61) at the KAN_L (KAN_U) stations during the 11 July and 5 August 2012 peak discharge events. These surface conditions contributed to a peak discharge of 3189 m^3 s^{-1} on 11 July 2012 and 2356 m^3 s^{-1} on 5 August 2012 (Fig. 5.4d).

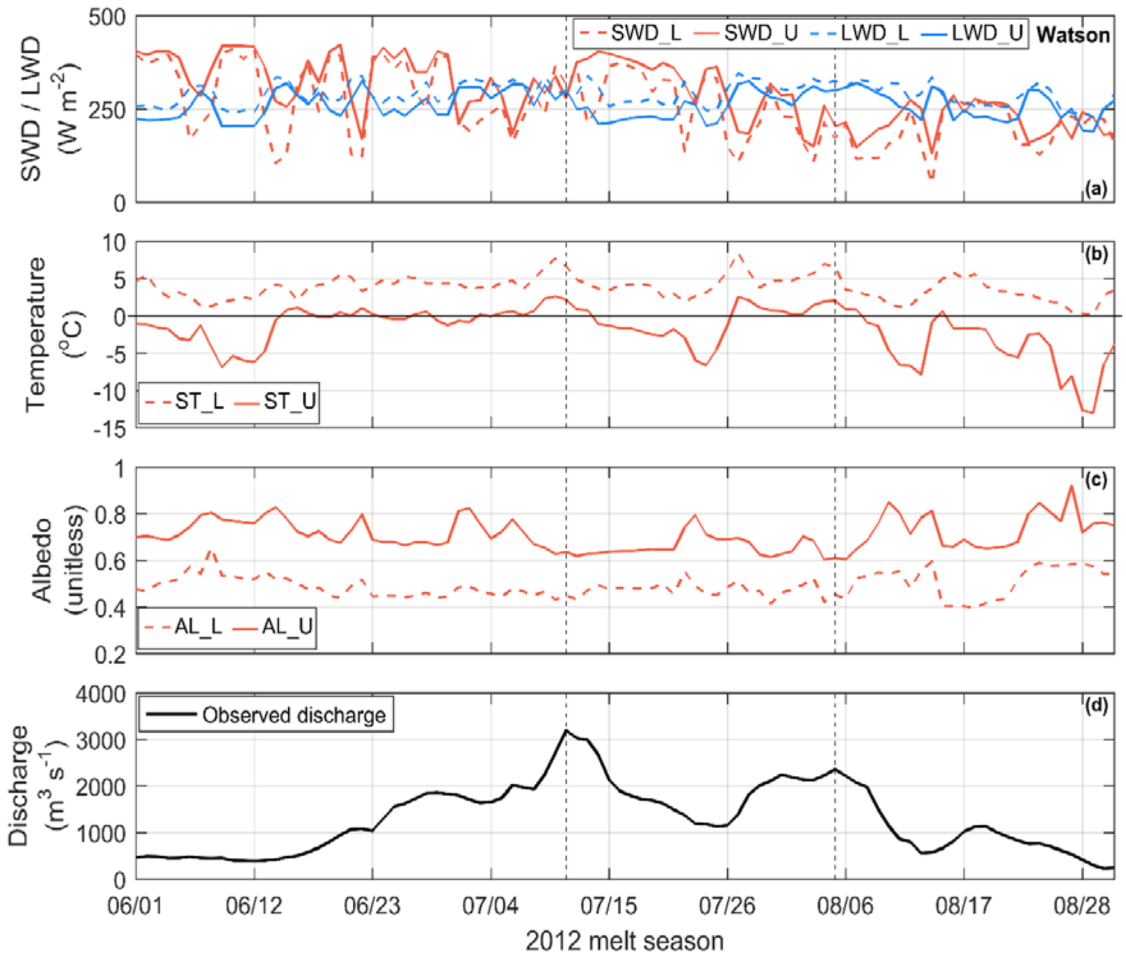

Figure 5.4 Same as Figure 5.2, but panel (c) contains surface albedo (AL) at KAN_L (red stippled line) and KAN_U (red solid line). Also, panel (d) now shows the proglacial discharge for the Watson basin (black solid line). The dashed vertical black lines indicate the occurrence of the two peak discharge events occurring on 11 July and 5 August 2012.

The Nuuk basin is marked by large, abrupt variations in SWD, and less variability in LWD at both lower and upper elevation stations (Fig. 5.5a). Altitudinal differences are limited as both NUK_L and NUK_U stations are located well below the equilibrium line for this region (Overeem et al., 2015). Lowered SWD (~92.50 W m^{-2}) and higher LWD (~344.80 W m^{-2}) are observed at both stations during the first peak discharge event on 10 July 2012 (Fig. 5.5a). In contrast, higher SWD (~258.30 W m^{-2})

and similar LWD (~317.40 W m^{-2}) fluxes are observed during the second peak discharge event on 29 July 2012. Air temperature at both elevations is characterized by above-freezing temperatures throughout nearly the entire 2012 melt season near the Nuuk basin (Fig. 5.5b). ST peaked to 10.21 °C (7.75 °C) at NUK_L (NUK_U) stations on 10 July 2012. Lower, yet positive air temperatures are also observed during the second discharge event on 29 July 2012 (4.91 °C and 2.68 °C at NUK_L and NUK_U, respectively). While the NUK_L and NUK_U stations are not located within the Nuuk basin, above-freezing air temperatures in this Nuuk discharge drainage basin are expected, given its location in southern Greenland and the ice area of the basin situated below the equilibrium line. These surface conditions are augmented by considerably low surface albedo values during the latter half of June 2012 (Fig. 5.5c), setting the stage for the rest of the exceptional melt season. AL went as low as 0.37 (0.35) at the lower NUK_L station on 10 July 2012 (29 July 2012). The AL remained low before a late season snowfall event occurred around 10 August 2012 (0.80; Fig. 5.5c). These surface conditions result in peak daily discharge of 240.40 m^3 s^{-1} (193.40 m^3 s^{-1}) on 10 July (29 July) 2012 (Fig. 5.5d). Secondary and tertiary peak discharge events, not observed at the Thule and Watson basins, occurred shortly after the first melt episode on 10 July 2012. These additional peaks occurred from 15 and 20 July 2012, corresponding to peak discharge of 223.20 m^3 s^{-1} and 234.80 m^3 s^{-1}, respectively (Fig. 5.5d). In contrast to the peaks on July 10 and 29, these peaks are associated with SWD exceeding LWD, and no marked departure in near-surface air temperature on or at the days before the event.

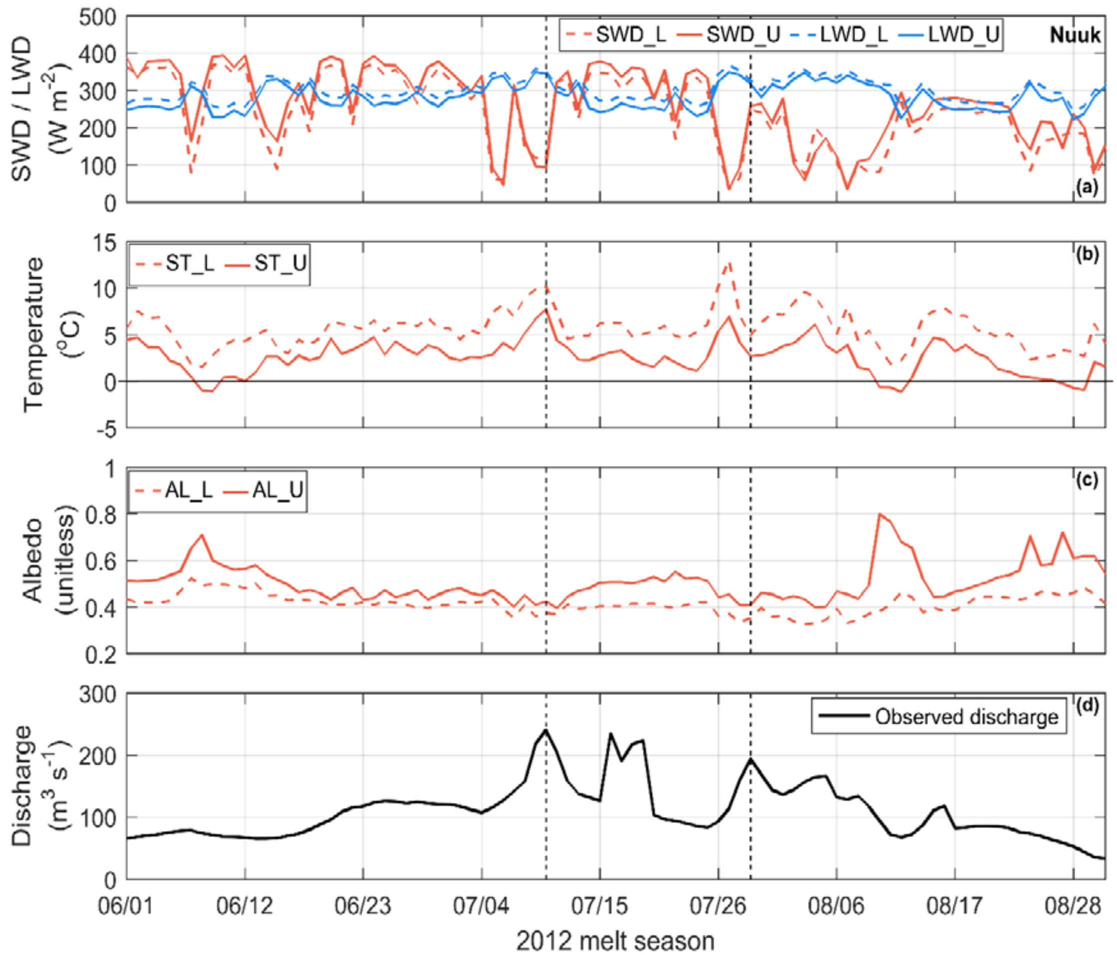

Figure 5.5 Same as Figure 5.3, but panel (c) contains surface albedo (AL) at NUK_L (red stippled line) and NUK_U (red solid line). Also, panel (d) now shows the proglacial discharge for the Nuuk basin (black solid line). The dashed vertical black lines indicate the occurrence of the two peak discharge events occurring on 10 and 29 July 2012.

5.3.4 Atmospheric circulation patterns

Large-scale atmospheric circulation patterns contributed to the two melt episodes and subsequent runoff at each basin (Figs. 5.6-5.7). Positive 500 mb GPH anomalies are observed over the GrIS on 10-12 July 2012, driving the extensive, ice sheet wide surface melt (Fig. 5.6). On 10 July 2012, GPH anomalies are centered over south-southeast Greenland (Fig. 5.6a). One day later, the spatial distribution of GPH anomalies are positioned over central Greenland, extending along the western region of the ice sheet, and upwards towards northwest Greenland (Fig. 5.6b). By 12 July 2012, the GPH anomalies extend across almost the entire ice sheet, centered over the interior of central Greenland (Fig. 5.6c).

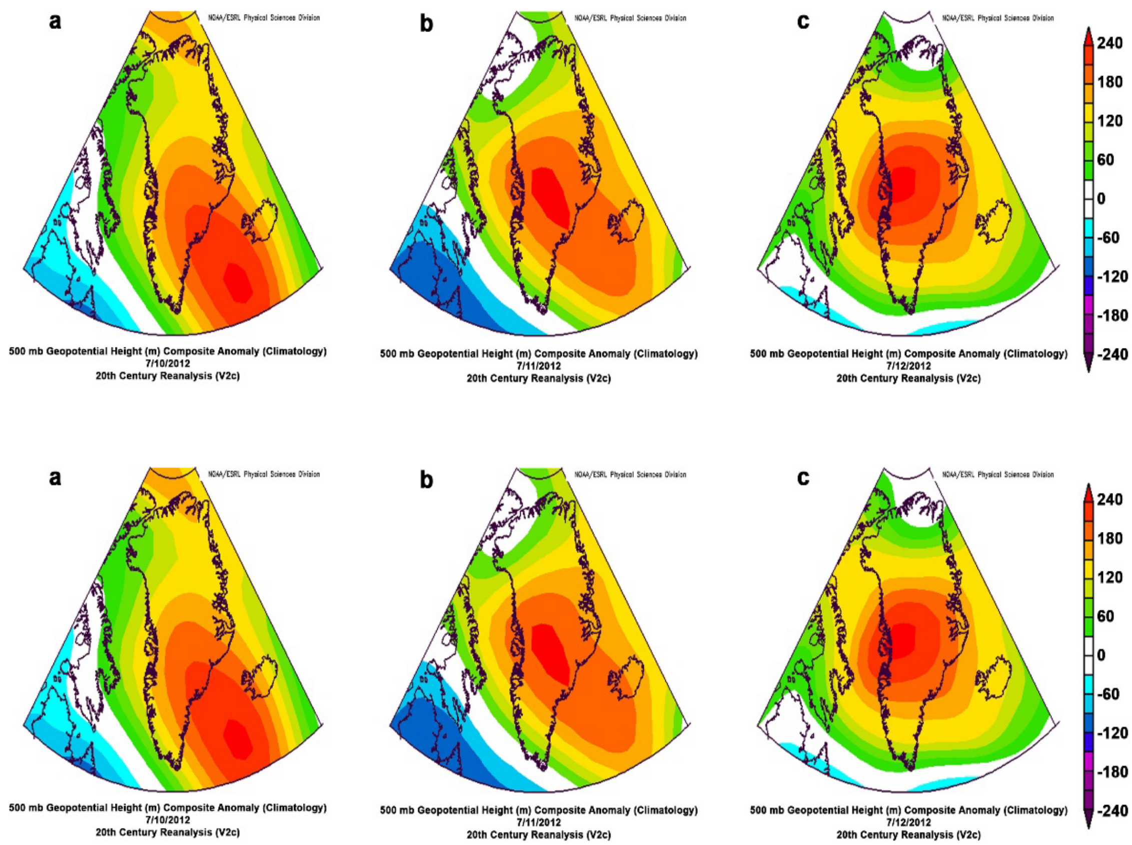

Figure 5.6 The 500 mb geopotential height daily composite anomalies for July 10 (a), 11 (b), and 12 (c) 2012. Data are from NOAA/ESRL, Boulder, CO: http://www.esrl.noaa.gov/psd/.

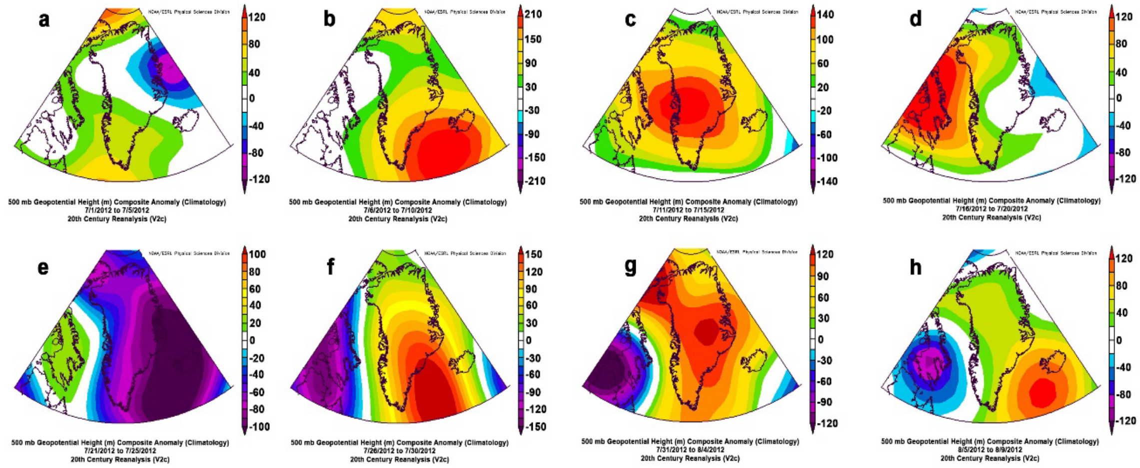

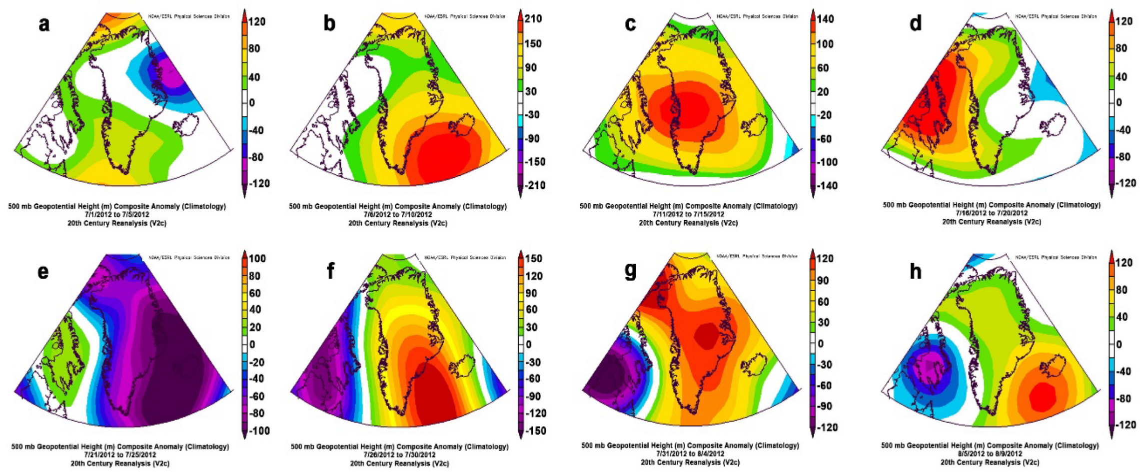

Figure 5.7 The 500 mb geopotential height five-day composite anomalies for July 1-5 (a), July 6-10 (b), July 11-15 (c), July 16-20 (d), July 21-25 (e), July 26-30 (f), July 31 to August 4 (g), and August 5-9 (h) 2012. Data are from NOAA/ESRL, Boulder, CO: http://www.esrl.noaa.gov/psd/.

Five-day 500 mb GPH anomalies provide snap shots of the seasonal progression and structure of atmospheric circulation patterns over the GrIS (Fig. 5.7). On 1-5 July, a strong dipole in GPH anomalies is observed, with negative anomalies concentrated over northeast Greenland and the Greenland Sea, while slightly positive anomalies exist over southwest Greenland and the Labrador Sea (Fig. 5.7a). Within the next five days, strong, positive GPH anomalies begin to solidify into a structured phenomenon over southeast

Greenland and the North Atlantic Ocean (Fig. 5.7b). The first peak discharge event observed at all three basins coincide with the 11-15 July 2012 GPH anomalies covering nearly all of Greenland in Fig. 5.7c. Between 16-20 July 2012, the GPH anomalies move westward off the Greenland continent (Fig. 5.7d) to make way for strong, negative GPH anomalies that set up over the entire ice sheet between 21-25 July 2012 (Fig. 5.7e), and likely correspond to a brief hiatus or reduction in surface meltwater production and runoff (associated with cooler air temperatures). However, these strong negative anomalies are rapidly replaced by a second, positive GPH anomaly originating from the North Atlantic Ocean during 26-30 July 2012 (Fig. 5.7f). Between 31 July and 4 August 2012, these positive GPH anomalies spread across nearly the entire ice sheet (Fig. 5.7g). The GPH conditions between 26 July and 4 August coincide with the second melt episode and associated peak discharge event experienced at all three basins (Figs. 5.7f-g). The strong, positive GPH anomalies are once again replaced with lower, yet still positive anomalies during 5-9 August 2012 (Fig. 5.7h). The mildly positive GPH anomalies extend nearly the entire ice sheet, contrasted with two extreme positive and negative dipoles off the east and west coasts of Greenland, respectively (Fig. 5.7h). The GPH anomalies in early August 2012 indicate that energy for melting is still available.

5.4 Discussion and Conclusions

Our analysis reveals that the extreme melt event of 2012 was experienced and unprecedented at all three basins since observational record began. A latitudinal gradient in normalized total flow volume from south-to-north was observed, with a 28%, 38%, and 40% increase in total discharge in 2012 relative to the 2011, 2011, and 2014 melt seasons at Nuuk, Watson, and Thule basins, respectively (Fig. 5.1). The latitudinal gradient of the 2012 discharge fraction corresponds to the more frequent ablation in the south (warmer air temperatures) as compared to the north (cooler air temperatures). The 2010 melt season closely followed 2012 as a high melt year at the Watson basin (Fig. 5.1). This agrees with other studies that have found a similar response at the Watson River for 2010 and 2012 (Mikkelsen et al., 2016). Mikkelsen et al. (2016) also found that the prevailing atmospheric conditions and runoff response in 2010 and 2012 were distinctly different.

Exceptional melt events in 2012 were concentrated during two periods in mid-July and late July, as first identified in Nghiem et al. (2012). These two melt periods were followed by large peak discharge events observed at each basin (Fig. 5.2). The subsequent discharge response at each basin, including the timing, magnitude, and duration were noticeably different during the two melt episodes (Fig. 5.2). In the mid-July event peak flow was recorded in a three-day period within the roughly five-day long melt episode. In the late-July melt episode, peak flow occurred over an eight-day time span over the almost twenty-day long period with anomalously high flow.

The southernmost basin, Nuuk, experienced the first peak discharge event (Fig. 5.2) followed by a secondary peak shortly after from 15 and 20 July 2012, not observed at the other basins. Given the rapid variability in discharge between 11-20 July, we hypothesize that the secondary pulse of discharge at Nuuk is associated with a lake drainage event on the ice sheet or ice dammed lakes along the ice sheet margin. This is plausible given that several such lakes can be seen within the Nuuk basin (Fig. 5.8).

Similar huge lake drainage events have been observed in the Watson River (Mernild and Hasholt, 2009; Russell et al., 2011).

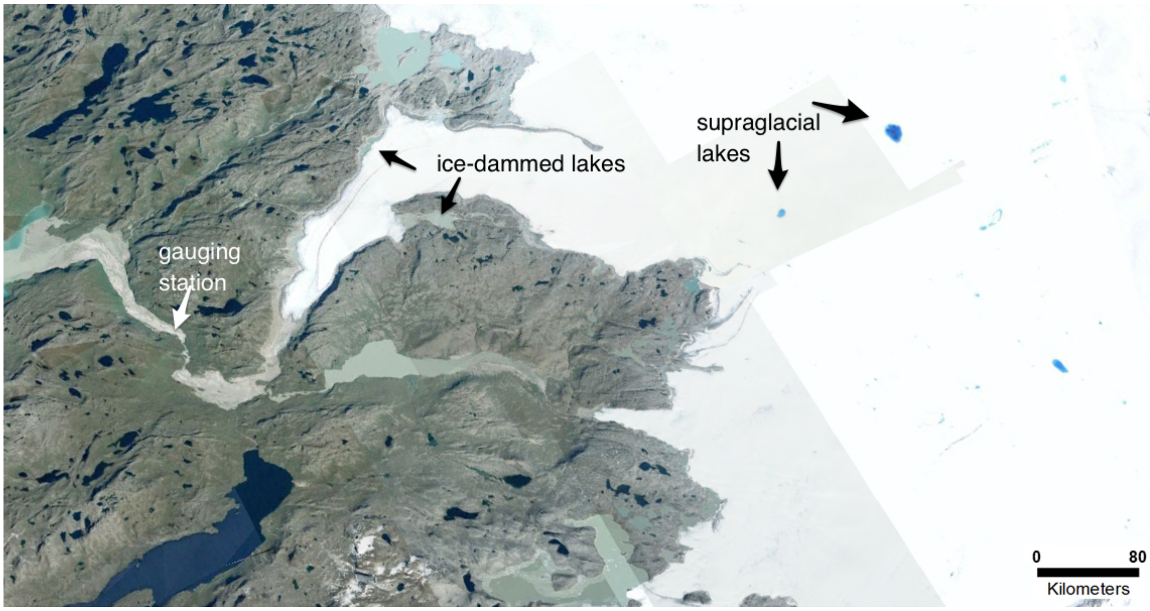

Figure 5.8 Nuuk basin gauging site with the location of ice-dammed and supraglacial lakes in the catchment area. Snapshot from Google Earth.

The timing and magnitude of the peak daily discharge events at the Watson basin are consistent with the 11 July and 5 August 2012 proglacial discharge peak timings in Van As et al. (2017) and Mikkelsen et al. (2016) using the data from the same discharge station. The KAN weather stations (Fig. 5.4) near surface temperature records reveal that the first melt episode regionally started on 8 July and continued until 11 July, coinciding with a rapid rise in Watson River proglacial river discharge, peaking at nearly 3200 m^3 s^{-1}, agreeing with the results of Van As et al. (2017) and Mikkelsen et al. (2016). This first peak discharge event is unprecedented for the Watson basin, and was likely enhanced by surface conditions at higher elevations (e.g. KAN_U station at 1840 m a.s.l.), including lower surface albedos, warmer air temperatures, and large shortwave radiative fluxes (Fig. 5.4). The additional area above the mean equilibrium line (~1550 m a.s.l.) exposed to surface melt contributed to additional runoff at the Watson gauging site. Although not investigated here, hypsometric amplification of melting at higher elevations was shown to contribute to the extraordinary runoff from the Watson basin (van As et al., 2017; Mikkelsen et al., 2016). The high shortwave radiative fluxes also dominated during the first melt episode in the Watson basin at the mid-elevation KAN_M station (Fausto et al., 2016). The high downward longwave radiation observed right before the first melt-episode, and during the two second melt episodes in the Watson basin (Fig. 5.4) was associated with positive temperature perturbations at both KAN sites, and also were rare occurrences of above-freezing atmospheric temperatures at KAN_U. These findings are consistent with summer (JJA) averages of SWD and LWD at KAN_U in Charalampidis et al. (2015; see Fig. 6a and Table 5).

Radiative energy fluxes at the THU_U site (Fig. 5.3) appear to govern the two peak discharge events observed in the Thule basin. Fausto et al. (2016) found that while turbulent energy fluxes dominated (~60% of the melt energy) surface melt contributions in south and southwest Greenland, the THU_U site was an exception during both 2012 melt episodes (melt-dominated by radiative fluxes). Our results at the upper elevation THU station (Fig. 5.3a) agree with these findings from Fausto et al. (2016) as this is the only basin without near-surface temperature perturbations during the peak events. Interestingly, the northernmost basin, Thule, exhibited the largest daily z-score (as compared to Watson and Nuuk basins), peaking +3 standard deviations above the baseline, during the first melt episode (Fig. 5.2). We would expect the Watson basin to have the largest daily peak in z-score values because of the large catchment area and therefore higher potential for hypsometric amplification, yet this is not what is observed.

The sharp rise in daily discharge at Thule during the peak events may be due to the small basin area (it is the smallest of the three basins), and thus, a short runoff delay time between meltwater production and outflow observed at the gauging station. Therefore, the Thule basin's surface rapidly ablates and efficiently evacuates meltwater to the proglacial river. In contrast, the complexity of the hydrologic systems encompassed in the much larger Watson basin results in a more dampened river discharge signal due to longer transport times on and within the ice sheet (e.g., van As et al., 2017, also see Chapter 4).

During the first melt event in mid-July, the large positive anomalies in GPH time steps appear to be in sync with proglacial river discharge peak discharge events observed on 10, 11 and 12 July (Figs. 5.2 and 5.6). Prior to the mid-July melt episode (before 11 July 2012), a structured trough-ridge pattern formed along west Greenland, with significant northward transport of warm, humid air (Fettweis et al., 2013; Neff et al., 2014). The high 500 mb GPH anomalies observed over Greenland on 12 July 2012 (Fig. 5.6c) are consistent with the 700 mb GPH anomalies in Neff et al. (2014; see Figure S3). The addition of warm, low-level liquid clouds assisted in raising LWD and/or surface temperatures observed at all weather stations (Figs. 5.3-5.5) during the first melt episode (Bennartz et al., 2013). Despite the lack of observational data, we hypothesize that the temporary increase in downwelling longwave radiation observed at most of the weather stations during the first and second melt episode may be partly attributed to the increase in atmospheric heat content (i.e., as observed in the GPH anomalies; Figs. 5.6-5.7), and also to the temporary presence of clouds (Bennartz et al., 2013). A recent study by van Tricht et al. (2016) found that clouds are responsible for reducing the meltwater refreezing capacity, thereby enhancing meltwater runoff on the ice sheet. Additional atmospheric forcings, including a blocking high pressure feature, corresponding to negative NAO (and Arctic Oscillation) conditions, and an increase in water vapor from an Atmospheric River over the Atlantic to Greenland, contributed to the first melt episode, as identified by several studies (Hanna et al., 2013; Overland et al., 2012; Tedesco et al., 2013; Neff et al., 2014).

Between the two melt episodes, a period of lower daily discharge was observed (Figs. 5.3-5.5). Large, negative anomalies in GPHs were observed July 21-25 (Fig. 5.7e) corresponding to lower daily discharge anomalies at Nuuk and Watson basins (Fig. 5.2). However, the northernmost basin, Thule, exhibited discharge anomalies that continued to increase during the same time period, and appeared to be unaffected by the transient ‘cold spell’.

During the second melt event in late July, a less organized story was observed between the timing and spatial distribution of GPH anomalies. The second melt episode corresponded to a lagged, second, lower magnitude peak discharge event observed at each basin (Fig. 5.2 and Fig. 5.7f-g). The second peak discharge event spiked at the Thule (northernmost) basin first on 28 July 2012, followed by Nuuk (southernmost) basin on 29 July 2012, and finally at the Watson basin on 5 August 2012 (assisted by the large positive GPH anomalies preceding the peak discharge event between 31 July to 4 August 2012; see Fig. 5.7g). During the late July 2012 second melt episode, the spatial pattern of positive GPH anomalies were restricted eastward of Davis Strait (Fig. 5.7f), agreeing with the results of Neff et al. (2014), and moved poleward by 31 July to 4 August 2012 (Fig. 5.7g), contributing to the second peak discharge events (Figs. 5.3-5.5).

The 2012 melt season produced exceptional melt on the GrIS, with the preceding similar melt episode occurring as far back as 1889 (Nghiem et al., 2012). The surface conditions, enhanced ice-albedo feedback (e.g., Tedesco et al., 2013b), increased poleward heat advection from atmospheric circulation patterns, increased near-surface air temperatures and radiative energy fluxes, and drainage-specific features (e.g., hypsometry amplification, supraglacial features) contributed to the abrupt rise in proglacial river discharge and large daily discharge variability observed at the Thule, Watson, and Nuuk basins. Secondary and tertiary peak discharge events, within the two major melt episodes have been identified in the daily discharge. With continued atmospheric warming, future changes in basin area are expected – with the largest changes occurring in the Watson basin followed by the Thule basin due to their relative potential for hypsometric amplification. Nuuk basin has lower potential for melt expansion in upper elevations since large part of it melts each summer. A latitudinal gradient in discharge response at all three basins was observed in melt episode one that coincided with the spatial progression of atmospheric circulation anomalies. The anomalies can also explain the general pattern of observed discharge variability in summer 2012. Finally, increases in downward longwave radiation fluxes appears to be an important driver for enhancing surface melt, and subsequent runoff. With peak melt episodes expected to become more frequent in the future (McGarth et al., 2013), continued decline of surface albedo (Tedesco et al., 2016), and runoff contributions expected to continue to dominate mass loss (Vernon et al., 2013), characterizing river discharge is crucial for improving our understanding of Greenland’s complex hydrologic system.

5.5 References

Ahlstrøm, A.P., Gravesen, P., Bech Andersen, S., van As, D., Citterio, M., Fausto, R.S., Nielsen, S., Jepsen, H.F., Kristensen, S.S., Christensen, E.L. and Stenseng, L.: A new programme for monitoring the mass loss of the Greenland ice sheet, Geological Survey of Denmark and Greenland Bulletin, 15, 61-64, 2008.

Van As, D., Andersen, M. L., Petersen, D., Fettweis, X., Van Angelen, J. H., Lenaerts, J. T. M., Van Den Broeke, M. R., Lea, J. M., Bøggild, C. E., Ahlstrøm, A. P. and Steffen, K.: Increasing meltwater discharge from the Nuuk region of the Greenland ice sheet and implications for mass balance (1960-2012), J. Glaciol., 60(220), 314–322, doi:10.3189/2014JoG13J065, 2014.

van As, D., Bech Mikkelsen, A., Holtegaard Nielsen, M., Box, J., Claesson Liljedahl, L., Lindbäck, K., Pitcher, L. and Hasholt, B.: Hypsometric amplification and routing moderation of Greenland ice sheet meltwater release, Cryosph. Discuss., (January), 1–30, doi:10.5194/tc-2016-285, 2017.

Banwell, A. F., Arnold, N. S., Willis, I. C., Tedesco, M. and Ahlstrøm, A. P.: Modeling supraglacial water routing and lake filling on the Greenland Ice Sheet, J. Geophys. Res., 117(F4), F04012, doi:10.1029/2012JF002393, 2012.

Bennartz, R., Shupe, M. D., Turner, D. D., Walden, V. P., Steffen, K., Cox, C. J., Kulie, M. S., Miller, N. B. and Pettersen, C.: July 2012 Greenland melt extent enhanced by low-level liquid clouds., Nature, 496(7443), 83–6, doi:10.1038/nature12002, 2013.

Box, J. E., Cappelen, J., Chen, C., Decker, D., Fettweis, X., Mote, T., Tedesco, M., van de Wal., R.S.W., and Wahr, J., 2012: Greenland ice sheet [in Arctic Report Card 2012], http://www.arctic.noaa.gov/reportcard.

Box, J. E., Cressie, N., Bromwich, D. H., Jung, J.-H., van den Broeke, M., van Angelen, J. H., Forster, R. R., Miège, C., Mosley-Thompson, E., Vinther, B. and McConnell, J. R.: Greenland Ice Sheet Mass Balance Reconstruction. Part I: Net Snow Accumulation (1600–2009), J. Clim., 26(11), 3919–3934, doi:10.1175/JCLI-D-12-00373.1, 2013.

van den Broeke, M. R., Enderlin, E. M., Howat, I. M., Kuipers Munneke, P., Noël, B. P. Y., van de Berg, W. J., van Meijgaard, E. and Wouters, B.: On the recent contribution of the Greenland ice sheet to sea level change, Cryosph., 10(5), 1933–1946, doi:10.5194/tc-10-1933-2016, 2016.

Charalampidis, C., Van As, D., Box, J. E., Van Den Broeke, M. R., Colgan, W. T., Doyle, S. H., Hubbard, A. L., MacFerrin, M., Machguth, H. and P. Smeets, C. J. P.: Changing surface-atmosphere energy exchange and refreezing capacity of the lower accumulation area, West Greenland, Cryosphere, 9(6), 2163–2181, doi:10.5194/tc-9-2163-2015, 2015.

Compo, G. P., Whitaker, J. S., Sardeshmukh, P. D., Matsui, N., Allan, R. J., Yin, X., Gleason, B. E., Vose, R. S., Rutledge, G., Bessemoulin, P., BroNnimann, S., Brunet, M., Crouthamel, R. I., Grant, A. N., Groisman, P. Y., Jones, P. D., Kruk, M. C., Kruger, A. C., Marshall, G. J., Maugeri, M., Mok, H. Y., Nordli, O., Ross, T. F., Trigo, R. M., Wang, X. L., Woodruff, S. D. and Worley, S. J.: The Twentieth Century Reanalysis Project, Q. J. R. Meteorol. Soc., 137(654), 1–28, doi:10.1002/qj.776, 2011.

Dingman, S. L.: Physical hydrology, Waveland press, 2015.

Doyle, S. H., Hubbard, A. L., Dow, C. F., Jones, G. A., Fitzpatrick, A., Gusmeroli, A., Kulessa, B., Lindback, K., Pettersson, R. and Box, J. E.: Ice tectonic deformation during the rapid in situ drainage of a supraglacial lake on the Greenland Ice Sheet, Cryosph., 7(1), 129–140, doi:10.5194/tc-7-129-2013, 2013.

Enderlin, E. M., Howat, I. M., Jeong, S., Noh, M.-J., van Angelen, J. H. and van den Broeke, M. R.: An improved mass budget for the Greenland ice sheet, Geophys. Res. Lett., 41(3), 866–872, doi:10.1002/2013GL059010, 2014.

Fausto, R. S., Van As, D., Box, J. E., Colgan, W., Langen, P. L. and Mottram, R. H.: The implication of nonradiative energy fluxes dominating Greenland ice sheet exceptional ablation area surface melt in 2012, Geophys. Res. Lett., 43(6), 2649–2658, doi:10.1002/2016GL067720, 2016.

Fettweis, X., Tedesco, M., van den Broeke, M. and Ettema, J.: Melting trends over the Greenland ice sheet (1958–2009) from spaceborne microwave data and regional climate models, Cryosph., 5(2), 359–375, doi:10.5194/tc-5-359-2011, 2011.

Fettweis, X., Hanna, E., Lang, C., Belleflamme, a., Erpicum, M. and Gallée, H.: *Brief communication* “Important role of the mid-tropospheric atmospheric circulation in the recent surface melt increase over the Greenland ice sheet,” Cryosph., 7(1), 241–248, doi:10.5194/tc-7-241-2013, 2013.

Hall, D. K., Comiso, J. C., DiGirolamo, N. E., Shuman, C. a., Box, J. E. and Koenig, L. S.: Variability in the surface temperature and melt extent of the Greenland ice sheet from MODIS, Geophys. Res. Lett., 40(10), 2114–2120, doi:10.1002/grl.50240, 2013.

Hanna, E., Huybrechts, P., Cappelen, J., Steffen, K., Bales, R. C., Burgess, E., McConnell, J. R., Steffensen, J. P., Van Den Broeke, M., Wake, L., Bigg, G., Griffiths, M. and Savas, D.: Greenland Ice Sheet surface mass balance 1870 to 2010 based on Twentieth Century Reanalysis, and links with global climate forcing, J. Geophys. Res. Atmos., 116(24), 1–20, doi:10.1029/2011JD016387, 2011.

Hanna, E., Navarro, F. J., Pattyn, F., Domingues, C. M., Fettweis, X., Ivins, E. R., Nicholls, R. J., Ritz, C., Smith, B., Tulaczyk, S., Whitehouse, P. L. and Zwally, H. J.: Ice-sheet mass balance and climate change, Nature, 498(7452), 51–59, doi:10.1038/nature12238, 2013.

Hanna, E., Fettweis, X., Mernild, S. H., Cappelen, J., Ribergaard, M. H., Shuman, C. a., Steffen, K., Wood, L. and Mote, T. L.: Atmospheric and oceanic climate forcing of the exceptional Greenland ice sheet surface melt in summer 2012, Int. J. Climatol., 34(4), 1022–1037, doi:10.1002/joc.3743, 2014.

Harper, J., Humphrey, N., Pfeffer, W. T., Brown, J. and Fettweis, X.: Greenland ice-sheet contribution to sea-level rise buffered by meltwater storage in firn., Nature, 491(7423), 240–3, doi:10.1038/nature11566, 2012.

Hasholt, B., Bech Mikkelsen, A., Holtegaard Nielsen, M. and Andreas Dahl Larsen, M.: Observations of Runoff and Sediment and Dissolved Loads from the Greenland Ice Sheet at Kangerlussuaq, West Greenland, 2007 to 2010, Zeitschrift für Geomorphol. Suppl. Issues, 57(2), 3–27, doi:10.1127/0372-8854/2012/S-00121, 2013.

Hirahara, S., Ishii, M. and Fukuda, Y.: Centennial-Scale Sea Surface Temperature Analysis and Its Uncertainty, J. Clim., 27(1), 57–75, doi:10.1175/JCLI-D-12-00837.1, 2014.

Kean, J. W. and Smith, J. D.: Generation and verification of theoretical rating curves in the Whitewater River basin, Kansas, J. Geophys. Res. Earth Surf., 110(F4), doi:10.1029/2004JF000250, 2005.

Kean, J. W. and Smith, J. D.: Calculation of stage-discharge relations for gravel bedded channels, J. Geophys. Res., 115(F3), F03020, doi:10.1029/2009JF001398, 2010.

Leeson, A. A., Shepherd, A., Briggs, K., Howat, I., Fettweis, X., Morlighem, M., & Rignot, E.: Supraglacial lakes on the Greenland ice sheet advance inland under warming climate, *Nature Climate Change*, *5*(1), 51-55, 2015.

McGrath, D., Colgan, W., Bayou, N., Muto, A. and Steffen, K.: Recent warming at Summit, Greenland: Global context and implications, Geophys. Res. Lett., 40(10), 2091–2096, doi:10.1002/grl.50456, 2013.

Mernild, S. H. and Hasholt, B.: Observed runoff, jökulhlaups and suspended sediment load from the Greenland ice sheet at Kangerlussuaq, West Greenland, 2007 and 2008, J. Glaciol., 55(193), 855–858, doi:10.3189/002214309790152465, 2009.

Mernild, S. H., Liston, G. E., Hiemstra, C. a. and Christensen, J. H.: Greenland Ice Sheet Surface Mass-Balance Modeling in a 131-Yr Perspective, 1950–2080, J. Hydrometeorol., 11(1), 3–25, doi:10.1175/2009JHM1140.1, 2010.

Mikkelsen, A. B., Hubbard, A., Macferrin, M., Eric Box, J., Doyle, S. H., Fitzpatrick, A., Hasholt, B., Bailey, H. L., Lindb??ck, K. and Pettersson, R.: Extraordinary runoff from the Greenland ice sheet in 2012 amplified by hypsometry and depleted firn retention, Cryosphere, 10(3), 1147–1159, doi:10.5194/tc-10-1147-2016, 2016.

Mioduszewski, J. R., Rennermalm, A. K., Hammann, A., Tedesco, M., Noble, E. U., Stroeve, J. C. and Mote, T. L.: Journal of Geophysical Research : Atmospheres, , 1–20, doi:10.1002/2015JD024550.Received, 2016.

Neff, W., Compo, G. P., Martin Ralph, F. and Shupe, M. D.: Continental heat anomalies and the extreme melting of the Greenland ice surface in 2012 and 1889, J. Geophys. Res. Atmos., 119(11), 6520–6536, doi:10.1002/2014JD021470, 2014.

Nghiem, S. V., Hall, D. K., Mote, T. L., Tedesco, M., Albert, M. R., Keegan, K., Shuman, C. A., DiGirolamo, N. E. and Neumann, G.: The extreme melt across the Greenland ice sheet in 2012, Geophys. Res. Lett., 39(20), 1–6, doi:10.1029/2012GL053611, 2012.

Overeem, I., Hudson, B., Welty, E., Mikkelsen, A., Bamber, J., Petersen, D., Lewinter, A. and Hasholt, B.: River inundation suggests ice-sheet runoff retention, J. Glaciol., 61(228), 776–788, doi:10.3189/2015JoG15J012, 2015.

Overland, J., Key, J., Kim, B.-M., Liu, Y., Walsh, J., Wang, M., and Bhatt, U., 2012: Air Temperature, Atmospheric Circulation and Clouds [in Arctic Report Card 2012], http://www.arctic.noaa.gov/reportcard.

Palmer, S., McMillan, M. and Morlighem, M.: Subglacial lake drainage detected beneath the Greenland ice sheet, Nat. Commun., 6(October 2015), 8408, doi:10.1038/ncomms9408, 2015.

de la Peña, S., Howat, I. M., Nienow, P. W., van den Broeke, M. R., Mosley-Thompson, E., Price, S. F., Mair, D., Noël, B. and Sole, a. J.: Changes in the firn structure of the western Greenland Ice Sheet caused by recent warming, Cryosph., 9(3), 1203–1211, doi:10.5194/tc-9-1203-2015, 2015.

Pfeffer, W. T., Meier, M. F. and Illangasekare, T. H.: Retention of Greenland runoff by refreezing: Implications for projected future sea level change, J. Geophys. Res., 96(C12), 22117, doi:10.1029/91JC02502, 1991.

Russell, A. J., Carrivick, J. L., Ingeman-Nielsen, T., Yde, J. C. and Williams, M.: A new cycle of jökulhlaups at Russell Glacier, Kangerlussuaq, West Greenland, J. Glaciol., 57(202), 238–246, doi:10.3189/002214311796405997, 2011.

Smith, L. C., Chu, V. W., Yang, K., Gleason, C. J., Pitcher, L. H., Rennermalm, A. K., Legleiter, C. J., Behar, A. E., Overstreet, B. T., Moustafa, S. E., Tedesco, M., Forster, R. R., LeWinter, A. L., Finnegan, D. C., Sheng, Y. and Balog, J.: Efficient meltwater drainage through supraglacial streams and rivers on the southwest Greenland ice sheet, Proc. Natl. Acad. Sci., 112(4), 1001–1006, doi:10.1073/pnas.1413024112, 2015.

Stevens, L. A., Behn, M. D., Das, S. B., Joughin, I., No??l, B. P. Y., van den Broeke, M. R. and Herring, T.: Greenland Ice Sheet flow response to runoff variability, Geophys. Res. Lett., 43(21), 11,295-11,303, doi:10.1002/2016GL070414, 2016.

Sundal, A. V., Shepherd, A., Nienow, P., Hanna, E., Palmer, S. and Huybrechts, P.: Melt-induced speed-up of Greenland ice sheet offset by efficient subglacial drainage., Nature, 469(7331), 521–4, doi:10.1038/nature09740, 2011.

Tedesco, M., Willis, I. C., Hoffman, M. J., Banwell, A. F., Alexander, P. and Arnold, N. S.: Ice dynamic response to two modes of surface lake drainage on the Greenland ice sheet, Environ. Res. Lett., 8, 34007, doi:10.1088/1748-9326/8/3/034007, 2013.

Tedesco, M., Fettweis, X., Mote, T., Wahr, J., Alexander, P., Box, J. E. and Wouters, B.: Evidence and analysis of 2012 Greenland records from spaceborne observations, a regional climate model and reanalysis data, Cryosph., 7(2), 615–630, doi:10.5194/tc-7-615-2013, 2013.

Tedesco, M., Mote, T., Fettweis, X., Hanna, E., Jeyaratnam, J., Booth, J. F., Datta, R. and Briggs, K.: Arctic cut-off high drives the poleward shift of a new Greenland melting record, Nat. Commun., 7(11723), 6pp, doi:10.1038/ncomms11723, 2016.

Tedstone, A. J., Nienow, P. W., Sole, A. J., Mair, D. W. F., Cowton, T. R., Bartholomew, I. D. and King, M. a: Greenland ice sheet motion insensitive to exceptional meltwater forcing., Proc. Natl. Acad. Sci. U. S. A., 110(49), 19719–24, doi:10.1073/pnas.1315843110, 2013.

Van Tricht, K., Lhermitte, S., Lenaerts, J. T. M., Gorodetskaya, I. V, L'Ecuyer, T. S., Noël, B., van den Broeke, M. R., Turner, D. D. and van Lipzig, N. P. M.: Clouds enhance Greenland ice sheet meltwater runoff, Nat. Commun., 7(May), 10266, doi:10.1038/ncomms10266, 2016.

Vernon, C. L., Bamber, J. L., Box, J. E., van den Broeke, M. R., Fettweis, X., Hanna, E. and Huybrechts, P.: Surface mass balance model intercomparison for the Greenland ice sheet, Cryosph., 7(2), 599–614, doi:10.5194/tc-7-599-2013, 2013.

Whitaker, J. S. and Hamill, T. M.: Ensemble Data Assimilation without Perturbed Observations, Mon. Weather Rev., 130(7), 1913–1924, doi:10.1175/1520-0493(2002)130<1913:EDAWPO>2.0.CO;2, 2002.

Zwally, H. J., Abdalati, W., Herring, T., Larson, K., Saba, J. and Steffen, K.: Surface melt-induced acceleration of Greenland ice-sheet flow., Science (80-.)., 297(5579), 218–22, doi:10.1126/science.1072708, 2002.

Chapter 6: Conclusions and Future Work

6.1 Summary and General Conclusions

The distribution of distinct surface types such as snow, clean ice, impurity-rich ice, melt ponds, and streams are identified as an additional mechanism (in addition to snow grain metamorphic rates and bare ice expansion) to controlling surface albedos in the ablation area of the GrIS. Satellite and in situ observations reveal that the spatial extent of these surface types produce a multi-modal albedo distribution in parts of southwest Greenland. In this part of Greenland, seasonal changes in ablation area and subsequent melt are controlled by the transition from light- to dark-dominated surfaces and melting of outcropped impurity-rich ice layers. A major implication of these results is that as the atmosphere warms, the ice surface will continue to darken, likely contributing to the accumulation of surface impurities, and thereby increase surface melt and runoff. Yet, these processes are not fully represented in current regional climate models (RCMs). Results stemming from a more focused study comparing satellite retrievals with in situ observations of surface albedo confirm the spatial complexity of the ablation area surface. It is also shown that the multiple 'point-to-pixel' comparison is superior to the single 'point-to-pixel' validation technique. These results point to the importance of evaluating the spatial representativeness of ground albedo measurement sites (e.g., automatic weather stations) prior to validation of satellite-derived albedo products. Furthermore, this has implications for current and future adaptation of albedo schemes in RCMs, as some models rely on satellite and surface-based albedo observations to produce spatiotemporally varying albedo estimates.

Prior to this research, RCMs, such as the widely-used MAR model, have not evaluated modeled runoff estimates against drainage basin-scale observations at multiple sites. The inter-comparison between model-observation discharge at three basins located north-to-south in west Greenland reveal that MAR improves its ability to capture discharge variability at longer time aggregations. No systematic explanation for model-observation discrepancies could be readily identified at the three basins. However, investigation into surface conditions and radiative fluxes reveal that the overestimation of shortwave downward radiation is a likely contender, probably due to poor cloud cover simulations. Runoff is expected to continue to dominate mass loss from the GrIS in the future, and RCMs are the primary means of simulating runoff, and subsequent, sea level rise estimates to surrounding oceans. A major implication of these results is therefore that improving hydrologic processes representations in RCMs and validating runoff loss estimates from RCMs with observational data are needed to better constrain modeled runoff estimates. These results also revealed large discrepancies in model discharge estimates during peak discharge events. Through a more directed study examining discharge variability during the extreme melt season of 2012, results from the three discharge basin confirm unprecedented runoff losses occurred during two distinct melt episodes from south-to-northwest Greenland. Anomalous atmospheric circulation patterns, in conjunction with changing surface conditions (e.g., albedo, surface temperature) and radiative effects (particularly downward longwave radiation) contributed to north-to-south differences in daily discharge variability in summer 2012.

6.2 Specific Findings

An analysis of ablation area albedos in southwest Greenland revealed the following:

1) The seasonal ablation area albedos in 2013 follow a bimodal distribution, with snow and ice facies characterizing the two peaks, corresponding to an observed melt rate increase of 51.5% (between 10-14 July and 20-24 July 2013).
2) The seasonal ablation area albedos in 2012 exhibited a more complex multimodal distribution, reflecting a transition from a light to dark-dominated surface, and sensitivity to the "dark-band" region in southwest Greenland.
3) In addition to a darkening surface from ice crystal growth (and snow grain metamorphic rates), the fractional coverage of snow, bare ice, and impurity-rich surface types act as an additional control to seasonal changes in GrIS ablation area albedos.

A multiple 'point-to-pixel' method using in situ spectral albedo observations, high resolution WorldView-2 (WV-2) surface reflectances, and two corresponding MODIS Collection V006 daily blue-sky albedo pixels, and semivariogram analysis, reveal:

1) Within the more homogenous pixel area, in situ and MODIS albedos were very close (error varied from -4% to +7%) and within the range of in situ albedo standard errors. The semiovariogram analysis revealed that the minimum observational footprint needed for a spatially representative sample is 30 m.
2) In contrast, over the more spatially heterogeneous surface pixel, a minimum footprint size was not quantifiable due to spatial autocorrelation, and far exceeds

the effective resolution of the MODIS retrievals. Over the high spatial heterogeneity surface pixel, MODIS is lower than ground measurements by 4-7%, partly due to a known in situ undersampling of darker surfaces that often are impassable by foot (e.g., meltwater features and shadowing effects over crevasses).

3) Despite the sampling issue, our analysis errors are very close to the stated general accuracy of the MODIS product of 0.05. Thus, our study suggests that the MODIS albedo product performs well in a very heterogeneous, low-albedo, area of the ice sheet ablation zone.
4) We demonstrate that single ‘point-to-pixel’ methods alone are insufficient in characterizing and validating the variation of surface albedo displayed in the lower ablation area. This is true because the distribution of in situ data deviations from MODIS albedo show a substantial range, with the average values for the 10^{th} and 90^{th} percentiles being -0.30 and 0.43 across all bands. Thus, if only single point is taken for ground validation, and is randomly selected from either distribution tails, the error would appear to be considerable.

An analysis of model and observed discharge at three drainage basins – Thule, Watson, and Nuuk – located north-to-south in west Greenland, reveals the following:

1) While the MAR model’s ability to resolve daily discharge variability is poor, its ability to capture discharge variability improves at longer time aggregations.
2) The agreement between model-observation discharge is reduced during peak discharge events, such as the exceptional melt season of 2012, for the Thule and

Watson basins. The peak discharge events are underestimated by as much as 110% and 19% at the Thule and Watson basins, on 11 and 12 July 2012, respectively.

3) For the optimal drainage basin delineation, MAR overestimated discharge at the Thule and Nuuk basins, while the Watson basin obtained a good fit. The average error for all available observational years is 63.2%, 3%, and 101.5% of the mean JJA observed river discharge for Thule, Watson, and Nuuk, respectively.
4) No systematic explanation for discrepancies between model-observation discharge across the three sites is discernable. Comparison of model-observation discharge discrepancies are likely caused by an underestimation of cloud cover, brighter surface albedos than are actually realized on the ice sheet surface, and a frequent warm-bias in near-surface air temperatures. Despite these competing forces on melt and subsequent runoff, it appears that overestimation of downward shortwave fluxes dominated, likely due to poor cloud cover simulations, contributing to the overestimation of discharge observed at the Thule and Nuuk basins.
5) Based on our findings, we determine that the Thule basin is the best site to examine model-observation differences because it minimizes the drainage basin delineation uncertainty, and additional 'Thule-like' catchments should be identified to further investigate modeled runoff at the basin-scale.

An analysis of proglacial river discharge during summer 2012 at the three drainage basins discussed above, reveals the following:

1) Annual and daily peak river discharge was unprecedented at all basins in summer 2012. Exceptional flows in all three rivers were observed corresponding with two ice sheet wide surface melt episodes in mid- and late-July 2012.
2) The timing and magnitude of peak discharge during the two melt episodes, and runoff responses, differed at each basin. The timing of peak discharge events during the first melt episode coincided with large atmospheric circulation patterns, resulting in a one-day time lag between peak discharge events at Nuuk, Watson, and Thule basins, moving south-to-north.
3) Drainage basin outflow decreased in magnitude during the second melt episode. Less correspondence is observed between the timing of peak discharge events and atmospheric circulation patterns during the second melt episode.

6.3 Overview of Future Work

The research presented in this dissertation can be expanded upon with current expertise, while some of the research requires additional observations and model adaptation. Below, I identify portions of this research that if furthered would increase our understanding of Greenland surface hydrology and albedo.

The most apparent improvement to the continued study of Greenland surface water hydrology and surface albedo is an increase in observational data collection. Our understanding of Greenland's hydrologic system, and its coupling with albedo, is limited to the current distribution of automatic weather stations (AWSs) and a few gauging stations. The spatial and temporal distribution of these observations are inadequate to robustly validate and improve parameterization of physical processes in RCMs. Until recently, runoff and surface albedo, were understudied components of Greenland's hydrologic system. Our understanding of runoff and albedo has relied primarily on models, often validated with satellite observations or AWS data. This is particularly problematic over spatially heterogeneous surfaces, like the ablation zone, as identified in this dissertation. Additional field observations of river discharge and ablation area albedos are needed. Currently, the three basins investigated in this study represent 1.21% of the total ice sheet area. A significant uptick in ground observational studies is needed. In the absence of ground observations, airborne and satellite observations (and drones), preferably with high spatial and temporal resolution, are desirable. These efforts will serve to improve current and future versions of RCMs to represent hydrometeorological conditions on the ice sheet surface.

To expand upon the research conducted here with additional satellite, airborne and ground observations, computing resources would need to be upgraded. This includes expansion of storage capacity as well as computing performance. By including additional remote sensing and field observations, and more computing resources, this research can be extended across the entire ablation area in Greenland. In addition to a recommended expansion of observational data collection, the next logical step is to incorporate these data and subsequent results into RCMs. To do so, would also require additional computing resources.

With a better understanding of how ablation area albedos and drainage basin runoff losses vary regionally and inter-annually, future directions of research become apparent. First, a comprehensive assessment of surface albedo, particularly in the ablation area is needed. Few in situ observations of surface albedo in Greenland's ablation area have been made. High spatial resolution satellite imagery of surface albedo would allow for adequate characterization of ice sheet surface types and their corresponding albedos. Second, the expansion of the proglacial river discharge research conducted here is timely for the scientific community. While few gauging sites exist in Greenland, the current discharge data set at the three north-to-south drainage basins, can be used to investigate additional RCM's runoff estimates, as it provides latitudinal coverage of basin-scale discharge. These two future studies are outlined below.

6.4 Characterization of Regional-Scale Changes in Ice Surface Types

Expansion of research conducted in Chapter 2 is an important follow-up study given the recent and projected darkening trend in ablation area albedo (e.g., Tedesco et al., 2016). Since few in situ observations of surface albedo have been made in Greenland's ablation area, high spatial resolution satellite imagery of surface albedo provides a realistic alternative to adequately characterize ice sheet surface types, resolve finer-scale patterns and capture the seasonal evolution of surface types, including impurities, dust and sediment-rich surfaces. As projections of increased warming and meltwater generation is expected, future changes in GrIS albedo patterns and feedbacks are also anticipated.

In this project, I propose to do the following: (1) identify spatiotemporal patterns in ablation area albedo and its regional differences, (2) quantify the importance of ice surface types on albedo, and hence, runoff, and (3) develop a seasonally-evolving ice surface type scheme in the MAR model. To carry out this study, a combination of Landsat 8 Operational Land Imager (OLI) data (30 m spatial resolution), with its improved spatial and radiometric resolution, would be used to derive surface reflectance over Greenland’s ablation areas. In addition, higher spatial resolution Sentinel-2 (20 m) and WV-2 data (2 m) would be integrated to examine the spatial and temporal variability in ablation area albedo and produce a spatially-detailed ablation area albedo data set. Using this created data set, dominant surface types (e.g., clean ice, dirty ice, surface water, snow, cryoconite holes, and fractures) would be automatically detected using a classification method developed in remote sensing software. To characterize the seasonal evolution of ice surface types, Landsat 8 derived surface albedo data that encompasses multiple ‘snapshots’ across the melt season will be used and separated by region. If there is a lack of a coherent Landsat 8 time series for a region (e.g., due to persistent cloud cover), then the daily MODIS albedo product (MCD43) Version 6 (500 m spatial resolution), which includes more clear-sky scenes and corrects for known sensor degradation (Wang et al., 2012), will be utilized to assess the temporal evolution of classified ice surface types across the melt season.

To date, no parameterization of spatially and temporally varying light-absorbing impurities have been incorporated into the MAR model albedo scheme. The Landsat 8 surface albedo data set (described above) will be used as input to the adapted MAR albedo scheme. Given the limited temporal resolution of the Landsat 8 dataset, initially, the development of a distributed ice surface type scheme will emphasize changes in the spatial variability of ablation area albedo within the model. The development of a fully integrated surface type and impurity scheme, which varies in space and time, will require the incorporation of the daily MODIS MCD43 albedo product data. These efforts will allow for a detailed evaluation of model performance, the suitability of the new albedo scheme, and how it differs from previous model estimates, current satellite estimates, and affects simulated runoff estimates.

6.5 Integration of River Discharge Research into Regional Climate Models

The gauging data set at the three north-to-south drainage basins, identified in Chapters 4 and 5, affords the research community a unique opportunity to assess seasonal, and inter-annual variability in river discharge at distinctly different drainage basins across the ice sheet. The research in Chapters 4 and 5 provide a framework for investigating additional RCMs, including HIRHAM (e.g., Fausto et al., 2016) and RACMO2.3 (e.g., Noël et al., 2015) RCMs.

In this second project, I propose to (1) quantify model-observation discharge differences in additional RCMs, (2) identify plausible reasons for model-observation discrepancies, and (3) pinpoint additional idealistic basins for model-observation inter-comparison. Here, a blend of time series analysis, similar to the methods of Chapters 4 and 5, as well as meteorological variables from nearby automatic weather stations, would be used. To evaluate model performance and discharge differences more thoroughly, an assessment of simulated meltwater production and retention would be investigated. This would be done by comparing modeled meltwater production estimates with estimates produced by a surface energy balance model driven with AWS-station data (van As et al., 2012, 2017). This would allow for an assessment into whether model-discharge discrepancies can be explained by model estimates of how much meltwater is produced at the ice surface, or if simulated surface and radiative conditions, such as radiative energy fluxes or surface albedo, are responsible for inter- and intra-model differences. Non-radiative fluxes, including sensible and latent heat fluxes, derived from the SEB and RCMs will be compared. Lastly, the runoff delay function will be examined and optimized for each RCM, as it has been identified to dampen modeled daily discharge values (see Chapter 4). While the runoff delay function is present in the MAR model, it is non-existent in the HIRHAM and RACMO2.3 models. The current runoff delay function in MAR is optimized using time lag coefficients based on observations collected in Summit, Greenland (Lefebre et al., 2003). To obtain more realistic runoff delay function times, the latest runoff delay function equation reported in van As et al. (2017) would be applied. This calculation would be tested against previous runoff delay function equations found in Zuo and Oerlemans (1996). These three runoff delay functions would be applied to each RCM, and the runoff estimates would be inter-compared to identify the best lag time. These efforts will be particularly important for the Watson and Nuuk basins, where meltwater production and runoff experiences a time delay due to supraglacial features as well as transport in en- and sub-glacial systems. Lastly, a probability-based catchment delineation routine (Carroll et al., 2016) integrated into a continental-wide drainage basin routine (Rennermalm et al., *in prep*., 2017) would be applied to identify suitable catchments (similar to the Thule basin identified in Chapter 4). Identifying suitable drainage basins in the southwest region of Greenland would be emphasized, as they have exhibited the greatest increase in runoff trends (Mernild and Liston, 2012) and outflow to surrounding oceans (Bamber et al., 2012). These additional drainage basins would be compared against modeled discharge estimates for the three drainage basins with river discharge data available. These efforts will allow for a detailed evaluation of inter- and intra-model performance, the suitability of the previous and updated runoff delay functions, and improve modeled runoff estimates from several RCMs.

6.6 References

van As, D., Hubbard, a. L., Hasholt, B., Mikkelsen, a. B., van den Broeke, M. R. and Fausto, R. S.: Large surface meltwater discharge from the Kangerlussuaq sector of the Greenland ice sheet during the record-warm year 2010 explained by detailed energy balance observations, Cryosph., 6(1), 199–209, doi:10.5194/tc-6-199-2012, 2012.

van As, D., Bech Mikkelsen, A., Holtegaard Nielsen, M., Box, J., Claesson Liljedahl, L., Lindbäck, K., Pitcher, L. and Hasholt, B.: Hypsometric amplification and routing moderation of Greenland ice sheet meltwater release, Cryosph. Discuss., (January), 1–30, doi:10.5194/tc-2016-285, 2017.

Bamber, J., Van Den Broeke, M., Ettema, J., Lenaerts, J. and Rignot, E.: Recent large increases in freshwater fluxes from Greenland into the North Atlantic, Geophys. Res. Lett., 39(19), 8–11, doi:10.1029/2012GL052552, 2012.

Carroll, D., Sutherland, D. A., Hudson, B., Moon, T., Catania, G. A., Shroyer, E. L., Nash, J. D., Bartholomaus, T. C., Felikson, D., Stearns, L. A., Noël, B. P. Y. and van den Broeke, M. R.: The impact of glacier geometry on meltwater plume structure and submarine melt in Greenland fjords, Geophys. Res. Lett., 43(18), 9739–9748, doi:10.1002/2016GL070170, 2016.

Fausto, R. S., van As, D., Box, J. E., Colgan, W., Langen, P. L. and Mottram, R. H.: The implication of nonradiative energy fluxes dominating Greenland ice sheet exceptional ablation area surface melt in 2012, Geophys. Res. Lett., (April), doi:10.1002/2016GL067720, 2016.

Lefebre, F., Gallée, H., vanYpersele, J. and Greuell, W.: Modeling of snow and ice melt at ETH Camp (West Greenland): A study of surface albedo, J. Geophys. Res., 108, 4231, doi:10.1029/2001JD001160, 2003.

Mernild, S. H. and Liston, G. E.: Greenland Freshwater Runoff. Part II: Distribution and Trends, 1960–2010, J. Clim., 25(17), 6015–6035, doi:10.1175/JCLI-D-11-00592.1, 2012.

Noël, B., Van De Berg, W. J., Van Meijgaard, E., Kuipers Munneke, P., Van De Wal, R. S. W. and Van Den Broeke, M. R.: Evaluation of the updated regional climate model RACMO2.3: Summer snowfall impact on the Greenland Ice Sheet, Cryosphere, 9(5), 1831–1844, doi:10.5194/tc-9-1831-2015, 2015.

Tedesco, M., Mote, T., Fettweis, X., Hanna, E., Jeyaratnam, J., Booth, J. F., Datta, R. and Briggs, K.: Arctic cut-off high drives the poleward shift of a new Greenland melting record, Nat. Commun., 7(11723), 6pp, doi:10.1038/ncomms11723, 2016.

Wang, Z., Schaaf, C. B., Chopping, M. J., Strahler, A. H., Wang, J., Román, M. O., Rocha, A. V., Woodcock, C. E. and Shuai, Y.: Evaluation of Moderate-resolution

Imaging Spectroradiometer (MODIS) snow albedo product (MCD43A) over tundra, Remote Sens. Environ., 117, 264–280, doi:10.1016/j.rse.2011.10.002, 2012.

Zuo, Z. and Oerlemans, J.: Modelling albedo and specific balance of the Greenland ice sheet: Calculations for the Søndre Strømfjord transect, J. Glaciol., 42(141), 305–316, doi:10.3198/1996JoG42-141-305-317, 1996.

Acknowledgement of Prior Publications

The four main chapters of this thesis (Chapters 2-5) were either previously published, in review for publication, or are expected to be published in peer-reviewed journals. Chapter 2 was previously published by *The Cryosphere* under the title "Multi-modal albedo distributions in the ablation area of the southwestern Greenland Ice Sheet". *The Cryosphere* holds the copyright to this published work. Chapter 3 is under review for publication with the *Remote Sensing of Environment* under the title "Evaluation of satellite remote sensing albedo retrievals over the ablation area of the southwestern Greenland ice sheet" and the appendix contains another published dataset with *PANGAEA* under the title "Spectral and broadband albedo transects in the lower ablation zone, Southwest Greenland, June 2013". The majority of the analysis and writing in these papers are my own, done with the help, advice and feedback from co-authors, colleagues, and reviewers.